SYNTHESIS AND CHARACTERIZATION OF TRANSITION METAL DICHALCOGENIDE HETEROSTRUCTURES

by

AARON M. MILLER

A DISSERTATION

Presented to the Department of Chemistry and Biochemistry and the
Division of Graduate Studies of the University of Oregon
in partial fulfillment of the requirementsfor the degree of
Doctor of Philosophy

December 2022

DISSERTATION APPROVAL PAGE

Student: Aaron M. Miller

Title: Synthesis and Characterization of Transition Metal Dichalcogenide Heterostructures

This dissertation has been accepted and approved in partial fulfillment of the requirements for the Doctor of Philosophy degree in the Department of Chemistry and Biochemistry by:

Prof. Carl Brozek	Chairperson
Prof. David C. Johnson	Advisor
Prof. Shannon W. Boettcher	Core Member
Prof. Eric Corwin	Institutional Representative

and

Krista Chronister	Vice Provost for Graduate Studies

Original approval signatures are on file with the University of Oregon Division of Graduate Studies.

Degree awarded December 2022

© 2022 Aaron M. Miller

DISSERTATION ABSTRACT

Aaron M. Miller

Doctor of Philosophy

Department of Chemistry & Biochemistry

December 2022

Title: SYNTHESIS AND CHARACTERIZATION OF TRANSITION METAL DICHALCOGENIDE HETEROSTRUCTURES

Synthesis of new materials drives technological advances, but the ability to consistently predict and synthesize a material with specific properties remains unrealized, especially for metastable materials. Using the modulated elemental reactants (MER) method provides additional experimental parameters that can be used to drive the reaction towards formation of the desired product. This work leverages the MER synthetic approach to study a variety of transition metal dichalcogenide (TMD) thin films and heterostructures based on TMD's.

This work begins with an overview of conventional synthetic approaches used to grow TMD thin films – highlighting the advantages and disadvantages of each technique, along with key reaction steps and examples of typical reaction conditions. After this introductory section, a method to extract the maximum possible quantity of structural information from x-ray diffraction patterns containing Laue oscillations is presented. Next, an automated system to measure the temperature-dependent electrical resistivity and Hall Effect for thin film samples, which is utilized in subsequent experimental chapters to characterize electrical transport properties, is discussed.

The latter half of this dissertation contains several experimental

synthetic investigations of TMD thin film and TMD heterostructure systems leveraging the MER synthetic method – including synthesis and characterization of a family of $[(PbSe)_{1+\delta}]_4[TiSe_2]_4$ isomers, a novel compound $(BiSe)_{0.97}(Bi_2Se_3)_{1.26}(BiSe)_{0.97}(MoSe_2)$ containing metallic 1T-$MoSe_2$, and a metastable heterostructure based on intergrowths of crystalline $TiSe_2$ and amorphous Si layers.

CURRICULUM VITAE

NAME OF AUTHOR: Aaron M. Miller

GRADUATE AND UNDERGRADUATE SCHOOLS ATTENDED:

University of Oregon, Eugene, OR
Gustavus Adolphus College, St. Peter, MN

DEGREES AWARDED:

Doctor of Philosophy, Chemistry, 2021, University of Oregon
Master of Science, Chemistry, 2020, University of Oregon
Bachelor of Arts, Chemistry, ACS Certified, 2018, Gustavus Adolphus College

AREAS OF SPECIAL INTEREST:

Materials Science
Thin Film Deposition
Materials Characterization
Process Control

PROFESSIONAL EXPERIENCE:

Research Assistant, D. C. Johnson Research Group, University of Oregon, 2019 - 2022

Research Assistant, B. O'Brien Research Group, Gustavus Adolphus College, 2016 – 2018

Statistics and Metrology Intern, PQI Inc., 2017-2017

PUBLICATIONS:

Miller, A.M.; Johnson, D.C. Challenges in synthesis of heterostructures. *J. Mater. Chem C.* 2022. 10, 6546-6562 DOI: 10.1039/D2TC00324D

Miller, A.M.; Lemon, M.; Choffel, M.A.; Rich, S.R.; Harvel, F.; Johnson, D.C. Extracting information from X-ray diffraction patterns containing Laue oscillations. *Zeitschrift für Naturforschung B.* 2022. 77(4-5)b, 313-

322. DOI: 10.1515/znb-2022-0020

Choffel, M.A.; Gannon, R.N.; Göhler, F.; Miller, A.M.; Medlin, D.L.; Seyller, T.; Johnson, D.C. Synthesis and Electrical Properties of a New Compound $(BiSe)_{0.97}(Bi_2Se_3)_{1.26}(BiSe)_{0.97}(MoSe_2)$ Containing Metallic 1T-$MoSe_2$. *Chem Mater*. 2021, 33, 16, 6403-6411. 10.1021/acs.chemmater.1c01623

Miller, A.M.; Hamann, D.M.; Hadland, E.C.; Johnson, D.C. Investigating the Formation of $MoSe_2$ and $TiSe_2$ Films from Artificially Layered Precursors. *Inorg. Chem*. 2020, 59 (17), 12536-44. 10.1021/acs.inorgchem.0c01416

Hamann, D.M.; Bauers, S.R, Miller, A.M.; Ditto, J.; Moore, D.B.; Johnson, D.C. Synthesis and Characterization of $[(PbSe)_{1+\delta}]_4[TiSe_2]_4$ Isomers. *Inorg. Chem*, 2020, 59 (15), 10928-37. doi.org/10.1021/acs.inorgchem.0c01416

LeRoy, M.A.; Mroz, A.M.; Mancuso, J.L.; Miller, A.M.; Van Cleve, A.; Check, C.; Heinz, H.; Hendon, C.H.; Brozek, C.K. Post-Synthetic Modification of Ionic Liquids Using Ligand-Exchange and Redox Coordination Chemistry. *J. Mater. Chem. A*., 2020, 8, 22674-22685. doi.org/10.1039/D0TA06195F

ACKNOWLEDGMENTS

I would like to acknowledge the numerous people who have supported me throughout my graduate school journey – you have all been an essential part of my success at UO and I will be forever grateful for your role in ensuring that I had the energy, willpower, and/or knowledge to continue to make progress toward my thesis. I need to begin by expressing my gratitude for my wonderful advisor, Dr. David C. Johnson, who let me work in his research lab, offered me constant guidance and advice on research challenges, and continued to push me to grow as a critical thinker, chemist, and materials scientist throughout my time at UO. I also need to thank my colleagues, Dr. Danielle Hamann, Dr. Renae Gannon, Dr. Marisa Choffel, Mellie Lemon, Hannah Blackwood, Sarah Rich, Fischer Harvel, and Celsey Price. My labmates were instrumental in helping me succeed, especially during challenging times when equipment issues and pandemic-related supply chain problems interfered with research. Additionally, I need to acknowledge the efforts of the previous Dave Johnson lab members, without which I would've never been able to pursue the topics discussed in my thesis – we go forwards on the shoulders of those who came before us.

I also need to acknowledge the CAMCOR staff members and UO Technical Services Administration (TSA) for your support of our lab. Specifically, Steve Weimholt, Jeffrey Garman, John Boosinger, and Cliff Dax were crucial in helping to repair broken equipment and fabricate custom parts for our lab. Your willingness to share your knowledge and perspective and work on the revolving-door array of broken equipment was absolutely vital to my success.

This research would not be possible without the support of my collaborators. Specifically, I've learned a lot from Yu Wang and Professor Stephen B. Cronin about electrical transport measurements.

I also need to acknowledge funding from the U.S. Department of Energy (DOE), Office of Science, Basic Energy Sciences (BES) under Award #DE-SC0020095. Chapter IX of this work was additionally supported by National Science Foundation under grants DMR-1710214 and 1905185. Sandia National Laboratories was instrumental for HAADF-STEM images. Sandia National Laboratories is a multi-mission laboratory managed and operated by National Technology and Engineering Solutions of Sandia, LLC, a wholly owned subsidiary of Honeywell International Inc. for the U.S. Department of Energy's National Nuclear Security Administration under contract DE-NA-0003525. This paper describes objective technical results and analysis. Any subjective views or opinions that might be expressed in the paper do not necessarily represent the views of the U.S. Department of Energy or the United States Government.

Thank you to all the past professors, teachers, mentors that have taught me and helped form me into the scientist and person I've become. I'm forever indebted to you for indulging my constant questions and curiosity.

Thanks to my committee members, who always pushed me to keep deepening and extending my understanding of science. Thanks to the Department of Chemistry staff and faculty for support and guidance.

Last, but certainly not least, I would have been successful without the unconditional love and support from my parents, grandparents, relatives, and friends. I love you all.

TABLE OF CONTENTS

Chapter | Page

I. INTRODUCTION 22

1.1 Dissertation Overview 22

1.2 Brief History of Materials Discovery 24

1.3 Bridge 28

II. CHALLENGES IN SYNTHESIS OF HETEROSTRUCTURES 32

2.1 Introduction 32

2.2 Direct Reaction of Elements and/or Compounds 38

2.3 Fluid-assisted Synthesis Techniques 40

2.4 Chemical vapor transport (CVT) 42

2.5 Chemical vapor deposition (CVD) 44

2.6 Micromechanical assembly 47

2.7 Molecular beam epitaxy (MBE) 51

2.8 Modulated elemental reactants (MER) 53

2.9 Conclusion 61

2.10 Bridge 67

III. EXPERIMENTAL METHODS 79

3.1 Synthesis of Layered Precursors with Modulated Elemental Reactants 79

3.2 X-Ray Fluorescence and Statistical Process Control 80

3.3 Structural Characterization Techniques 83

3.4 Electrical Characterization Techniques 84

3.5 Bridge 84

Chapter Page

IV. EXTRACTING INFORMATION FROM X-RAY DIFFRACTION PATTERNS CONTAINING LAUE OSCILLATIONS 87

4.1 Introduction 87

4.2 X-ray reflectivity (XRR) and Kiessig fringes 89

4.3 Laue oscillations 93

4.4 Developing structural models from Kiessig Fringes and Laue oscillations 100

4.5 Conclusions 104

4.6 Experimental 104

4.7 Bridge 106

V. AUTOMATED TEMPERATURE-DEPENDENT ELECTRICAL RESISTIVITY AND HALL EFFECT MEASUREMENT SYSTEM 111

5.1 Van der Pauw method 111

5.2 System Overview 114

5.3 Temperature Stabilization 117

5.4 Electrical Resistivity 118

5.5 Hall Effect 119

5.6 Bridge 120

VI. INVESTIGATING THE FORAMTION OF $MOSE_2$ AND $TISE_2$ FILMS FROM ARTIFICIALLY LAYERED PRECURSORS 122

6.1 Introduction 122

6.2 Materials and Methods 124

6.3 Results and Discussion 125

6.4 Conclusions 140

Chapter Page

6.5 Bridge 141

VII. SYNTHESIS AND CHARACTERIZATION OF $SI(TISE_2)_n$ HETEROSTRUCTURES 146

7.1 Introduction 146

7.2 Results and Discussion 150

7.3 Conclusion 160

7.4 Bridge 161

VIII. SYNTHESIS AND CHARACTERIZATION OF $[(PBSE)_{1+\delta}]_4[TISE_2]_4$ ISOMERS 165

8.1 Introduction 165

8.2 Materials and Methods 167

8.3 Results and Discussion 168

8.4 Conclusion 190

8.5 Bridge 191

IX. SYNTHESIS AND ELECTRICAL PROPERTIES OF A NEW COMPOUND $(BISE)_{0.97}(BI_2SE_3)_{1.26}(BISE)_{0.97}(MOSE_2)$ CONTAINING METALLIC 1T-$MOSE_2$ 198

9.1 Introduction 198

9.2 Materials and Methods 200

9.3 Results and Discussion 202

9.4 Conclusion 218

9.5 Bridge 219

X. CONCLUSIONS AND SUMMARY 227

APPENDICES

A. SUPPORTING INFORMATION FOR CHAPTER VI 230

Chapter Page

B. SUPPORTING INFORMATION FOR CHAPTER VIII 232

C. SUPPORTING INFORMATION FOR CHAPTER IX 234

LIST OF FIGURES

Figure Page

1.1 Change in impurity concentration in metal with Blowing time in Bessemer process and Gilchrist-Thomas process. 25

2.1 Image showing complexity of Cu interconnect structure of a 14 nm logic integrated circuit. 33

2.2 The ability to prepare heterostructures by stacking 2D layers in designed sequences enables preparation of 2D electronic devices, such as this hypothetical stack of alternating p- and n-type semiconducting layers. 34

2.3 Representative HAADF-STEM images of six of the possible “isomer” 35

2.4 Schematic depiction of the reaction of elements Pb, Ti, and Se to form binary intermediates PbSe and $TiSe_2$, and ternary product and misfit layered compound, $(PbSe)_{1.18}(TiSe_2)_2$ 40

2.5 Schematic depiction of the evolution of the nucleation of crystalline phases during the cooling of a fluid-assisted synthesis reaction 44

2.6 Schematic depiction of the CVT synthesis of MoS_2 43

2.7 Schematic depictions of two types of CVD reactors. 45

2.8 Schematic of MBE reactor 51

2.9 Schematic depiction of two different reaction pathways in the reaction between ultra-thin layers of Mo and Se 57

2.10 Schematic depiction of two sample layering sequences for deposition of MER precursors. 59

2.11 Schematic free energy surface for the BiSe-$NbSe_2$ system showing some of the possible kinetically stable heterostructures containing an equal number of BiSe and $NbSe_2$ layers and the thermodynamically stable product $(BiSe)(NbSe_2)_1$ 62

3.1 Schematic side-view of the high-vacuum chamber used to

Figure Page

deposit ultrathin elemental layers to form nanostructured precursors. 81

3.2 Plots of the measured XRF intensity for Ti and Sn using samples that display Laue oscillations, allowing for the determination of the integral number of crystalline unit cells 82

4.1 Experimental X-ray reflectivity pattern of a 50.10(5) nm $TiSe_2$ film.. 90

4.2 Simulated reflectivity patterns from a 30.19 nm $TiSe_2$ film with different amounts of interfacial roughness......... 92

4.3 Simulated XRR patterns of TiO_2 and $TiSe_2$ films 93

4.4 Experimental XRR and XRD patterns of a 79-layer crystalline $TiSe_2$ film... 94

4.5 Comparison of the experimental Laue oscillations with that calculated from the Laue interference function and a simulation that includes reflectivity using the BedeREFS simulation software................................. 97

4.6 Experimental diffraction data of a $(BiSe)_{0.97}(Bi_2Se_3)_{1.26}(BiSe)_{0.97}(MoSe_2)$ heterostructure........ 98

4.7 Simulated XRR patterns of a 50-layers $TiSe_2$ film on a Si substrate illustrating how the roughness affects the symmetry of the satellite reflections around the Bragg reflections.. 99

4.8 Simulations of diffraction patterns from different distributions of coherently diffracting domains................ 100

4.9 Experimental XRR (*gray*) and XRD (*black*) patterns of a 271.0(2) Å thick crystalline $Fe_xV_{1-x}Se_2$ film and simulated XRR pattern (teal) for a 267.9 Å thick $Fe_xV_{1-x}Se_2$ film consisting of 44 unit cells. 102

4.10 Experimental XRR (*grey*) and XRD (*black*) patterns of a $(BiSe)_{0.97}(Bi_2Se_3)_{1.26}(BiSe)_{0.97}(MoSe_2)$ heterostructure annealed at 350 °C 103

5.1 Top-down schematic of thin film sample holder with soldered In contacts in each of the four corners of the sample's top Hall Cross. 112

Figure Page

5.2 Schematic overview of the structure for the automated system's code. 116

6.1 XRR and XRD patterns from an annealing study of an as-deposited Mo|Se precursor... 126

6.2 Grazing incidence in-plane diffraction of a $MoSe_2$ film after being annealed at 650 °C for 60 min. 129

6.3 $MoSe_2$ crystal quality as determined by specular diffraction reflection intensity and peak width graphed vs the composition of the Mo|Se precursor. 129

6.4 XRR and XRD patterns from an annealing study of an as-deposited Ti|Se precursor with a starting composition of 1:2.24 (Ti / Se)... 132

6.5 Representative specular and in-plane XRD patterns of Ti|Se thin films with various compositions..... 135

6.6 Line widths (fwhm) of the 110 reflection in the in-plane XRD pattern (top) and 001 reflection in the specular XRD pattern (middle) and 001 reflection net area (bottom) as a function of precursor composition. 138

6.7 Experimental specular XRD patterns (*red*) for the highest quality annealed $TiSe_2$ films overlaid with the theoretical Laue oscillations expected for n layers of $TiSe_2$ (*black*).. 138

6.8 Proposed atomic-level pictures for the evolution of Mo|Se and Ti|Se precursors as they are annealed to form crystalline $MoSe_2$ and $TiSe_2$................................. 140

7.1 Schematic depiction of the reaction of a layered $(Ti|Se)_4$|Si precursor to form a $(TiSe_2)_4$|Si heterostructure.. 149

7.2 XRR (left) and XRD (right) patterns for the n = 4, 7, and 9 $Si(TiSe_2)_n$ heterostructures collected immediately after deposition and prior to annealing. 151

7.3 XRR and XRD patterns for the n = 4, 7, and 9 $Si(TiSe_2)_n$ heterostructures collected after annealing at 350 °C for 30 m. 153

Figure Page

7.4 Plot of *c*-axis lattice parameter vs *n* for the three films shown in Figure 7.3 154

7.5 Representative grazing-incidence in-plane x-ray diffraction patterns for as-deposited and annealed $(TiSe_2)_n$Si heterostructure. 154

7.6 Simulated x-ray reflectivity (XRR) patterns for $(TiSe_2)_n$|Si heterostructures with "perfect" nanoarchitecture 155

7.7 Schematic depiction of a $n = 4$ heterostructure, depicting 3 out of the 7 actual RU's. 157

7.8 Simulated x-ray reflectivity (XRR) patterns for $(TiSe_2)_n$|Si heterostructures with variance in the thickness of each *a*-Si layer 158

7.9 Schematic depiction of a $n = 4$ heterostructure, depicting 3 out of the 7 actual RU's. 159

7.10 Simulated x-ray reflectivity (XRR) patterns for $(TiSe_2)_n$|Si heterostructures with variance in the number of $TiSe_2$ layers crystallized in each RU. 160

8.1 Representative as-deposited XRR and XRD for a 2**1**1**2**1**1** isomer demonstrating behavior observed in all of the $[(PbSe)_{1+\delta}]_4(TiSe_2)_4$ isomer heterostructures. 169

8.2 Experimental and simulated XRR patterns for the 3**2**1**2** structural isomer. 173

8.3 Schematic representation of the variation of electron density through a unit cell for each of the $[(PbSe)_{1+\delta}]_4(TiSe_2)_4$ isomers 175

8.4 X-ray reflectivity patterns (*in color*) shown against simulated patterns created using models of the targeted isomers (*in black*) described in Figure 8.3. 177

8.5 Specular and in-plane XRD patterns of the $[(PbSe)_{1+\delta}]_4(TiSe_2)_4$ structural isomers. 179

8.6 HAADF-STEM image of the 44 $[(PbSe)_{1+\delta}]_4(TiSe_2)_4$ structural isomer showing the entire film from substrate

Figure Page

to surface........ 181

8.7 HAADF-STEM images of each isomer heterostructure highlighting the formation of the targeted nanoarchitecture, sharp interfaces between constituents, and rotational misregistration between layers........ 182

8.8 Atomistic picture demonstrating the initial crystallization in the isomers and a snapshot showing the movement of atoms and further crystal growth upon annealing. 184

8.9 Temperature-dependent resistivity of six $[(PbSe)_{1+\delta}]_4(TiSe_2)_4$ isomer heterostructures, with both measured and normalized values. 186

8.10 Temperature-dependent carrier concentration and mobility) of six $[(PbSe)_{1+\delta}]_4(TiSe_2)_4$ isomer heterostructures. 188

8.11 Room-temperature Seebeck coefficients for each of the $[(PbSe)_{1+\delta}]_4(TiSe_2)_4$ isomer heterostructures........ 189

8.12 Schematic demonstrating charge donation occurring in isomers containing different numbers of buried interfaces........ 190

9.1 XRR and specular X-ray diffraction and representative in-plane X-ray diffraction patterns of the samples after annealing to 350 °C. 205

9.2 Amounts of Bi and Mo in the samples compared to the estimated amounts to form $[(Bi_2Se_3)_{1+y}]_2(MoSe_2)$ and $(BiSe)_{1+x}(Bi_2Se_3)_{1+y}(BiSe)_{1+x}(MoSe_2)$ 207

9.3 XRR and specular XRD patterns and in-plane XRD patterns of sample 1 as a function of temperature........ 209

9.4 Representative HAADF-STEM image of the $(BiSe)_{0.97}(Bi_2Se_3)_{1.26}(BiSe)_{0.97}(MoSe_2)$ heterostructure annealed to 350 °C........ 210

9.5 HAADF-STEM image of the $(BiSe)_{0.97}(Bi_2Se_3)_{1.26}(BiSe)_{0.97}(MoSe_2)$ heterostructure with zone axes labeled.. 212

Figure Page

9.6 HAADF-STEM images, which show a region of (a) 1T-$MoSe_2$ and (b) 2H-$MoSe_2$. 213

9.7 XPS analysis of the (a) Mo 3d, (b) Se 3d, and (c) Bi 5d core levels. 215

9.8 Temperature-dependent resistivity data of $(BiSe)_{0.97}(Bi_2Se_3)_{1.26}(BiSe)_{0.97}(MoSe_2)$ samples are plotted as a function of temperature for comparison with the $(BiSe)_{0.97}(MoSe_2)$ heterostructures. 216

9.9 Temperature-dependent Hall data plotted as a function of temperature for $(BiSe)_{0.97}(Bi_2Se_3)_{1.26}(BiSe)_{0.97}(MoSe_2)$. 217

A.1 XRR of Ti|Se annealing study showing evolution of film thickness and roughness as energy is applied to the system. 230

A.2 Specular and in-plane XRD patterns for additional Ti|Se precursors annealed at 350°C showing the influence of precursor composition on structure.............. 230

A.3 XRR patterns for various Ti|Se precursors annealed at 350 °C showing the variation in roughness and loss of layers as a function of stoichiometry. 231

A.4 Experimental and simulated XRR patterns demonstrating effect of oxide growth. Based on the amount of excess material in each film, the annealed films developed either a thin (~9 Å) or thick (~60 Å) oxide layer. 231

B.1 Representative as-deposited XRR patterns demonstrating the initial layering and rearrangement occurring in the sample before annealing occurs. 232

B.2 Representative grazing incidence in-plane diffraction of an as-deposited $[(PbSe)_{1+\delta}]_1[TiSe_2]_1$ heterostructure demonstrating the initial nucleation of both PbSe and $TiSe_2$ crystallites before annealing............ 233

B.3 STEM-EDS showing the relative intensity of characteristic X-ray signals from Pb and Ti when moving down the k=2**3**2**1** structure................................ 233

Figure Page

C.1 Electron dispersive x-ray spectroscopy (EDS) line profile from substrate to surface of $(BiSe)_{0.97}(Bi_2Se_3)_{1.26}(BiSe)_{0.97}(MoSe_2)$ 234

LIST OF TABLES

Table Page

2.1 A Summary of synthetic techniques typically used in the synthesis of van der Waal's heterostructures.................... 64

4.1 Experimental and target atomic areal density for the Fe-doped VSe_2 and $(BiSe)_{0.97}(Bi_2Se_3)_{1.26}(BiSe)_{0.97}(MoSe_2)$ films as determined from XRF measurements 103

6.1 Structure and Composition Summary for the As-Deposited Ti|Se Precursors....................................... 132

6.2 Compositions and Lattice Parameters for Annealed Ti|Se Films As Determined from Full Pattern XRD Le Bail Fits 134

7.1 Structural data extracted from experimental x-ray diffraction and x-ray reflectivity patterns for as-deposited $(Ti|Se)_nSi$ heterostructures.. 147

7.2 Composition data extracted from experimental x-ray fluorescence intensities for as-deposited (Ti|Se)nSi heterostructures 148

7.3 Structural data extracted from experimental x-ray diffraction and x-ray reflectivity patterns for $(TiSe_2)_nSi$ heterostructures annealed at 350 °C 149

8.1 Total Atoms/Å^2 in Each of the Annealed $[(PbSe)_{1+\delta}]_4(TiSe_2)_4$ Isomer Films 171

8.2 Calculated Number of Atoms/Å^2 for Each Element in the $[(PbSe)_{1+\delta}]_4(TiSe_2)_4$ Isomers for Different Film Thicknesses....................................... 171

8.3 Parameters Extracted from the XRR Patterns as Described in the Text 176

Table Page

9.1 Amounts of Material and Repeating Thicknesses for Samples Targeting the $(BiSe)_{1+x}(Bi_2Se_3)_{1+y}(BiSe)_{1+x}(MoSe_2)$ Nanoarchitecture......... 203

B.4 Total Film thickness and repeat layer

thickness for representative
$[(PbSe)_{1+\delta}]_4[TiSe_2]_4$ isomer heterostructures....................... 232

CHAPTER I

INTRODUCTION

1.0 Authorship Statement

This chapter was written for this work alone with no intention of publishing it elsewhere. I am the primary author and wrote the following with editorial assistance from my advisor, David C. Johnson.

1.1 Dissertation Overview

This thesis explores the synthesis and characterization of transition-metal dichalcogenide (TMD) thin films and TMD heterostructures, created by stacking ultrathin layers of 2D materials. The thesis is split into two sections – the first presents a comprehensive discussion of each experimental technique, along with several chapters that advance existing experimental methods. The second half of the work presents experimental studies on different TMD material systems, leveraging the advances in experimental methods described in the first section to assist in the synthesis and characterization of novel TMD heterostructures.

The opening section, containing Chapters II – V, details the experimental methods used to synthesize and characterize thin film samples, including a literature review that summarizes current challenges in conventional synthetic approaches to 2D heterostructures (Chapter II was previously published in the *Journal for Materials Chemistry C* in 2022).[1] The following chapter reviews the suite of x-ray characterization techniques that are used to elucidate the sample's structure and composition. Next, Chapter IV (previously published in *Zeitschrift für Naturforschung B* in 2022) contains an extensive discussion of the physics involved in x-ray reflectivity diffraction experiments and leverages this understanding of the underlying physics to show how structural information can be extracted from x-ray diffraction patterns containing Laue oscillations.[2] The final chapter in the first section of this work contains a description of the automated measurement system built

and coded by the author, which is used by the Johnson Lab to measure the electrical resistivity and Hall effect as a function of temperature for thin film samples.

The final section, Chapters VI – X, presents experimental studies exploring various TMD systems, with an emphasis on heterostructures and thin films containing titanium and molybdenum diselenide ($TiSe_2$ and $MoSe_2$). The opening chapter of this section presents my initial efforts to synthesize TMD's, which could be used as components for more heterostructures with more complex nanoarchitecture later. By studying the effect of precursor composition on the resulting annealed binary $MoSe_2$ and $TiSe_2$ thin films, we were able to conclude that depositing layered precursors with approximately 15% excess selenium results in high-quality thin films with large crystallite sizes and visible Laue oscillations up to the 30th order (Chapter VI was previously published in *Inorganic Chemistry* in 2020).[3]

After optimizing the synthesis of binary TMD films, I attempted to grow heterostructures using a crystalline and an amorphous component. I interleaved few-layer crystalline $TiSe_2$ between layers of amorphous Si of varying thickness, resulting in films with a unique combination of a defined superlattice, but with the inclusion of a material with a complete lack of periodic structure. This chapter describes the initial efforts of the synthetic exploration of the $TiSe_2$ + *a*-Si intergrowth system.

Next, I studied more complex layering sequences, synthesizing six novel isomer heterostructures, making up the six possible combinations of an eight-layer-thick unit cell consisting of four PbSe layers and four $TiSe_2$ layers. Chapter VIII presents the preparation and characterization of these heterostructures. The precursors used in the study were deposited with compositions that were far from the desired values, but surprisingly, the heterostructures still crystallized with the desired nanoarchitecture. Extensive structural modeling was used to understand the complex x-ray

reflectivity patterns (previously published in *Inorganic Chemistry).*[4]

The penultimate chapter describes the synthesis and characterization of another novel compound $(BiSe)_{0.97}(Bi_2Se_3)_{1.26}(BiSe)_{0.97}(MoSe_2)$. This heterostructure was found to contain a significant amount of metallic 1T-$MoSe_2$ as a result of the increased charge transfer from the two adjacent BiSe layers (Chapter IX was previously published in *Chemistry of Materials* in 2021).[5]

1.2 Brief history of materials discovery

Materials discovery is a significant factor driving the development of new technology. The history of humanity is even discussed through the lens of materials discoveries, with eras named after materials that enabled significant advances or cultural shifts. Early humans constructed tools and weapons from materials they encountered in their environments. Archaeological evidence suggests early humans knapped stone into tools and sought other materials like bone, feathers, animal skins, and clays for specific purposes.[6] Copper (Cu) is among the elements that can rarely be found in nature in its native state, so it is probable that early humans discovered Cu nuggets and began to shape them into basic forms. Shaped Cu artifacts dating back to 5000 BCE have been found.[7] It is unknown exactly when early humans discovered these metals can be heated to make them malleable again after work hardening occurs. During re-heating, the metal's hardness increases, and if the Cu-bearing ore or the smelting container contains other metals, the resulting alloy can have improved properties. It is likely that alloys were initially discovered by accident. Once discovered, it is likely that humans enhanced this effect through experimentation. By 3000 BCE, copper-arsenic alloys were used for tools and ritual weapons.[8,9] It was soon discovered, again probably by accident, that alloying Cu with Sn gave a superior alloy, bringing about the Bronze Age.[10,11]

Additional advances brought about widespread use of additional

metals, ceramics, and cements. At the end of the Middle Ages, advances in metalworking resulted in iron alloys with improved properties, bringing about the Iron Age. While steel was rarely prepared as an Fe alloy for many years prior to the Industrial Revolution, resulting in the “magic” swords known in several cultures, there were no known processes that allowed for reproducible or industrial-scale production, severely limiting its use.[12] The Bessemer process, which involves blowing air through molten pig iron to oxidize impurities into easily separable slag, was invented in the 1850s. Widespread implementation of this process caused the cost of steel production to plummet, enabling steel to replace iron as the material of choice in weaponry, construction, and manufacturing.[13] The development of the basic Bessemer (or Thomas-Gilchrist) process in 1879, which used dolomite-based ($(Ca,Mg)CO_3$) furnace liners, enabled the use of more common phosphorus-rich iron ores.[14] Eventually, both the acidic Bessemer and basic Thomas-Gilchrist processes were fully understood and optimized, allowing control over the concentration of dopants remaining in the alloy, as shown in Figure 1.1. Gradual improvements to this process, a variation of which is still universally used today, enabled the use of steel and cast iron in complex structures such as those in bridges, buildings, ships, trains, and cars.

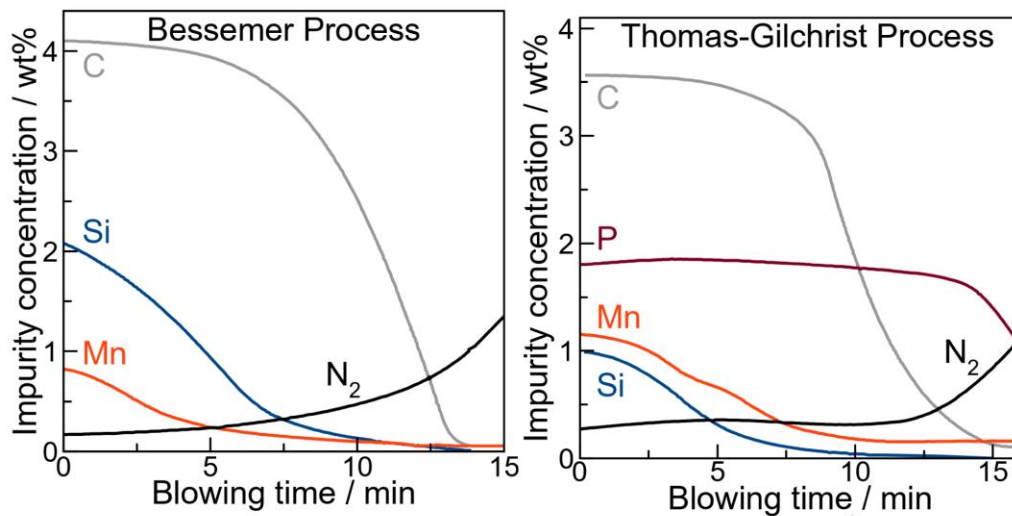

Figure 1.1. Change in impurity concentration in hot metal with blowing time in the acidic Bessemer process (*left*) and the basic Gilchrist-Thomas process

(*right*). These processes helped enable industrial-scale manufacturing of steels, which marks the beginning of the Industrial Revolution.[13,15]

During the nineteenth and twentieth centuries, chemists improved on natural polymers, such as gums, horns, or shellac, which had been widely utilized in the past, discovering how to prepare man-made polymers. The French chemist Henri Braconnot discovered the first semi-synthetic plastic, a material he called xyloidine, by treating plant matter with concentrated nitric acid. Today, we know that this process converts approximately half of the hydroxyl groups (-OH) to nitrate esters ($-ONO_2$) and that xyloidine nominally consists of cellulose dinitrate.[16,17] Later improvements by German chemist Friedrich Schöbein using stronger acidic conditions resulted in more conversion of hydroxyl groups, giving a material closer to cellulose trinitrate, known as pyroxyline or guncotton.[18,19] British inventor Alexander Parkes discovered that adding a plasticizer, vegetable oils partially solidified with sulfur dichloride, to pyroxyline resulted in a heat-moldable plastic material. This became known as Parkesine and was patented in 1865.[20,21] Further development of these synthetic materials, enabled by chemists thinking about materials at the atomic scale and tuning properties by rationally changing the atomic or molecular structure of the material, launched the Age of Polymers.

This brings us to the modern era, the Silicon Age, where electronic devices built on Si have become ubiquitous in everyday life. Indeed, it's nearly impossible for individuals to spend a day in a city without interacting with this technology. The Silicon Age was launched by the invention of the transistor in 1947 by Shockley, Bardeen, and Brattain, who used a germanium (Ge) crystal with extremely delicate gold (Au) point contacts to build the first working transistor.[22] Ge remained the dominant semiconducting material until the late 1950s because of its superior properties relative to commercially available Si at that time. While Ge was constrained in its applications because of its small bandgap - about 0.80 eV - it remained the material of choice until the early 1960s due to Si's higher

reactivity.[23] Eventually, researchers figured out how to grow Si crystals comparable in purity to Ge. Combined with other innovations associated with integrated circuit manufacturing, such as the effective and easy to prepare SiO_x gate dielectrics, the semiconductor industry soon switched their efforts to focus their manufacturing efforts on Si-based devices.

Reducing feature size to increase device density of integrated circuits and computational speed has been a major driver for Si technology. Since 1970, the number of transistors per unit area has doubled approximately every two years, a phenomenon known as Moore's Law.[24,25] Maintaining Moore's Law has required overcoming several limiting factors via the inclusion of additional materials and elements in the chip design, thereby vastly increasing the complexity of these systems. An example is the issue of leakage currents through the gate oxide in MOSFET devices. Leakage current due to tunnelling becomes a significant factor as the thickness of the gate oxide approaches 2 nm.[26,27] Since gate capacitance scales inversely with oxide thickness and directly with the oxide material's relative dielectric constant, industry developed materials with a larger dielectric constant than SiO_2, so-called "high-κ materials" (first, silicon oxynitride and later, hafnium-based gate dielectrics).[28–31] Another limiting factor in reducing feature size was the integrated circuit's RC time constant, which increased as device size decreased and eventually exceeded the speed of the transistors.[32] In 1997, IBM shocked the industry when it announced it had successfully replaced the industry-standard aluminum interconnects with copper.[33,34] The rest of the semiconductor industry quickly followed IBM's lead in using Cu interconnects, while also pursuing other "low-κ" materials, including HF-treated SiO_2 and lower density materials.[35]

Current chip designs have feature sizes at the nanometer scale and material properties are beginning to no longer scale with dimensions due to quantum effects and reduced material dimensionality.[36] This thesis focuses on approaches to prepare and characterize materials with reduced

dimensionality. By advancing our understanding of the fundamental science surrounding the preparation, characterization, and structure-property relationships of low-dimensional materials, we can better understand how to effectively exploit their properties in desired applications.

1.3 Bridge

Chapter I contains an unpublished overview of the following dissertation. I am the sole author, but had editorial assistance from my advisor, David C. Johnson. The following chapter, published in the *Journal of Materials Chemistry C*, continues the discussion above, detailing the conventional synthetic methods used to prepare 2D heterostructures and thin films, focusing on the advantage and disadvantages to each technique, and the advances for each technique that will be required in order to synthesize high-quality 2D heterostructures at scale.

REFERENCES CITED

(1) Miller, A. M.; Johnson, D. C. Challenges in Synthesis of Heterostructures. *J. Mater. Chem. C* **2022**. https://doi.org/10.1039/d2tc00324d.

(2) Miller, A. M.; Lemon, M.; Choffel, M. A.; Rich, S. R.; Harvel, F.; Johnson, D. C. Extracting Information from X-Ray Diffraction Patterns Containing Laue Oscillations. *Zeitschrift für Naturforsch. B* **2022**, *0* (0), 313–322. https://doi.org/10.1515/znb-2022-0020.

(3) Miller, A. M.; Hamann, D. M.; Hadland, E. C.; Johnson, D. C. Investigating the Formation of MoSe2and TiSe2 Films from Artificially Layered Precursors. *Inorg. Chem.* **2020**, *59* (17), 12536–12544. https://doi.org/10.1021/acs.inorgchem.0c01626.

(4) Hamann, D. M.; Bauers, S. R.; Miller, A. M.; Ditto, J.; Moore, D. B.; Johnson, D. C. Synthesis and Characterization of [(PbSe)1+δ]4[TiSe2]4Isomers. *Inorg. Chem.* **2020**, *59* (15), 10928–10937. https://doi.org/10.1021/acs.inorgchem.0c01416.

(5) Choffel, M. A.; Gannon, R. N.; Göhler, F.; Miller, A. M.; Medlin, D. L.; Seyller, T.; Johnson, D. C. Synthesis and Electrical Properties of a New Compound (BiSe)0.97(Bi2Se3)1.26(BiSe)0.97(MoSe2) Containing Metallic 1T-MoSe2. *Chem. Mater.* **2021**, *33* (16), 6403–6411. https://doi.org/10.1021/acs.chemmater.1c01623.

(6) Hummel, R. E. *Understanding Materials Science: History, Properties, Applications*, 2nd ed.; Springer-Verlag: New York, 2004. https://doi.org/10.1007/b137957.

(7) Radetzki, M. Seven Thousand Years in the Service of Humanity-the History of Copper, the Red Metal. *Resour. Policy* **2009**, *34* (4), 176–184. https://doi.org/10.1016/j.resourpol.2009.03.003.

(8) Moorey, P. R. S. The Chalcolithic Hoard from Nahal Mishmar, Israel, in Context. *World Archaeol.* **1988**, *20* (2), 171–189. https://doi.org/10.1080/00438243.1988.9980066.

(9) Radivojević, M.; Rehren, T.; Kuzmanović-Cvetković, J.; Jovanović, M.; Northover, J. P. Tainted Ores and the Rise of Tin Bronzes in Eurasia, c. 6500 Years Ago. *Antiquity* **2013**, *87* (338), 1030–1045. https://doi.org/10.1017/S0003598X0004984X.

(10) Stetch, T.; Pigott, V. C. The Metals Trade in Southwest Asia in the Third Millennium BC. *Iraq* **1986**, *48*, 39–64.

(11) Helwing, B. Rethinking the Tin Mountains: Patterns of Usage and Circulation of Tin in Greater Iran from the 4th to the 1st Millennium BC. *T ̈urkiye Bilim. Akad. Arkeol. Derg.* **2009**, *12*, 209–221.

(12) Komatsu, M.; Yamaguchi, A.; Ito, M.; Yoneda, S.; Saito, T.; Ohgane, T.;

Hayashi, T.; Sakamoto, M.; Mikouchi, T.; Kimura, M. Ryuseito: The Japanese Swords Made from Shirahagi Iron Meteorite. In *82nd Annual Meeting of The Meteoritical Society*; 2019; Vol. 54.

(13) Holappa, L. Historical Overview on the Development of Converter Steelmaking from Bessemer to Modern Practices and Future Outlook. *Miner. Process. Extr. Metall. Trans. Inst. Min. Metall.* **2019**, *128* (1–2), 3–16. https://doi.org/10.1080/25726641.2018.1539538.

(14) Barracglough, R. F. *Steelmaking 1850-1900*; The Institute of Metals: London, 1990.

(15) Barth, O. *Metallurgian Oppikirja – Osa 2 (Textbook on Metallurgy, Part 2 Ironmaking and Steelmaking)*, 1st ed.; Otava: Turku, 1942.

(16) Braconnot, H. No Title. *Ann. Chim.* **1833**, *52*, 290–294.

(17) Seymour, R. B.; Kauffman, G. B. The Rise and Fall of Celluloid. *J. Chem. Educ.* **1992**, *69* (4), 311–314. https://doi.org/10.1021/ed069p311.

(18) Schöbein, C. F. Improvement in Preparation of Cotton-Woll and Other Substances as Substitutes for Gunpowder. 4874, 1846.

(19) Gladstone, J. H. Contributions to the Chemical History of Gun-Cotton and Xyloidine. *Mem. Proc. Chem. Soc.* **1845**, *3*, 412–421.

(20) White, J. L. Fourth in a Series: Pioneers of Polymer Processing Alexander Parkes. *Int. Polym. Process.* **1998**, *13* (4), 326–326. https://doi.org/10.3139/217.980326.

(21) Rasmussen, S. C. From Parkesine to Celluloid: The Birth of Organic Plastics. *Angew. Chemie - Int. Ed.* **2021**, *60* (15), 8012–8016. https://doi.org/10.1002/anie.202015095.

(22) Bardeen, J.; Brattain, W. H. The Transistor, a Semiconductor Triode. *Phys. Rev.* **1948**, *74* (1), 230. https://doi.org/10.1109/JPROC.1998.658753.

(23) Seidenberg, P. From Germanium to Silicon: A History of Change in the Technology of the Semiconductors. In *Facets: New Perspectivies on the History of Semiconductors*; Goldstein, A., Aspray, W., Eds.; IEEE Center for the History of Electrical Engineering: New Brunswick, 1997; pp 35–74. https://doi.org/10.1016/b978-0-08-019857-6.50006-5.

(24) Moore, G. E. Cramming More Components onto Integrated Circuits. *Electronics* **1965**, *38* (8), 114.

(25) Moore, G. E. Progress in Digital Integrated Electronics. In *International Electron Devices Meeting*; 1975; pp 11–13.

(26) Roy, K.; Mukhopadhyay, S.; Mahmoodi-Meimand, H. Leakage Current Mechanisms and Leakage Reduction Techniques in Deep-Submicrometer CMOS Circuits. *Proc. IEEE* **2003**, *2*, 305–327.

(27) Taur, Y. The Incredible Shrinking Transistor. *IEEE Spectr.* **1996**, *36* (7), 25–29.

(28) Lee, D.; Kwong, W.; Blaauw, D.; Sylvester, D. Simultaneous Subthreshold and Gate-Oxide Tunneling Leakage Current Analysis in Nanometer CMOS Design. *Proc. - Int. Symp. Qual. Electron. Des. ISQED* **2003**, *1*, 287. https://doi.org/10.1109/ISQED.2003.1194747.

(29) Ito, T.; Nakamura, T.; Ishikawa, H. Advantages of Thermal Nitride and Nitroxide Gate Films in VLSI Process. *IEEE J. Solid-State Circuits* **1982**, *17* (2), 128–132. https://doi.org/10.1109/JSSC.1982.1051704.

(30) Intel's Fundamental Advance in Transistor Design Extends Moore's Law, Computing Performance. *Intel News Releases*. November 11, 2007.

(31) Southwick, R. G. I. An Investigation of Carrier Transport in Hafnium Oxide/Silicon Dioxide MOS Gate Dielectric Stacks from 5.6-400K, Boise State University, 2014.

(32) Zhou, D.; Preparata, F. P.; Kang, S. M. Interconnection Delay in Very High-Speed VLSI. *IEEE Trans. Circuits Syst.* **1991**, *38* (7), 779–790.

(33) Wada, Y.; Sasaoka, K.; Imamura, E.; Odaira, H. A New Circuit Substrate for MCM-L. In *Proceedings of CARTS EUROPE 95, 9th European Passive Components Symposium*; Amsterdam, 1995; pp 94–99.

(34) Copper Interconnects: The Evolution of Microprocessors. *IBM Press Release*. 2004.

(35) Shamiryan, D.; Abell, T.; Iacopi, F.; Maex, K. Low-k Dielectric Materials. *Mater. Today* **2004**, *7* (1), 34.

(36) Waldrop, M. M. More than Moore. *Nature* **2016**, *530*, 144–147. https://doi.org/10.1038/530144a.

CHAPTER II

CHALLENGES IN SYNTHESIS OF HETEROSTRUCTURES

2.0 Authorship Statement

Chapter II was published in the Journal of Materials Chemistry C in 2022. David C. Johnson and I contributed equally to the text.

2.1 Introduction

Materials discovery is a significant factor driving the development of new technology. The history of humanity is even discussed through the lens of materials discoveries, with eras named after materials that enabled significant advances or cultural shifts. As technology has improved, it has done so in part by increasing the fundamental understanding of material properties at ever decreasing scales and with increasing precision. Indeed, it has only been about a century since the mathematical frameworks describing quantum mechanics were theorized.[1,2] While modern devices based on silicon (Si) exploit our understanding of bulk material transport physics, there are still many remaining unanswered questions and poorly investigated physical phenomena in the quantum regime.

In today's era, the Silicon Age, electronic devices built on Si have become ubiquitous in everyday life. Reducing feature size to increase device density of integrated circuits and computational speed has been a major driver for Si technology. Current chip designs have feature sizes at the nanometer scale and material properties are beginning to no longer scale with dimensions due to quantum effects and reduced material dimensionality.[3] The increased complexity of today's chips is evident in the microscope image shown in Figure 2.1, which depicts a typical Cu interconnect structure. As feature size continues to decrease, more and more elements are also being used to tailor properties. As feature size continues to decrease, it will be necessary to develop a more complete understanding of the interactions between different materials at interfaces. Device properties will no longer predictably scale with size due to quantum

effects and emergent properties from the interactions occurring at interfaces.

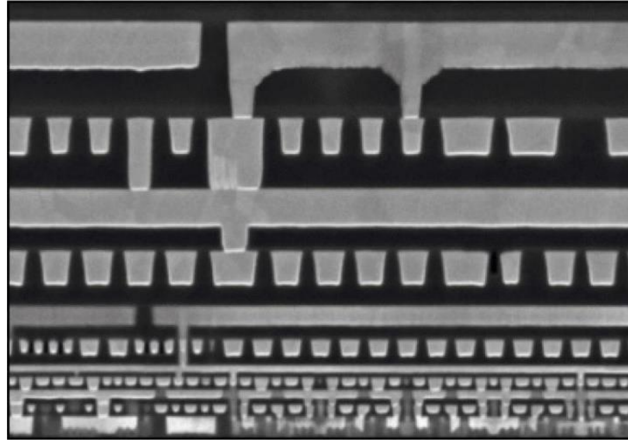

Figure 2.1. Image showing the complexity of the Cu interconnect structure of a 14 nm logic integrated circuit featuring FinFET's and air-gapped interconnect. Reprinted, with permission, from Natarajan et. al.[4] © 2014 IEEE.

It seems likely that the next era of human materials use will involve manipulating materials at ever smaller scales, eventually being limited by the size of the constituent material's unit cells. In 2004, Novoselov and Geim observed that the properties of graphite changed significantly when it is a monolayer thick.[5] Monolayer thick graphite – now called graphene - has a gapless Fermi surface due to the removal of interlayer interactions between adjacent layers, which results in graphene's emergent properties.[6,7] These discoveries were made possible by the 'scotch tape' synthesis method and the discovery that layer thickness could be observed optically due to an interference effect when the resulting flakes were deposited on a thin layer of SiO_2.[8,9] Energetic research efforts resulted in subsequent reports of emergent properties in other two-dimensional (2D) materials, along with the discovery that the emergent properties had a significant dependence on the identity of the substrate the 2D material was grown on.[10–16] Theorists have been able to predict unusual emergent properties for specific arrangements of layers, including new quantum states created by the interaction of the properties of different constituent layers.[17–22] Using exquisite micromechanical manipulation of cleaved flakes, assembly of different 2D layers into stacked heterostructures has been

successfully used to verify several of these theoretical predictions and construct basic electronic devices.[23–26] 2D layers can be stacked like bricks in different sequences, as shown in Figure 2.2, to create desired properties. These discoveries launched the field of 2D materials, as researchers explore tuning the interactions between 2D layers by stacking them in different orders and thickness to form metastable heterostructures.[27]

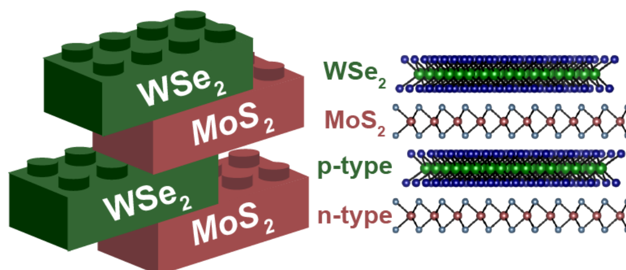

Figure 2.2. The ability to prepare heterostructures by stacking 2D layers in designed sequences enables preparation of 2D electronic devices, such as this hypothetical stack of alternating p- and n-type semiconducting layers.

The rapid growth of research focused on 2D materials results from the fundamental differences between heterostructures and composites. While both contain regions with distinctly different structures and properties, the properties of composite materials typically scale from those found in the bulk phases, although interfaces can increasingly impact properties as the size of the structural domains decrease to the nanoscale. In heterostructures, properties and/or structures distinct from those found in the bulk constituents arise as the thickness of constituent layers are reduced to monolayers. The lack of adjacent layers changes the band structure of monolayers, causing changes in electronic properties. For example, graphene has a gapless Fermi surface,[28] monolayers of semiconducting dichalcogenides have a direct band gap rather than the indirect banc gaps found in the bulk compounds,[29–31] and the charge density wave onset temperature and structure of VSe_2 differ from that found in the bulk.[32–35] The changes in electronic bonding as thickness is reduced to a single unit cell can also result in structural changes. These structural distortions are typically small

in layers exfoliated from 2D solids with very anisotropic bonding, as the perturbation of removing adjacent layers bound via van der Waals bonding is small. The distortions can be much larger if the constituent's bulk structure is less anisotropic. For example, a bilayer of PbSe has a 0.4 Å puckering compared to the bulk structure.[36] Charge transfer between adjacent layers can also cause significant structural changes. For example, a charge donating layer next to $MoSe_2$ can cause the 1T polytype to form.[37–39]

Since layer properties vary with thickness and identity of adjacent layers, the building-block approach of stacking 2D layers in specific sequences to form van der Waal's heterostructures results in an inexhaustible number of different target materials/heterostructures.[40–43] For example, consider an 8 layer heterostructure constructed from 4 layers of 1T-$TiSe_2$ and 4 layers of PbSe (total thickness of ~5 nm). One could construct 6 different heterostructures by varying the stacking sequences of the 4 PbSe and four $TiSe_2$ layers – all having the same size repeating unit and the same overall composition. The simplest case would be a 4 layer thick block of $TiSe_2$ stacked sequentially with a 4 layer thick block of PbSe. Five other possible heterostructures can be created by varying the order in which the $TiSe_2$ and PbSe layers are stacked. Representative HAADF-STEM image cross-sections of these isomeric heterostructures are shown in Figure 2.3.[40] An experimental approach needs to be developed where varying experimental parameters enables the stacking sequence and the number of constituent layers to be freely varied to optimize the properties of the resulting devices.

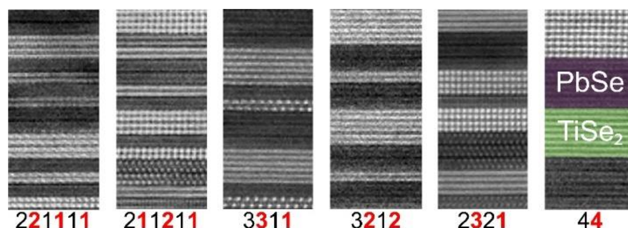

Figure 2.3. Representative HAADF-STEM images of six of the possible "isomer" heterostructures constructed from a unit cell consisting of various layering schemes of four layers of 1T-TiSe2 and four layers of PbSe. Because HAADF-STEM intensity

increases with atomic number, the PbSe layers are significantly brighter than the TiSe2 layers.

There typically are large differences between the strength of bonding within 2D layers versus between 2D layers. The prototypical 2D layer – graphene – illustrates this case. The carbon atoms in graphene layers are strongly covalently bonded to one another. Monolayers of graphene can be exfoliated from graphite because there is only bonding between the layers in graphite. The strong in plane bonding found in 2D layers that can be exfoliated from the bulk typically make them chemically stable. When on a substrate or adjacent to another 2D layer there will be chemical interactions in addition to van der Waals forces because the wavefunctions of both will overlap, often to a significant degree. The difference in chemical composition and structure between the layers will also result in a chemical potential difference. Charge transfer will occur to equalize the chemical potential. These additional interactions can be surprisingly strong, as evidence by the occurrence of minerals with misfit layer structures that can contain interwoven monolayers of two different constituent layers. Like artificially stacked monolayers, these minerals and analogous thermodynamically stable synthesized compounds consist of two structurally distinct layers whose lattices do not structurally match, resulting in an incommensurate structural mismatch. An excellent review by Wiegers details the structure and properties of misfit layer compounds containing transition metal dichalcogenide constituent layers.[44,45] Despite the structural misfit, the bonding between the constituent layers is strong enough to make them chemically stable with respect to mixtures of the constituent compounds. In some of these compounds significant charge transfer between constituent layers results in strong ionic bonding between layers, for example $(LaS)_{1.2}(CrS_2)$, where the subscript 1.2 results from the lattice misfit between the in-plane unit cell of the distorted rock salt structured LaS layer and the distorted hexagonal CrS_2 dichalcogenide layer. The LaS layer is positively charged while the CrS_2 layer is negatively charged.[46] The origin of the strong interlayer interaction is less

obvious in other misfit layer compounds, for example $(SnS)_{1.17}(NbS_2)$. As the variety of heterostructures that are prepared expands, the range of interlayer interactions will expand.

Historically, many material discoveries have occurred via serendipity.[47] This is largely because traditional synthesis approaches typically make only the most thermodynamically stable product, which may or may not be the targeted compound. Despite its successes and the discovery of many unpredicted structures and phenomena, these approaches are quite inefficient, especially when targeting a specific structure. Traditional organic synthesis, with its toolbox of well-known reactions and the ability to retrosynthetically design a sequence of steps to systematically assemble a complex structure, is perhaps the most developed synthetic chemistry field. However, even in organic synthesis, the crystal structure of the resulting compound cannot be experimentally controlled. In an ideal world, materials scientists would be able to predict the existence of new compounds with desired properties, including metastable phases, and synthetic approaches would be available to make targeted compounds. While this review focuses on approaches to make targeted heterostructures, there is a broader need for synthetic advances. In the last decade, significant advances have been made in predicting possible new phases through targeted programs such as NIST's Materials Genome Initiative, the Materials Project, and other related coordinated efforts.[48,49] Of the thousands of predicted compounds, only a small percentage have been made experimentally.[50] While this may be partially due to the accuracy of the calculations, synthesis limitations also play a significant role.

The remainder of this review focuses on synthetic approaches to heterostructures, briefly describing the reaction pathway(s) typically involved in these synthetic approaches. Since most heterostructures are metastable, they cannot be prepared as bulk compounds by direct, high temperature reaction of the elements and it will be challenging to prepare targeted metastable compounds as films on substrates using flux-based synthetic methods. A short

summary of various solid-state synthesis techniques used to grow crystals of thermodynamically stable heterostructures introduces basic concepts. We then discuss vapor phase deposition approaches, which have classically been used to prepare thin films and superlattices, showing how the rate limiting steps in crystal formation can be controlled by experimental parameters. Micromechanical assembly is discussed next, with a focus on more recent advances that may enable wafer scale. We discuss molecular beam epitaxy (MBE), where substrate structure and reacting fluxes are controlled to define the structure and control orientation thickness of constituent layers in metastable superlattice structures, traditionally of constituents with 3D structures. The final part of this review focuses on a more extensive discussion of the modulated elemental reactant growth technique, a newer alternative approach to heterostructure synthesis that involves nanostructured precursors.

2.2 Direct Reaction of Elements and/or Compounds

The direct reaction of elements and/or binary compounds to form products is a classic solid-state synthesis technique. Because of the non-uniform initial distribution of each element and the different diffusion rates of elements in the different reactants, a variety of local concentration gradients and intermediate compounds develop during these reactions. The reaction typically contains one or more reaction pathways that may involve multiple intermediate compounds. Since diffusion rates in solids are small, it is necessary to increase diffusion rates and/or decrease diffusion distances to obtain reasonably fast reaction rates. The most common approach uses high temperatures to overcome the small diffusion rates and large diffusion distances necessary to form the desired product from the initial reaction mixture. While increasing temperature significantly increases diffusion rates, the resulting composition gradients at interfaces also result in the formation of many of the compounds in the relevant phase diagram as reaction intermediates. The final state is typically the thermodynamically stable mixture of compounds expected from the appropriate phase diagram.

For example, consider the synthesis of misfit layer compound (MLC)

$(PbSe)_{1.18}(TiSe_2)_2$ from the direct reaction of elemental Pb, Ti, and Se, as shown in Figure 2.4.[51] Typical conditions for traditional synthesis reactions involve mixing stoichiometric amounts of each element in an evacuated quartz ampule and raising the temperature slowly before heating to high temperatures for a week or more. Due to the relatively large differences in melting points of the elements, Se melts and reacts with the surfaces of the Pb and Ti while temperature is being raised. While intuition might predict the most metal-rich phase on the relevant phase diagram would form first, this is not always true. However, the compound that forms first will be the phase with the lowest energy barrier to nucleation. The literature suggests that in this case, the metal rich phase, Ti_2Se is the first Ti-Se-containing phase to nucleate and PbSe is first to form on the surface of the Pb.[52] The amount of each of these compounds will increase with time as diffusion of elements through the surface product layers occurs. As heat is continually applied to the reaction mixture, the longer diffusion paths through the increasingly thick surface layers decrease the reaction rates. At some point, the targeted thermodynamically stable ternary MLC may nucleate and grow in the composition gradients, but the growth rate is slow due to the low diffusion rates of the elements in the intermediates formed, PbSe and $TiSe_2$. Grinding the intermediate reaction mixture and pressing a dense pellet of the resulting powder decreases the diffusion distances, which speeds the formation of the thermodynamically stable MLC.

While this approach is effective at synthesizing MLC's and other thermodynamically stable heterostructures, it lacks any control over the reaction pathway and thermodynamically unstable compounds cannot be prepared using this approach. Repeated grinding or ball-milling the reaction charge is one of the simplest approaches that can be used to reduce the average particle size by breaking up the product forming on the surfaces of each particle. This decreases the time it takes to convert the reaction mixture to products. While this can be effective at reducing diffusion distances by orders of magnitude (~mm to ~µm or smaller), multiple grindings can be required. Researchers often turn to other

synthetic techniques that are less diffusion limited, especially when single crystals are desired.

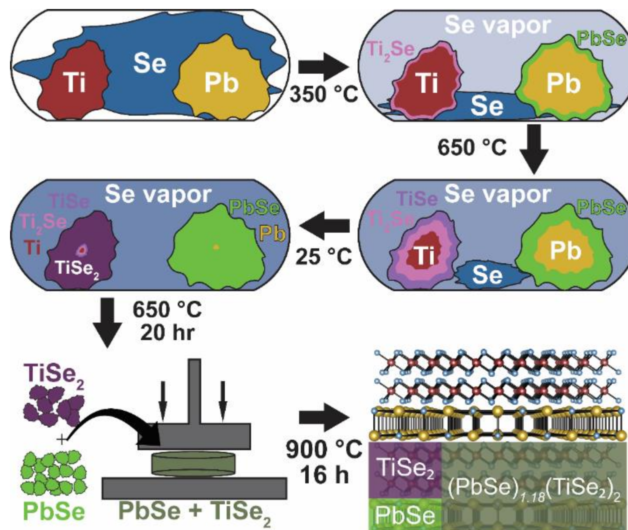

Figure 2.4. Schematic depiction of the reaction of elements Pb, Ti, and Se to form binary intermediates PbSe and TiSe2, and ternary product and misfit layered compound, $(PbSe)_{1.18}(TiSe_2)_2$.[51] The direct reaction of elements results in nucleation based on the local composition at that moment in time – here we assume TiSe and Ti_2Se will be the first to form. Since compositions exist from 0 to 100% of each element, there is no control over the reaction pathway.

2.3 Fluid-assisted Synthesis Techniques

Another strategy to bypass large diffusion distances is to use a fluid phase to significantly increase diffusion rates, which can both lower reaction temperatures and decrease reaction times. The large increase in diffusion rates relative to those found in solids allows for facile transport and mixing of reactants across the fluid portion of the reaction mixture. The choice of fluid is diverse and goes by a plethora of different identities and names, including solvent, melt, mineralizer, eutectic melt, flux, or reactive flux. When forming a solid crystal from a fluid phase, nucleation is typically the rate limiting step.[53] The compound with the lowest activation energy to nucleate will form, not necessarily the compound that is most thermodynamically stable. Having nucleation be the rate limiting step in crystal formation has the added advantage of allowing for the direct formation of ternary phases without proceeding through binary

intermediates, providing the ternary phase is the easiest to nucleate.

The reaction pathway in a fluid-based synthesis can be quite complex. There are basically two strategies used by researchers. Either the initial reaction mixture can be heated to a high enough temperature for long enough time that all the reactants dissolve in the fluid or researchers will focus their search for compounds formed during the initial heating, before all the reactants dissolve. In both cases, crystal growth will deplete the fluid of the solvated species contained in the compound, potentially causing significant differences in the speciation of the fluid phase. In the case of a heterogenous reaction mixture of a fluid and undissolved reactants, nucleation and growth impacts the rate that reactants dissolve. In-situ studies of melts frequently report nucleation of kinetically stable compounds at short times. A sequence of nucleation events as the reaction proceeds results in a series of new compounds forming, which can cause those previously formed to dissolve.[54–58] Figure 2.5 depicts a schematic of this sequence of phase formation.

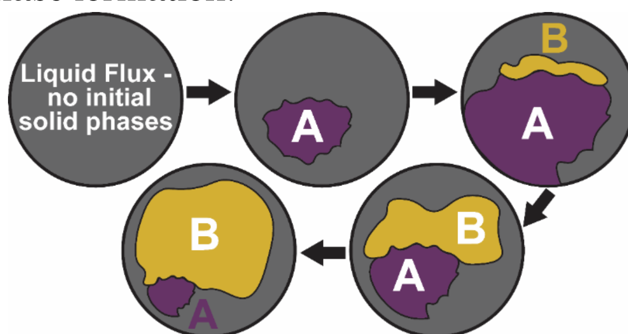

Figure 2.5. Schematic depiction of the evolution of the nucleation of crystalline phases during the cooling of a fluid-assisted synthesis reaction. The first phase to nucleate as the reaction is cooled to create supersaturation is simply the easiest to nucleate from the liquid (Phase A), given the species in the fluid and their concentrations. This phase is not necessarily the most thermodynamically stable phase. Growth of the first phase changes the speciation of the flux, potentially resulting in nucleation and growth of a subsequent phase (Phase B). As Phase B grows, it depletes the flux of species, which may result in Phase A dissolving.

There is unfortunately little systematic understanding of speciation and how speciation varies with time, composition, or temperature in fluid-assisted

solid-state synthesis. While recent in-situ total scattering and diffraction experiments have provided insights to the evolution of structure in fluids during reactions and on the sequence of crystalline phases that form in specific systems, it is still not straightforward to predict how reaction parameters can be manipulated to achieve a specific product.[59] Recent advances in machine learning have provided encouraging insights into understanding how varying the reaction parameters affect the observed reaction pathway, and this approach may be particularly useful for reactions in fluids, which contain many coupled parameters (including the amounts of undissolved reactants and products, the concentration of different species in solution, the reaction time and temperature) that all impact the resulting nucleation and crystal growth processes.[60]

Relative to the direct reaction of elements, the added experimental parameters in fluid-assisted synthesis provide more degrees of freedom to steer the reaction towards desired products. Researchers have used chemical insight to prepare homologous series of related compounds by tuning reaction parameters.[61]

2.4 Chemical vapor transport (CVT)

Chemical vapor transport (CVT) reactions are a common approach used by researchers when growing bulk crystals of transition metal dichalcogenides (TMD's) and other layered materials.[62] As shown in Figure 2.6, reactants are typically sealed in an evacuated quartz ampule with a transport agent (or mineralizer) and placed in a temperature gradient. CVT reactions involve three basic steps: reaction of the transport agent with the material to be transported to form a vapor phase compound, transport of this compound to the other end of the ampule, and the decomposition of this compound as the product forms.[62] The transport agent released by the decomposition of the transport compound returns to the reactant side of the vessel to react again. To nucleate the desired phase, the ampule must become super-saturated with the vapor species needed to form the product. Heterogenous nucleation typically occurs at the surface of

the substrate or on the ampule walls.[63] Once a crystal forms, it is easier to grow the crystal than nucleate a second one. The example shown in Figure 2.6 involves a reaction to form MoS_2, a well-studied 2D TMD.[64] In this example, elemental Mo reacts with the chosen transport agent, I_2, at the hot end of the temperature gradient producing a vapor phase mixture of MoI_x and Sn intermediate species. These intermediate species react at the other end of the temperature gradient, known as the deposition zone, forming MoS_2 crystals and reforming the I_2 transport agent.

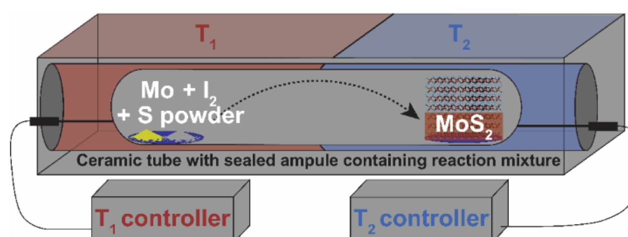

Figure 2.6. Schematic depiction of the CVT synthesis of MoS_2. A stoichiometric mixture of Mo + S powders and the chosen transport agent, I_2, are sealed inside an evacuated quartz ampule. The ampule is placed across a well-defined temperature gradient within a multi-zone tube furnace. The temperature gradient is chosen such that the reaction and vapor-phase transport of the reactants to the other side of the ampule, where they are deposited as products, is thermodynamically favorable.[64]

The change in the Gibbs free energy as the transport agent reacts with the material to be transported can be used to identify potential transport agents. If the reaction of the transport agent with the material to be transported has a very large negative ΔG and hence a very large ($>10^4$) equilibrium constant, the gas phase product will not readily decompose at the other end of the reaction vessel. If the reaction of the transport agent with the material to be transported has a very small ($<10^{-4}$) equilibrium constant, then the concentration of the vapor phase species will be very small. Either of these thermodynamic conditions make transport of the reactant very inefficient and impractical.[65] Finding a suitable transport agent becomes more difficult when attempting to synthesize compounds containing more than one metal constituent, as the above constraints must be satisfied for all species that can be formed by reaction of the

transport agent with non-volatile elements. Recently it was demonstrated that μm^2 area MoS_2 monolayer crystals and few-layer ReS_2, $MoSe_2$, and $TiSe_2$ could be grown using CVT by designing reaction vessels with constrictions.[64] This is a very encouraging breakthrough, showing that with sufficient control over and understanding of how experimental parameters affect the chemistry involved, the reaction pathway for CVT-based growth can be controlled to obtain monolayer crystals. To the best of our knowledge, however, growing a unique second material as a monolayer on top of a first monolayer has yet to be demonstrated via a closed system CVT reaction.

2.5 Chemical vapor deposition (CVD)

Chemical vapor deposition (CVD) reactions are like CVT reactions, but epitaxial substrates are typically used to reduce the activation energy for heterogeneous nucleation of a targeted structure. The ability to individually vary the partial pressure of species by varying the source temperatures allows control over the relative concentration of gas phase species in the growth zone to achieve conditions for nucleation and growth. By controlling deposition time, one can control the thickness of the resulting film.[66] Typically, CVD synthesis begins with solid or gaseous precursors which are heated to generate a partial pressure of each reactant in a carrier gas. The carrier gas containing the precursors is flowed through the reaction chamber. When the precursors impinge on the heated substrate, they decompose and the resulting species react to form the product, as shown in Figure 2.7.

An important feature of CVD reactions is the significant number of experimental parameters available to tune product formation relative to traditional solid-state synthesis. Perhaps the most critical parameter to control is the residency time of each reactant in the reacting zone. This is done by controlling the partial pressures of each reactant in the carrier gas at the substrate, which is typically done by setting the temperature of the sources of the precursors.[67] The flow of a carrier gas controls the residency time of each reactant in the reacting zone. The carrier gas is typically an inert gas such as

nitrogen or a noble gas but occasionally hydrogen or another reactive gas is

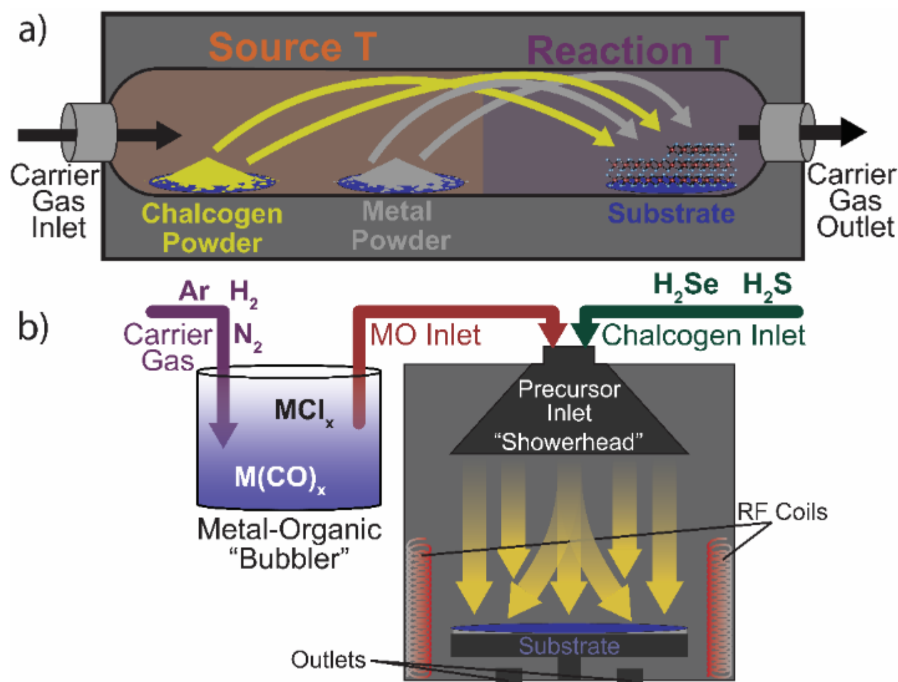

Figure 2.7. Schematic depictions of two types of CVD reactors. a) Powder-based chemical vapor deposition (CVD), in which powdered sources are used to generate the vapor, which is transported via carrier gas to the substrate. b) Metal-organic CVD, in which the carrier gas is bubbled through a metal-organic-containing solution prior to being injected into the reactor. Both experimental setups are open systems, with the carrier gas and remaining reactants continually removed from the reaction vessel. Adapted from [68].

mixed in to help decompose precursors at lower temperatures. The carrier gas, its temperature, and the partial pressures of the reactants, all affect the number of collisions between reactants, the gas phase reaction between them and the number of reactant species impacting the substrate surface. The ratio $\eta/\eta 0$ affects the initial incubation time observed prior to regular growth for many CVD reaction,[69] which is probably related to the initial nucleation of the target structure. The substrate temperature controls the decomposition rates of the precursors that impact and adsorb, the surface mobility of the resulting species and their residency time, and the nucleation rate and growth rate of forming solids.

The manipulation of the experimental parameters has significant effects on the observed growth mechanism of the deposited material. CVD growth typically begins with an incubation time prior to a period of regular growth. During the incubation period, the concentration of species on the substrate surface increases until supersaturation is reached, and nucleation occurs. Differences in nucleation energy can result in the formation of metastable compounds, which is typically encouraged by choosing substrates with an epitaxial relationship with the metastable phase. High temperatures result in thermodynamic-controlled processes, while low temperatures result in kinetic-controlled processes.[70] Once nucleation occurs, growth rate is limited either by the rate of the chemical reaction or by the rate of material reaching the surface. A high concentration of reactants in the vapor phase and low substrate temperatures lead to crystal growth being limited by the rate of the chemical reaction. A low concentration of reactants in the vapor phase and high substrate temperatures result in a mass-transport limited growth mechanism.

There is often a balancing act between using a sufficiently high substrate temperature to promote crystal growth but a low enough temperature to avoid desorption of reacting species from the surface. For example, in the growth of dichalcogenides reaction rates initially increase with temperature before decreasing as concentration of chalcogen on the substrate surface decreases due to its significantly higher vapor pressure than the other reactants. Since many TMD's lose chalcogen atoms when heated to high temperatures, the substrate temperatures must remain low enough to inhibit the formation of chalcogen vacancies. The number of chalcogen vacancies can dominate the properties of the resulting film.[71]

Three distinct growth modes have been observed in CVD growth, depending on reaction conditions: 2D layer-by-layer growth, also known as Frank-van der Merwe (FM) growth, 3D island-based growth, known as Volmer-Weber (VW) growth, and Stanski-Krastanow (SK) growth, which is a combination of the first two, involving formation of a few 2D layers followed by 3D island

formation.[69,72–74] FM growth occurs when the interaction between the incident reactants and the substrate is greater than that between the incident reactants and itself ($\eta < \eta0$), resulting in preferential growth of each complete layer before nucleation of the next layer.[75] VW growth occurs when the interaction between the incident reactants and the substrate is weaker than the interaction between the incident reactants and itself, which causes mostly vertical growth of the nucleated islands, typically resulting in films with very rough surfaces.[76] SK growth is a mixed growth mode that occurs when the interaction between the incident reactants and the substrate is about equal to that between the incident reactants and itself, resulting in competition between island nucleation and layer growth.[77] None of these growth mode models account for the initial incubation time.[74] While strides have been made to modify the growth models to account for these other involved processes, a complete understanding of CVD reactions has remained elusive.[69]

There are still significant challenges to using CVD reactions to synthesize metastable 2D films and heterostructures. One challenge is exactly determining when a layer's growth is complete, because incubation times vary and are sensitive to experimental conditions. When growing multiple constituents, one must determine exactly when layer growth is completed, such that growth of the first material can be halted prior to switching sources and growth of the second material. This requires reproducibly controlling two different incubation periods that may require different reaction conditions. In an encouraging breakthrough, Zheng et. al. used a sequential two-step CVD method to grow a monolayer PbI_2 on monolayer WS_2 and WSe_2.[78] This was enabled by the much lower growth temperature of PbI_2 relative to WSe_2 and WS_2 (400 °C vs. 1050 °C). These different growth temperatures, however, prevents the growth of WSe_2 or WS_2 on PbI_2.

2.6 Micromechanical assembly

The mechanical assembly processes for synthesis of heterostructures is conceptually straightforward, involving the sequential stacking of 2D layers in

the same way that one might stack bricks or Lego blocks, as depicted earlier in Figure 2.2. The steps involved in mechanical assembly consist of the initial growth of films or crystals that provide the source of the 2D layers, the exfoliation of the 2D layer of desired thickness from the crystal or substrate, the transfer of the layer to the growing assembly, and the removal of the substrate used to transfer the layer. One of the first reports of high-quality micromechanically assembly utilized small flakes of mechanically exfoliated mono- and bilayer graphene to make simple devices on single-crystal h-BN substrates.[79] The ability to prepare targeted structures with designed architectures in such a straightforward manner has resulted in literally thousands of papers published further optimizing each of the steps involved or using an assembly process to make targeted heterostructures. We will not attempt to comprehensibly review all this literature, as excellent reviews on targeted aspects already exist,[80–82] but will highlight what we believe were key synthesis advances as the size of the assembled structures increase towards wafer scale.

Major advances and remaining challenges in growing 2D materials over large areas were discussed earlier in this article. It is now possible to prepare large area, monolayer thick films of many 2D materials with near complete coverage of the substrate.[83,84] Since this technique allows one to individually prepare each layer, ensuring it is the correct thickness and composition, the challenges in finding compatible growth conditions to sequentially deposit different materials is avoided altogether. However, one challenge in developing growth techniques for a new 2D material is finding a substrate that enables crystallographically aligned growth, while also permitting the film to be exfoliated as a large area film from the substrate. It is necessary to optimize the CVD growth of the 2D layers to generate surface properties that enable the 2D layers to be cleanly isolated from substrates they were grown on without the use of any etchants or solvents.

The exfoliation of 2D layers from both crystals and growth substrates has undergone significant advances since Frindt first used tape to exfoliate $NbSe_2$

crystals to measure the effect of sample thickness on superconductivity.[85] Early methods typically used an adhesive layer, which needed to have a stronger adhesion with the material being cleaved than the interaction of the material with either the neighboring layers of itself in a crystal or to the substrate if grown as a film. An alternative approach to create large amounts of monolayer material is chemical exfoliation, in which ions and/or solvent intercalate between the 2D layers resulting in free floating solvated layers in solution.[86–88] Like mechanical exfoliation, the solvation energy of the solvated layers must be larger than bonding between the layers in the 2D crystal for this approach to be successful. It is often challenging to completely remove the adhesive or solvent from the 2D layer when they are being mechanically stacked via either of these approaches. One successful approach to isolate 2D layers of CVD grown films is to spin-coat the grown film with an adhesive polymer film, which is then mechanically peeled from the growth substrate using a thermal release tape.[89]

To get around organic contamination, gold-assisted exfoliation methods were developed.[90–92] Ultrasmooth gold layers result in a significant degree of charge transfer between the monolayer being transferred and the gold layer as the chemical potentials are equalized on contact, resulting in a bond to the gold that is stronger than the van der Waals forces between the 2D layers themselves. While contamination still can occur when removing gold films with chemical solvents in subsequent processing steps, the Au transfer process works for a wide variety of 2D materials.[25]

Initial micromechanical assembly was done manually on small, cleaved layers from crystals to discover emergent properties and to test theoretical predictions. Approaches were developed that enabled layers to be stacked with control of the rotational angle between the crystal structures of adjacent layers.[93] More recently, automated assembly techniques have been developed to improve reproducibility, decrease incorporated material between the 2D layers, and increase throughput on large area substrates.[89,94] These advances enable researchers to consistently synthesize wafer-scale heterostructures, which is an

essential step towards being able to manufacture devices made from heterostructures.

2.7 Molecular beam epitaxy (MBE)

Molecular beam epitaxy (MBE) growth is a well-developed and understood technique and is one of the few synthesis techniques able to target and grow metastable materials and superlattices. This ability positions MBE as a potential source of 2D layers that cannot be prepared as bulk compounds or via CVD. MBE is similar to CVD reactions in some respects, but MBE reactions differ by taking place in a high or ultra-high vacuum environment. An advantage of utilizing high-vacuum and ultra-pure sources is the lower occurrence of impurity inclusions from carrier gas molecules or other source impurities, relative to films grown via CVD.[68] A second advantage is that in-situ characterization tools are available to monitor film growth during deposition, including surface-sensitive reflection high-energy electron diffraction (RHEED), quartz crystal deposition monitors (QCM), auger spectroscopy, and scanning tunnelling microscopy (STM).[68] These analytical tools have enabled researchers to develop and understand the reaction pathways and how and why experimental parameters change growth modes.

MBE involves heating ultra-pure reactant sources with effusion cells and/or electron beam guns to generate “beams” of vaporized reactant, which are co-incident on an actively heated substrate, as shown in Figure 2.8. The heated substrate allows for significant surface diffusion of the reactants after they impact the substrate, enabling them to find energetically favorable locations such as step edges on the growing surface. Relatively low temperatures can be used, which minimizes the formation of vacancy defects and limits interlayer diffusion to keep interfaces abrupt.

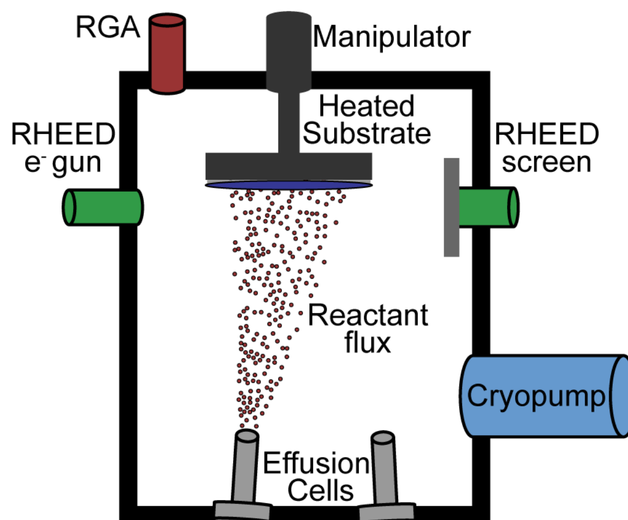

Figure 2.8. Schematic of MBE reactor, showing effusion cells with a reactant flux incident on the heated substrate, along with in-*situ* RHEED instrument for characterization of film growth during deposition.

MBE exploits the difference in activation energies between surface and bulk diffusion, providing enough thermal energy for adatoms to move and react with already nucleated layers, but not enough for bulk diffusion. By changing the substrate temperature, the observed growth mechanism during deposition can be varied. To target a specific structure, an epitaxial match between the substrate and the targeted product is used to favor nucleation of the targeted structure. When the incident reactants impact the substrate, they interact with the dangling bonds present on the substrate's surface, initially taking on the lattice constant of the substrate.[95] In practice, the crystal lattices of the chosen substrate and the desired material have lattice parameters that are typically within 5% of one another. If there is a mismatch between the lattice constants of the deposited material and the substrate, increasing strain-induced distortions with thickness result in the formation of dislocation defects.[96–98] The critical thickness where dislocations occur is dependent on the system, dictated by the extent of the lattice mismatch and the activation barrier to nucleation of the dislocation defect.[99] The presence of periodic dislocation defects in the lattice of the thin film can degrade the electrical performance of devices fabricated from these materials.[100]

The development of so-called “van der Waal’s epitaxy” (VDWE) by Atsushi Koma’s group in the late 1980s opened a new regime where epitaxy is no longer a strict requirement for ordered growth. Koma utilized typical MBE growth conditions but used substrates with a lack of dangling bonds on the surface.[101–104] Koma showed that the materials grown had the lattice parameters of the bulk compounds, not those of the substrate. Large lattice mismatch’s of up to 20% or more were possible, because the lattice of the material being grown no longer adapted to the substrate’s lattice during the first few layers of growth.[105] VDWE epitaxy has been used to grow transition metal chalcogenides, TMD’s, and other 2D materials of interest,[106–109] and to grow TMD heterostructures and topologically insulating materials, such as Bi_2Te_3.[110–112]

The growth of large domain size mono- or few-layer transition metal dichalcogenide films via MBE, however, has been surprisingly difficult. For MBE-grown transition metal dichalcogenides (TMD’s), typical growth conditions (<500 °C, with a ~20:1 chalcogen:metal flux ratio) result in a relatively high nucleation rate.[113,114] This leads to a dense distribution of small grains in the resulting film, with the high density of grain boundaries limiting electrical performance of devices fabricated with these materials. As of 2017, the largest reported grain sizes for an MBE-grown TMD were relatively small, around 250 nm, observed in separate reports of $NbSe_2$ and WSe_2 films.[115,116] In the WSe_2 case, the authors report that the grain size significantly increased with the substrate growth temperature, although the nucleation density was still so high that the overall maximum grain size was restricted due to space considerations on the substrate.[116] To achieve larger grain sizes, surface diffusion rates must be increased while the nucleation rates must be decreased, which is challenging given that both diffusion and nucleation rates increase with temperature.[95] When using high substrate temperatures, sticking coefficients are much lower relative to those observed at lower temperatures. This results in a lower density of surface adsorbed atoms (adatoms) at high temperatures leading to a lower probability of the formation of nuclei of critical size.

Hinkle's group recently showed that applying the above concepts result in over an order of magnitude increase in the observed grain sizes for MBE-grown WSe_2 films.[113] The challenge in applying these ideas to TMD growth, however, is that chalcogen adatoms have a significantly increased likelihood of desorbing, due to their much higher vapor pressure relative to metal adatoms. Consequently, the disparity in reactant fluxes needed to form stoichiometric dichalcogenides is closer to 1000:1 chalcogen:metal. The high substrate growth temperatures also result in significantly slower growth rates (around 0.05 monolayer/hour) due to the increase in adatom desorption. While the much slower growth rate observed at high growth temperatures make it unsuitable for industrial-scale production of these materials, it does make it easier to terminate growth with a completed layer. It was recently shown that using a shutter to interrupt the metal beam at regular intervals during MBE growth of TMD's, reduces the probability of metal-metal adatom interactions during deposition and allows more time for the chalcogen reactants to react and bond with adsorbed metal atoms. This clever way to increase the effective chalcogen:metal flux ratio resulted in stoichiometric films and was used to prepare the first reported MBE-grown WTe_2 film.[117,118]

In summary, the layer-by-layer growth enabled by MBE is an extremely powerful tool in the synthesis of metastable materials and heterostructures. However, there are still significant challenges to extending these advances to the growth of heterostructures using MBE. For example, it can be extremely challenging to grow Material A on Material B AND Material B on Material A, due to the large differences in growth conditions required. The ability to prepare 2D layers not found in equilibrium phase diagrams, however, make MBE potentially a key growth technique to supply micromechanical assembly platforms with 2D layers that cannot be obtained via other approaches.[119–123]

2.8 Modulated elemental reactants (MER)

MER is the newest of the synthesis approaches outlined in this review, hence we will provide a longer description of this technique. MER is based on the

idea that a homogenous, amorphous intermediate is a valuable and general starting point for the synthesis of metastable compounds, as all crystalline compounds will be more thermodynamically stable than the amorphous phase.[124] Nucleation is the rate limiting step in forming a crystalline solid from an amorphous state, which depends on the local concentration and on the prior thermal history of the sample. To nucleate a compound with a stoichiometry different from the composition of the amorphous phase, diffusion needs to occur. Since diffusion rates are low in solids, the nucleation of a compound with stoichiometry close to that of the amorphous phase is favored.

A challenge in using the amorphous state as a reaction intermediate was finding a general experimental approach to prepare amorphous alloys of controlled composition. One solution to this challenge was discovered in the early 1980's, when W. L. Johnson's group showed that amorphous metals can be formed by heating crystalline metal foils at low temperatures. The formation of the amorphous alloy is driven by the large enthalpy of mixing.[125–127] The D. C. Johnson group showed that if the thicknesses of reactant layers are below a critical thickness, an amorphous phase forms before any crystalline phases in a wide variety of different systems.[128–130] This group also showed that the composition of the amorphous intermediate controls which compound nucleates first.[131] Since the activation energy required to nucleate a metastable compound from the amorphous alloy with a composition that corresponds to the stoichiometry of the metastable compound can be smaller than that required to disproportionate and nucleate the more thermodynamically stable mixture of binary compounds, this provided a systematic approach to preparing metastable binary compounds. New metastable binary ($FeSb_3$, $NiSb_3$ and $RuSb_3$)[132,133] and ternary ($Hf_{1-x}Fe_4Sb_{12}$, and $Y_{1-x}Fe_4Sb_{12}$)[133] antimonide compounds with the skutterudite structure were prepared using this approach, showing the ability to make targeted compounds using amorphous intermediates. W. Bensch's group also used designed precursors to prepare amorphous intermediates to synthesize a number of new metastable binary compounds. His group used an array of in-

situ experiments to show that forming these metastable compounds was a result of the reaction pathway avoiding more stable compounds.[134,135] Jansen's group synthesized amorphous precursors by simultaneously depositing the relevant elemental sources onto a liquid-N-cooled substrate with compositions matching the stoichiometries of intended phases.[136,137] They synthesized several novel alkali nitride phases, including Na_3N, and a previously unknown LiBr phase by gently heating the amorphous precursors.[138,139]

The modulated elemental reactants (MER) approach is an extension of these initial findings, based on the hypothesis that the nanoarchitecture of a precursor (elemental layer thicknesses and the layer sequence) can be used to control the resulting reaction pathway. One of MER's advantages is the large number of parameters available to manipulate reaction pathways.[140,141]

MER precursors are created by depositing sequences of ultra-thin elemental layers (~3-30 Å thick) designed to minimize the total diffusion distance that the reacting atoms need to travel from their initial positions in the layered precursor to their final positions in the targeted crystalline product. Changing the absolute layer thicknesses while maintaining a constant ratio of reactants per repeated sequence has a significant effect on the observed reaction pathway by changing the time required for interdiffusion, which scales as thickness squared. If the layer thickness is above some critical thickness, nucleation of the binary phase will happen at the layer interfaces prior to the formation of an amorphous intermediate. Below the critical thickness, the layers will interdiffuse and mix before a nucleation event occurs, forming a homogenous amorphous intermediate. The exact value of the critical thickness for each system is defined by the energy and time required to diffuse each reactant through the surrounding matrix relative to the activation energy and time required to nucleate a crystalline phase. As the absolute layer thickness increases, the time required for diffusion will increase until it becomes larger than that required for nucleation.[142] The typical total diffusion distance for reacting atoms is nanometers in MER, which is smaller than the ~μm-scale surface diffusion

lengths found in CVD and MBE, and much less than the ~mm-scale bulk diffusion lengths present in the direct reaction of the elements. The local composition is another important parameter, which is controlled by the relative layer thicknesses of each element deposited.[129,143] The activation barrier for nucleating a crystalline compound depends on the local composition. For homogenous amorphous alloys, the lowest nucleation energy is observed for amorphous intermediate compositions that corresponded to the stoichiometry of the compound.[144] This gives MER an advantage over other synthetic techniques when attempting to synthesize phases that are predicted to be kinetically stable, because local compositions are controlled by the design of the precursor. If the reactant contains layers or particles thicker than the critical thickness, composition gradients formed during interdiffusion provide opportunities for a variety of different compounds to nucleate. The goal in designing a MER precursor is to have the nucleation and growth of the intended phase be the fastest way for the system to reduce its free energy.

In most systems, the reaction pathway can be controlled by designing precursors with specific interdiffusion lengths and layer sequences to avoid unwanted intermediate crystalline compounds. Low temperatures are sufficient to enable the elements to mix, due to the short diffusion lengths, permitting the initial formation of an amorphous intermediate. What forms from the amorphous intermediate depends on the relative magnitude of nucleation energies of different potential compounds, which is a function of local composition. The reaction between ultrathin layers of Mo and Se, depicted schematically in Figure 2.9, illustrates the importance of both composition and repeat layer thickness. When Mo and Se are deposited in a metal rich repeating unit that deviates enough from a 1:2 ratio of Mo:Se and has a total thickness of the repeating unit less than 27 Å, heating the layered precursor at low temperatures (~125 °C) causes the interdiffusion of layers and formation of a homogenous amorphous alloy.[129] Heating the amorphous alloy at 575 °C results in the formation of $MoSe_2$, indicating that it is the easiest compound to nucleate. If the thickness of the

repeating unit is larger than 38 Å at this composition, nucleation of $MoSe_2$ occurs at the interface between Mo and Se layers during annealing at ~250 °C. Depositing bilayers that are Se rich with respect to $MoSe_2$ results in $MoSe_2$ nucleating at the interfaces during the deposition for all repeat thicknesses that were studied, which were smaller than 2 nm.[52] Annealing at higher temperatures results in the growth of $MoSe_2$ layers perpendicular to the substrate and the loss of the excess Se at higher annealing temperatures.

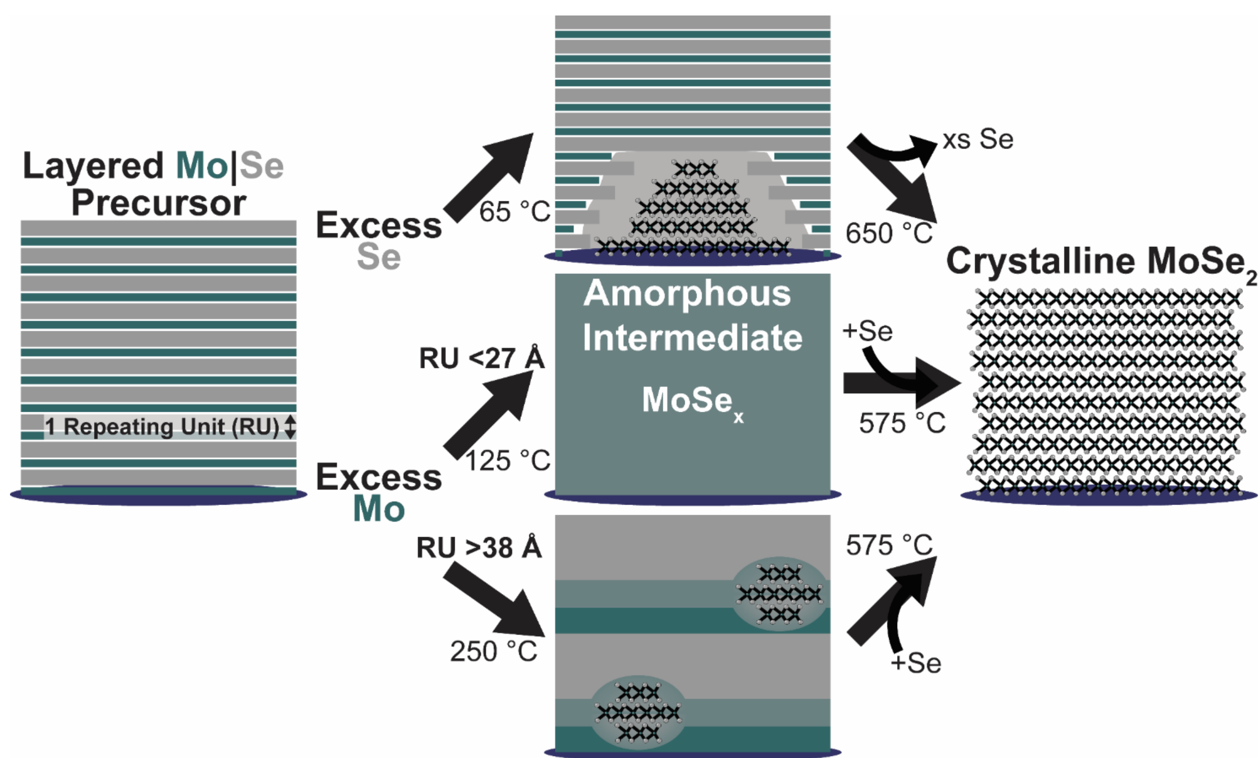

Figure 2.9. Schematic depiction of two different reaction pathways in the reaction between ultra-thin layers of Mo and Se. If the precursor's composition is Se-rich, small grains of MoSe2 nucleate during the precursor's deposition. If the precursor is Mo-rich, the thickness of the repeating sequence of layers (Mo|Se) controls the reaction pathway. If the thickness of the deposited Mo|Se sequence is less than 27 Å, heating the precursor causes interdiffusion of the layers and formation of a homogenous amorphous intermediate state. Further heating crystallizes the majority of the intermediate into the desired $MoSe_2$ structure, depending on how closely the composition of the intermediate matches the compound's stoichiometry. If the Mo|Se thickness is greater than 38 Å, nucleation occurs at the interface between Mo and Se

layers, trapping any local composition gradients that might be present in the layers. The $MoSe_2$ grains grow until the trapped local composition gradients have come to equilibrium.

In ternary systems, additional experimental parameters can be used to avoid the formation of crystalline binary compounds as reaction intermediates. Addition of a third element to an amorphous intermediate increases the activation barrier to nucleation of possible binary compounds.[145] The layer sequence can also be used to avoid binary compounds as reaction intermediates by controlling the sequence of interdiffusion.[146] If layers are deposited in an A|B|C sequence, all elements are adjacent to one another. If layers are deposited in more complex layer sequences, for example A|B|A|C, one separates the elements B and C to avoid the formation of binary B-C compounds. The ability to control the sequence of interdiffusion to avoid the formation of binary compounds by design of the precursor makes MER an effective approach to use when trying to prepare an unknown ternary phase.

By preparing more complex MER precursors, it is possible to mimic the composition profiles of misfit layer compounds, naturally occurring heterostructures with lattice mismatched constituents. The planar nature of the composition gradients in as deposited MER precursors combined with the low nucleation energy of dichalcogenide compounds often leads to their low temperature nucleation before the deposited layers can mix.[52,147] In the Ti|Se|Sn|Se precursor shown in Figure 2.10, monolayers of $TiSe_2$ form during the deposition, provided the deposited Ti|Se layers each contain the number of atoms required for a single unit cell of $TiSe_2$. The $TiSe_2$ layers are separated by amorphous $SnSe_x$. If the deposited Sn|Se layers contained enough Sn and Se to form one unit cell of SnSe, annealing at higher temperatures results in the formation of a $(SnSe)_{1.2}TiSe_2$ heterostructure.[148] Depositing two Sn|Se layers and one Ti|Te layer results in the formation of the $[(SnSe)_{1.2}]_2(TiSe_2)_1$ heterostructure.[149,150] By varying the number of and sequence of deposited Sn|Se and Ti|Se layers in the precursor, MER enables the synthesis of a nearly

unlimited number of unique heterostructures, including structural isomers.

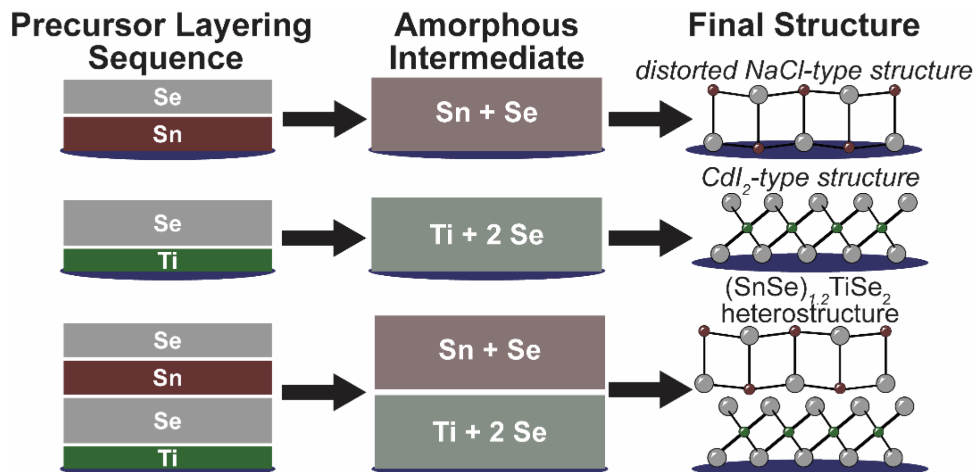

Figure 2.10. Schematic depiction of two sample layering sequences for deposition of MER precursors used when targeting materials with the distorted NaCl-type structure (top), the CdI_2-type structure (middle), and a heterostructure combining both layer types.

For example, consider heterostructures containing four layers of compound A and four layers of compound B. There are six different layer sequences that can be constructed containing four layers of A and B that all have the approximately the same c-axis lattice parameter: AAAABBBB, AAABBBAB, AAABBABB, AABBBAAB, AABBABAB, AABABBAB. One can prepare these structural isomers via MER by simply depositing the correct sequence of elemental layers to mimic the composition profiles of these heterostructures. However, as an overall synthetic approach, this results in an extremely large number of potential heterostructures, since the number of possible configurations in the final compound increases rapidly with the number of constituents. Even when limiting selections to those with <20 unique layers in the unit cell, there are nearly 60,000 possible unique heterostructures constructed from only two constituents. With three constituents, this number increases to over 130,000,000; with four constituents, the number of possible structures is more than 35,000,000,000.[151]

MER also enables the synthesis of heterostructures that have no homologs

in the systems equilibrium phase diagram. For example, sequentially depositing one Bi|Te bilayer (with a 2 to 3 ratio of Bi to Te) and one Ti|Te bilayer (with a 1 to 2 ratio of Ti to Te) in a MER precursor results in the $(Bi_2Te_3)_1(TiTe_2)_1$ heterostructure.[152,153] Heterostructures containing $MoSe_2$ or WSe_2 layers with SnSe, PbSe or BiSe have also been prepared.[43,154–157] Other heterostructures incorporating novel constituents and combinations of constituents that do not exist on equilibrium phase diagrams have also been reported, based on intergrowths of different layered compounds (including Bi_2Te_3, $TiTe_2$, $TiSe_2$, $MoSe_2$, VSe_2,) and structural fragments of compounds with 3D structures, (including PbSe, SnSe, BiSe, LaSe, and $GeSe_2$).[40,142,153,154,158–161] Key to the formation of a specific heterostructure is controlling the deposition parameters so that the precursors contain the desired ratio of metal atoms to chalcogen atoms (2:3, 1:2, or 1:1) for the Bi_2Te_3-type, CdI_2-type structures and MX layers respectively) and the correct number of atoms to form an integer number of crystalline layers of the targeted constituents.

Advances in thin film analytical and characterization techniques have been critical to enable the development of the MER synthesis approach. Low angle x-ray reflectivity quantifies the thickness of repeating layer sequence and infer their compositions.[162–164] X-ray fluorescence provides a fast and non-destructive technique to determine the absolute number of atoms in each sample.[165] X-ray total scattering techniques and atomic pair distribution function (PDF) analysis can used to probe the structure of amorphous intermediates.[166] High angle annular dark field scanning transmission electron microscopy (HAADF-STEM) and energy dispersive spectroscopy (STEM-EDS) provide critical atomic scale information about composition, local structure, and morphology.[167] The relative positions and compositions of atomic planes from both HAADF-STEM and STEM-EDS data provide initial structural models for Rietveld structural refinement of specular and in plane diffraction data. When the resulting refinements match the initial model, it indicates that the STEM data is representative of the majority of the sample.

2.9 Conclusion

A free energy landscape, first introduced by Schön and Jansen, provides a useful way to discuss the challenges involved in synthesis and the attributes of the different synthetic approaches discussed in this review.[136,168,169] Consider the schematic of a portion of the free energy surface for the BiSe-NbSe2 system, shown in Figure 2.11, which shows some of the kinetically stable and the thermodynamically stable heterostructure with a 1 : 1 ratio of BiSe to $NbSe_2$ layers in their unit cell. Like lakes that occupy minima in the local topography, each heterostructure is a local free energy minimum in the energy landscape. Differences in the minimum value for each lake reflect differences in the bonding in and between the constituent layers in each heterostructure. The "lake" at the lower left side of the map, labeled 11, has the lowest "altitude" and hence is the thermodynamic product, $(BiSe)_{1.10}(NbSe_2)_1$. It has a unit cell containing one BiSe bilayer and one $NbSe_2$ layer and the strong in interaction between the layers make it more stable than heterostructures with thicker layers. The upper right hand lake basin of the map contains 6 isomeric heterostructures containing 4 bilayers of BiSe and 4 layers of $NbSe_2$ in different sequences, analogous to those discussed in Figure 2.3, but with different constituents. The lakes in the bottom part of the map represent the two heterostructures that can be created with three layers of BiSe and $NbSe_2$ layers. Because of the stabilizing electronic interaction between BiSe and $NbSe_2$ layers, the relative stability of each compound in this system is controlled by the number of interfaces between each constituent layer present in the unit cell. The 11 heterostructure realizes the maximum number of these interactions by layering alternating BiSe and $NbSe_2$ layers, making it the most globally stable compound in the system. The depth of the valleys relative to the saddle points leaving them reflects the kinetic stability of each isomer. While the 6 isomers in the upper right are relatively close in elevation, their relative stability is dictated by the number of interfaces present, 1 for the 44 isomer, 3 for the 3311, 2321, and 3212 isomers, and 5 for the 221111 and

211211 isomers.

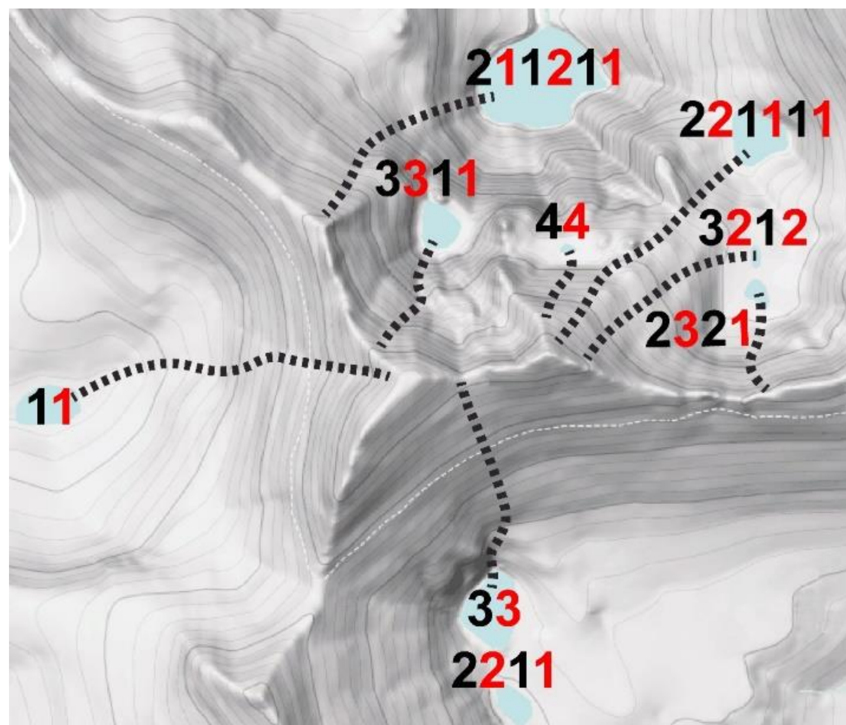

Figure 2.11. Schematic free energy surface for the BiSe-NbSe2 system showing some of the possible kinetically stable heterostructures containing an equal number of BiSe and $NbSe_2$ layers and the thermodynamically stable product $(BiSe)(NbSe_2)_1$ (labeled 11). By varying the layering sequence or the composition of the MER precursor, one can select a starting position on the energy landscape where the steepest slope results in the precursor evolving into a specific heterostructure. This is analogous to raindrops falling to Earth and flowing down the surrounding topography into a lake.

To prepare a specific heterostructure, one needs an approach with experimental parameters that can be used to avoid both the other metastable heterostructures and the thermodynamically stable phase at this composition. Traditional high temperature synthesis and vapor transport reactions both yield only $(BiSe)_{1.16}(NbSe_2)_1$, as they do not have parameters that can be used to control the reaction pathway and composition alone will not work, as all of these heterostructures have the same composition.[170] Synthesis using CVD would require shuttling the sample between different experimental conditions to prepare BiSe on $NbSe_2$ and $NbSe_2$ on BiSe. Precise deposition control would be

required to stop growth at the correct number of completed layers for each constituent. MBE growth would involve the same challenges as CVD, but with added difficulties due to the high vapor pressure of Se at the temperatures required for Nb to have sufficient surface mobility. It may not be possible to find conditions to grow both $NbSe_2$ on BiSe and BiSe on $NbSe_2$ using either CVD or MBE growth.

The challenges in synthesizing a specific heterostructure using the MER approach are designing the nanoarchitecture of the precursor (elemental layer thicknesses and the layer sequence) and finding annealing conditions that yield the desired product. The nanoarchitecture of the precursor determines the initial position on the free energy landscape, which needs to be somewhere within the local valley of the targeted product. Since solid state diffusion rates are small at low temperatures, the initial rearrangements that occur are constrained around the structure defined by the as-deposited precursor. Like water flowing downhill, the steepest slope of the energy landscape controls the pathway that the reaction takes, which is illustrated as dashed lines in Figure 2.11 for potential starting points. Therefore, it is essential to find a precursor nanoarchitecture that allows the reaction to begin in a spot on the energy landscape where, when annealed, it will flow downhill towards the desired lake. For example, if one wanted to deposit a MER precursor targeting the 211211 isomer, one would need to deposit both the correct number of constituent atoms in each repeating sequence to form 4 total layers of each constituent and the layer sequence needs to be constructed such that the precursor will nucleate and grow the 211211 heterostructure. This is achieved by depositing the correct number of constituent atoms in an order that mimics the composition profile of the desired heterostructure's nanoarchitecture. The annealing conditions must provide sufficient time and thermal energy for the atoms to diffuse and nucleate the targeted structure, but not so much that the precursor moves through a saddle point in the energy landscape into an adjacent valley. Too much time or too high a temperature will cause the precursor to move out of the local minimum, forming a more

thermodynamically stable compound. While MER provides access to the desired heterostructure, the trade-off is the lack of control of the rotational order of the constituent layers.

While each of the synthesis methods discussed have different experimentally adjustable parameters that provide some control over the products formed, as summarized in Table 1, further advances are required. Ideally, one would be able to combine the strengths of each, for example the flexibility of fluid-based synthesis approaches, the ability to control what phase nucleates as done in MBE, and ability to prepare single crystals as done using chemical vapor transport, and the ability to define starting parameters as in MER. While the MER approach can prepare many metastable compounds and heterostructures, additional experimental parameters need to be developed to control the structure of what nucleates, both as bulk phases and as individual layers in heterostructures. Controlling nucleation density in MER would also be valuable, as this would provide control of the in-plane grain size of the constituent layers in heterostructures. The Age of Heterostructures will be based on the exciting developments enabled by emergent properties created by controlling structure and composition on the scale of a unit cell.

Table 2.1 Summary of synthetic techniques typically used in the synthesis of van der Waal's heterostructures

Synthetic Approach	Typical Conditions	Advantages	Disadvantages
Direct reaction of the elements	open or sealed reaction vessels, temperatures >1000 °C, long synthesis times (days to months)	Easy, low-cost, direct approach to thermodynamically stable compounds	Thermodynamics controls which phase forms, low diffusion rates in solids lead to long synthesis times and/or high reaction temperatures

Table 2.1, continued

Synthetic Approach	Typical Conditions	Advantages	Disadvantages
Fluid-assisted synthesis	in open or sealed reaction vessels, lower temperatures than direct reaction, short synthesis times (seconds to days)	Increased diffusion in fluids allows for shorter synthesis times, additional experimental parameters (composition of fluid) relative to direct reaction of the elements	No control over which phase nucleates first, fluid speciation as a function of time is extremely challenging to determine experimentally, solubility constants not known for most systems, elements from fluid can be incorporated in product
Chemical vapor transport (CVT)	Evacuated ampule filled with reagents and placed across a temperature gradient	Results in growth of single crystals. Few-layer and monolayer growth of films possible with specially designed reaction vessels and appropriate substrates	Can be challenging to find suitable transport agent for systems with multiple metal constituents, suitable substrates may be difficult to find for film growth
Micromechanical assembly	In air , inert atmosphere or vacuum, assembly takes place at room temperature or with low heat to remove adhesive layers	Automated assembly platforms provide consistent and repeatable assembly of individual layers into heterostructures or devices, recent advances have approached wafer-scale assembly, ability to control relative rotation angle between layers.	Extremely sensitive to source of constituent layers, which require other synthesis techniques to make, multiple processing steps increase chances of inter-layer contaminants

Table 2.1, continued

Synthetic Approach	Typical Conditions	Advantages	Disadvantages
Molecular beam epitaxy (MBE)	Deposition takes place at < 10^{-8} Torr, Substrate heated to increase surface diffusion rates.	In-situ characterization, layer-by-layer growth modes possible, produces epitaxial films, deposition time controls film thickness, wafer-scale	Requires epitaxial lattice match between substrate and desired material (VDWE is an exception), extremely challenging to deposit heterostructures or films with multiple constituents due to the difference in synthesis conditions
Modulated elemental reactants (MER)	Deposition takes place at < 10^{-7} Torr, annealing to self-assembly precursors typically occurs at T < ~650 °C,	Allows access to metastable compounds and heterostructures not accessible via other techniques, deposition time controls film thickness, wafer-scale	Produces films with turbostratic disorder, high grain boundary density

The development of experimental methods and tools will continue to be an important part of research on heterostructures and devices made using them. The discovery of optical contrast of thin layers on thin layers of SiO_2 distinguishes between layer thicknesses with single layer resolution[8,9] and the use of x-ray fluorescence to determine the absolute number of atoms per unit area[165] are two examples of fast and non-destructive techniques that have accelerated discoveries. Advances in focused ion beam[171] and electron microscopy[172–175] enable detailed atomic level structural, compositional, and vibrational analysis of chosen analytical volumes. The need for enhanced analytical tools will become more important as heterostructure devices enter the development stage. Modern manufacturing, especially of complex devices and integrated circuits, is facilitated by intensive statistical analysis of process data and application of aggressive statistical process control. Analysis tools are the foundation of this approach, both defining baseline conditions and identifying

deviations from statistical expectations. The importance of obtaining data on each manufacturing step will drive the development of new analytical approaches and tools.

2.10 Bridge

This chapter describes the current challenges in the synthesis of metastable 2D heterostructures, describing the key reaction steps and methods involved in various conventional synthetic techniques. The following chapter describes the suite of experimental techniques that are utilized extensively in the following chapters to synthesize and characterize the compounds discussed

REFERENCES CITED

1 W. Heisenberg, *Zeitschrift für Physik*, 1927, **43**, 172–198.

2 von E. Schrödinger, *Ann Phys*, 1926, **384**, 361–376.

3 M. M. Waldrop, *Nature*, 2016, **530**, 144–147.

4 S. Natarajan, M. Agostinelli, S. Akbar, M. Bost, A. Bowonder, V. Chikarmane, S. Chouksey, A. Dasgupta, K. Fischer, Q. Fu, T. Ghani, M. Giles, S. Govindaraju, R. Grover, W. Han, D. Hanken, E. Haralson, M. Haran, M. Heckscher, R. Heussner, P. Jain, R. James, R. Jhaveri, I. Jin, H. Kam, E. Karl, C. Kenyon, M. Liu, Y. Luo, R. Mehandru, S. Morarka, L. Neiberg, P. Packan, A. Paliwal, C. Parker, P. Patel, R. Patel, C. Pelto, L. Pipes, P. Plekhanov, M. Prince, S. Rajamani, J. Sandford, B. Sell, S. Sivakumar, P. Smith, B. Song, K. Tone, T. Troeger, J. Wiedemer, M. Yang and K. Zhang, in *2014 IEEE International Electron Devices Meeting*, 2014, pp. 3.7.1-3.7.3.

5 K. S. Novoselov, A. K. Geim, S. v Morozov, D. Jiang, Y. Zhang, S. v. Dubonos, I. v Grigorieva and A. A. Firsov, *Science (1979)*, 2004, **5**, 1–12.

6 P. Chandrasekhar, in *Conducting Polymers, Fundamentals and Applications*, Springer, Cham, 2018, pp. 175–249.

7 B. Partoens and F. M. Peeters, *Physical Review B - Condensed Matter and Materials Physics*, 2006, **74**, 1–11.

8 A. E. Mag-Isa, J. H. Kim, H. J. Lee and C. S. Oh, *2D Materials*, , DOI:10.1088/2053-1583/2/3/034017.

9 P. Blake, E. W. Hill, A. H. Castro Neto, K. S. Novoselov, D. Jiang, R. Yang, T. J. Booth and A. K. Geim, *Applied Physics Letters*, , DOI:10.1063/1.2768624.

10 W. Li, L. Kong, C. Chen, J. Gou, S. Sheng, W. Zhang, H. Li, L. Chen, P. Cheng and K. Wu, *Science Bulletin*, 2018, **63**, 282–286.

11 F. F. Zhu, W. J. Chen, Y. Xu, C. L. Gao, D. D. Guan, C. H. Liu, D. Qian, S. C. Zhang and J. F. Jia, *Nature Materials*, 2015, **14**, 1020–1025.

12 L. M. Schneider, S. Lippert, D. Renaud, J. Kuhnert, K. N. Kang, O. Ajayi, M. U. Halbich, O. M. Abdulmunem, X. Lin, K. Hassoon, S. Edalati-Boostan, Y. D. Kim, W. Heimbrodt, E. H. Yang, J. C. Hone and A. Rahimi-Iman, *2D Materials*, 2017, **4**, 025045.

13 H. M. Dong, Z. H. Tao, L. L. Li, F. Huang, W. Xu and F. M. Peeters, *Applied Physics Letters*, , DOI:10.1063/5.0006617.

14 S. Park, T. Schultz, X. Xu, B. Wegner, A. Aljarb, A. Han, L. J. Li, V. C. Tung, P. Amsalem and N. Koch, *Communications Physics*, , DOI:10.1038/s42005-019-0212-y.

15 L. Li, S. Z. Lu, J. Pan, Z. Qin, Y. Q. Wang, Y. Wang, G. Y. Cao, S. Du and H. J. Gao, *Advanced Materials*, 2014, **26**, 4820–4824.

16 J. L. Zhang, S. Zhao, C. Han, Z. Wang, S. Zhong, S. Sun, R. Guo, X. Zhou, C. D. Gu, K. di Yuan, Z. Li and W. Chen, *Nano Letters*, 2016, **16**, 4903–4908.

17 C. Brosseau and A. Beroual, *Progress in Materials Science*, 2003, **48**, 373–456.

18 S. Schulz and G. Czycholl, *Physical Review B - Condensed Matter and Materials Physics*, 2005, **72**, 1–13.

19 G. Bester, *Journal of Physics Condensed Matter*, , DOI:10.1088/0953-8984/21/2/023202.

20 X. Zhang, K. H. Jin, J. Mao, M. Zhao, Z. Liu and F. Liu, *npj Computational Materials*, 2021, **7**, 1–8.

21 L. Kou, S. C. Wu, C. Felser, T. Frauenheim, C. Chen and B. Yan, *ACS Nano*, 2014, **8**, 10448–10454.

22 U. Dey, M. Chakraborty, A. Taraphder and S. Tewari, *Scientific Reports*, 2018, **8**, 1–11.

23 M. R. Rosenberger, H. J. Chuang, K. M. McCreary, A. T. Hanbicki, S. v. Sivaram and B. T. Jonker, *ACS Applied Materials and Interfaces*, 2018, **10**, 10379–10387.

24 H. W. Guo, Z. Hu, Z. B. Liu and J. G. Tian, *Advanced Functional Materials*, 2021, **31**, 1–32.

25 Y. Huang, Y. H. Pan, R. Yang, L. H. Bao, L. Meng, H. L. Luo, Y. Q. Cai, G. D. Liu, W. J. Zhao, Z. Zhou, L. M. Wu, Z. L. Zhu, M. Huang, L. W. Liu, L. Liu, P. Cheng, K. H. Wu, S. B. Tian, C. Z. Gu, Y. G. Shi, Y. F. Guo, Z. G. Cheng, J. P. Hu, L. Zhao, G. H. Yang, E. Sutter, P. Sutter, Y. L. Wang, W. Ji, X. J. Zhou and H. J. Gao, *Nature Communications*, , DOI:10.1038/s41467-020-16266-w.

26 C. H. Lee, G. H. Lee, A. M. van der Zande, W. Chen, Y. Li, M. Han, X. Cui, G. Arefe, C. Nuckolls, T. F. Heinz, J. Guo, J. Hone and P. Kim, *Nature Nanotechnology*, 2014, **9**, 676–681.

27 K. S. Novoselov, A. Mishchenko, A. Carvalho and A. H. Castro Neto, *Science (1979)*, , DOI:10.1126/science.aac9439.

28 K. S. Novoselov, S. v. Morozov, T. M. G. Mohinddin, L. A. Ponomarenko, D. C. Elias, R. Yang, I. I. Barbolina, P. Blake, T. J. Booth, D. Jiang, J. Giesbers, E. W. Hill and A. K. Geim, *Physica Status Solidi (B) Basic Research*, 2007, **244**, 4106–4111.

29 E. Blundo, M. Felici, T. Yildirim, G. Pettinari, D. Tedeschi, A. Miriametro, B. Liu, W. Ma, Y. Lu and A. Polimeni, *Physical Review Research*, 2020, **2**, 1–7.

30 C. Ernandes, L. Khalil, H. Almabrouk, D. Pierucci, B. Zheng, J. Avila, P. Dudin, J. Chaste, F. Oehler, M. Pala, F. Bisti, T. Brulé, E. Lhuillier, A. Pan and A. Ouerghi, *npj 2D Materials and Applications*, 2021, **5**, 1–7.

31 Y. Sun, D. Wang and Z. Shuai, *Journal of Physical Chemistry C*, 2016, **120**, 21866–21870.

32 M. Falmbigl, A. Fiedler, R. E. Atkins, S. F. Fischer and D. C. Johnson, *Nano Letters*, 2015, **15**, 943–948.

33 J. Feng, D. Biswas, A. Rajan, M. D. Watson, F. Mazzola, O. J. Clark, K. Underwood, I. Marković, M. McLaren, A. Hunter, D. M. Burn, L. B. Duffy, S. Barua, G. Balakrishnan, F. Bertran, P. le Fèvre, T. K. Kim, G. van der Laan, T. Hesjedal, P. Wahl and P. D. C. King, *Nano Letters*, 2018, **18**, 4493–4499.

34 G. Duvjir, B. K. Choi, I. Jang, S. Ulstrup, S. Kang, T. Thi Ly, S. Kim, Y. H. Choi, C. Jozwiak, A. Bostwick, E. Rotenberg, J. G. Park, R. Sankar, K. S. Kim, J. Kim and Y. J. Chang, *Nano Letters*, 2018, **18**, 5432–5438.

35 P. Chen, W. W. Pai, Y. H. Chan, V. Madhavan, M. Y. Chou, S. K. Mo, A. v. Fedorov and T. C. Chiang, *Physical Review Letters*, 2018, **121**, 1–6.

36 M. D. Anderson, C. L. Heideman, Q. Lin, M. Smeller, R. Kokenyesi, A. A. Herzing, I. M. Anderson, D. A. Keszler, P. Zschack and D. C. Johnson, *Angewandte Chemie - International Edition*, 2013, **52**, 1982–1985.

37 A. L. Friedman, A. T. Hanbicki, F. K. Perkins, G. G. Jernigan, J. C. Culbertson and P. M. Campbell, *Scientific Reports*, 2017, **7**, 1–9.

38 M. A. Choffel, R. N. Gannon, F. Göhler, A. M. Miller, D. L. Medlin, T. Seyller and D. C. Johnson, *Chemistry of Materials*, 2021, **33**, 6403–6411.

39 M. A. Choffel, T. M. Kam and D. C. Johnson, *Inorganic Chemistry*, 2021, **60**, 9598–9606.

40 D. M. Hamann, S. R. Bauers, A. M. Miller, J. Ditto, D. B. Moore and D. C. Johnson, *Inorganic Chemistry*, 2020, **59**, 10928–10937.

41 M. Esters, M. B. Alemayehu, Z. Jones, N. T. Nguyen, M. D. Anderson, C. Grosse, S. F. Fischer and D. C. Johnson, *Angewandte Chemie - International Edition*, 2015, **54**, 1130–1134.

42 M. Noh and D. C. Johnson, *J Am Chem Soc*, 1996, **118**, 9117–9122.

43 N. S. Gunning, J. Feser, M. Beekman, D. G. Cahill and D. C. Johnson, *J Am Chem Soc*, 2015, **137**, 8803–8809.

44 J. Rouxel, A. Meerschaut and G. A. Wiegers, *Journal of Alloys and Compounds*, 1995, **229**, 144–157.

45 G. A. Wiegers and A. Meerschaut, *Materials Science Forum*, 1992, **100–101**, 101–172.

46 K. Kato, I. Kawada and T. Takahashi, *Acta Crystallographica Section B Structural Crystallography and Crystal Chemistry*, 1977, **33**, 3437–3443.

47 J. R. Chamorro and T. M. McQueen, *Accounts of Chemical Research*, 2018, **51**, 2918–2925.

48 A. Jain, S. P. Ong, G. Hautier, W. Chen, W. D. Richards, S. Dacek, S. Cholia, D. Gunter, D. Skinner, G. Ceder and K. A. Persson, *APL Materials*, 2013, **1**, 1–11.

49 J. J. de Pablo, N. E. Jackson, M. A. Webb, L. Q. Chen, J. E. Moore, D. Morgan, R. Jacobs, T. Pollock, D. G. Schlom, E. S. Toberer, J. Analytis, I. Dabo, D. M. DeLongchamp, G. A. Fiete, G. M. Grason, G. Hautier, Y. Mo, K. Rajan, E. J. Reed, E. Rodriguez, V. Stevanovic, J. Suntivich, K. Thornton and J. C. Zhao, *npj Computational Materials*, 2019, **5**, 1–23.

50 K. Kovnir, *Chemistry of Materials*, 2021, **33**, 4835–4841.

51 N. Giang, Q. Xu, Y. S. Hor, A. J. Williams, S. E. Dutton, H. W. Zandbergen and R. J. Cava, *Physical Review B - Condensed Matter and Materials Physics*, 2010, **82**, 1–5.

52 A. M. Miller, D. M. Hamann, E. C. Hadland and D. C. Johnson, *Inorganic Chemistry*, 2020, **59**, 12536–12544.

53 P. G. Vekilov, *Crystal Growth and Design*, 2010, **10**, 5007–5019.

54 K. A. Jackson, *Industrial & Engineering Chemistry*, 1965, **57**, 28–32.

55 E. Mura and Y. Ding, *Advances in Colloid and Interface Science*, 2021, **289**, 102361.

56 J. Q. Geisenhoff, A. K. Tamura and A. M. Schimpf, *Chemical Communications*, 2019, **55**, 8856–8859.

57 M. S. Sokolikova, P. C. Sherrell, P. Palczynski, V. L. Bemmer and C. Mattevi, *Nature Communications*, , DOI:10.1038/s41467-019-08594-3.

58 J. H. Perepezko, *Progress in Materials Science*, 2004, **49**, 263–284.

59 D. J. Kelly, N. Clark, M. Zhou, D. Gebauer, R. v. Gorbachev and S. J. Haigh, *Advanced Materials*, , DOI:10.1002/adma.202100668.

60 M. Moliner, Y. Román-Leshkov and A. Corma, *Accounts of Chemical Research*, 2019, **52**, 2971–2980.

61 M. G. Kanatzidis, *Accounts of Chemical Research*, 2005, **38**, 359–368.

62 D. Wang, F. Luo, M. Lu, X. Xie, L. Huang and W. Huang, *Small*, 2019, **15**, 1–12.

63 R. P. Sear, *Journal of Physics Condensed Matter*, , DOI:10.1088/0953-8984/19/3/033101.

64 D. Hu, G. Xu, L. Xing, X. Yan, J. Wang, J. Zheng, Z. Lu, P. Wang, X. Pan and L. Jiao, *Angewandte Chemie - International Edition*, 2017, **56**, 3611–3615.

65 M. Binnewies, R. Glaum, M. Schmidt and P. Schmidt, *Chemical Vapor Transport Reactions*, , DOI:10.1515/9783110254655.

66 J. You, M. D. Hossain and Z. Luo, *Nano Convergence*, , DOI:10.1186/s40580-018-0158-x.

67 W. M. Haynes, *CRC Handbook of Chemistry and Physics*, CRC Press, 2014.

68 N. Briggs, S. Subramanian, Z. Lin, X. Li, X. Zhang, K. Zhang, K. Xiao, D. Geohegan, R. Wallace, L. Q. Chen, M. Terrones, A. Ebrahimi, S. Das, J. Redwing, C. Hinkle, K. Momeni, A. van Duin, V. Crespi, S. Kar and J. A. Robinson, *2D Materials*, , DOI:10.1088/2053-1583/aaf836.

69 Y. Kajikawa and S. Noda, *Applied Surface Science*, 2005, **245**, 281–289.

70 Z. Cai, B. Liu, X. Zou and H. M. Cheng, *Chemical Reviews*, 2018, **118**, 6091–6133.

71 F. J. J. di Salvo, D. E. E. Moncton and J. V. v. Waszczak, *Physical Review B*, 1976, **14**, 4321–4328.

72 K. A. Lozovoy, A. G. Korotaev, A. P. Kokhanenko, V. v. Dirko and A. v. Voitsekhovskii, *Surface and Coatings Technology*, 2020, **384**, 125289.

73 B. Daudin, F. Widmann, G. Feuillet, Y. Samson, M. Arlery and J. Rouvière, *Physical Review B - Condensed Matter and Materials Physics*, 1997, **56**, R7069–R7072.

74 Y. Kajikawa, T. Tsuchiya, S. Noda and H. Komiyama, *Chemical Vapor Deposition*, 2004, **10**, 128–133.

75 F. C. Frank and J. H. van der Merwe, *Proceedings of the Royal Society A: Mathematical, Physical and Engineering Sciences*, 1949, **198**, 216–225.

76 M. Volmer and A. Weber, *Zeitschrift für Physikalische Chemie*, 1926, **119U**, 277–301.

77 I. N. Stranski and L. Krastanow, *Monatshefte für Chemie*, 1939, **72**, 76.

78 W. Zheng, B. Zheng, C. Yan, Y. Liu, X. Sun, Z. Qi, T. Yang, Y. Jiang, W. Huang, P. Fan, F. Jiang, W. Ji, X. Wang and A. Pan, *Advanced Science*, , DOI:10.1002/advs.201802204.

79 C. R. Dean, A. F. Young, I. Meric, C. Lee, L. Wang, S. Sorgenfrei, K. Watanabe, T.

Taniguchi, P. Kim, K. L. Shepard and J. Hone, *Nature Nanotechnology*, 2010, **5**, 722–726.

80 X. Cao, C. Jiang, D. Tan, Q. Li, S. Bi and J. Song, *Journal of Science: Advanced Materials and Devices*, 2021, **6**, 135–152.

81 S. Wang, X. Cui, C. Jian, H. Cheng, M. Niu, J. Yu, J. Yan and W. Huang, *Advanced Materials*, 2021, **33**, 1–21.

82 Z. Hu, Z. B. Liu and J. G. Tian, *Chinese Journal of Chemistry*, 2020, **38**, 981–995.

83 M. Seol, M. H. Lee, H. Kim, K. W. Shin, Y. Cho, I. Jeon, M. Jeong, H. I. Lee, J. Park and H. J. Shin, *Advanced Materials*, 2020, **32**, 1–8.

84 H. Park, J. Kang, M. Kim, J. Seo, J. Kim, J. S. Moon, J. Lee and J. H. Kim, *ACS Nano*, 2021, **15**, 3038–3046.

85 R. F. Frindt, *Physical Review Letters*, 1972, **28**, 299–301.

86 J. N. Coleman, M. Lotya, A. O'Neill, S. D. Bergin, P. J. King, U. Khan, K. Young, A. Gaucher, S. De, R. J. Smith, I. v. Shvets, S. K. Arora, G. Stanton, H. Y. Kim, K. Lee, G. T. Kim, G. S. Duesberg, T. Hallam, J. J. Boland, J. J. Wang, J. F. Donegan, J. C. Grunlan, G. Moriarty, A. Shmeliov, R. J. Nicholls, J. M. Perkins, E. M. Grieveson, K. Theuwissen, D. W. McComb, P. D. Nellist and V. Nicolosi, *Science (1979)*, 2011, **331**, 568–571.

87 X. Fan, P. Xu, D. Zhou, Y. Sun, Y. C. Li, M. A. T. Nguyen, M. Terrones and T. E. Mallouk, *Nano Letters*, 2015, **15**, 5956–5960.

88 D. Sangian, Y. Ide, Y. Bando, A. E. Rowan and Y. Yamauchi, *Small*, 2018, **14**, 1–14.

89 K. Kang, K. H. Lee, Y. Han, H. Gao, S. Xie, D. A. Muller and J. Park, *Nature*, 2017, **550**, 229–233.

90 S. B. Desai, S. R. Madhvapathy, M. Amani, D. Kiriya, M. Hettick, M. Tosun, Y. Zhou, M. Dubey, J. W. Ager, D. Chrzan and A. Javey, *Advanced Materials*, 2016, **28**, 4053–4058.

91 G. Z. Magda, J. Petõ, G. Dobrik, C. Hwang, L. P. Biró and L. Tapasztó, *Scientific Reports*, 2015, **5**, 3–7.

92 M. Velický, G. E. Donnelly, W. R. Hendren, S. McFarland, D. Scullion, W. J. I. DeBenedetti, G. C. Correa, Y. Han, A. J. Wain, M. A. Hines, D. A. Muller, K. S. Novoselov, H. D. Abruńa, R. M. Bowman, E. J. G. Santos and F. Huang, *ACS Nano*, 2018, **12**, 10463–10472.

93 Y. Cao, V. Fatemi, S. Fang, K. Watanabe, T. Taniguchi, E. Kaxiras and P. Jarillo-Herrero, *Nature*, 2018, **556**, 43–50.

94 S. J. Yang, J. H. Jung, E. Lee, E. Han, M. Y. Choi, D. Jung, S. Choi, J. H. Park, D. Oh, S. Noh, K. J. Kim, P. Y. Huang, C. C. Hwang and C. J. Kim, *Nano Letters*, 2021, 1–7.

95 L. A. Walsh and C. L. Hinkle, *Applied Materials Today*, 2017, **9**, 504–515.

96 C. W. Liu, J. J. Dai, S. K. Wu, N. Q. Diep, S. H. Huynh, T. T. Mai, H. C. Wen, C. T. Yuan, W. C. Chou, J. L. Shen and H. H. Luc, *Scientific Reports*, 2020, **10**, 1–8.

97 P. Sheldon, K. M. Jones, M. M. Al-Jassim and B. G. Yacobi, *Journal of Applied Physics*, 1988, **63**, 5609–5611.

98 K. Mohammed, D. A. Cammack, R. Dalby, P. Newbury, B. L. Greenberg, J. Petruzzello and R. N. Bhargava, *Applied Physics Letters*, 1987, **50**, 37–39.

99 B. Harold, in *Surface and Interface Science, Volume 4: Solid-Solid Interfaces and Thin Films*, ed. K. Wandelt, Wiley-VCH Verlag, 1st edn., 2014.

100 K. Ismail, *Journal of Vacuum Science & Technology B: Microelectronics and Nanometer Structures*, 1996, **14**, 2776.

101 A. Koma and K. Yoshimura, *Surface Science*, 1986, **174**, 556–560.

102 A. Koma, K. Sunouchi and T. Miyajima, *Microelectronic Engineering*, 1984, **2**, 129–136.

103 K. Ueno, T. Shimada, K. Saiki and A. Koma, *Applied Physics Letters*, 1990, **56**, 327–329.

104 S. G. Liu, S. N. Subbarao, A. Rosen, D. Sarnoff and C. H. Lee, *Microwave and Optical Technology Letters*, 1993, **6**, 32–33.

105 A. Koma, K. Saiki and Y. Sato, *Applied Surface Science*, 1989, **42**, 451–456.

106 K. Ueno, K. Sasaki, K. Saiki and A. Koma, *Japanese Journal of Applied Physics, Part 1: Regular Papers and Short Notes and Review Papers*, 1999, **38**, 511–514.

107 T. Löher, Y. Tomm, A. Klein, D. Su, C. Pettenkofer and W. Jaegermann, *Journal of Applied Physics*, 1996, **80**, 5718–5722.

108 R. Schlaf, C. Pettenkofer and W. Jaegermann, *Journal of Applied Physics*, 1999, **85**, 6550–6556.

109 M. Iqbal, B. Utama, Z. Peng, R. Chen, B. Peng, X. Xu, Y. Dong, M. Wong, S. Wang, H. Sun and Q. Xiong, *Nano Lett*, 2011, **11**, 3051–3057.

110 Y. L. Chen, J. G. Analytis, J.-H. Chu, Z. K. Liu, S.-K. Mo, X. L. Qi, H. J. Zhang, D. H. Lu, X. Dai, Z. Fang, S. C. Zhang, I. R. Fisher, Z. Hussain and Z.-X. Shen, *Science (1979)*, 2009, **325**, 178–181.

111 H. C. Diaz, R. Chaghi, Y. Ma and M. Batzill, *2D Materials*, , DOI:10.1088/2053-1583/2/4/044010.

112 H. C. Diaz, Y. Ma, S. Kolekar, J. Avila, C. Chen, M. C. Asensio and M. Batzill, *2D Materials*, , DOI:10.1088/2053-1583/aa6e6a.

113 R. Yue, Y. Nie, L. A. Walsh, R. Addou, C. Liang, N. Lu, A. T. Barton, H. Zhu, Z. Che, D. Barrera, L. Cheng, P. R. Cha, Y. J. Chabal, J. W. P. Hsu, J. Kim, M. J. Kim, L. Colombo, R. M. Wallace, K. Cho and C. L. Hinkle, *2D Materials*, , DOI:10.1088/2053-1583/aa8ab5.

114 B. A. Joyce, D. D. Vvedensky, G. R. Bell, J. G. Belk, M. Itoh and T. S. Jones, *Materials Science and Engineering B: Solid-State Materials for Advanced Technology*, 1999, **67**, 7–16.

115 T. Hotta, T. Tokuda, S. Zhao, K. Watanabe, T. Taniguchi, H. Shinohara and R. Kitaura, *Applied Physics Letters*, , DOI:10.1063/1.4963178.

116 L. Jiao, Doctoral, The University of Hong Kong, 2015.

117 D. L. Partin, C. M. Thrush, S. J. Simko and S. W. Gaarenstroom, *Journal of Applied Physics*, 1989, **66**, 6115–6120.

118 L. A. Walsh, R. Yue, Q. Wang, A. T. Barton, R. Addou, C. M. Smyth, H. Zhu, J. Kim, L. Colombo, M. J. Kim, R. M. Wallace and C. L. Hinkle, *2D Materials*, , DOI:10.1088/2053-1583/aa61e1.

119 H. Liu and Y. Xue, *Advanced Materials*, 2021, **2008456**, 2–9.

120 S. Chen, H. Liu, F. Chen, K. Zhou and Y. Xue, *ACS Nano*, 2020, **14**, 11473–11481.

121 X. Sun, W. Li, X. Wang, Q. Sui, T. Zhang, Z. Wang, L. Liu, D. Li, S. Feng, S. Zhong, H. Wang, V. Bouchiat, M. Nunez Regueiro, N. Rougemaille, J. Coraux, A. Purbawati, A. Hadj-Azzem, Z. Wang, B. Dong, X. Wu, T. Yang, G. Yu, B. Wang, Z. Han, X. Han and Z. Zhang, *Nano Research*, 2020, **13**, 3358–3363.

122 B. Li, Z. Wan, C. Wang, P. Chen, B. Huang, X. Cheng, Q. Qian, J. Li, Z. Zhang, G. Sun, B. Zhao, H. Ma, R. Wu, Z. Wei, Y. Liu, L. Liao, Y. Ye, Y. Huang, X. Xu, X. Duan, W. Ji and X. Duan, *Nature Materials*, 2021, **20**, 818–825.

123 M. Kan, S. Adhikari and Q. Sun, *Physical Chemistry Chemical Physics*, 2014, **16**, 4990–4994.

124 M. Aykol, S. S. Dwaraknath, W. Sun and K. A. Persson, *Science Advances*, 2018, **4**, 1–8.

125 R. B. Schwarz and W. L. Johnson, *Physical Review Letters*, 1983, **51**, 415–418.

126 E. J. Cotts, W. J. Meng and W. L. Johnson, *Physical Review Letters*, 1986, **57**, 2295.

127 R. B. Schwarz, K. L. Wong, W. L. Johnson and B. M. Clemens, *Journal of Non-Crystalline Solids*, 1984, **61–62**, 129–134.

128 T. Novet, J. M. Mcconnell and D. C. Johnson, *Chemistry of Materials*, 1992, **4**, 473–478.

129 L. Fister and D. C. Johnson, *J Am Chem Soc*, 1992, **114**, 4639–4644.

130 M. Fukuto, M. D. Hornbostel and D. C. Johnson, *J Am Chem Soc*, 1994, **116**, 9136–9140.

131 T. Novet and D. C. Johnson, *J Am Chem Soc*, 1991, **113**, 3398–3403.

132 J. R. Williams, M. Johnson and D. C. Johnson, *J Am Chem Soc*, 2001, **123**, 1645–1649.

133 M. D. Hornbostel, E. J. Hyer, J. Thiel and D. C. Johnson, *J Am Chem Soc*, 1997, **119**, 2665–2668.

134 N. Pienack and W. Bensch, *Angewandte Chemie - International Edition*, 2011, **50**, 2014–2034.

135 M. Regus, S. Mankovsky, S. Polesya, G. Kuhn, J. Ditto, U. Schürmann, A. Jacquot, K. Bartholomé, C. Näther, M. Winkler, J. D. König, H. Böttner, L. Kienle, D. C. Johnson, H. Ebert and W. Bensch, *Journal of Solid State Chemistry*, 2015, **230**, 254–265.

136 M. Jansen, *Angewandte Chemie - International Edition*, 2002, **41**, 3746–3766.

137 D. Fischer and M. Jansen, *J Am Chem Soc*, 2002, **124**, 3488–3489.

138 D. Fischer, A. Müller and M. Jansen, *Zeitschrift fur Anorganische und Allgemeine Chemie*, 2004, **630**, 2697–2700.

139 D. Fischer and M. Jansen, *Angewandte Chemie - International Edition*, 2002, **41**, 1755–1756.

140 D. C. Johnson, *Current Opinion in Solid State and Materials Science*, 1998, **3**, 159–167.

141 M. Noh, J. Thiel and D. C. Johnson, *Science (1979)*, 1995, **270**, 1181–1184.

142 M. Beekman, S. Disch, S. Rouvimov, D. Kasinathan, K. Koepernik, H. Rosner, P. Zschack, W. S. Neumann and D. C. Johnson, *Angewandte Chemie - International Edition*, 2013, **52**, 13211–13214.

143 D. L. Mesoza Cordova, T. M. Kam, R. N. Gannon, P. Lu and D. C. Johnson, *J Am Chem Soc*, 2020, **142**, 13145–13154.

144 O. Oyelaran, T. Novet, C. D. Johnson and D. C. Johnson, *J Am Chem Soc*, 1996, **118**, 2422–2426.

145 J. R. Williams, M. B. Johnson and D. C. Johnson, *J Am Chem Soc*, 2003, **125**, 3589–3592.

146 M. D. Anderson, J. O. Thompson and D. C. Johnson, *Chemistry of Materials*, 2013, **25**, 3996–4002.

147 M. Overbay, T. Novet and D. C. Johnson, *Journal of Solid State Chemistry*, 1996, **123**, 337–343.

148 D. R. Merrill, D. B. Moore, J. Ditto, D. R. Sutherland, M. Falmbigl, M. Winkler, H. F. Pernau and D. C. Johnson, *European Journal of Inorganic Chemistry*, 2015, **2015**, 83–91.

149 D. M. Hamann, D. Bardgett, S. R. Bauers, T. W. Kasel, A. M. Mroz, C. H. Hendon, D. L. Medlin and D. C. Johnson, *Chemistry of Materials*, 2020, **32**, 5802–5813.

150 D. M. Hamann, A. C. Lygo, M. Esters, D. R. Merrill, J. Ditto, D. R. Sutherland, S. R. Bauers and D. C. Johnson, *ACS Nano*, 2018, acsnano.7b07506.

151 D. R. Merrill, D. R. Sutherland, D. B. Moore, M. Falmbigl, L. Medlin and D. C. Johnson, *Nanoscale*, 2016, **8**, 13646–13651.

152 F. R. Harris, S. Standridge and D. C. Johnson, *J Am Chem Soc*, 2005, **127**, 7843–7848.

153 F. R. Harris, S. Standridge, C. Feik and D. C. Johnson, *Angewandte Chemie - International Edition*, 2003, **42**, 5296–5299.

154 C. L. Heideman, S. Tepfer, Q. Lin, R. Rostek, P. Zschack, M. D. Anderson, I. M. Anderson and D. C. Johnson, *J Am Chem Soc*, 2013, **135**, 11055–11062.

155 E. Hadland, H. Jang, M. Falmbigl, R. Fischer, D. L. Medlin, D. G. Cahill and D. C. Johnson, *Chemistry of Materials*, 2019, **31**, 5699–5705.

156 Q. Lin, M. Smeller, C. L. Heideman, P. Zschack, M. Koyano, M. D. Anderson, R. Kykyneshi, D. A. Keszler, I. M. Anderson and D. C. Johnson, *Chemistry of Materials*, 2010, **22**, 1002–1009.

157 Q. Lin, S. Tepfer, C. Heideman, C. Mortensen, N. Nguyen, P. Zschack, M. Beekman and D. C. Johnson, *Journal of Materials Research*, 2011, **26**, 1866–1871.

158 D. B. Moore, M. Beekman, S. Disch and D. C. Johnson, *Angewandte Chemie*, 2014, **126**, 5778–5781.

159 D. Bardgett, R. N. Gannon, D. M. Hamann, D. M. Roberts, S. R. Bauers, P. Lu and D. C. Johnson, *Chemistry of Materials*, 2021, **33**, 2585–2592.

160 A. C. Lygo, D. M. Hamann, D. B. Moore, D. R. Merrill, J. Ditto, M. Esters, J. Orlowicz, S. R. Wood and D. C. Johnson, *J Am Chem Soc*, 2018, **140**, 3385–3393.

161 N. S. Gunning, T. Dankwort, M. Falmbigl, U. Ross, G. Mitchson, D. M. Hamann, A. Lotnyk, L. Kienle and D. C. Johnson, *Chemistry of Materials*, 2017, **29**, 8292–8298.

162 Z. Xu, Z. Tang, S. D. Kevan, T. Novet and D. C. Johnson, *Journal of Applied Physics*, 1993, **74**, 905–912.

163 T. Novet, S. Kevan and D. C. Johnson, *Materials Science and Engineering A*, 1995, **195**, 21–27.

164 T. Phung, J. Jensen, D. Jonshon, J. Donovan and B. McBurnett, *X-Ray Spectrometry*, 2008, **37**, 608–614.

165 D. M. Hamann, D. Bardgett, D. L. M. Cordova, L. A. Maynard, E. C. Hadland, A. C. Lygo, S. R. Wood, M. Esters and D. C. Johnson, *Chemistry of Materials*, 2018, **30**, 6209–6216.

166 S. R. Bauers, S. R. Wood, K. M. Ø. Jensen, A. B. Blichfeld, B. B. Iversen, S. J. L. Billinge and D. C. Johnson, *J Am Chem Soc*, 2015, **137**, 9652–9658.

167 J. Ditto, D. R. Merrill, G. Mitchson, J. J. Gabriel, K. Mathew, R. G. Hennig, D. L. Medlin, N. D. Browning and D. C. Johnson, *Angewandte Chemie - International Edition*, 2017, **56**, 14448–14452.

168 M. Jansen, *Pure and Applied Chemistry*, 2014, **86**, 883–898.

169 M. Jansen and J. C. Schön, *Angewandte Chemie - International Edition*, 2006, **45**, 3406–3412.

170 W. Y. Zhou, A. Meetsma, J. L. de Boer and G. A. Wiegers, *Materials Research Bulletin*, 1992, **27**, 563–572.

171 N. Bassim, K. Scott and L. A. Giannuzzi, *MRS Bulletin*, 2014, **39**, 317–325.

172 R. R. Schröder, *Archives of Biochemistry and Biophysics*, 2015, **581**, 25–38.

173 G. Guzzinati, T. Altantzis, M. Batuk, A. de Backer, G. Lumbeeck, V. Samaee, D. Batuk, H. Idrissi, J. Hadermann, S. van Aert, D. Schryvers, J. Verbeeck and S. Bals, *Materials*, , DOI:10.3390/ma11081304.

174 D. J. Stokes, *Philosophical Transactions of the Royal Society A: Mathematical, Physical and Engineering Sciences*, 2003, **361**, 2771–2787.

175 *Nature Methods*, 2016, **13**, 1.

CHAPTER III

EXPERIMENTAL METHODS

3.0 Authorship Statement

This chapter was written for this work alone with no intention of publishing it elsewhere. I am the primary author and wrote the following with editorial assistance from my advisor, David C. Johnson.

3.1 Synthesis of Layered Precursors with Modulated Elemental Reactants (MER)

All of the compounds presented and discussed in the following text were synthesized using the modulated elemental reactants (MER) method, which was discussed in detail in the introduction and briefly summarized again here.[1,2]

Conventional solid-state synthesis techniques generally are diffusion-limited due to the extremely low diffusion rates in solids. While there are many creative solutions to increase the diffusion rates, including applying higher temperatures, decreasing particle size, or using a liquid phase, MER solves this problem using nanostructured layered precursors built from ultrathin elemental layers. Using physical vapor deposition, each layer of atoms is sequentially deposited in an order that mimics the structure of the target compound(s), with the goal of depositing the required number of each atom for the target compound(s).) Because the layered precursor very closely resembles the target compound(s) in composition and structure on an atomic scale, the total diffusion distances required in the reaction are significantly decreased relative to traditional solid-state synthesis reactions (on the order of Å with MER vs. ~cm - ~µm with conventional solid-state methods).

Because of the six order-of-magnitude reduction of diffusion lengths, diffusion is no longer the rate-limiting step in most MER syntheses. Instead, heterogenous nucleation is generally limiting. Because the system is no

longer diffusion limited, so long as the composition of the layered precursor matches that of the target compound, the target compound should be the easiest compound to nucleate at that composition and will therefore be the first compound to form. This enables the synthesis of many metastable and kinetically stable products that are not accessible via other synthetic techniques.[3–5] Naturally, compounds that include van der Waal's gaps make excellent synthetic targets using the MER method, such as transition meal dichalcogenides (TMD's). MER allows for the preparation of stacked layers of 2D compounds, termed van der Waal's heterostructures, in a nearly infinite number of different sequences, which represent a huge unexplored parameter-space for materials discovery.[6,7]

Experimentally, our MER setup utilizes electron-beam guns and a Knudsen effusion cell to evaporate elemental sources, each of which are placed in their own ports in the bottom of a high-vacuum chamber, as shown in Figure 3.1. The resulting plumes of vaporized atoms are all aimed at a substrate holder, which spins to average out any mis-aligned or asymmetric elemental plumes. During deposition, each source's flux is monitored via quartz crystal microbalances, placed just below the gate valve. A deposition controller instructs pneumatic shutters above each element to open and close for the appropriate period such that the number of atoms / $Å^2$ deposited in each layer is within error of the target value. This allows each precursor to be constructed layer-by-layer in a controlled and sequential manner, enabling precise control over the nanoarchitecture of the resulting compound or heterostructure.

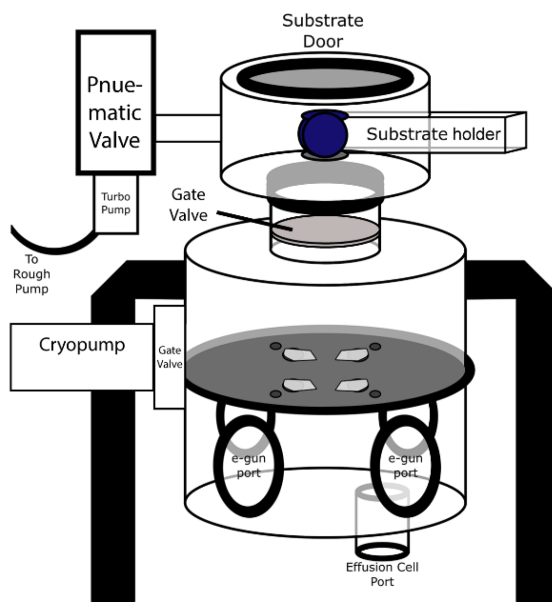

Figure 3.1. Schematic side-view of the high-vacuum chamber used to deposit ultrathin elemental layers to form nanostructured precursors. Elemental sources are placed in electron-beam gun hearths or an effusion cell and aimed at a substrate. Computer-controlled shutters placed between the substrate and the sources allow for control over the sequence and thickness of deposited layers.

3.2 X-ray Fluorescence and Statistical Process Control

X-ray fluorescence (XRF) experiments are used to determine the amount of atoms / $Å^2$ that were experimentally deposited in each precursor. Using a wavelength-dispersive XRF (WD-XRF) instrument (Rigaku Primus II), the fluorescence intensity of each element that was deposited in the sample is determined. Previous work in the Johnson group has shown that there is a linear relationship between the XRF intensity and the number of atoms / $Å^2$, provided the sample is within the thin film regime (i.e. x-ray absorption remains negligible). Using calibration curves that relate the XRF intensity to the number of atoms / $Å^2$, the absolute number of atoms / $Å^2$ in a sample can be determined, with a sub-monolayer accuracy.[8]

While the publication referenced above was critical in establishing the accuracy and repeatability of the XRF method, ideally, the calibration curves are continually updated as more high-quality thin film samples are synthesized by the group. This iterative adjustment of the calibration curves as the number of samples included in the curve increases will only serve to ensure the maximum accuracy of the method. As shown in Figure 3.2, creating sample calibration curves utilizing only samples synthesized by this author during his time at UO gives slopes that are within error of those

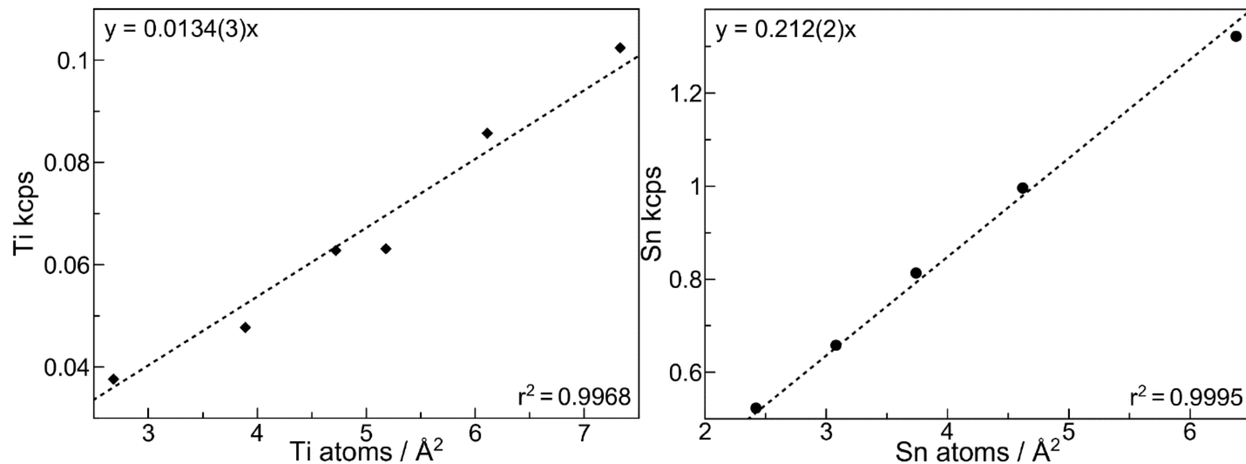

published in 2018 by Hamann et. al.

Figure 3.2. Plots of the measured XRF intensity for Ti (*left*) and Sn (*right*) using samples made by this author that display Laue oscillations, allowing for the determination of the integral number of crystalline unit cells in the sample (and therefore, the total number of atoms / Å^2). The slopes match those published in Hamann et. al. (0.0133(3) kcps*Å^2/Ti atoms and 0.211(2) kcps*Å^2/Sn atoms).[8]

The ability to quickly measure the composition and determine the absolute number of atoms in each sample via a non-destructive method has revolutionized the way that MER is practiced. This method allows for the application of statistical process control, which provides iterative adjustment of subsequent deposition parameters such that the maximum yield of on-target samples may be obtained. Another significant impact of being able to determine sample composition quickly and easily is the near

order-of-magnitude reduction in the number of samples needed to obtain one with the desired composition.

An index for measuring the consistency of the deposition plume shape for each source can be obtained by normalizing the observed XRF signal for each element to the number of units of material programmed into the deposition controller. After each set of samples is deposited, the background corrected total XRF intensity for each element is normalized to the amount programmed into the deposition controller. The average normalized value is used to iteratively determine the appropriate deposition controller parameters for the next samples deposited, such that the number of atoms deposited are within error of the target values.

3.3 Structural Characterization Techniques

As discussed in detail in Chapter IV and briefly summarized here, x-ray reflectivity (XRR) and x-ray diffraction (XRD) experiments are used to determine the structure of the deposited precursors. Unless otherwise specified, all diffraction or reflectivity data presented was collected on a Bruker D8-Discover or a Rigaku SmartLab.

At low angles, the intensity of the reflected beam dominates the signal at the detector. The difference in path length between rays that reflect off the air-film interface and those that reflect off the film-substrate interface creates a phase difference that can be observed as an oscillatory interference effect in most low angle reflectivity patterns, known as Kiessig fringes. The period of the Kiessig fringes can be used to extract the total film thickness, inclusive of any extra material that may not necessarily be incorporated into the coherent crystalline domains contributing to the diffraction signal. The angle of the last observable Kiessig fringe can be used to roughly estimate the interfacial roughness of the top and bottom of the film.

As one moves to higher angles, the reflected intensity falls off as $f(\theta) =$

θ^{-4}, but the diffracted intensity remains significant. Bragg's law predicts the angles that planes of atoms will scatter diffracted x-rays constructively. By measuring the spacing of observed Bragg maxima in the XRD pattern, Bragg's law can be used to calculate the interplanar spacing of the atoms (i.e. the *c*-axis lattice parameter) in thin film compounds or heterostructures. The intensity and width of the reflections can be used to estimate the size of the crystallites in the sample. The experimental setup of the diffractometer for XRR and XRD experiments is identical, aside from some minor differences in the detector optics to avoid saturating the sensor.

Sequential XRR and XRD experiments of the same film as a function of temperature are used to determine the optimal annealing conditions for each compound or family of heterostructures and elucidate reaction pathways.

Additionally, high-angle annular dark field scanning transmission electron microscopy (HAADF-STEM) is used to image lift-outs of sample cross-sections with atomic-level resolution. The lift-outs are prepared via standard technique using a focused ion beam (FIB) to mill a small, electron-transparent section of the annealed film.[9] Finally, unless otherwise specified, all microscopy images presented were collected with a probe-corrected Thermo Fisher Scientific Themis Z STEM.

3.4 Electrical Characterization Techniques

The van der Pauw method is used to measure the electrical resistivity and Hall effect for thin film samples. Further details about the Van der Pauw method and these measurements are given in Chapter V.

3.5 Bridge

This chapter describes experimental techniques that are utilized extensively in the following chapters to synthesize and characterize the compounds discussed. The next chapter presents a method for extracting structural information from x-ray diffraction patterns that contain Laue

oscillations.

REFERENCES CITED

(1) Fister, L.; Li, X.; Mcconnell, J.; Novet, T.; Johnson, D. C. Deposition System for the Synthesis of Modulated, Ultrathin-Film Composites. *J. Vac. Sci. Technol. A* **1993**, *11* (6), 3014. https://doi.org/10.1116/1.578290.

(2) Noh, M.; Johnson, C. D.; Hornbostel, M. D.; Thiel, J.; Johnson, D. C. Control of Reaction Pathway and the Nanostructure of Final Products through the Design of Modulated Elemental Reactants. *Chem. Mater.* **1996**, *8* (8), 1625–1635. https://doi.org/10.1021/cm9601087.

(3) Hornbostel, M. D.; Hyer, E. J.; Thiel, J.; Johnson, D. C. Rational Synthesis of Metastable Skutterudite Compounds Using Multilayer Precursors. *J. Am. Chem. Soc.* **1997**, *119* (11), 2665–2668. https://doi.org/10.1021/ja964084g.

(4) Bauers, S. R.; Wood, S. R.; Jensen, K. M. Ø.; Blichfeld, A. B.; Iversen, B. B.; Billinge, S. J. L.; Johnson, D. C. Structural Evolution of Iron Antimonides from Amorphous Precursors to Crystalline Products Studied by Total Scattering Techniques. *J. Am. Chem. Soc.* **2015**, *137* (30), 9652–9658. https://doi.org/10.1021/jacs.5b04838.

(5) Hamann, D. M.; Rudin, S. P.; Asaba, T.; Ronning, F.; Cordova, D. L. M.; Lu, P.; Johnson, D. C. Predicting and Synthesizing Interface Stabilized 2D Layers. *Chem. Mater.* **2021**, *33* (13), 5076–5084. https://doi.org/10.1021/acs.chemmater.1c01064.

(6) Merrill, D. R.; Sutherland, D. R.; Moore, D. B.; Falmbigl, M.; Medlin, L.; Johnson, D. C. The Synthesis of [(PbSe)1+δ]m(TiSe2)n[(SnSe2)1+γ]m(TiSe2)n Heterostructures with Designed Nanoarchitectures by Self Assembly of Amorphous Precursors. *Nanoscale* **2016**, *8*, 13646–13651. https://doi.org/10.1039/c6nr03406c.

(7) Miller, A. M.; Johnson, D. C. Challenges in Synthesis of Heterostructures. *J. Mater. Chem. C* **2022**. https://doi.org/10.1039/d2tc00324d.

(8) Hamann, D. M.; Bardgett, D.; Cordova, D. L. M.; Maynard, L. A.; Hadland, E. C.; Lygo, A. C.; Wood, S. R.; Esters, M.; Johnson, D. C. Sub-Monolayer Accuracy in

Determining the Number of Atoms per Unit Area in Ultrathin Films Using X-Ray Fluorescence. *Chem. Mater.* **2018**, *30*, 6209–6216. https://doi.org/10.1021/acs.chemmater.8b02591.

(9) Schaffer, M.; Schaffer, B.; Ramasse, Q. Sample Preparation for Atomic-Resolution STEM at Low Voltages by FIB. *Ultramicroscopy* **2012**, *114*, 62–71. https://doi.org/10.1016/j.ultramic.2012.01.005.

CHAPTER IV

EXTRACTING INFORMATION FROM X-RAY DIFFRACTION PATTERNS CONTAINING LAUE OSCILLATIONS

4.0 Authorship Statement

Chapter IV was published in Zeitschrift für Naturforschung B in 2022. I am the primary author of the text with David C. Johnson providing extensive editorial assistance. Mellie Lemon and Marisa Choffel contributed experimental data, while Sarah Rich and Fischer Harvel helped search the literature for all references mentioning Laue oscillations.

4.1 Introduction

Laue oscillations result from the incomplete destructive interference of a finite number of unit cells and occur when a sample consists of domains with the same number of unit cells across most of the area being probed. First predicted by Max von Laue, the Laue interference function relates the number of unit cells in the diffracting crystal to the distribution of diffracted intensity.[1] Generally, the presence of Laue oscillations are taken as confirmation that grown films are of high quality, homogenous, contain only the targeted compound, and have smooth and planar top and bottom interfaces.[2–11] The presence of Laue oscillations is frequently used as evidence of "the high crystallinity of samples"[12] , "the uniformity of the film and smoothness of the interfaces"[13] or that "the out-of-plane order is high and coherent over the entire film thickness"[14].

While it is true that Laue oscillations are a qualitative indicator of sample quality, the presence of Laue oscillations also provides an opportunity to gain significant structural information about films. The most common quantitative analysis of Laue oscillations utilizes an equation derived from the Laue interference function to extract the total thickness of the crystalline phase.[15–25] The thickness obtained in this manner is often taken to be the total film thickness, which assumes that there is no additional thickness from amorphous or non-crystallographically-aligned layers present above and/or below the

diffracting crystal. There are only a few reports in the literature where both the oscillations in the X-ray reflectivity (XRR) at low diffraction angles and the Laue oscillations observed in the vicinity of a Bragg reflection are used to detect potential excess material. In these reports, differences between the total film thickness calculated from Kiessig fringes in the XRR data and the thickness of the crystalline layers obtained via the Laue oscillations were found.[26,27] Furthermore, the intensity of experimental Laue oscillations often differs from those predicted from the Laue function. The Laue function results in symmetric intensities of satellite reflections on either side of the Bragg maxima, but an asymmetric distribution of intensities on each side is also frequently observed.[9,26–28] In addition, the number of Laue oscillations observed on either side of the Bragg reflection varies significantly from sample to sample.[2–28] The extraction of structural information from Laue oscillations has been challenging due to the lack of a discussion of all relevant physical phenomena in a single reference that relates structural parameters to Laue intensities and provides examples illustrating the development of structural models from experimental data.

This paper addresses this challenge by presenting a summary of the relevant physical phenomena, showing how structural features in films impact the intensity and number of both Kiessig fringes and Laue oscillations that are observed, and provides examples of developing a structural model from experimental data. The first example illustrates an approach to simultaneously model reflectivity and diffraction patterns when these two phenomena are relatively uncoupled. The second example involves a more complex example where these two phenomena are both important in the same angular regions. Further efforts are required to create simulation software that enables the development of atom-level structural descriptions of films using the intensities of Kiessig fringes and Laue oscillations.

4.2 Results and Discussion

We begin this section with a short review of the physical origin of Kiessig

fringes and show how increasing the structural complexity of films effects the intensity of the fringes with increasing angle using simulations. Examples show how to extract structural information from experimental data. Next, we discuss the origin of Laue oscillations and use examples to demonstrate how Laue oscillation intensities calculated using the Laue function differ from experimental patterns. We illustrate how the interaction between reflectivity and diffraction effects cause the asymmetry in Laue intensities around the central Bragg reflection and use simulations to show the impact of structural imperfections on the intensities of Laue oscillations. We conclude by developing structural models from two experimental data sets where the total film thickness (calculated from the period of the Kiessig oscillations) is different from the thickness derived from the period of the Laue oscillations (defined as the product of the number of coherently diffracting unit cells and the c-axis lattice parameter).

4.3 X-ray Reflectivity (XRR) and Kiessig Fringes:

Figure 4.1. shows XRR patterns for an experimental TiSe2 film, along with simulated reflectivity patterns for 5.00 nm (*bottom*) and 25.00 nm (*2nd from bottom*) $TiSe_2$ films assuming a uniform electron density slab using the BedeREFS software.[29] The oscillations observed at low angles in these patterns are known as Kiessig fringes, first reported in 1931[30], which result from interference between X-rays reflected off the top air/sample interface and those reflected off the sample/substrate interface. The position and spacing of the maxima (or minima) can be used to quantitatively determine the film thickness using a modified version of Bragg's law that includes a correction for refraction, as shown in Eq. 4.1.[31]

$$\sin^2(\theta_i) = \theta_c^2 + (((n_i+\Delta n)^2\lambda^2) / (4t^2)) \qquad \text{Eq. 4.1.}$$

In this equation, θ_i is the angle of the observed Kiessig fringe maxima, θ_c is the critical angle, n_i is the index of the observed Kiessig fringe maxima, λ is the wavelength of the radiation utilized, and t is the total film thickness. As shown in Figure 4.1., the period of the observed Kiessig fringes is inversely related to the thickness of the films. The thickness of the experimental $TiSe_2$ film calculated using this equation is 50.10(5) nm (*top*).

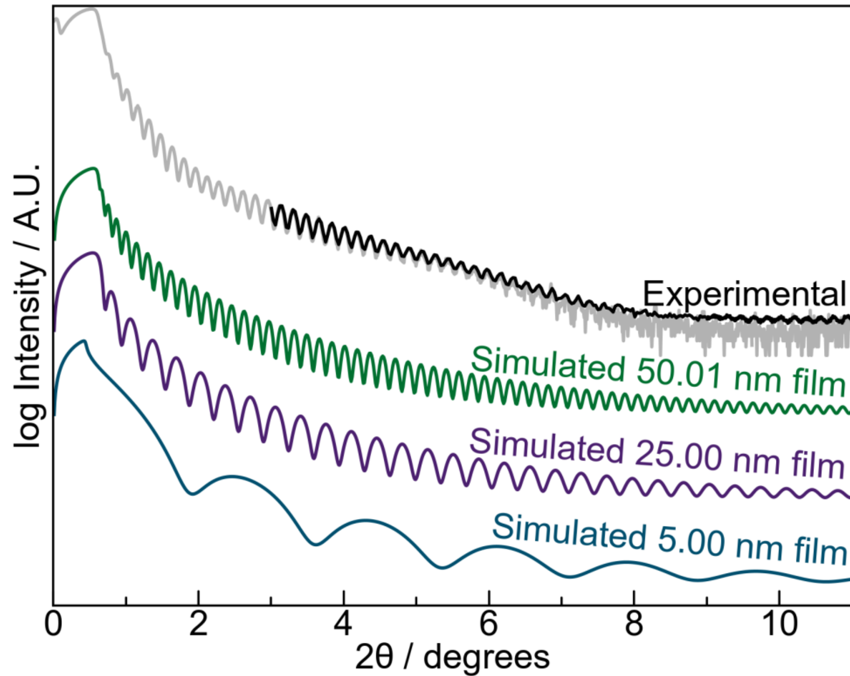

Figure 4.1. Experimental X-ray reflectivity pattern of a 50.10(5) nm (*top curve*) $TiSe_2$ film. Simulated reflectivity patterns from 50.1 nm (*2nd from top*), 25 nm (*2nd from bottom*), and 5 nm (*bottom*) $TiSe_2$ films are also shown. The period of the Kiessig fringes is inversely related to the film's thickness.

An important point is that Kiessig fringes result solely from reflectivity phenomena - their presence and period do not depend on the crystallinity of the sample. Kiessig fringes will be observed in the reflectivity pattern for any thin enough sample with sufficiently smooth planar air/sample and sample/substrate interfaces, provided there is a difference in the index of refraction between the sample and the substrate. The intensity of the Kiessig fringes scales with the difference in electron density between the substrate and the film, with a larger difference producing more intense oscillations. Additionally, because the critical angle for total internal reflection (θ_c) scales with electron density, the angle of each Kiessig fringe shifts depending on the average

electron density of the film (Eq. 4.1.).

The rate of decay in the intensity of Kiessig fringes with increasing angle depends on interface roughness. Simulated reflectivity patterns from models containing atomically abrupt interfaces have Kiessig fringes that continue throughout the angular range, decreasing in intensity as the angle increases. The Kiessig fringes in the experimental pattern become unresolvable at an angle of ~7° 2θ. Parratt showed that the angle where Kiessig fringes are no longer visible depends on the sample's average top and bottom surface roughness and derived the relationship:

$$\Delta t = \lambda \ / \ (4 * (\theta_m^2 - \theta_c^2)^{1/2})) \qquad \text{Eq. 4.2.}$$

where θ_m is the angle of the last observed Kiessig maxima and θ_c is the critical angle.[32] The roughness of both the top and bottom interfaces controls the angle to which the Kiessig interference pattern will be visible. Figure 4.2. demonstrates how different amounts of roughness in the bottom sample/substrate ($\sigma_{substrate}$) and the top air/sample (σ_{sample}) interfaces reduce the intensity of the Kiessig fringes. The slope of the initial decay of the intensity of the Kiessig fringes is different for the bottom and top interfaces. The shape of the intensity envelope can therefore be used to distinguish between roughness at the top or bottom interfaces. Kiessig fringes observed out to 7° 2θ correspond to an interfacial roughness of about 5 Å according to the Parratt relationship, eq. (2).

Further information about a sample's structure can be extracted from deviations in the shape of its XRR pattern from that expected for a single layer.[29] The reflectivity from a film with a single constituent and perfect, planar interfaces is described by the Fresnel equations and the intensity decay is smooth, even, and continues to the angle at which the average scattered intensity is less than the background intensity.[33] If there are two layers in the film with different electron densities, Kiessig fringes from the two layers will both be apparent in the X-ray reflectivity scan.

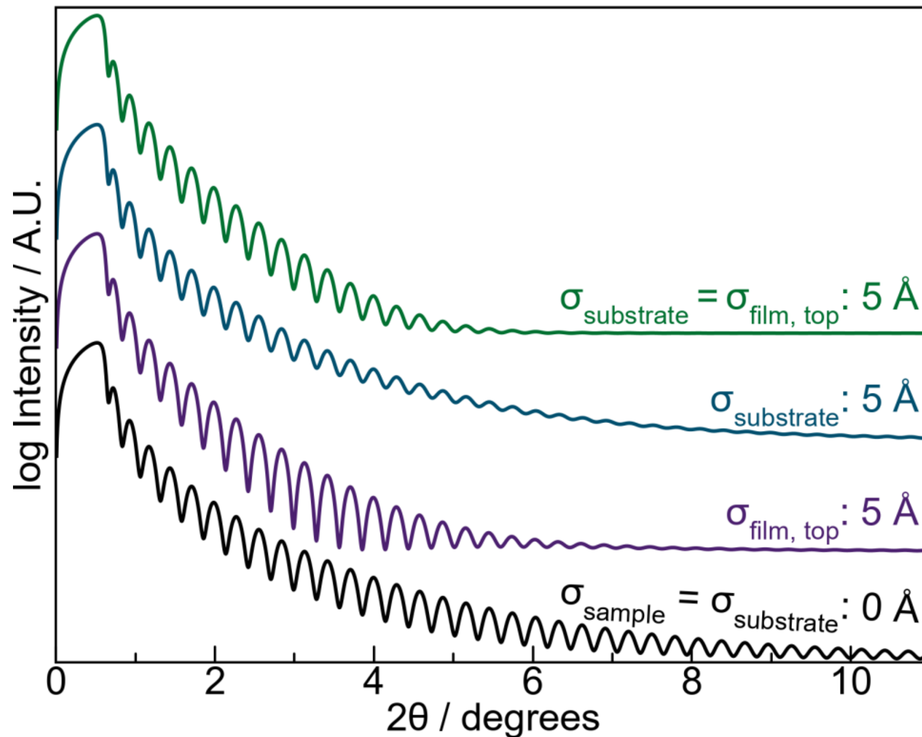

Figure 4.2. Simulated reflectivity patterns from a 30.19 nm $TiSe_2$ film with different amounts of interfacial roughness. The amount of interfacial roughness determines the maximum angle at which the Kiessig interference fringes are visible. The shape of the intensity decay differs depending on whether the roughness is at the top or at the bottom interface.

Figure 4.3. illustrates this effect, showing separate simulated reflectivity patterns for 2.42 nm TiO_2 (*bottom*) and 50.05 nm $TiSe_2$ (*middle*) films, along with the calculated reflectivity patterns for a film containing a 2.42 nm TiO_2 layer on top of a 50.05 nm $TiSe_2$ film on a silicon (Si) substrate (*top*). The presence of oscillations with two different frequencies indicates that a second layer of material with a unique electron density and thickness is present in a film. Although somewhat subtler, the experimental pattern in Figure 4.1. also shows this effect, with a weak, low frequency oscillation apparent under the higher intensity oscillations from the total film thickness. The large period of the underlying oscillation suggests that the additional layer is much thinner than the TiSe2 layer.

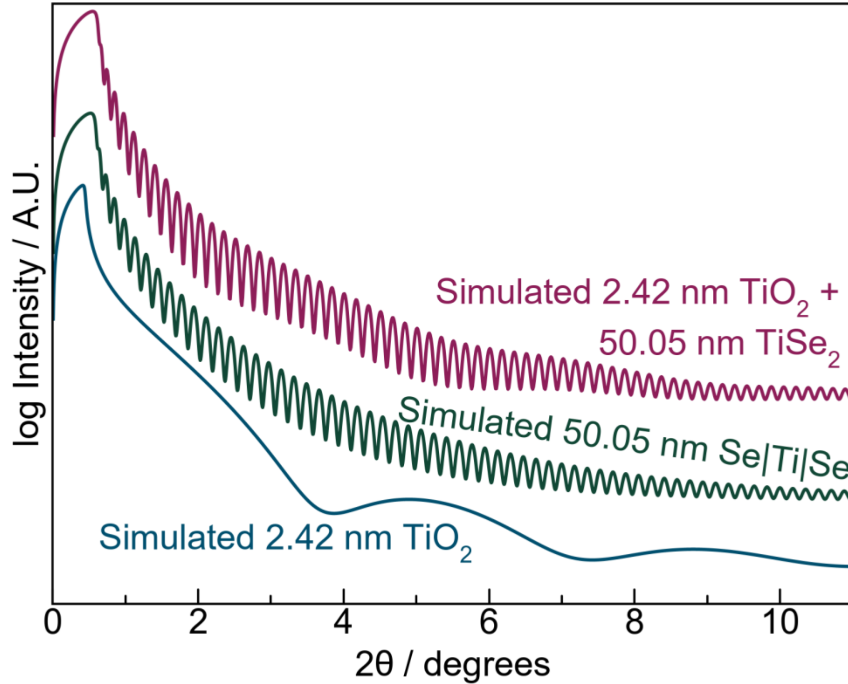

Figure 4.3. Simulated XRR patterns of 2.42 nm TiO_2 (*bottom*) and 50.05 nm $TiSe_2$ (*middle*) films, along with the simulated pattern for a film containing 2.42 nm TiO_2 on top of 50.05 nm $TiSe_2$ (*top*).

4.4 Laue Oscillations

If the sample consists of a crystallographically aligned film or contains a repeating sequence of deposited amorphous layers with different electron densities, the interference caused by the periodic changes in electron density results in Bragg reflections at angles given by Bragg's Law:

$$n\lambda = 2d\sin(\theta) \quad \text{Eq. 4.3.}$$

where n is an integer, and $n\lambda$ is the difference in distance traveled by a wave scattered by repeating planes of equal electron density that are a distance (*d*) apart. The resulting evenly spaced set of reflections can be indexed as a one-dimensional crystal. Using Bragg's Law, the thickness of the layers (or the size of the unit cell of crystals orientated perpendicular to the substrate) can be extracted from the diffraction pattern. Figure 4.4. shows the XRD pattern for a 79-layer thick $TiSe_2$ film, displaying four evenly spaced Bragg maxima, which can be indexed as 00l reflections consistent with those expected for a unit cell with a c-axis lattice parameter of 6.036(1) Å. The inset of Figure 4.4. expands the

intensity and angular scale about the 001 reflection. The weak subsidiary maxima seen on the sides of this Bragg reflections are Laue oscillations. The positions and intensities of these satellite reflections are predicted by the Laue interference function:

$$I(Q) \propto \sin^2(0.5*N*Q_c) / (\sin^2(0.5*Q_c) \qquad \text{Eq. 4.3.}$$

where c is the relevant lattice parameter, Q is the scattering vector, and N is the integral number of coherently diffracting unit cells.[23,33] Because Laue oscillations originate from the incomplete destructive interference of a finite number of diffracting unit cells between Bragg reflections, their presence suggests a low defect density.

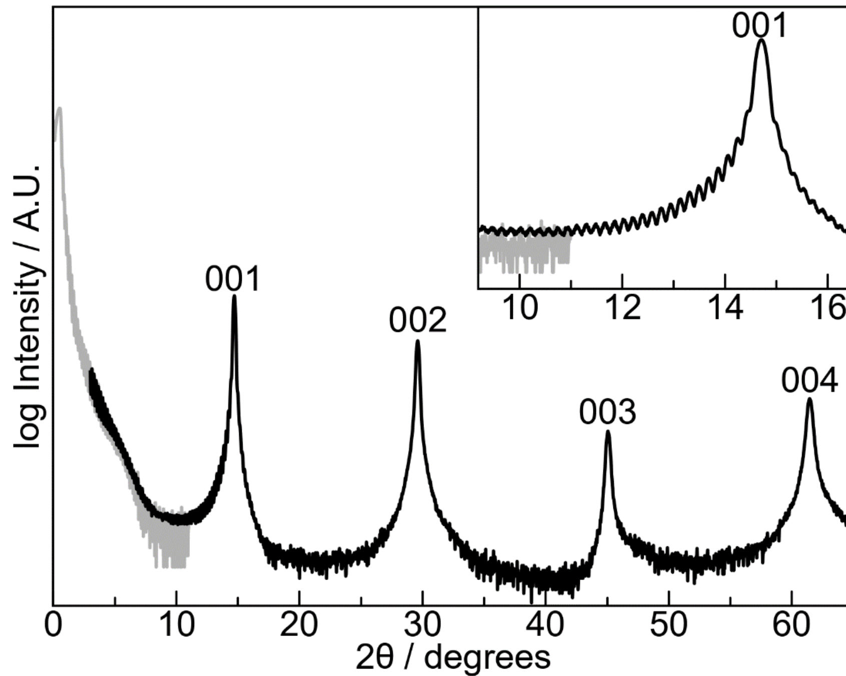

Figure 4.4. Experimental XRR (gray) and XRD (black) patterns of a 79-layer crystalline $TiSe_2$ film. The four Bragg reflections can be indexed as 00l reflections yielding a c-axis lattice parameter of 6.036(1) Å. The inset highlights the Laue oscillations observed on the 001 reflection.

Kiessig fringes and Laue oscillations provide complementary structural information about the sample. The period of the Kiessig fringes determines the total film thickness (t_{sample}), inclusive of any impurity layers or amorphous material, while the period of the Laue oscillations determines the number of coherently diffracting unit cells in the film (N), which can be multiplied by the c-

axis lattice parameter (*c*) to obtain the thickness of the coherently diffracting crystal.

Structural defects typically prevent experimental diffraction data from exactly matching that expected for a perfect film. For example, the total amount of material in a film is difficult to control so the total film thickness is typically not equal to the thickness of the coherently diffracting crystal. Thus, the angular positions of the Kiessig fringes will differ from those calculated from the thickness of the coherently diffraction domain obtained from the Laue oscillations. The experimental amplitude of Laue oscillations is also typically much smaller than calculated, often asymmetric with respect to the Bragg reflection, and the rate of decay of the oscillations as one moves away from the main Bragg reflection varies significantly from sample to sample. These differences in amplitude are not often discussed when Laue oscillations are observed.

The Laue interference function predicts a symmetric distribution of satellite reflections centered on each Bragg maximum, as shown in Figure 4.5a (blue trace), but experimentally the intensity of the Laue oscillations is often different on either side of the Bragg reflection. Asymmetry of intensities was present in slightly more than half of the 27 representative reports we examined in a non-exhaustive literature search. This asymmetry occurs whether the Bragg reflection is dominated by the substrate, as in epitaxially grown films, or if the Bragg reflection is caused only by the film itself. The TiSe*2* film in Figure 4.5a (black trace) illustrates a typical intensity asymmetry around a Bragg reflection. The cause of the asymmetry in the intensity in this sample is the changing phase relationship between Kiessig fringes and Laue oscillations as the diffraction angle moves through that of a Bragg reflection. Figure 5b illustrates the effect of this changing phase relationship in a simulated diffraction pattern of a structurally perfect 301.8 nm thick film containing fifty 6.036 Å thick $TiSe_2$ layers. Here we use the approach of Zwiebler et. al., approximating the unit cell structure with slabs of the appropriate element in the simulation.[34] For the $TiSe_2$ layers, equal

thickness slabs of Se, Ti, and Se were used totaling the thickness of the c-axis of the unit cell. Before the 001 reflection, the Kiessig and Laue effects are constructively interfering. Between the 001 and 002 reflections, the two are destructively interfering, resulting in the much lower average intensity between these reflections. The average intensity between the 2nd and 3rd reflections increases because the Kiessig and Laue effects are again constructively interfering. The bottom XRR pattern (black trace) in Figure 4.5 shows an expanded view of the oscillations around the 001 reflection, which are asymmetric. Asymmetry caused by interference of the Kiessig and Laue effects is most likely to be observed for Bragg reflections at smaller 2θ values due to the decay of Kiessig fringe intensities as 2θ increases.

Experimentally observing the shift in phase between the Kiessig and Laue interference effects through Bragg reflections requires a film with extremely smooth interfaces, which is challenging to prepare experimentally. Figure 4.6. shows an experimental diffraction pattern where the changing sign relation between the two interference effects is clearly visible. This pattern also shows how the changing relative intensity of the Kiessig and Laue effects can cause a very weak Bragg reflection, resulting from the location of atoms in the unit cell, to appear split as the relative phase changes moving through the center of the 001 reflection.

The intensities of both Kiessig and Laue oscillations also depend on the abruptness and smoothness of the interfaces in the film. The relative magnitude of intensities of Kiessig oscillations depends on the smoothness of interfaces and the magnitude of the electron density differences between the constituents. The intensity of Laue oscillations depends on the percentage of the film that contains the dominant thickness of coherently diffracting crystalline domains, the distribution of thickness of the crystalline domains (a form of roughness, as the entire area measured might contain several thicknesses), and the inherent intensity of the Bragg reflections, which depend on the location of atoms within the unit cell. Figure 4.7. shows the effects of increasing the substrate and sample

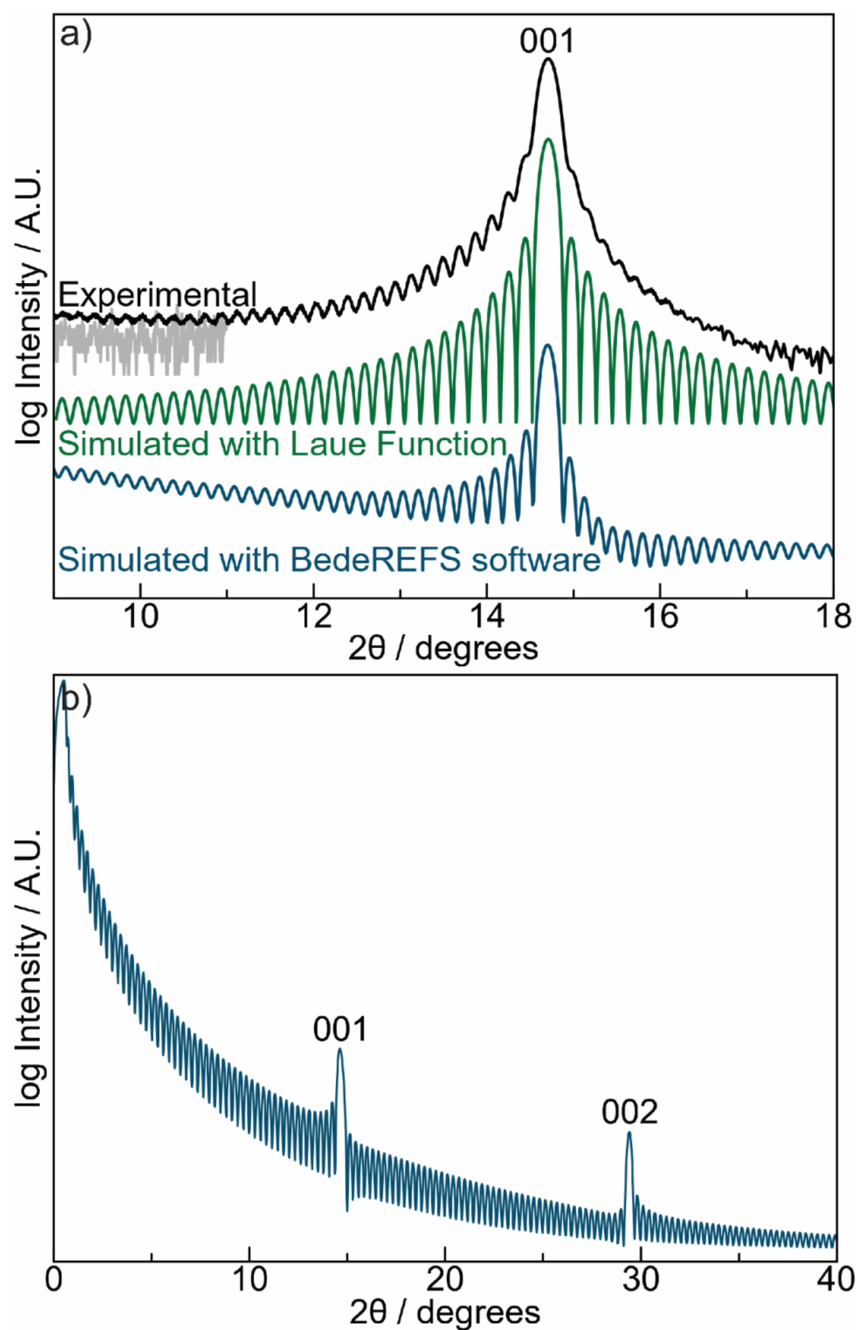

Figure 4.5. (a) Comparison of the experimental Laue oscillations observed on either side of the 001 reflection of a $TiSe_2$ film with that calculated from the Laue interference function and a simulation that includes reflectivity using the BedeREFS simulation software. (b) A simulated XRR/XRD pattern of a 50-layer Se|Ti|Se film with a *c*-axis lattice parameter of 6.036 Å. The changing phase relationship between Kiessig fringes and Laue oscillations as the scattering angle moves through that of Bragg reflections is apparent in the lower average intensity between the 1st and 2nd Bragg reflections.

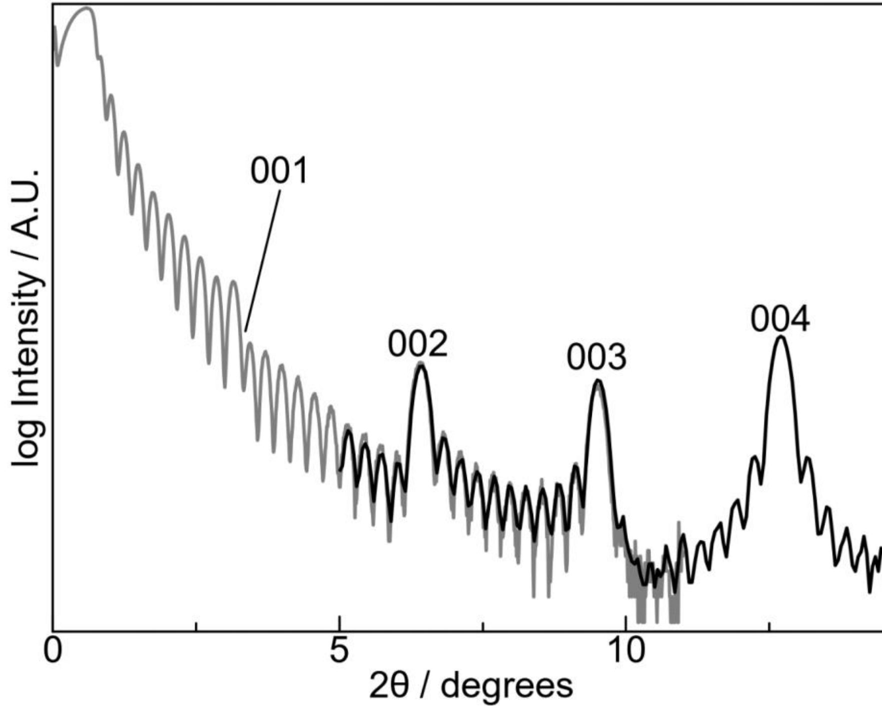

Figure 4.6. Experimental diffraction data of a $(BiSe)_{0.97}(Bi_2Se_3)_{1.26}(BiSe)_{0.97}(MoSe_2)$ heterostructure.

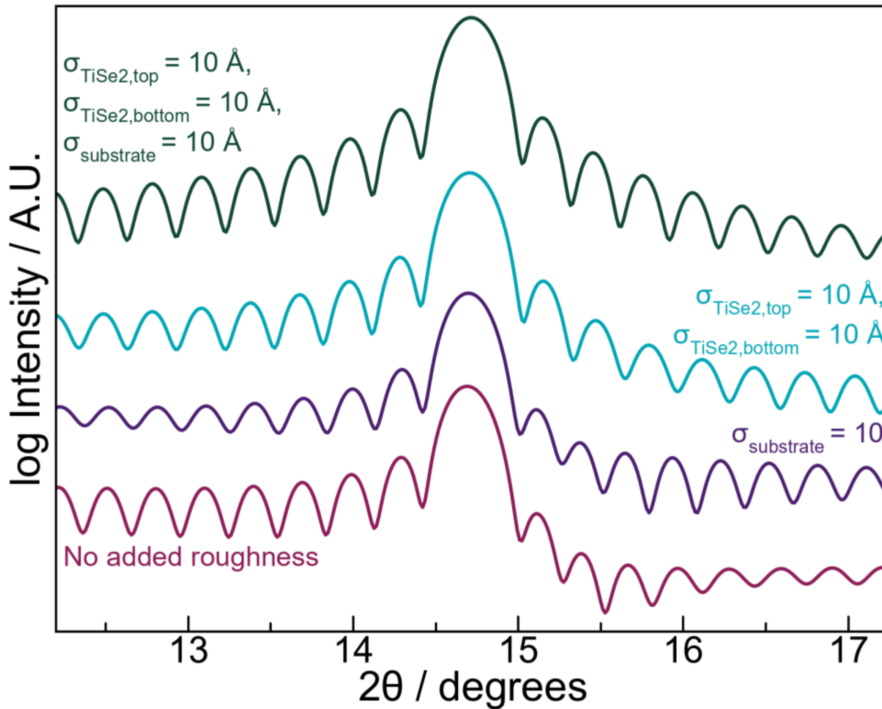

Figure 4.7. Simulated XRR patterns of a 50-layers $TiSe_2$ film on a Si substrate illustrating how the roughness affects the symmetry of the satellite reflections around the Bragg reflections. Increasing roughness of the substrate and/or surface damps the intensity of the Kiessig fringes, making the Laue oscillations more symmetric.

interfacial roughness on the appearance of the interference pattern around the 001 reflection in simulated diffraction patterns of $TiSe_2$. The simulations approximate roughness by replacing an abrupt change in electron density at interfaces with a smooth gradient of width σ. Kiessig interference fringes are damped out as the magnitude of the roughness at the interfaces increases. Increasing roughness can damp out the Kiessig fringes enough that a symmetrical distribution of satellite reflections occurs around the Bragg maxima at higher angles. This infers that samples with an asymmetric distribution of the intensity of Laue oscillations have smooth interfaces.

The experimentally observed decrease in the intensities of Laue oscillations as one moves further away from the central Bragg maxima is typically much faster than predicted by the Laue oscillation function. While some of this intensity decrease is caused by substrate and/or surface roughness of “extra” material, a distribution in the thickness of the coherently diffracting domain also contributes to this accelerated decrease in intensity. Figure 4.8. contains several simulations, where the percentage of coherent domains of different thicknesses was varied. If there are only two different thicknesses present, the interference pattern between the two different Laue oscillation functions is evident and the fringes closest to the Bragg maxima yield the average value of the coherent diffracting domain thicknesses. The fringes close to the Bragg maxima also yield the average value for the thickness for broader distributions, but the intensity of the oscillations decreases as one moves away from the Bragg maxima. These simulations suggest that the further the angular distance that Laue oscillations are observed from the Bragg maxima, the narrower the size distribution of coherently diffracting domains.

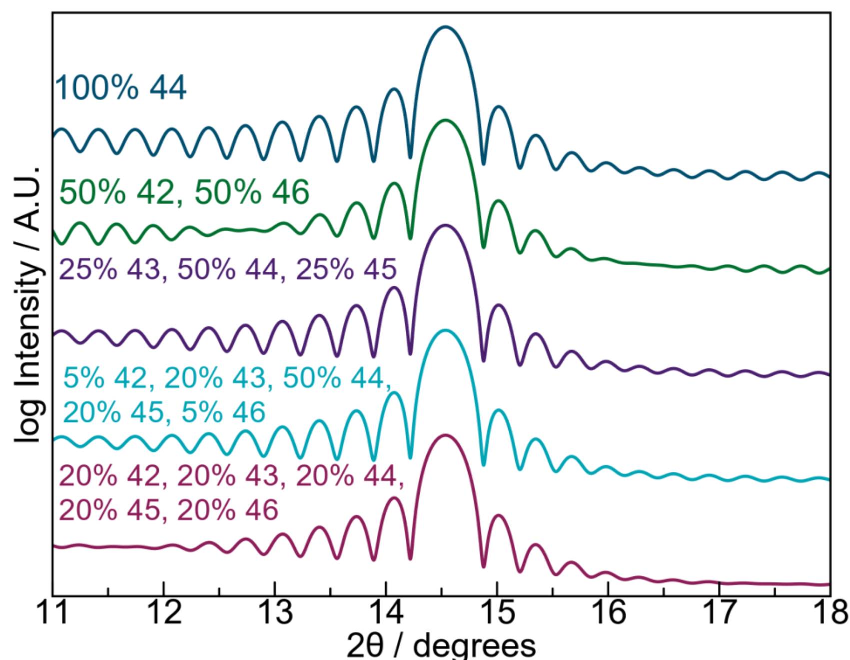

Figure 4.8. Simulations of diffraction patterns from different distributions of coherently diffracting domains. The top simulation is from a sample with 44 $TiSe_2$ layers. The simulations below this are from different percentages of film area with the indicated number of $TiSe_2$ layers in the coherently diffracting domain.

4.5 Developing Structural Models From Kiessig Fringes and Laue Oscillations

We conclude with two examples demonstrating how to systematically construct structural models using extracted structural information from X-ray reflectivity and X-ray diffraction data on samples with both Kiessig fringes and Laue oscillations. The first example is an Fe-doped VSe_2 film whose XRR and XRD scans are shown in Figure 4.9. The total thickness of the film can be extracted from the Kiessig oscillations using Eq. 4.1, yielding a film thickness of 271.0(2) Å. The Laue oscillations are used to determine the number of unit cells in the coherently diffracting domain from their positions. The Laue oscillations are consistent with 44 unit cells in the diffracting domain. The positions of the 00l Bragg reflections are used to determine the c-axis lattice parameter of 6.088(3) Å. The product of the number of unit cells (44) and the c-axis lattice parameter (6.088(3) Å) yields the thickness of the coherently diffracting domain – 267.9(1) Å. The Kiessig derived thickness is 3.1 Å larger, indicating that there is a thin layer of excess material. Independent corroborating evidence for a small

amount of excess material was obtained from the absolute number of atoms / Å^2 of each element determined from x-ray fluorescence (XRF) data, which indicated that the excess material is vanadium oxide.[35]

A structural model of the film to simulate the diffraction data below 20° 2θ was created from the data derived from the Kiessig and Laue oscillations. A model with a 267.9(1) Å thick $Fe_xV_{1-x}Se_2$ layer and top 3.1 Å thick surface layer of vanadium oxide was used to determine the top and bottom roughness of the film. Figure 4.9 shows the simulated pattern with interfacial roughness of σ_{VSe2} = 5.75 Å, σ_{oxide} = 5 Å, and $\sigma_{substrate}$ = 2.5 Å, which reasonably matches the low angle experimental reflectivity pattern. Dividing the 267.9(1) Å thick $Fe_xV_{1-x}Se_2$ layer into 44 explicit unit cells of $Fe_xV_{1-x}Se_2$ by using elemental slabs as discussed earlier provides a good fit to the experimentally observed positions of the Laue oscillations around the 001 reflection (see Figure 4.9). The intensities of the Laue oscillations, however, are too large, as the actual sample probably does not contain exactly 44 unit cells across the entire area probed by the X-ray beam, and we need to add the effect of substrate roughness. Including the substrate roughness determined from the $Fe_xV_{1-x}Se_2$ slab model does a reasonable job of matching the experimental pattern except that the Laue intensities are still too intense. The intensities of the Laue oscillations can be reduced by assuming that the film consists of regions that contain thinner coherently scattering domains, as discussed above. However, this will not yield a unique structural model for the film.

Diffraction patterns and their analysis become increasingly complicated as the Kiessig and Laue intensities interact across a large angular range. The XRR/XRD patterns collected of a $(BiSe)_{0.97}(Bi_2Se_3)_{1.26}(BiSe)_{0.97}(MoSe_2)$ heterostructure, displayed in Figure 4.10, illustrates these challenges.[36] The extracted total film thickness from the Kiessig fringes is 309.6(5) Å. From the period of the Laue oscillations at higher angles, it was determined that there are 10 unit cells in the coherently diffracting domains. The product of 10 unit cells times the c-axis lattice parameter (27.97 (10) Å) gives a crystal thickness of

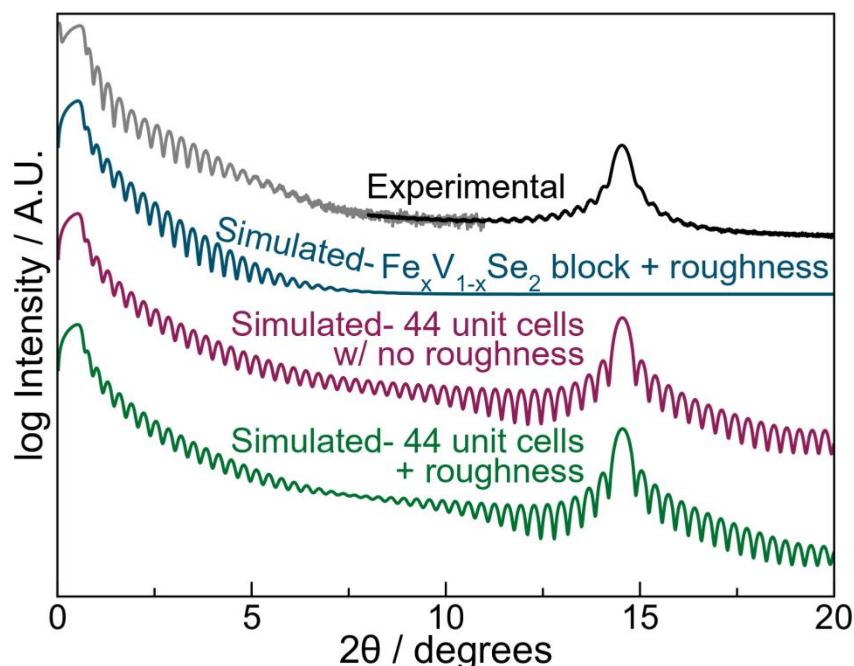

Figure 4.9. Experimental XRR (gray) and XRD (black) patterns of a 271.0(2) Å thick crystalline $Fe_xV_{1-x}Se_2$ film and simulated XRR pattern (teal) for a 267.9 Å thick $Fe_xV_{1-x}Se_2$ film consisting of 44 unit cells. The difference in Kiessig fringe period causes a poor fit of the simulated film above ~3 °2*θ*. Including the excess material not incorporated into the coherent diffraction domain results in a simulated pattern that provides a reasonable fit over the entire range of the scan.

279.7 Å. The difference between these two values is 29.9 Å. The question is how does one divide this thickness between the top and bottom of the crystalline domains? Figure 4.10 contains several simulated XRR patterns from models that distribute the 30 Å of excess material between the top and/or the bottom of the $(BiSe)_{0.97}(Bi_2Se_3)_{1.26}(BiSe)_{0.97}(MoSe_2)$ diffracting domain (Se was used as the excess material in these models). The simulated patterns are very sensitive to the exact distribution of the excess material between the front and back of the film. While we assumed in these simulations that the composition of excess material at the bottom and the top were the same, this is not necessarily true, which adds another unknown parameter to potential models. This experimental pattern does not contain an explicit feature that allows us to estimate or separate the roughness of the substrate, the film, or the excess material. The large number of potential variables makes it currently impossible to extract additional information through simulations. Additional information, for example from

HAADF-STEM images of film cross sections, is needed to limit the parameter space.

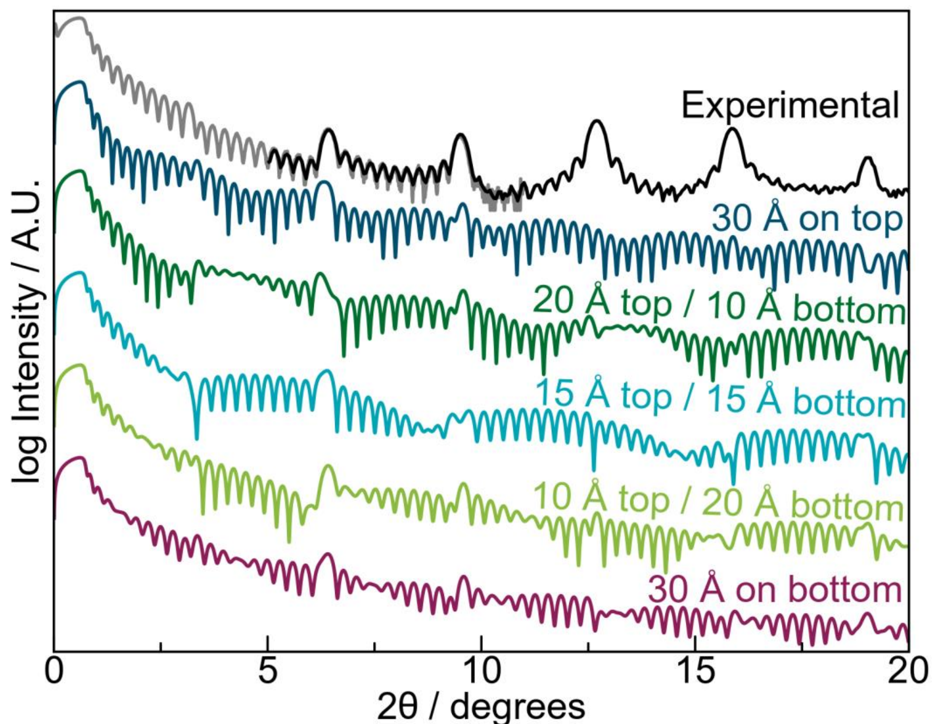

Figure 4.10: Experimental XRR (grey) and XRD (black) patterns of a $(BiSe)_{0.97}(Bi_2Se_3)_{1.26}(BiSe)_{0.97}(MoSe_2)$ heterostructure annealed at 350 °C, along with simulated patterns for models that consist of 10 unit cells of the targeted heterostructure, plus 30 Å of additional material distributed between either the top and/or the bottom of the heterostructure. No interfacial roughness was added to these models.

4.6 Conclusion

This manuscript shows how to extract quantitative structural information from Laue oscillations and Kiessig fringes. The thickness of the coherently diffracting domain can be calculated from the product of the c-axis lattice parameter and the number of unit cells present determined from the Laue oscillations. If there is extra material in the film, there will be a difference between total film thickness from the period of the Kiessig fringes and the thickness of the coherently diffracting crystal domain. When the Kiessig fringes damp out before Laue oscillations are observed, it is possible to extract the roughness of the substrate and of the deposited layers. Samples with large differences between the total film thickness and crystal thickness are challenging

to analyze, because the simulated patterns vary considerably as the extra thickness is partitioned above or below the coherently diffracting domain. Also challenging are samples with large angular regions where both the Laue and Kiessig interference effects contribute significantly. In films where Laue oscillations occur around reflections at high angles, however, the approach presented provides valuable additional information. Additional simulation tools need to be developed to get access to the additional structural information present in Laue oscillations obtained from experimental data.

4.7 Experimental

Films for this study were prepared using a custom high vacuum physical vapor deposition (PVD) chamber. Artificially layered precursors for binary thin films were prepared by repeatedly depositing M|Se bilayers, where ideally the number of atoms / Å^2 deposited in each bilayer is identical to the number required to form one unit cell of the targeted compound. Similarly, precursors for heterostructures were prepared by repeatedly depositing M|Se|M'|Se layers in the same manner. Metal layers were deposited using electron-beam guns, while Se was deposited with a Knudsen effusion cell. All precursors were deposited onto ⟨100⟩ Si substrates with a native SiO_2 layer. A pressure of less than 1 × 10−7 Torr was maintained during the deposition. In-house deposition software was used to control and monitor the amount of material deposited in each layer using pneumatic-controlled shutters and quartz crystal microbalances. After deposition, the precursors were removed from the vacuum chamber, briefly exposed to atmosphere, and brought into a dry-box (N_2 with <0.2 ppm O_2) where they were heated for 30 minutes at 500 °C and 350 °C for the Fe-doped VSe_2 and the $(BiSe)_{0.97}(Bi_2Se_3)_{1.26}(BiSe)_{0.97}(MoSe_2)$ films, respectively.

Structural characterization was carried out via x-ray reflectivity (XRR) and x-ray diffraction (XRD), while composition was determined using x-ray fluorescence (XRF). XRR and specular XRD patterns were collected on a Bruker D-8 Discover diffractometer. All diffraction measurements utilized a Cu Kα

radiation source. Special care must be taken when aligning each sample to the diffractometer, as the positions and intensities of reflectivity/diffraction features are extremely sensitive to sample alignment. To confirm the alignment of the sample in the goniometer, rocking curve scans were collected at two different small 2θ values. The maxima in both rocking curve scans occurring when the incident and exit angles are equal are evidence that the sample is correctly aligned in the center of the goniometer.

The absolute amount of each element deposited was determined using XRF data collected on a Rigaku ZSX Primus II with a rhodium source. Previously published calibration curves were used to relate the background-corrected integrated raw intensity to the atoms / $Å^2$ for each element.[35] Table 4.1. contains the calculated amount of each element required for the crystalline domains that contribute to the observed Laue oscillations along with the total number of atoms per unit area (areal density) of each element, as determined from the XRF measurements of each film.

Table 4.1. Experimental and target atomic areal density for the Fe-doped VSe_2 and $(BiSe)_{0.97}(Bi_2Se_3)_{1.26}(BiSe)_{0.97}(MoSe_2)$ films as determined from XRF measurements

Exp. V Atoms/Å²	Exp. Fe Atoms/Å²	Exp. Se Atoms/Å²	Target V Atoms/Å²	Target Fe Atoms/Å²	Target Se Atoms/Å²	Target # of Unit Cells
3.43(7)	1.4(1)	10.2(3)	3.43	1.71	10.29	44

Exp. Bi Atoms/Å²	Exp. Mo Atoms/Å²	Exp. Se Atoms/Å²	Target Bi Atoms/Å²	Target Mo Atoms/Å²	Target Se Atoms/Å²	Target # of Unit Cells
3.88(8)	1.15(2)	6.5(3)	3.37	1.18	6.8	10

Simulated XRR/XRD patterns were created using the BedeREFS software, which incorporates both reflectivity and diffraction physics that are required to accurately simulate thin film X-ray patterns.[29] BedeREFS uses “slabs” of electron density that are appropriately scaled to match the thickness and electron density of each layer in the film’s structure. Unless otherwise specified, the “slab” models

created to simulate the reflectivity patterns, shown in Figures 1, 2, 3, 5, 7, 8, 9, and 10, had no added interfacial roughness, and were generated using a Si substrate with 10-20 Å of SiO_2.

4.8 Bridge

This chapter described a method for extracting the maximum possible quantity of structural information from x-ray diffraction patterns that contain Laue oscillations, describing best practices to follow in order to avoid potentially misleading conclusions about the sample. The next chapter describes the work I did to repair and update an automated system used to measure thin film sample's electrical resistivity and Hall effect.

REFERENCES CITED

(1) Woodbridge, R. W. *The Optical Principles of The Diffraction of X-Rays*; Ox Bow Press: CT, 1982.

(2) Miyadera, T.; Auchi, Y.; Yamamoto, K.; Ohashi, N.; Koganezawa, T.; Yaguchi, H.; Yoshida, Y.; Chikamatsu, M. Insights into Microscopic Crystal Growth Dynamics of CH3NH3PbI3under a Laser Deposition Process Revealed by in Situ X-Ray Diffraction. *ACS Applied Materials and Interfaces* **2021**, *13* (19), 22559–22566. https://doi.org/10.1021/acsami.1c04488.

(3) Forst, M.; Caviglia, A. D.; Scherwitzl, R.; Mankowsky, R.; Zubko, P.; Khanna, V.; Bromberger, H.; Wilkins, S. B.; Chuang, Y. D.; Lee, W. S.; Schlotter, W. F.; Turner, J. J.; Dakovski, G. L.; Minitti, M. P.; Robinson, J.; Clark, S. R.; Jaksch, D.; Triscone, J. M.; Hill, J. P.; Dhesi, S. S.; Cavalleri, A. Spatially Resolved Ultrafast Magnetic Dynamics Initiated at a Complex Oxide Heterointerface. *Nature Materials* **2015**, *14* (9), 883–888. https://doi.org/10.1038/nmat4341.

(4) Du, C.; Wang, H.; Yang, F.; Hammel, P. C. Systematic Variation of Spin-Orbit Coupling with d -Orbital Filling: Large Inverse Spin Hall Effect in 3d Transition Metals. *Physical Review B - Condensed Matter and Materials Physics* **2014**, *90* (14), 1–5. https://doi.org/10.1103/PhysRevB.90.140407.

(5) Tsuchiya, Y.; Norota, K.; Watabe, Y.; Kuroda, T.; Iwata, N.; Hashimoto, T.; Yamamoto, H. Growth Difference of LaFeO3 Thin Films by Pulsed Laser Deposition Method Using the Targets Prepared by Pechini and Conventional Solid Solution Methods. *Transactions of the Materials Research Society of Japan* **2012**, *37* (3), 369–372. https://doi.org/10.14723/tmrsj.37.369.

(6) Iwata, N.; Watabe, Y.; Tsuchiya, Y.; Norota, K.; Hashimoto, T.; Huijben, M.; Rijnders, G.; Blank, D. Growth and Evaluation of [AFeOx/REFeO3] (A=Ca, Sr, RE=La, Bi) Superlattices by Pulsed Laser Deposition Method Using High Density Targets Prepared by Pechini Method. *Materials Research Society Symposium Proceedings* **2012**, *1477*, 61–66. https://doi.org/10.1557/opl.2012.

(7) Grelet, E.; Dardel, S.; Bock, H.; Goldmann, M.; Lacaze, E.; Nallet, F. Morphology of Open Films of Discotic Hexagonal Columnar Liquid Crystals as Probed by Grazing Incidence X-Ray Diffraction. *European Physical Journal E* **2010**, *31* (4), 343–349. https://doi.org/10.1140/epje/i2010-10586-2.

(8) Krauss, T. N.; Barrena, E.; Zhang, X. N.; de Oteyza, D. G.; Major, J.; Dehm, V.; Würthner, F.; Cavalcanti, L. P.; Dosch, H. Three-Dimensional Molecular Packing of Thin Organic Films of PTCDI-C 8 Determined by Surface X-Ray Diffraction. *Langmuir* **2008**, *24* (22), 12742–12744. https://doi.org/10.1021/la8030182.

(9) Abe, Y.; Kawamura, M.; Sasaki, K. Highly Textured (100) RuO2/(001) Ru Multilayers Prepared by Sputtering. *Japanese Journal of Applied Physics, Part 1: Regular Papers and Short Notes and Review Papers* **2002**, *41* (11 B), 6857–6861. https://doi.org/10.1143/JJAP.41.6857.

(10) Naito, M.; Karimoto, S.; Yamamoto, H.; Nakada, H.; Suzuki, K. Production of Double-Sided Large-Area High-Tc Wafers by Molecular Beam Epitaxy. *IEEE Transactions on Applied Superconductivity* **2001**, *11* (1 III), 3848–3851. https://doi.org/10.1109/77.919904.

(11) Brangham, J. T.; Meng, K. Y.; Yang, A. S.; Gallagher, J. C.; Esser, B. D.; White, S. P.; Yu, S.; McComb, D. W.; Hammel, P. C.; Yang, F. Thickness Dependence of Spin Hall Angle of Au Grown on Y3 F E5 O12 Epitaxial Films. *Physical Review B* **2016**, *94* (5), 6–11. https://doi.org/10.1103/PhysRevB.94.054418.

(12) Shu, X.; Zhou, J.; Liu, L.; Lin, W.; Zhou, C.; Chen, S.; Xie, Q.; Ren, L.; Xiaojiang, Y.; Yang, H.; Chen, J. Role of Interfacial Orbital Hybridization in Spin-Orbit-Torque Generation in Pt -Based Heterostructures. *Physical Review Applied* **2020**, *14* (5), 1. https://doi.org/10.1103/PhysRevApplied.14.054056.

(13) Xu, J.; Katoch, J.; Ahmed, A. S.; Pinchuk, I. v.; Young, J. R.; Johnston-Halperin, E.; Pelz, J.; Kawakami, R. K. Growth of Uniform CaGe2 Films by Alternating Layer Molecular Beam Epitaxy. *Journal of Crystal Growth* **2017**, *460* (December 2016), 134–138. https://doi.org/10.1016/j.jcrysgro.2016.12.102.

(14) Song, Y.; Li, Z.; Li, H.; Tang, S.; Mu, G.; Xu, L.; Peng, W.; Shen, D.; Chen, Y.; Xie, X.; Jiang, M. Epitaxial Growth and Characterization of High Quality Bi2O2Se Thin Films on SrTiO3 Substrates by Pulsed Laser Deposition. *Nanotechnology* **2020**, *31* (16). https://doi.org/10.1088/1361-6528/ab6686.

(15) Switzer, J. A.; Hill, J. C.; Mahenderkar, N. K.; Liu, Y. C. Nanometer-Thick Gold on Silicon as a Proxy for Single-Crystal Gold for the Electrodeposition of Epitaxial Cuprous Oxide Thin Films. *ACS Applied Materials and Interfaces* **2016**, *8* (24), 15828–15837. https://doi.org/10.1021/acsami.6b04552.

(16) Watabe, Y.; Iwata, N.; Oikawa, T.; Hashimoto, T.; Huijben, M.; Rijnders, G.; Yamamoto, H. Fabrication and Crystal Structure of [ABO3/REMO3] (A = Ca, La, B = Fe, Mn, RE = Bi, La, M = Fe, Fe0.8Mn0.2) Superlattices Grown by Pulsed Laser Deposition Method. *Japanese Journal of Applied Physics* **2014**, *53* (5 SPEC. ISSUE 1). https://doi.org/10.7567/JJAP.53.05FB12.

(17) Onbasli, M. C.; Kehlberger, A.; Kim, D. H.; Jakob, G.; Kläui, M.; Chumak, A. v.; Hillebrands, B.; Ross, C. A. Pulsed Laser Deposition of Epitaxial Yttrium Iron Garnet Films with Low Gilbert Damping and Bulk-like Magnetization. *APL Materials* **2014**, *2* (10). https://doi.org/10.1063/1.4896936.

(18) Peters, B.; Alfonsov, A.; Blum, C. G. F.; Hageman, S. J.; Woodward, P. M.; Wurmehl, S.; Büchner, B.; Yang, F. Y. Epitaxial Films of Heusler Compound Co2FeAl0.5Si 0.5 with High Crystalline Quality Grown by off-Axis Sputtering. *Applied Physics Letters* **2013**, *103* (16), 0–5. https://doi.org/10.1063/1.4825338.

(19) Hauser, A. J.; Soliz, J. R.; Dixit, M.; Williams, R. E. A.; Susner, M. A.; Peters, B.; Mier, L. M.; Gustafson, T. L.; Sumption, M. D.; Fraser, H. L.; Woodward, P. M.; Yang, F. Y. Fully Ordered Sr2CrReO 6 Epitaxial Films: A High-Temperature

Ferrimagnetic Semiconductor. *Physical Review B - Condensed Matter and Materials Physics* **2012**, *85* (16), 4–7. https://doi.org/10.1103/PhysRevB.85.161201.

(20) Switzer, J. A.; Gudavarthy, R. v.; Kulp, E. A.; Mu, G.; He, Z.; Wessel, A. J. Resistance Switching in Electrodeposited Magnetite Superlattices. *J Am Chem Soc* **2010**, *132* (4), 1258–1260. https://doi.org/10.1021/ja909295y.

(21) Asanuma, S.; Fukunaga, M.; Uesu, Y.; Haumont, R.; Dkhil, B.; Malibert, C.; Kiat, J. M. Fabrications of Pb(Sc1/2Nb1/2)O 3/XPbTiO3 Thin Films and Their Structural Characterizations. *Japanese Journal of Applied Physics, Part 1: Regular Papers and Short Notes and Review Papers* **2004**, *43* (9 B), 6581–6584. https://doi.org/10.1143/JJAP.43.6581.

(22) Dürr, A. C.; Schreiber, F.; Münch, M.; Karl, N.; Krause, B.; Kruppa, V.; Dosch, H. High Structural Order in Thin Films of the Organic Semiconductor Diindenoperylene. *Applied Physics Letters* **2002**, *81* (12), 2276–2278. https://doi.org/10.1063/1.1508436.

(23) Ern, C.; Donner, W.; Dosch, H.; Adams, B.; Nowikow, D. Temperature-Dependent Interfacial Stiffness of the Disorder Layer in a Thin Cu3Au Alloy Film. *Physical Review Letters* **2000**, *85* (9), 1926–1929. https://doi.org/10.1103/PhysRevLett.85.1926.

(24) Mahenderkar, N. K.; Chen, Q.; Liu, Y.; Duchild, A. R.; Hofheins, S.; Chason, E.; Switzer, J. A. Epitaxial Lift-off of Electrodeposited Single-Crystal Gold Foils for Flexible Electronics. *Science (1979)* **2017**, *355*, 1203–1206.

(25) Lu, W.; Yang, P.; Song, W. D.; Chow, G. M.; Chen, J. S. Control of Oxygen Octahedral Rotations and Physical Properties in SrRuO3 Films. *Physical Review B - Condensed Matter and Materials Physics* **2013**, *88* (21), 1–11. https://doi.org/10.1103/PhysRevB.88.214115.

(26) Xu, S. J.; Shi, Z.; Zhou, S. M. Clear Evidence of Interfacial Anomalous Hall Effect in Epitaxial L10 FePt and FePd Films. *Physical Review B* **2018**, *98* (2), 1–5. https://doi.org/10.1103/PhysRevB.98.024413.

(27) Sojková, M.; Dobročka, E.; Hutár, P.; Tašková, V.; Pribusová Slušná, L.; Stoklas, R.; Píš, I.; Bondino, F.; Munnik, F.; Hulman, M. High Carrier Mobility Epitaxially Aligned PtSe2 Films Grown by One-Zone Selenization. *Applied Surface Science* **2021**, *538* (May 2020), 147936. https://doi.org/10.1016/j.apsusc.2020.147936.

(28) Lee, A. J.; Brangham, J. T.; Cheng, Y.; White, S. P.; Ruane, W. T.; Esser, B. D.; McComb, D. W.; Hammel, P. C.; Yang, F. Metallic Ferromagnetic Films with Magnetic Damping under 1.4 × 10-3. *Nature Communications* **2017**, *8* (1), 1–6. https://doi.org/10.1038/s41467-017-00332-x.

(29) Wormington, M.; Panaccione, C.; Matney, K. M.; Bowen, D. K. Characterization of Structures from X-Ray Scattering Data Using Genetic Algorithms.

Philosophical Transactions of the Royal Society A: Mathematical, Physical and Engineering Sciences **1999**, *357* (1761), 2827–2848.

(30) Kiessig, von H. Interferenz von Röntgenstrahlen an Dünnen Schichten. *Ann Phys* **1931**, *402* (7), 769–788. https://doi.org/10.1002/andp.19314020702.

(31) Huang, T. C.; Gilles, R.; Will, G. Thin-Film Thickness and Density Determination from x-Ray Reflectivity Data Using a Conventional Power Diffractometer. *Thin Solid Films* **1993**, *230* (2), 99–101. https://doi.org/10.1016/0040-6090(93)90499-F.

(32) Wainfan, N.; Parratt, L. G. X-Ray Reflection Studies of the Anneal and Oxidation of Some Thin Solid Films. *Journal of Applied Physics* **1960**, *31* (8), 1331–1337. https://doi.org/10.1063/1.1735837.

(33) Schierle, E. Antiferromagnetism in Thin Films Studied by Resonant Magnetic Soft X-Ray Scattering. PhD Thesis, Freie Univ. Berlin, 2006.

(34) Zwiebler, M.; Hamann-Borrero, J. E.; Vafaee, M.; Komissinskiy, P.; Macke, S.; Sutarto, R.; He, F.; Büchner, B.; Sawatzky, G. A.; Alff, L.; Geck, J. Electronic Depth Profiles with Atomic Layer Resolution from Resonant Soft X-Ray Reflectivity. *New Journal of Physics* **2015**, *17* (8). https://doi.org/10.1088/1367-2630/17/8/083046.

(35) Hamann, D. M.; Bardgett, D.; Cordova, D. L. M.; Maynard, L. A.; Hadland, E. C.; Lygo, A. C.; Wood, S. R.; Esters, M.; Johnson, D. C. Sub-Monolayer Accuracy in Determining the Number of Atoms per Unit Area in Ultrathin Films Using X-Ray Fluorescence. *Chemistry of Materials* **2018**, *30*, 6209–6216. https://doi.org/10.1021/acs.chemmater.8b02591.

(36) Choffel, M. A.; Gannon, R. N.; Göhler, F.; Miller, A. M.; Medlin, D. L.; Seyller, T.; Johnson, D. C. Synthesis and Electrical Properties of a New Compound (BiSe)0.97(Bi2Se3)1.26(BiSe)0.97(MoSe2) Containing Metallic 1T-MoSe2. *Chemistry of Materials* **2021**, *33* (16), 6403–6411. https://doi.org/10.1021/acs.chemmater.1c01623.

CHAPTER V

AUTOMATED TEMPERATURE-DEPENDENT ELECTRICAL RESISTIVITY AND HALL EFFECT MEASUREMENT SYSTEM

5.0 Authorship Statement

This chapter was written for this work alone with no intention of publishing it elsewhere. I am the primary author and wrote the following with editorial assistance from my advisor, David C. Johnson.

5.1 van der Pauw Method

The van der Pauw method is commonly used to measure the electrical resistivity and Hall effect of thin film samples.[1–3] Using four electrodes placed around the edges of an arbitrarily shaped sample and making multiple current-potential measurements, the average resistivity can be determined via the van der Pauw equation. However, the van der Pauw method makes several assumptions that must be satisfied for the van der Pauw equation to hold: the sample must be homogenous (i.e. uniform in thickness and no isolated holes/changes in density as a function of position in sample), all four contacts must be ohmic, all contacts must be placed at the edge of the sample, and the area of each contact must be at least an order of magnitude smaller than the sample area.[4]

The van der Pauw method for measuring resistivity consists of making sequential measurements passing current and measuring potential along the vertical and horizontal edges of the sample. Figure 5.1 depicts a thin film sample attached to the measurement system in the custom-built sample holder. The sample was deposited through an X-shaped Hall cross shadow mask. As shown, the electrical contacts made from elemental In are attached to each corner of the cross. The contacts are labeled 1 – 4, beginning in the upper left and moving counter-clockwise. Measurements made along the vertical edge are obtained by passing current between contacts 1 & 2 while measuring the potential between contacts 3 & 4 ($I_{12}V_{34}$), or vice versa. Measurements along the horizontal edge

are obtained by passing current between contacts 1 & 4 while measuring the potential between contacts 2 & 3 ($I_{14}V_{23}$), or vice versa. Using Ohm's Law (V = IR), the electrical resistance along the horizontal and vertical edges can be calculated.

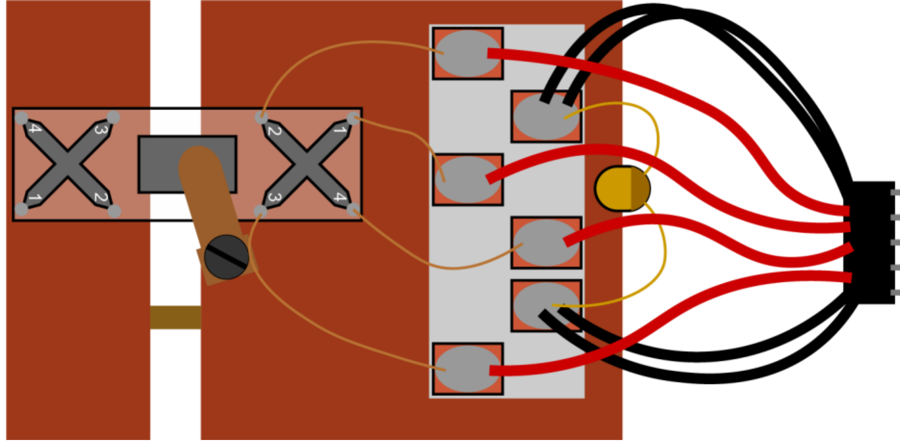

Figure 5.1. Top-down schematic of thin film sample holder with soldered In contacts in each of the four corners of the sample's top Hall Cross.

As shown in Eq. 5.1, the van der Pauw equation relates the measured horizontal and vertical resistances (R_H and R_V, respectively) to the sheet resistance, R_S. The average resistivity, ρ, is obtained by multiplying the sheet resistivity by the sample's thickness.

$$1 = e^{-\pi R_V / R_s} + e^{-\pi R_H / R_s} \qquad \text{Eq. 5.1}$$

While the average resistivity of a sample can technically be obtained in as few as two measurements, to increase accuracy and reduce measurement error generally eight total electrode permutations are used, from which the results are averaged after correcting for the sign convention. The first two permutations can be thought of as resulting from swapping the direction that the current flows (i.e. changing the polarity of the current) while maintaining the voltage leads ($I_{21}V_{34}$ + $I_{12}V_{34}$). The remaining six permutations result from swapping the position of the voltmeter and ammeter leads (e.g. if the current was measured between 3 + 4, it would now be measured between 2 + 1) and again switching the polarity of the current ($I_{32}V_{41}$, $I_{23}V_{41}$, $I_{34}V_{12}$, $I_{43}V_{12}$, $I_{14}V_{23}$, $I_{41}V_{23}$). This totals eight possible

electrode permutations, which are measured at several different current strengths for maximum accuracy. The resulting current-potential data is plotted, and the slope is used to extract a resistance. The eight measurements can be split into two groups – those taken along the vertical edge ($I_{21}V_{34}$, $I_{12}V_{34}$, $I_{34}V_{12}$, $I_{43}V_{12}$) and those along the horizontal edge ($I_{32}V_{41}$, $I_{23}V_{41}$, $I_{14}V_{23}$, $I_{41}V_{23}$). By taking the absolute value of each of the four horizontal slopes and averaging the result, the horizontal resistance, R_V, is obtained. An identical calculation is used to determine the horizontal resistance, R_H. By adding additional measurements, any noise that occurs or offset voltage resulting from thermoelectric potentials generated by the difference in temperature across the sample or across the wires will be cancelled out.

To calculate the average resistivity of the sample, an iterative technique based on the Newton-Raphson method used in numerical analysis is used to repeatedly solve for the next R_S until the result converges to the desired precision, as shown in Eq 5.2, where R_S^+ is the next iteration and $S = e^{-\pi/R_S}$.[5] For the measurements made in this work, generally less than 50 iterations are required before the result converges to the desired accuracy.

$$R_S^+ = R_S + R_S^2 + \frac{1-S^{R_V}-S^{R_H}}{\pi(R_V S^{R_V} + R_H S^{R_H})} \qquad \text{Eq. 5.2}$$

The van der Pauw method for measuring the Hall effect of a sample is like the method described for resistivity, but with only four possible electrode permutations. However, in this measurement, current is passed between diagonally placed electrodes, while the potential is measured between the other pair of diagonal electrodes (e.g. $I_{13}V_{24}$). The field strength is varied and the potential measured again until all the desired field strengths have been measured.

Then, this process is repeated with the remaining three electrode permutations. Just as with the resistivity measurement, the first permutation is obtained by reversing the polarity of the current while maintaining identical

voltage leads (e.g. $I_{31}V_{24}$). Then the position of the current and voltage leads are switched ($I_{24}V_{13}$) and the current polarity is again flipped ($I_{42}V_{13}$). Once the measurement of each of the four electrode permutations has been completed, the module is finished.

5.2 System Overview

The automated system consists of many different instruments and devices that communicate through a standardized computer-facilitated GPIB interface. All code is implemented in Labview. A Keithley 706 Scanner with an installed Keithley 7065 Hall Effect card is used to connect the sample electrodes (numbered 1 – 4 per the discussion above) with the voltmeter, the ammeter, and the current source. By opening and closing the appropriate connections in the Hall Card, any of the instruments can be connected to any of the sample electrodes. A Keithley 220 Current Source is used to supply current, while a Keithley 6485 Picoammeter is used to measure the current passed and a Keithley 2182A Nanovoltmeter is used to measure potential. For the Hall Effect measurement, a LakeShore XEM4 electromagnet with a LakeShore 643 power supply is used to provide a variable magnetic field between +9 and -9 kG, while a LakeShore InAs Hall Sensor is used to measure the applied magnetic field at the sample.

Temperature control is provided by an Oxford Instruments Intelligent Temperature Controller ITC4 which varies the output to a heater anchored to a Cu thermal mass. A cold-head driven by a He-compressor is used to cool the system as low as 20 K. The cold-head and the heater (driven by the temperature controller) work together to vary the sample temperature between 20 K – 298 K.

Before beginning a temperature-dependent run, it is necessary to make an initial resistivity and Hall Effect measurement of the sample at room temperature. This measurement will ensure that the sample is properly connected to the measurement system and determines the initial value of the maximum allowed current for the repeated measurements during the upcoming

temperature-dependent run. After replacing the hollow cylindrical Cu thermal shield and Al vacuum shield over the sample holder / coldfinger, the pressure of the system can be reduced. The system contains two pumps – a roughing and a water-cooled turbomolecular pump that provide the vacuum for the system. Two valves are placed between the system and the pumps to allow the system to be vented to atmospheric pressure. Once the system reaches a sufficiently low pressure that there is no risk of atmospheric O_2 condensing on the coldhead ($< 5 \times 10^{-5}$ Torr), the He compressor is turned on, decreasing the system temperature towards its minimum temperature of ~20 K.

The general structure of the system's code is shown in Figure 5.2. This code is designed to be executed at the beginning of a measurement run – e.g. after one has contacted a new sample at room temperature and verified that the contacts are ohmic. The code begins with an initial cooldown period in which the system is reduced to its minimum temperature, followed by controlled heating of the system to the temperatures specified by the text file containing the "List of Temperatures". This begins at the system's minimum temperature, 20 K, and ascends in steps of approximately 10%. Since the thermal mass of the system is very large relative to the thermal mass of a single sample, the heating behavior is controlled by the system's mass. Because of this, a single list of set temperatures generally works for all samples. Before it can be executed, the code requires several user-defined initial values to set the parameters of the measurements (e.g. name of text file where data output will be saved, # of I-V steps in the resistivity measurement, # of B-field steps in Hall Effect measurement, Minimum and Maximum B-field strength, etc.). Users also need to enter the initial maximum current, which is obtained from the room temperature measurement discussed above. At the end of each resistivity measurement, the program scales the requested maximum current for the next resistivity measurement by the percent difference between the last resistivity measurement and the current one. In other words, if there is a 10% increase in the resistivity between the current measurement and the previous one, the

maximum current for the next measurement will be 10% less. In this manner, the maximum current for the measurement is allowed to vary in a manner that provides a sufficiently large signal, but a sufficiently small power dissipation that the sample is not heated. Immediately after turning on the He compressor, the user should plan to press the "Go" button, located on the program's front panel. This will begin the execution of the system's code, beginning with the Cooldown module. After the user enters the initial parameters and begins execution of the code, no further human interaction is required until the end of the run is reached, when the user is required to turn off the He compressor and vacuum pumps.

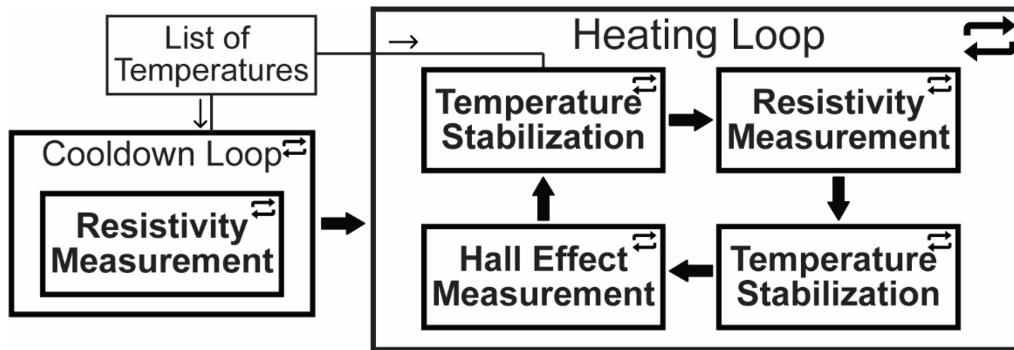

Figure 5.2. Schematic overview of the structure for the automated system's code. The system is based around iterative executions of the main Heating Loop, which contains three sub-modules: the first stabilizes the system at a desired temperature, the next measures the electrical resistivity of the sample, and the last measures the Hall effect of the sample. This Heating Loop is executed until all the set temperatures from the user-defined list have been exhausted.

The code begins with execution of the Cooldown Loop, which monitors the temperature of the system during the initial cooldown period. which continually measures the system temperature in two places – at the sample and at the heater, monitoring them until the heater temperature nears the first temperature on the list of set temperatures. During the cooldown sequence, which typically takes approximately ~2.5 hrs for the system to reach minimum temperature of ~20 K, the electrical resistivity module is repeatedly executed. This provides an estimate of the sample's resistivity before the run has begun, allowing for

increased accuracy by checking the cooldown data against the data collected during the heating run, along with detection of hysteresis in the sample. Each time the Cooldown Loop finishes, it checks whether the temperature of the system at the heater is within a certain range of the first set temperature in the list (range is modifiable, but currently set at ≤2 K). If the heater temperature is outside this range, the loop executes again. If it is, the Cooldown Loop exits and execution of the Heating Loop begins.

The Heating Loop executes once per desired temperature step, which are defined in the user-provided "List of Temperatures". As shown in Figure 5.2, the Heating Loop consists of three sub-modules: Temperature Stabilization, Resistivity Measurement, and the Hall Effect Measurement. Each time the Heating Loop executes, the Temperature Stabilization module begins to heat the system until it reaches and is stable at the next set temperature. When the stability criteria written into the module are met, the module finishes, writing the temperature vs. time data into a file and beginning the Resistivity Measurement. After the measurement finishes, the Temperature Stabilization module runs again to ensure that the sample temperature remains unchanged. After the stability criteria is again met, the Hall Measurement module measures the Hall coefficient of the sample at that temperature. The last iteratively scaled current used in the final execution of the Cooldown module is used in the initial execution of the Heating Loop. After the first execution, the maximum current is scaled in the same manner as previously described.

5.3 Temperature Stabilization

The Oxford ITC4 temperature controller utilizes a standard proportional-integral-derivative (PID) control loop mechanism to regulate the potential applied to the system's heater, working to bring the system temperature quickly and accurately to each user-defined set temperature. The first iteration of the Temperature Stabilization module in each iteration of the Heating Loop serves to heat the sample to the next set temperature, working to bring the system to stability as efficiently as possible (or it would if the code contained the ideal PID

parameters for the system at that temperature). The second iteration of the module in each iteration of the Heating Loop serves merely as a compliance check, ensuring that the sample temperature did not change during the resistivity measurement, correcting it and returning the system to stability if it did. The Temperature Stabilization loop measures the sample and heater temperatures as a function of time, monitoring the standard deviation of both temperatures over the last ~60 sec of measurement (exact value is a user-definable parameter in the code). The loop contains several criteria that must be met before the loop exits: the standard deviation of both the heater and sample temperature's must be less than certain values (currently 2 K and 0.2 K for the heater and sample, respectively) AND the difference between the heater temperature and the set temperature must be less than a certain value (currently 2 K).

A PID loop contains three terms, proportional, integral, and derivative, which, when properly tuned, work together to efficiently keep the process variable (in this case, temperature) close to the target value.[6] The proportional term sets the output (in this case, the heater voltage) in proportion to the current error between the set point and the current value of the process variable. The integral term changes the output by considering the magnitude of the error and the time for which the error has occurred, essentially integrating the difference between two functions, the step function that describes the set point as function of time and the curve that describes the process variable (in this case, heater temperature) as a function of time. As the error persists over time, the integral term's contribution to the output will increase to drive any persistent error to zero. Finally, the derivative term examines the derivative of the process variable as a function of time, attempting to drive this function to zero, which helps reduce overshoot as the system approaches the set point. The optimal PID terms change with the system temperature, as the total amount of thermal mass in the system also changes with temperature.

5.4 Electrical Resistivity

The Electrical Resistivity module communicates with the picoammeter, nanovoltmeter, and Hall Card to switch between the eight required electrode permutations described above. The module is quite simple, containing only an initialization step that ensures the instruments are all set to the correct function, a loop that measures each of the eight possible electrode permutations, and a final step that writes the measured data to an output file. Based on the user-defined parameters entered in the Heating Loop, the desired number of current strengths are measured for each electrode permutation. As of Summer 2022, this value was generally taken as five. The code plots the measured potential as a function of the current passed, using the slope of the resulting line as the measured resistance for that electrode permutation. After this step is completed eight times, the code uses the user-defined sample thickness to iteratively calculate the average resistivity of the sample via the Newton-Raphson method. After this measurement is completed for a given set temperature, the Temperature Stabilization sub-module executes again using the same set temperature, ensuring that the sample's temperature has not changed during the resistivity measurement.

5.5 Hall Effect

After the second execution of the Temperature Stabilization module, the Hall Effect module executes. This module communicates with the picoammeter, nanovoltmeter, Hall Card, the electromagnet power supply, and a multimeter (to measure the magnetic field) to switch between the four required electrode permutations described above and control the magnetic field applied to the sample. Practically, once the leads are connected, the potential is measured as a function of time, until the standard deviation of the last 10 seconds of measurements is less than the user defined value (currently ≤2% of the measured value). Once the potential is stable, the average potential is measured and recorded. After that, the applied magnetic field strength is changed, and the potential measured again until all the desired field strengths have been

exhausted (currently 5 different field strengths). After the potential has been measured at each field strength, the measured potential is plotted versus the measured field and the slope is used to extract the Hall coefficient. This process is repeated three additional times, until all four of the possible electrode permutations have been measured. The results are corrected for sign convention and averaged to obtain the Hall coefficient for the sample at that temperature.

At this point, the iteration of the Heating Loop is complete. As the next iteration begins, the next set temperature is pulled from the "List of Temperatures" and sent to the first execution of the Temperature Stabilization module.

5.6 Bridge

This chapter described the details of the automated system used to measure the electrical resistivity and Hall Effect of thin film samples presented in the following chapters. The next chapter presents my first synthetic efforts using the modulated elemental reactants method – a synthetic exploration of two binary transition metal dichalcogenide systems, $MoSe_2$ and $TiSe_2$.

REFERENCES CITED

(1) Ramadan, A. A.; Gould, R. D.; Ashour, A. On the Van Der Pauw Method of Resistivity Measurements. *Thin Solid Films* **1994**, *239* (2), 272–275. https://doi.org/10.1016/0040-6090(94)90863-X.

(2) Hemenger, P. M. Measurement of High Resistivity Semiconductors Using the van Der Pauw Method. *Rev. Sci. Instrum.* **1973**, *44* (6), 698–700. https://doi.org/10.1063/1.1686224.

(3) van der Pauw, L. J. A Method of Measuring Specific Restivity and Hall Effect of Discs of Arbitrary Shape. *Philips Res. Reports* **1958**, *13*, 1–9.

(4) Webster, J. G. *The Measurement, Instrumentation, and Sensors Handbook*; CRC Press in cooperation with IEEE Press: Boca Raton, Fla., 1999.

(5) Ypma, T. J. Historical Development of the Newton-Raphson Method. *SIAM Rev.* **1995**, *37* (4), 531–551.

(6) Bennett, S. A Brief History of Automatic Control. *IEEE Control Syst.* **1996**, *16* (3), 17–25. https://doi.org/10.1109/37.506394.

CHAPTER VI

INVESTIGATING THE FORMATION OF $MOSE_2$ AND $TISE_2$ FILMS FROM ARTIFICIALLY LAYERED PRECURSORS

6.0 Authorship Statement

Chapter VI was published in Inorganic Chemistry in 2020. Danielle Hamann, David C. Johnson, and I are the main contributors to the text. Eric Hadland contributed experimental data.

6.1 Introduction

In the 1980s and 1990s, the sequence of solid-state reactions between transition metals deposited on silicon substrates was intensely investigated, because transition-metal silicides were desired as low-resistance replacements for heavily doped polysilicon contacts to transistors in integrated circuits.[1−3] A focus of this research was understanding the reaction evolution between metals on silicon surfaces, as it was crucial to control the first phase formed in developing the self-aligned silicide or "salicide" process.[4] The first step in the reaction was proposed to be the formation of an amorphous layer at the interface between the metal and silicon, driven by the enthalpy of mixing of the elements.[4] Since diffusion rates roughly scale with melting temperatures, the amorphous phase was suggested to have the composition of the lowest melting eutectic in the phase diagram. The compound that is easiest to nucleate from this eutectic was suggested to form first, but there was debate over its identity. Walser and Bene suggested that the congruently melting compound with the highest melting point adjacent to the lowest-melting eutectic would form first. However, a second proposal suggested that the compound with the largest effective heat of formation at the eutectic composition would initially form.[5] Over time, the concepts developed for metal−silicon reactions were applied to a broad range of systems, from the formation of amorphous metallic alloys[6] to the sequence of intermetallic phase formation at reacting metal interfaces.[7]

Recent interest in preparing monolayers of compounds, either alone or as

constituents in heterostructures, has focused attention on understanding the formation of ultrathin crystalline layers. Key goals include developing an approach that is scalable to wafer-scale synthesis, capable of controlling thickness to a precise number of unit cells, and able to control defect levels. Thin-film transition-metal dichalcogenides (TMDs) and other layered chalcogenides, due to their diverse and exotic physical properties that can be manipulated by varying the thickness, substrate, or adjacent layers in heterostructures, have attracted significant attention from the two-dimensional (2D) research community.[8–13] While thickness-dependent properties were initially discovered by cleaving bulk samples, subsequent synthesis efforts have focused on developing wafer-scale preparation techniques, such as chemical vapor deposition (CVD).[14–16] More recently, atomic layer deposition,[17–19] metal−organic-CVD,[20–22] and direct deposition methods (sputtering, pulsed laser deposition, ebeam)[23–25] have been used to make high-quality layered TMDs.[26] These approaches use elevated temperatures or light to increase reaction rates, and the quality of the product depends on the temperature and the photon energy utilized (when applicable). The formation process for 2D materials also depends on other process parameters including the structure of the substrate, the pressure, and the carrier and reactant gas fluxes. While plausible chemical schemes have been proposed for many of these systems, there is little reported data of intermediate states and no overarching understanding of how changing reaction parameters impact the formation mechanism.

Here we present X-ray reflectivity (XRR) and X-ray diffraction (XRD) data on the reaction between ultrathin layers of two different metals, Mo and Ti, with amorphous Se. These systems were investigated due to obvious differences in the structure of the as-deposited precursors. The precursors were prepared by sequentially depositing metal and selenium layers on nominally room-temperature substrates. The amount of metal atoms in each of the layers was close to the number required to form a single dichalcogenide layer. For Mo|Se precursors, nucleation occurs during deposition, but there is little subsequent

crystal growth. The as-deposited film, while containing small isolated $MoSe_2$ crystallites, has a modulated amorphous structure containing alternating Mo-rich and Mo-poor layers. In contrast, the Ti|Se precursors nucleate both $TiSe_2$ and Ti_2Se during the deposition. There is no evidence for alternating Ti-rich and Ti-poor layers due to the repeated deposition of the Ti|Se bilayers. The $TiSe_2$ grains grow significantly during the deposition of subsequent layers, resulting in an as-deposited film dominated by layers of crystalline $TiSe_2$. It was experimentally determined that depositing ~10% excess Se in the precursors results in the largest grain sizes for the annealed films for both systems. It is likely that the excess Se not only compensates for the loss of Se to the open system during annealing but also acts as a flux to help facilitate diffusion of the metal atoms during the growth of the crystallites. In summary, these two different dichalcogenides have surprisingly different formation pathways. Annealing precursors with optimized precursor composition and nanoarchitecture at ideal annealing conditions resulted in the formation of layered $TiSe_2$ and $MoSe_2$ films with well-defined Laue oscillations, indicating an integral number of unit cells across the entire film.

6.2 MATERIALS AND METHODS

Precursors were prepared by repeatedly depositing elemental bilayers of Ti|Se or Mo|Se to form an artificially layered precursor. Mo and Ti layers were deposited using an electron-beam gun, while Se was deposited with a Knudsen effusion cell. Precursors were deposited onto silicon substrates with a native oxide layer while maintaining a vacuum of less than 1 × 10−7 Torr during the deposition. In each precursor, the thickness of the Ti and Mo elemental layers was held constant at the thickness required to provide enough metal to form a single Se-M-Se dichalcogenide trilayer. However, the thickness of the Se layer was varied to probe the influence of composition and excess Se on the nucleation and growth of the respective dichalcogenides. Inhouse deposition software was used to control and monitor the amount of material deposited in each layer using pneumatic-controlled shutters and quartz crystal microbalances.[27–30] After

deposition, the precursors were removed from the vacuum chamber, briefly exposed to air, and pumped into a drybox, where they were heated in an N_2 environment with less than 1 ppm of O_2 present to crystallize the deposited elemental layers.

Structure and composition were studied via a suite of X-ray techniques. The structures were characterized by X-ray reflectivity (XRR) and X-ray diffraction (XRD), while composition was determined using X-ray fluorescence (XRF). XRR and specular XRD were collected on a Bruker D-8 Discover diffractometer. In-plane XRD was collected on a Rigaku SmartLab diffractometer. All diffraction measurements utilized a copper K_α radiation source. The absolute amount of each element deposited was determined using XRF data collected on a Rigaku ZSX Primus II with a rhodium source. Previously published calibration curves were used to relate the background-corrected integrated raw intensity to the atoms / Å^2 for each element.[31]

6.3 RESULTS AND DISSCUSION

The initial structure and evolution of the $MoSe_2$ precursors during annealing were investigated using XRR and specular XRD. The as-deposited XRR pattern, shown in Figure 6.1, contains Kiessig fringes, reflecting the total thickness of the deposited films, and two Bragg reflections. The first narrow reflection at ~10.9° 2θ is caused by the artificial layering of the Mo|Se precursor, yielding a Mo|Se thickness of 8.1 Å. The total thickness calculated from the Kiessig fringes, 194 Å, is within error of what is expected for a film composed of 24 8.1 Å layers. The disappearance of the Kiessig fringes at 17.8° 2θ indicates that the roughness of the deposited film is on the order of 2.5 Å, which we calculated using the relationship derived by Parratt.[32] The broad reflection at 13.4° 2θ corresponds to the first-order Bragg reflection expected for $MoSe_2$ and indicates that the nucleation and growth of $MoSe_2$ grains perpendicular to the substrate have occurred during deposition. A potential second-order Bragg reflection, related to the broad reflection at 13.4° 2θ, may be present at higher angles but is very weak, suggesting there is significant variation in the distance between

crystallized $MoSe_2$ layers within the grains. Together, the XRR and specular XRD indicate that the precursor consists of 24 layers containing Mo-rich and Se-rich regions relative to the average composition that are each 8.1 Å thick. Within these layers are small regions that consist of several irregularly stacked $MoSe_2$ layers forming barely coherent grains of $MoSe_2$.

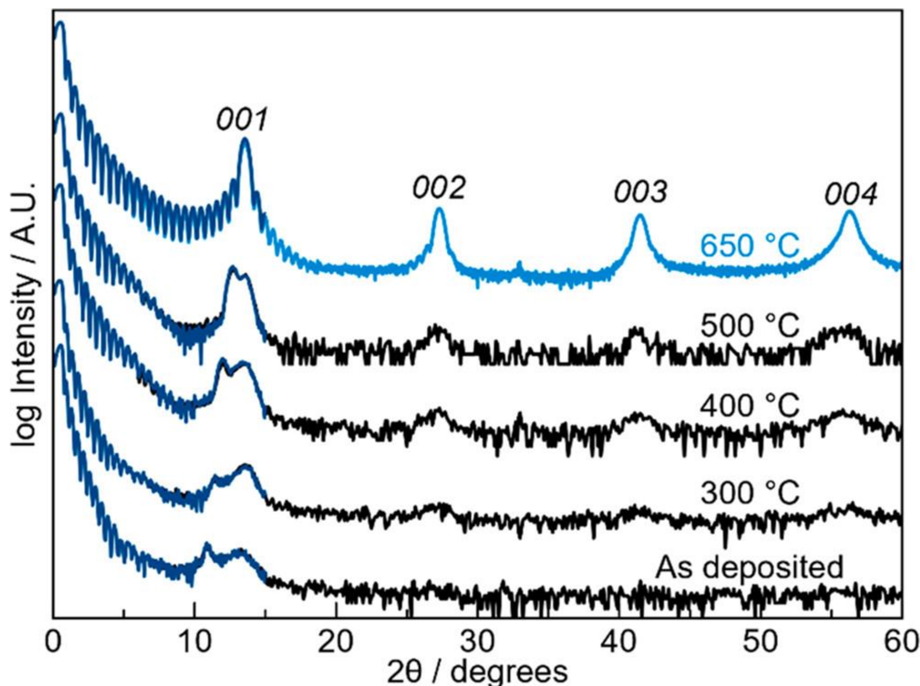

Figure 6.1. XRR and XRD patterns from an annealing study of an as-deposited Mo|Se precursor. The annealing temperatures are presented above the scans. XRR scans are from 0−15° 2θ, while XRD scans are from 6−60° 2θ; the patterns are overlaid and adjusted vertically. All reflections can be indexed to 00l values corresponding to a hexagonal unit cell with lattice parameters consistent with those of $MoSe_2$.

The specular XRD patterns evolve gradually as the annealing temperature is increased, and a very crystalline $MoSe_2$ $00l$ diffraction pattern is obtained after being annealed at 650 °C for 60 min. As the annealing temperature is increased, the reflection from artificial layering moves to higher angles, indicating that the period of the artificial layering is becoming smaller. The initial broad reflection at 13.4° 2θ also shifts to higher angles, becoming narrower and more intense as annealing temperature is increased, indicating that the spread of interlayer distances within each grain is decreasing. This also suggests that there are more

$MoSe_2$ layers within each coherent domain and more $MoSe_2$ domains in the film. After being annealed at 300 °C, second-, third-, and fourth-order reflections from the MoSe2 grains are observed, reflecting the increased order within the diffracting domains. These higher order reflections also increase in intensity and become narrower as annealing temperature is increased, reflecting the increased number and growing size of the $MoSe_2$ domains. The Kiessig fringes become more intense and extend out to higher angles as annealing temperature is increased, indicating that the film is becoming smoother. Finally, there is considerable growth in intensity and narrowing of diffraction line widths between the 500 and 650 °C annealing steps. The c-axis lattice parameter of the annealed film calculated from the position of the Bragg reflections after the 650 °C annealing is 6.52 Å, which is slightly larger than that previously reported for $MoSe_2$ (6.460(1) Å).[33] After being annealed at 650 °C, the low-angle reflection from the artificial layering is no longer visible, consistent with the transformation of the precursor from mostly amorphous layers to well-defined crystalline $MoSe_2$ layers. The Kiessig fringes observed in the XRR scan after being annealed at 650 °C are well-resolved and decay in intensity as expected for a film of uniform electron density and thickness. The presence of both Kiessig fringes and Laue oscillations at higher angles after being annealed at 650 °C indicates that the film becomes significantly smoother and that a constant thickness film with an integer number of $MoSe_2$ layers occurs across the majority of the substrate. The total film thickness calculated from the positions of the Kiessig fringes is 158 Å, which is within error of that expected for a 24-layer film of $MoSe_2$ with a c-axis lattice parameter of 6.52 Å. Between the first and second Bragg reflections, Laue oscillations are present. Laue oscillations result from the incomplete destructive interference between Bragg reflections due to a finite number of unit cells. Their presence indicates coherent diffraction from domains in the polycrystalline film that each consist of the same number of $MoSe_2$ layers. Analysis of the spacing of the Laue fringes indicates that the coherent domains contain 24 $MoSe_2$ layers, consistent with the number of Mo|Se bilayers deposited in the precursor and with the total film thickness.

In-plane diffraction data were collected for the Mo|Se film annealed at 650 °C and are shown in Figure 6.2. All observed reflections can be indexed to a hexagonal unit cell with an a-axis lattice parameter of 3.31(1) Å. This is slightly larger than what has been previously reported for bulk $MoSe_2$ (3.289(1) Å)33 and $MoSe_2$ thin films (3.246 Å).[34] The composition and diffraction data provide consistent evidence that the crystallized material is $MoSe_2$. Mo|Se precursors with different amounts of Se were annealed at 650 °C and characterized by XRD to probe the influence of composition on the growth and crystallinity of the final product. Figure 6.3 graphs the intensity and peak width of the 001 reflection of $MoSe_2$ as a function of the Se content in the precursor prior to being annealed. The peak width of the 00l reflections depends on the size and coherence of the $MoSe_2$ layers along the c-axis, with a minimum peak width occurring when the entire film thickness consists of a single coherent domain. The data in Figure 6.3. demonstrate that some excess Se is required to obtain the narrowest line widths, but too much excess increases the line width. The intensity of the 00l reflections is proportional to the number of $MoSe_2$ domains that are aligned parallel to the substrate, and the maximum intensity was observed for annealed films that began with a 10−15% excess of Se. Rocking curves taken on these samples are narrowest for those with the highest intensity of the 001 reflection, suggesting that the intensity maximum is due to the percentage of the sample that is crystallographically aligned. The variation of crystalline quality with Se concentration is likely caused by the excess Se acting as a flux, increasing the mobility of the Mo cations during annealing. However, too much Se results in the nucleation of grains of $MoSe_2$ that are not aligned with the basal plane perpendicular to the substrate, preventing the entire film thickness from becoming a single coherent domain.

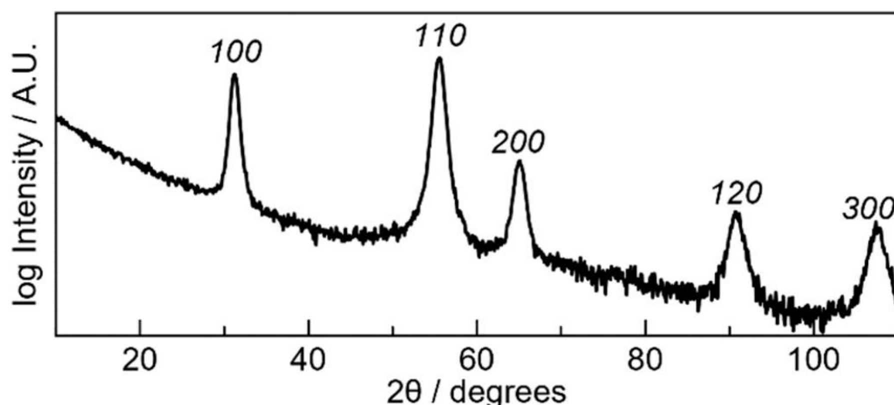

Figure 6.2. Grazing incidence in-plane diffraction of a $MoSe_2$ film after being annealed at 650 °C for 60 min. All reflections can be indexed as hk0 reflections (shown above each reflection) corresponding to a hexagonal unit cell with lattice parameters consistent with those of $MoSe_2$.

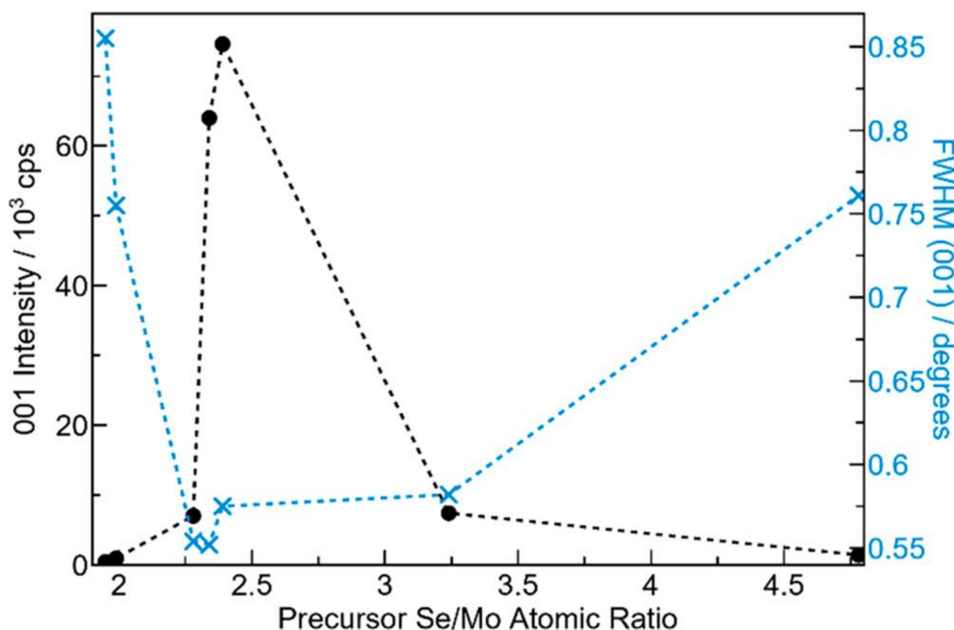

Figure 6.3. $MoSe_2$ crystal quality as determined by specular diffraction reflection intensity and peak width graphed vs the composition of the Mo|Se precursor.

A series of Ti|Se precursors with various Ti/Se ratios were prepared to compare their evolution to that found for Mo|Se precursors forming $MoSe_2$. Table 6.1. summarizes data obtained from each of the Ti|Se precursors. The XRF data show that all precursors were Se rich as-deposited, and the number of Ti atoms/Å^2 deposited per Ti|Se bilayer ranged from 2% above to 10% below the

number required for a single ideal crystalline $TiSe_2$ trilayer, 0.092 Ti atoms / Å^2. The total thicknesses for the samples were calculated from the Kiessig fringes and divided by the number of Ti|Se bilayers that were deposited to obtain the average Ti|Se bilayer thickness for each sample (Table 6.1). The thicknesses are consistent with the number of atoms deposited calculated from the XRF intensities (Table 6.1). The specular diffraction patterns of the as-deposited precursors all contain two to four $00l$ reflections from the crystalline $TiSe_2$ domains (see Figure 6.5.), indicating that the as-deposited films are much more crystalline than the corresponding Mo|Se films. The *c*-axis lattice parameters were all larger than those previously reported for $TiSe_2$, reflecting the high defect levels resulting from the low ambient temperature during the deposition. There is a systematic increase in the *c*-axis lattice parameter as the amount of Se deposited in the sample increases, suggesting that interstitial Se atoms may be trapped between layers due to limited diffusion at these low annealing temperatures. The in-plane diffraction patterns (shown in black in Figures 6.5 and S2) also reflect the more crystalline nature of the as-deposited Ti|Se films, containing reflections that can be indexed as $hk0$ reflections from $TiSe_2$ and broad reflections consistent with the presence of Ti_2Se deposited, and the number of Ti atoms / Å^2 deposited per Ti|Se bilayer ranged from 2% above to 10% below the number required for a single ideal crystalline $TiSe_2$ trilayer, 0.092 Ti atoms / Å^2 . The as-deposited XRR patterns (Figure S1) contained Kiessig fringes, reflecting the total thickness of the deposited films and a strong first-order reflection from crystalline $TiSe_2$. The disappearance of the Kiessig fringes at 7.4° 2θ indicates that the roughness of the deposited film is on the order of 6 Å, which we calculated using the relationship derived by Parratt.[32] Unlike the Mo|Se precursors, no reflection intensity was observed that could be attributed to the artificial layering of the Ti|Se precursors.

Table 6.1. Structure and Composition Summary for the As-Deposited Ti|Se Precursors

# Ti|Se layers deposited	Total film thickness (Å, ±0.5)	Average bilayer thickness (Å)	Average Ti atoms / Å^2 per bilayer (±0.07)	Average Se atoms / Å^2 per bilayer (±0.04)	Composition Ti/Se	As-deposited $TiSe_2$ *c*-axis lattice parameter (Å, ±0.01)
83	478	5.8	0.092	0.185	1:2.01	6.14
83	487	5.9	0.092	0.188	1:2.05	6.17
83	507	6.1	0.094	0.198	1:2.11	6.16
84	509	6.1	0.089	0.192	1:2.14	6.17
83	524	6.3	0.092	0.198	1:2.16	6.19
84	527	6.3	0.089	0.197	1:2.22	6.19
82	482	5.8	0.084	0.188	1:2.24	6.18
83	532	6.4	0.090	0.204	1:2.26	6.20
84	564	6.7	0.082	0.210	1:2.57	6.27

Taken together, the diffraction data indicate that the Ti|Se precursors substantially interdiffuse and react during deposition. Since the film's overall compositions are Se-rich, we suspect that the observed Ti_2Se is formed during the deposition when Se is deposited on top of the initial Ti layer. After the first Ti|Se bilayer is deposited, $TiSe_2$ nucleates, either at the surface of the Se layer or at the Ti_2Se surface below, by diffusing through the amorphous Se layer. When subsequent layers are deposited, Ti atoms must diffuse through the Se-rich matrix to the growth fronts of existing $TiSe_2$ crystallites. When this diffusion length becomes sufficiently large, new crystalline layers of $TiSe_2$ may nucleate near the surface of the sample. The reactions during the deposition result in large regions of crystalline $TiSe_2$ surrounded by a Se-rich matrix, with Ti_2Se adjacent to the Si substrate.

Figure 6.4. contains a series of XRR and XRD patterns collected as a function of the annealing temperature for a representative Ti|Se precursor with an initial Ti/Se composition of 1:2.24. The $00l$ reflections of the $TiSe_2$ crystallites

move noticeably to a higher angle as the annealing temperature is increased, indicating a decrease in the c-axis lattice parameter. Additionally, the reflection intensity increases while the line widths (full width at half-maximum (fwhm)) decrease as the annealing temperature is increased, suggesting the registration between the $TiSe_2$ planes increases excess atoms between layers and at grain boundaries are incorporated into the growing crystallites or diffuse to the surface. In all but the least Se-rich films, the in-plane reflections of Ti_2Se become unobservable. However, Ti_2Se in-plane reflections remain after being annealed in the most Ti-rich film studied. Films annealed at 350 °C have the greatest reflection intensity and narrowest peak widths. Annealing above 350 °C results in a decrease in intensity and an increase in peak width of the 00l reflections. On the basis of the above observations, the optimal annealing temperature for the Ti|Se precursors was determined to be 350 °C.

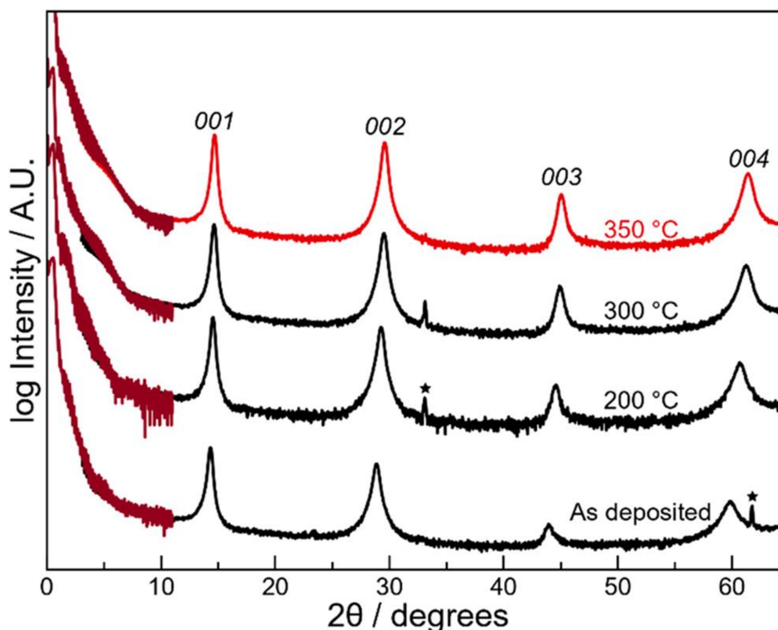

Figure 6.4. XRR and XRD patterns from an annealing study of an as-deposited Ti|Se precursor with a starting composition of 1:2.24 (Ti / Se). The sample was annealed for 30 min at the temperatures presented above each scan. XRR scans are from 0−11° 2θ, while XRD scans are from 3−65° 2θ; the patterns are overlaid and adjusted vertically. All reflections can be indexed to 00l values corresponding to a hexagonal unit cell with lattice parameters consistent with $TiSe_2$. Reflections marked with an asterisk correspond to the substrate.

As was done in the Mo|Se system, precursor films were prepared by holding the thickness of the Ti layer constant, varying the amount of Se, and annealing under identical conditions (350 °C for 30 min) to study the effects of precursor composition on film quality. For all the films, the XRF data show that Se was lost during annealing (Table 6.2). The XRR patterns, shown in Figures A.1 and A.3, all contain Kiessig fringes from the interference of the front and back of the film. In contrast to the Mo|Se system, the surface roughness of the films does not change significantly during annealing. Because of the loss of Se during the annealing, all the annealed films are thinner than the as-deposited precursors. Oscillations in the intensity of the Kiessig fringes in all the films indicate that a surface layer with a different electron density than the rest of the sample has formed, likely a surface layer of amorphous TiO_2. This oxide layer forms during annealing in an inert atmosphere with less than 1 ppm of O_2 present. This may seem surprising until recognizing that, despite the low oxygen concentration present, approximately a monolayer's worth of O_2 molecules impacts the film during each second of annealing.

Table 6.2. Compositions and Lattice Parameters for Annealed Ti|Se Films As Determined from Full Pattern XRD Le Bail Fits

AD composition (Ti/Se)	Annealed total film thickness (Å)	c-lattice parameter (Å)	a-lattice parameter (Å)	Annealed expt. Ti atoms / Å² (±0.08)	Annealed expt. Se atoms / Å² (±0.02)	Annealed composition (Ti/Se)
1:2.01	479	6.053(1)	3.551(1)	7.54	15.05	1:2.00
1:2.05	479	6.051(1)	3.558(1)	7.57	15.21	1:2.01
1:2.11	503	6.050(1)	3.559(1)	7.86	15.46	1:1.97
1:2.14	483	6.034(1)	3.558(1)	7.70	14.41	1:1.87
1:2.16	501	6.037(1)	3.560(1)	7.70	15.49	1:2.01
1:2.22	503	6.043(1)	3.553(1)	7.70	15.35	1:1.99
1:2.24	450	6.066(1)	3.549(1)	6.86	12.85	1:1.87
1:2.26	496	6.058(1)	3.554(1)	7.50	15.10	1:2.01
1:2.57	505	6.096(1)		6.80	13.80	1:2.03

The annealed XRR patterns fall into two general categories - those with a thicker (~50 Å) TiO_2 layer and those with a thinner (~10 Å) TiO_2 layer on top of the film

(Figure A.4). The specular diffraction patterns (Figures 6.5a and A.2a) contain 00l reflections from crystalline $TiSe_2$. The observed reflections are more intense, narrower, and occur at higher 2θ angles than those in the as-deposited precursors, indicating there are more 00l planes aligned with the substrate, the $TiSe_2$ crystalline domains are thicker, and that the c-axis lattice parameters are smaller. The *c*-axis lattice parameters obtained from full pattern Le Bail fits are summarized in Table 6.2. Samples that have a slight excess of Se, in the composition range between 1:2.14 and 1:2.22 on deposition, have *c*-axis lattice parameters that best match the reported values for $TiSe_2$. Films with initial compositions on either side of this regime have c-axis lattice parameters that are slightly larger than the literature value. Representative in-plane XRD patterns for the films are shown in Figures 5b and A.2b. The annealed patterns have narrower reflections than those found in the as-deposited samples, indicating a significant increase in the in-plane domain size. All of the reflections in the annealed samples can be indexed to a hexagonal unit cell with lattice parameters similar to the reported values for $TiSe_2$ (Table 6.2), except for broad reflections in the 1:2.01 sample, which correspond to an impurity phase of Ti_2Se.[35] This phase also appears to be present to some extent in all precursors prior to being annealed. The a-axis lattice parameters for all of the Ti|Se films, determined from the Le Bail fits of the in-plane diffraction patterns found in Figure 6.5b, are very similar to those previously reported for $TiSe_2$ (Table 2).[35] Unlike the *c*-axis lattice parameters, which were influenced by the amount of Se present in the precursor sample, the a-axis lattice parameter for the annealed $TiSe_2$ films does not depend on the precursor composition. The change in the crystallinity of the $TiSe_2$ films as a function of precursor composition was estimated by using the line widths of the specular and in-plane reflections in the diffraction patterns of the annealed precursors. Line widths of the 110 and 001 reflections in the in-plane and specular XRD patterns, respectively, were determined to help quantify the effect of precursor composition on crystal quality (Figure 6.6).

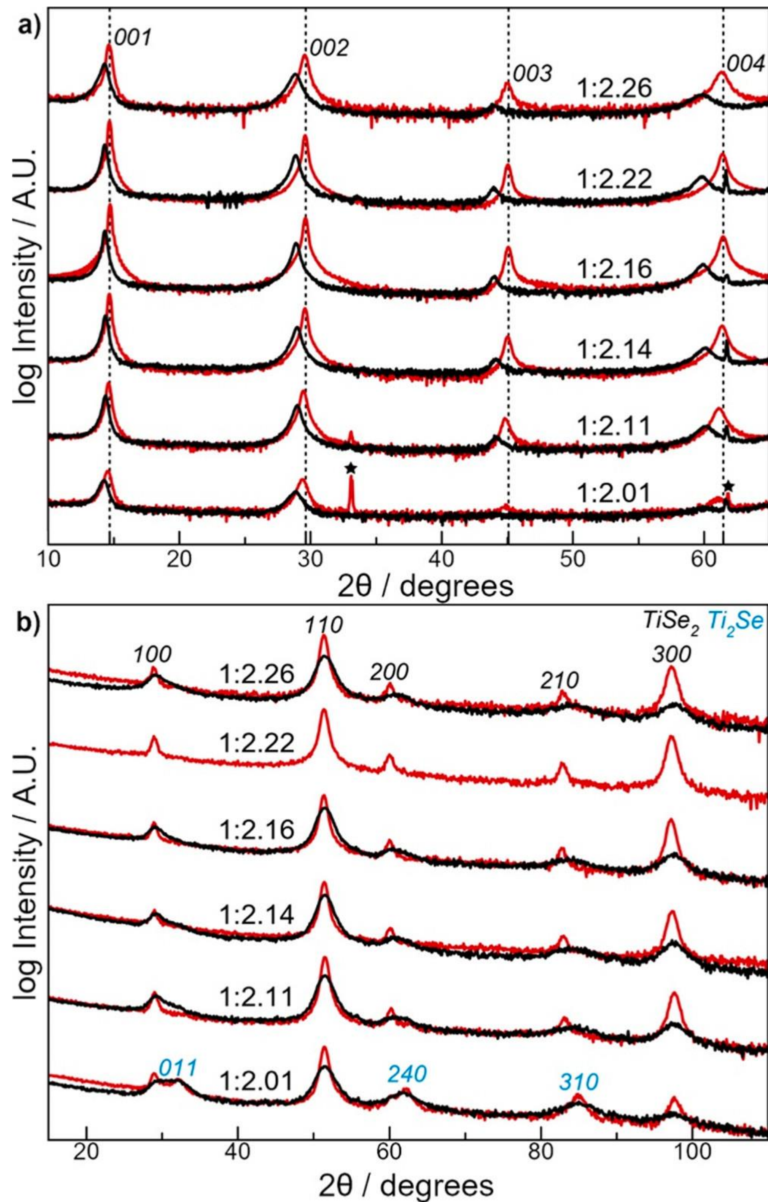

Figure 6.5. Representative specular (a) and in-plane (b) XRD patterns of Ti|Se thin films with various compositions. Black curves show the diffraction pattern of the precursor, while red curves show the pattern for the films annealed at 350 °C. All observed reflections that correspond to the $TiSe_2$ crystal structure are indexed in black. Reflections marked with an asterisk observed in the specular pattern are attributed to the Si substrate. Reflections for the observed Ti_2Se impurity phase are indexed in blue. Additional diffraction patterns can be found in Figure S2.

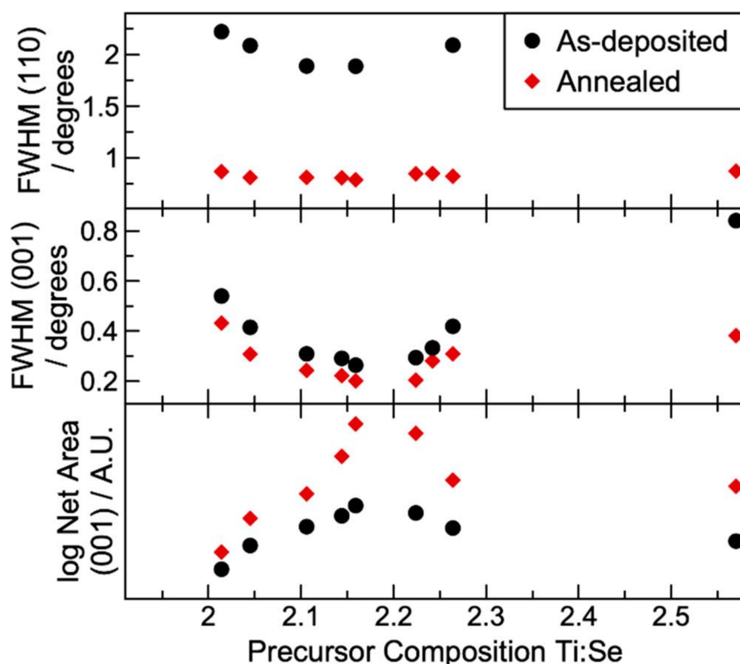

Figure 6.6. Line widths (fwhm) of the 110 reflection in the in-plane XRD pattern (top) and 001 reflection in the specular XRD pattern (middle) and 001 reflection net area (bottom) as a function of precursor composition. (●) As-deposited parameters. (◆) Annealed parameters. The diffraction patterns used to determine these parameters are found in Figure 6.4 and Figure A.2.

In the as-deposited films, both specular and in-plane line widths are smallest when the precursors have a Ti/Se ratio of 1:2.15−1:2.2. After being annealed, both the in-plane and specular diffraction patterns have the smallest line widths (and largest crystallite sizes) at a Se/Ti ratio of ~2.15−2.2; however, there is a much smaller range of in-plane line widths. A Scherrer analysis of the line widths for the sample with an as-deposited composition of 1:2.16 yields a c-axis crystallite size of 443 Å and an in-plane crystallite size of 117 Å. Similar to what was observed in the Mo|Se system, it is possible that the slight excess of Se acts as a flux to facilitate the transport of Ti atoms to the crystallite growth fronts, causing larger crystallite sizes in precursors with the ideal amount of excess Se. For the three $TiSe_2$ samples with the optimal amount of excess Se to obtain large coherent diffracting domains, Laue oscillations are visible surrounding the first Bragg reflection (Figure 6.7). The Laue oscillations occur due to the incomplete destructive interference of a finite number of unit cells in

a crystal. For a small number of unit cells N, the Laue function, sin(Nx)/ sin(x), results in a principle intensity maximum whose position is determined by the lattice parameters of the diffracting crystal and a series of evenly spaced maxima on either side whose spacing is determined by the number of unit cells in the crystal. To observe the Laue oscillations, the majority of the film must consist of crystallites with identical numbers of unit cells, because crystallites with different numbers of unit cells would contribute Laue intensities at different angles, destroying the interference pattern. Figure 6.7 shows the measured specular diffraction pattern around the first Bragg reflection for the annealed samples with Laue oscillations. The position of the highest intensity maxima is consistent with the *c*-axis lattice parameters given in Table 6.2. The spacing of the Laue oscillations is consistent with the diffracting crystallites having a specific number of unit cells, as shown by the simulated patterns overlaid on the experimental patterns in Figure 6.7. However, the total film thicknesses of these annealed samples are larger than the product of the number of unit cells calculated from the Laue oscillations multiplied by the appropriate c-axis lattice parameter. Since the number of Ti| Se bilayers deposited in the precursors was larger than the number of layers formed, there is more Ti in the samples than required for the number of $TiSe_2$ layers calculated from the Laue oscillations. This suggests that several Ti|Se bilayers were oxidized, formed Ti_2Se, and/or reacted with the substrate.

The combination of XRF, XRR, and XRD data allows us to speculate on an atomic-level picture of the structure of the as-deposited Mo|Se and Ti|Se precursors and how it evolves during annealing. Analysis of the diffraction data clearly indicates that the structure of the as-deposited Mo and Ti precursors are significantly different, which is illustrated schematically in Figure 6.8. The Mo|Se precursor, Figure 6.8a, has a composition modulation from the growth of the sequence of as-deposited layers with small crystallites of $MoSe_2$ several layers thick distributed throughout the film. Figure 6.8c illustrates how the Ti|Se precursor has reacted much more during deposition than the Mo|Se precursor.

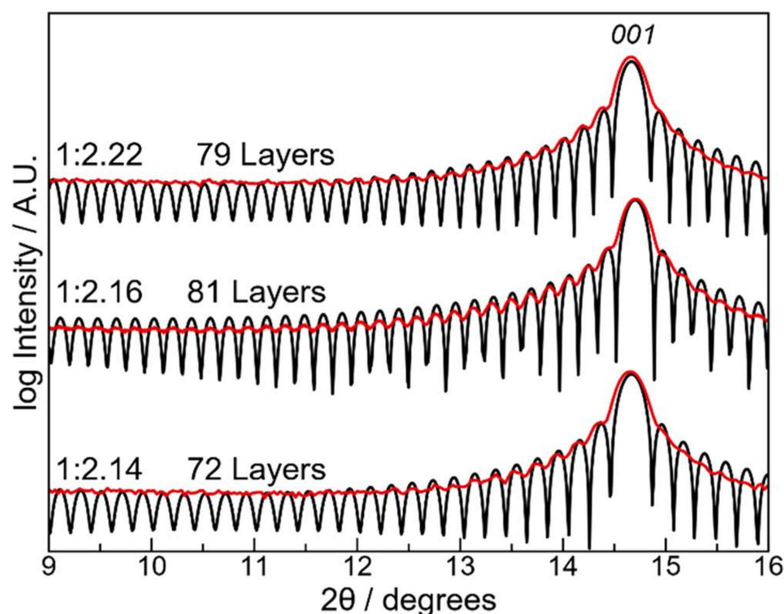

Figure 6.7. Experimental specular XRD patterns (red) for the highest quality annealed $TiSe_2$ films overlaid with the theoretical Laue oscillations expected for n layers of $TiSe_2$ (black).

In the Ti|Se precursors, there is no evidence of compositional modulation; Ti_2Se forms during the deposition of Se on the first layer of Ti deposited, and thick domains of poorly stacked $TiSe_2$ layers subsequently grow during the deposition. In both the Mo|Se and Ti|Se precursors, there is a gradient in metal concentration around the growth front as it is depleted around each crystallite.

For the Mo|Se precursor, the concentration gradient is not enough to induce diffusion during the deposition, likely a result of the high activation energies required for diffusion. However, in the Ti|Se precursors, smaller Ti atoms diffuse significantly during deposition to form the observed thick $TiSe_2$ domains. In both systems, annealing at elevated temperatures allows more diffusion to occur, leading to the growth of well-organized crystallites. A small amount of excess Se (10%) results in the formation of larger coherent domains of the dichalcogenide in both systems. The excess Se presumably acts as a flux to increase the rate of diffusion of the metal cations. However, too much excess Se results in less crystallographically aligned layers and smaller grain sizes. In both systems, the optimized precursor structure and annealing temperatures

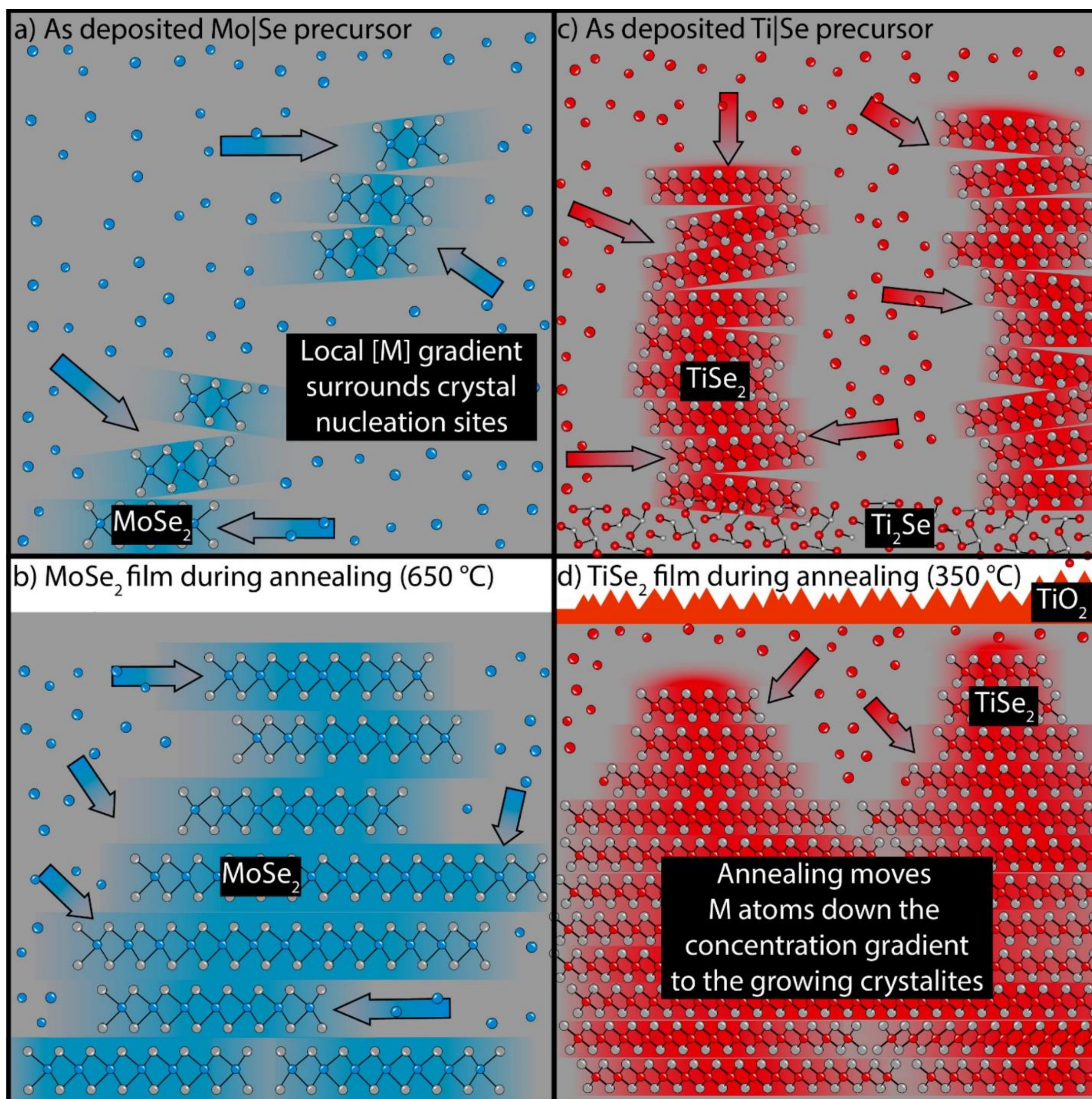

Figure 6.8. Proposed atomic-level pictures for the evolution of Mo|Se (a) and Ti|Se (c) precursors as they are annealed to form crystalline $MoSe_2$ (b) and $TiSe_2$ (d). There is much more interdiffusion during deposition of the lighter Ti atoms, resulting in larger crystalline domains in the as-deposited $TiSe_2$ precursor relative to the Mo|Se precursor.

resulted in the formation of polycrystalline films that predominantly contained a precise and identical number of dichalcogenide planes. For Mo|Se films with the correct amount of Mo per Mo|Se bilayer in the precursor, each Mo|Se layer evolved into a single $MoSe_2$ trilayer plane in the coherent domain. In analogous

Ti|Se films, all of the Ti|Se layers evolved into $TiSe_2$ except for two layers at the surface of the film that oxidized, forming a TiO_2 surface layer.

6.4 Conclusions

Highly crystalline transition-metal diselenide films can be prepared by depositing alternating layers of the metal and selenium. With the correct amount of metal and a slight excess of Se deposited per M|Se bilayer, each layer will evolve into a dichalcogenide plane upon annealing. This enables the thickness of the dichalcogenide film to be controlled to a specified number of unit cells over large areas. While a precise number of dichalcogenide planes was obtained in both the Ti− Se and Mo−Se systems, the reaction pathways were very different. $TiSe_2$ mostly self-assembles during the deposition process, while $MoSe_2$ mostly self-assembles during annealing. In both systems, concentration gradients drive the diffusion of metals to the crystallite growth fronts, aided by the short diffusion distances in the layered precursor during annealing or surface diffusion during the deposition. The diffraction data gathered on the as-deposited films and during annealing enabled the creation and comparison of atomistic pictures describing the self-assembly of $MoSe_2$ and $TiSe_2$ from their respective precursors. By understanding the film formation and developing control over the composition and morphology of the precursors, we demonstrate that growth of dichalcogenides can be controlled to achieve uniform thicknesses over large areas.

6.5 Bridge

This chapter presents the study of M|Se thin films, where M = Mo, Ti. By studying the reaction pathway as a function of the experimental parameters, we were able to conclude that synthesis of optimal quality films results from precursors deposited with a ~15% excess of Se. The next chapter describes the synthetic exploration of a heterostructure containing crystalline and amorphous components.

REFERENCES CITED

(1) Mayer, J. W.; Tu, K. N. Analysis of Thin-Film Structures with Nuclear Backscattering and x-Ray Diffraction. *Journal of Vacuum Science & Technology* **1974**, *11*, 86.

(2) Krautle, H.; Nicolet, M.-A.; Mayer, J. W. Kinetics of Silicide Formation by Thin Films of V on Si and SiO2 Substrates. *Journal of Applied Physics* **1974**, *45*, 3304.

(3) Mayer, J. W.; Poate, J. W.; Tu, K. N. Thin Films and Solid-Phase Reactions. *Science (1979)* **1975**, *190*, 223.

(4) Walser, R. M.; Bene, R. W. First Phase Nucleation in Silicon-Transition-Metal Planar Interfaces. *Applied Physics Letters* **1976**, *28*, 624.

(5) Pretorius, R.; Theron, C. C.; Vantomme, A.; Mayer, J. W. Compound Phase Formation in Thin Film Structures. *Critical Reviews in Solid State and Materials Sciences* **1999**, *24*, 1–62.

(6) Cotts, E. J.; Meng, W. J.; Johnson, W. L. Calorimetric Study of Amorphization in Planar, Binary, Multilayer, Thin-Film Diffusion Couples of Ni and Zr. *Physical Review Letters* **1986**, *57*, 2295.

(7) Schneider, L. M.; Lippert, S.; Renaud, D.; Kuhnert, J.; Kang, K. N.; Ajayi, O.; Halbich, M. U.; Abdulmunem, O. M.; Lin, X.; Hassoon, K.; Edalati-Boostan, S.; Kim, Y. D.; Heimbrodt, W.; Yang, E. H.; Hone, J. C.; Rahimi-Iman, A. Influence of the Substrate Material on the Optical Properties of Tungsten Diselendide Monolayers. *2D Materials* **2017**, *4*, 025045. https://doi.org/10.1364/CLEO_AT.2017.JTh2A.23.

(8) Schneider, L. M.; Lippert, S.; Kuhnert, J.; Renaud, D.; Kang, K. N.; Ajayi, O.; Halbich, M. U.; Abdulmunem, O. M.; Lin, X.; Hassoon, K.; Edalati-Boostan, S.; Kim, Y. D.; Heimbrodt, W.; Yang, E. H.; Hone, J. C.; Rahimi-Iman, A. The Impact of the Substrate Material on the Optical Properties of 2D WSe2 Monolayers. *Semiconductors* **2018**, *52* (5), 565–571. https://doi.org/10.1134/S1063782618050275.

(9) Niu, Y.; Gonzalez-Abad, S.; Frisenda, R.; Marauhn, P.; Drüppel, M.; Gant, P.; Schmidt, R.; Taghavi, N. S.; Barcons, D.; Molina-Mendoza, A. J.; de Vasconcellos, S. M.; Bratschitsch, R.; de Lara, D. P.; Rohlfing, M.; Castellanos-Gomez, A. Thickness-Dependent Differential Reflectance Spectra of Monolayer and Few-Layer MoS2, MoSe2, WS2 and WSe2. *Nanomaterials* **2018**, *8* (9). https://doi.org/10.3390/nano8090725.

(10) Hamann, D. M.; Lygo, A. C.; Esters, M.; Merrill, D. R.; Ditto, J.; Sutherland, D. R.; Bauers, S. R.; Johnson, D. C. Structural Changes as a

Function of Thickness in [(SnSe) 1+ δ] m TiSe 2 Heterostructures. *ACS Nano* **2018**, acsnano.7b07506. https://doi.org/10.1021/acsnano.7b07506.

(11) Biswas, R. K.; Khan, P.; Mukherjee, S.; Mukhopadhyay, A. K.; Ghosh, J.; Muraleedharan, K. Study of Short Range Structure of Amorphous Silica from PDF Using Ag Radiation in Laboratory XRD System, RAMAN and NEXAFS. *Journal of Non-Crystalline Solids* **2018**, *488* (February), 1–9. https://doi.org/10.1016/j.jnoncrysol.2018.02.037.

(12) Hamann, D. M.; Merrill, D. R.; Bauers, S. R.; Mitchson, G.; Ditto, J.; Rudin, S. P.; Johnson, D. C. Long-Range Order in [(SnSe)1.2]1[TiSe2]1 Prepared from Designed Precursors. *Inorganic Chemistry* **2017**, *56* (6), 3499–3505. https://doi.org/10.1021/acs.inorgchem.6b03063.

(13) Li, L. J.; O'Farrell, E. C. T.; Loh, K. P.; Eda, G.; Özyilmaz, B.; Castro Neto, A. H. Controlling Many-Body States by the Electric-Field Effect in a Two-Dimensional Material. *Nature* **2016**, *529* (7585), 185–189. https://doi.org/10.1038/nature16175.

(14) Novoselov, K. S.; Geim, A. K.; Morozov, S. v; Jiang, D.; Zhang, Y.; Dubonos, S. v.; Grigorieva, I. v; Firsov, A. A. Electric Field Effect in Atomically Thin Carbon Films. *Science (1979)* **2004**, *5* (1), 1–12. https://doi.org/10.1126/science.aab1343.

(15) Wang, X.; Gong, Y.; Shi, G.; Chow, W. L.; Keyshar, K.; Ye, G.; Vajtai, R.; Lou, J.; Liu, Z.; Ringe, E.; Tay, B. K.; Ajayan, P. M. Chemical Vapor Deposition Growth of Crystalline Monolayer MoSe2. *ACS Nano* **2014**, *8* (5), 5125–5131.

(16) Lu, X.; Utama, I. B.; Lin, J.; Gong, X.; Zhang, J.; Zhao, Y.; Pantelides, S. T.; Wang, J.; Dong, Z.; Liu, Z.; Zhou, W.; Xiong, Q. Large-Area Synthesis of Monolayer and Few-Layer MoSe2 Films on SiO2 Substrates. *Nano Letters* **2014**, *14* (5), 2419–2425.

(17) Tan, L. K.; Liu, B.; Teng, J. H.; Guo, S.; Low, H. Y.; Loh, K. P. Atomic Layer Deposition of a MoS2 Film. *Nanoscale* **2014**, *6* (18), 10584–10588.

(18) Song, J.-G.; Park, J.; Lee, W.; Choi, T.; Jung, H.; Lee, C. W.; Hwang, S.-H.; Myoung, J. M.; Jung, J.-H.; Kim, S.-H.; Lansalot-Matras, C.; Kim, H. Layer-Controlled, Wafer-Scale, and Conformal Synthesis of Tungsten Disulfide Nanosheets Using Atomic Layer Deposition. *ACS Nano* **2013**, *7* (12), 11333–11340.

(19) Jin, Z.; Shin, S.; Kwon, D. H.; Han, S.-J.; Min, Y.-S. Novel Chemical Route for Atomic Layer Deposition of MoS2 Thin Film on SiO2/Si

Substrate. *Nanoscale* **2014**, *6* (23), 14453–14458.

(20) Kang, K.; Xie, S.; Huang, L.; Han, Y.; Huang, P. Y.; Mak, K. F.; Kim, C. J.; Muller, D.; Park, J. High-Mobility Three-Atom-Thick Semiconducting Films with Wafer-Scale Homogeneity. *Nature* **2015**, *520*, 656–660.

(21) Eichfeld, S. M.; Hossain, L.; Lin, Y.-C.; Piasecki, A. F.; Kupp, B.; Birdwell, A. G.; Burke, R. A.; Lu, N.; Peng, X.; Li, J.; Azcatl, A.; McDonnell, S.; Wallace, R. M.; Kim, M. J.; Mayer, T. S.; Redwing, J. M.; Robinson, J. A. Highly Scalable, Atomically Thin WSe2 Grown via Metal–Organic Chemical Vapor Deposition. *ACS Nano* **2015**, *9* (2), 2080–2087.

(22) Lin, Y.-C.; Ghosh, R. K.; Addou, R.; Lu, N.; Eichfeld, S. M.; Zhu, H.; Li, M.-Y.; Peng, X.; Kim, M. J.; Li, L.-J.; Wallace, R. M.; Datta, S.; Robinson, J. A. Atomically Thin Resonant Tunnel Diodes Built from Synthetic van Der Waals Heterostructures. *Nature Communications* **2015**, *6*, 7311.

(23) Park, J.; Choudhary, N.; Smith, J.; Lee, G.; Kim, M.; Choi, W. Thickness Modulated MoS2 Grown by Chemical Vapor Deposition for Transparent and Flexible Electronic Devices. *Applied Physics Letters* **2015**, *106*, 012104.

(24) Zhan, Y.; Liu, Z.; Najmaei, S.; Ajayan, P. M.; Lou, J. Large-Area Vapor-Phase Growth and Characterization of MoS2 Atomic Layers on a SiO2 Substrate. *Small* **2012**, *8* (7), 966.

(25) Han, G. H.; Kybert, N. J.; Naylor, C. H.; Lee, B. S.; Ping, J.; Park, J. H.; Kang, J.; Lee, S. Y.; Lee, Y. H.; Agarwal, R.; Johnson, A. T. Seeded Growth of Highly Crystalline Molybdenum Disulphide Monolayers at Controlled Locations. *Nature Communications* **2015**, *6*, 6128.

(26) Choi, W.; Choudhary, N.; Han, G. H.; Park, J.; Akinwande, D.; Lee, Y. H. Recent Development of Two-Dimensional Transition Metal Dichalcogenides and Their Applications. *Materials Today* **2017**, *20* (3), 116–130.

(27) Johnson, D. C. Controlled Synthesis of New Compounds Using Modulated Elemental Reactants. *Current Opinion in Solid State and Materials Science* **1998**, *3* (2), 159–167. https://doi.org/10.1016/S1359-0286(98)80082-X.

(28) Esters, M.; Johnson, D. C. Targeted Synthesis of Metastable Compounds and Intergrowths: The Modulated Elemental Reactants Method. In *Crystal Growth: Concepts, Mechanisms, and Applications*; Li, J., Li, J., Chi, Y., Eds.; Nova Science Publishers: New York, 2017; pp 35–118.

(29) Atkins, R.; Wilson, J.; Zschack, P.; Grosse, C.; Neumann, W.; Johnson, D.

C. Synthesis of [(SnSe)1.15]m(TaSe2)n Ferecrystals: Structurally Tunable Metallic Compounds. *Chemistry of Materials* **2012**, *24* (23), 4594–4599. https://doi.org/10.1021/cm302948x.

(30) Merrill, D. R.; Moore, D. B.; Ditto, J.; Sutherland, D. R.; Falmbigl, M.; Winkler, M.; Pernau, H. F.; Johnson, D. C. The Synthesis, Structure, and Electrical Characterization of (SnSe)1.2TiSe2. *European Journal of Inorganic Chemistry* **2015**, *2015* (1), 83–91. https://doi.org/10.1002/ejic.201402814.

(31) Hamann, D. M.; Bardgett, D.; Cordova, D. L. M.; Maynard, L. A.; Hadland, E. C.; Lygo, A. C.; Wood, S. R.; Esters, M.; Johnson, D. C. Sub-Monolayer Accuracy in Determining the Number of Atoms per Unit Area in Ultrathin Films Using X-Ray Fluorescence. *Chemistry of Materials* **2018**, *30*, 6209–6216. https://doi.org/10.1021/acs.chemmater.8b02591.

(32) Wainfan, N.; Parratt, L. G. X-Ray Reflection Studies of the Anneal and Oxidation of Some Thin Solid Films. *Journal of Applied Physics* **1960**, *31* (8), 1331–1337. https://doi.org/10.1063/1.1735837.

(33) Bronsema, K. D.; de Boer, J. L.; Jellinik, F. On the Structure of Molybdenum Diselenide and Disulfide. *Zeitschrift fur Anorganische und Allgemeine Chemie* **1986**, *540*, 15–17.

(34) Sathe, D. J.; Chate, P. A. Hexagonal Nanosized Molybdenum Diselenide Thin Film Deposited at 333 K by Chemical Method. *Solid State Science* **2015**, *48*, 19–22.

(35) Huntley, D. R.; Sienko, M. J.; Hiebl, K. Magnetic Properties of Iron-Intercalated Titanium Diselenide. *Journal of Solid State Chemistry* **1984**, *52* (3), 233–243. https://doi.org/10.1016/0022-4596(84)90006-9.

CHAPTER VII

SYNTHESIS AND CHARACTERIZATION OF SI-TISE$_2$ MULTILAYERS

7.0 Authorship Statement

This chapter was written for this work alone with no intention of publishing it elsewhere. I am the primary author and wrote the following with assistance from my advisor, David C. Johnson.

7.1 Introduction

Research into crystalline layered materials over the last 50 years has proved extremely exciting and fruitful – yielding the development of lithium-ion batteries, high-temperature superconductors, and the discovery of graphene's gapless Fermi surface, just to name a few developments.[1–3] The 2019 Nobel Prize in Chemistry went to Goodenough, Whittingham, and Yoshino for their work with layered materials, such as TiS_2 and $LiCoO_2$, which resulted in the development and commercialization of lithium-ion batteries in 1980. The first known high-temperature superconductor, $Ba_{0.15}CuLa_{1.85}O_4$, is a perovskite-type structure, which is a layered material.[2] More recently, the 2001 discovery of Graphene's gapless Fermi surface spurred pursuit of Lego-type 2D heterostructures where properties can be tuned by varying the type of material used in each layer, the order that the layers are stacked in, the thickness of each constituent layer, or even the substrate that the heterostructure is grown upon.[4–9] These breakthroughs suggest that studying layered materials is well worth the time (and funding dollars), but there are still many remaining unrealized goals.

One longstanding goal is rational materials design – in which one could go into lab and synthesize a composite material (or heterostructure) that exploits the properties of its constituent materials in a predictable manner in order to achieve the desired material's application.[10] Novoselov and colleagues argue that 2D heterostructures could provide a platform for

realizing this goal, by advancing our knowledge of 2D interlayer interactions and our methods to prepare 2D layers and assemble them into device-quality heterostructures, we could enable the creation of heterostructures with properties that are individually tailored to meet the needs of each application.[11]

Heterostructures constructed from amorphous and crystalline materials are not well studied, but existing reports suggest that these materials can effectively exploit properties of both their amorphous and crystalline components. Perhaps the most widely known example of a device that contains and exploits the properties of both crystalline and amorphous materials is a Si-based heterojunction solar cell, which utilizes amorphous, crystalline, and Si:H for the emitter material, active material, and surface passivation, respectively.[12]

Other reports include materials with memristive behavior enabled by an amorphous-crystalline 2D oxide heterostructure, which was achieved via ALD synthesis of few-nm-thick Al_2O_3 layers onto atomically thin single-crystal ZnO nanosheets. In this system, the ZnO provides a 2D host for oxygen vacancies, while the a-Al_2O_3 enables the generation and stabilization of those vacancies.[13] Because of their modulated electronic structure and abundance of catalytically active but chemically stable sites, composite materials or heterostructures constructed from crystalline and amorphous constituents have shown impressive OER and HER performance.[13–15] However, existing synthesis techniques for these materials result in either nanocrystals or crystalline nanorods coated in an amorphous material – to the best of our knowledge there are no reports of a thin film heterostructure containing few-layer 2D blocks of a crystalline materials intergrown with ultrathin amorphous layers.

Lithium can electrochemically alloy with intermetallic elements to form $Li_{4.4}M$ (M = Si, Ge, Sn). While this gives intermetallic anodes for lithium-ion batteries a significantly increased theoretical energy density relative to the

current standard commercial anode, graphite, which forms LiC_6 upon lithiation, it also results in a huge volume change (300 – 400 %) during the lithiation reaction.[16,17] Earlier reports have shown that reducing the thickness of Si increases the stability of the layer towards lithium intercalation cycling.[18–22] Previous work with Si-based multilayers utilized amorphous chromium-silicide layered with amorphous Si, resulting in strongly enhanced structural stability, as demonstrated by the preservation of the heterostructure's layering during the reversible lithiation reaction.[18] This work describes the synthesis of 2D thin film heterostructures created by intergrowing few-layer crystalline $TiSe_2$ blocks with ultra-thin amorphous Si layers.

Ultimately, this experiment may result in the discovery of the optimal relative thicknesses of each constituent layer, ideally increasing the stability of the Si layer and maintaining/increasing the rate of Li intercalation. Li-intercalated $TiSe_2$ is a metal, with empty layers that enable Li cations to diffuse quickly even at room temperature.[23,24] Si is a semiconductor and the movement of both charge and Li cations is much slower than in $TiSe_2$. However, Si forms Li_4Si upon reversible intercalation, resulting in a large Li capacity and a large volume change. As shown in Figure 7.1, by creating a heterostructure where the thicknesses of each constituent layer are precisely controlled enables the diffusion distance of cations into Si to be tuned and the weak interfaces with the $TiSe_2$ platelets provides a mechanism to relieve the stress of intercalation.

These efforts were inspired by previous work done with $CrSi_x$-Si multilayers - the work presented here involves the synthesis of novel multilayers built from alternating ultrathin layers of amorphous Si and crystalline $TiSe_2$. Electron-beam evaporation was used to sequentially deposit ultrathin titanium, selenium, and silicon layers onto a room temperature substrate. A calibration curve is used to relate the number of atoms / $Å^2$ in the film to intensity of the measured x-ray fluorescence (XRF) signal. The

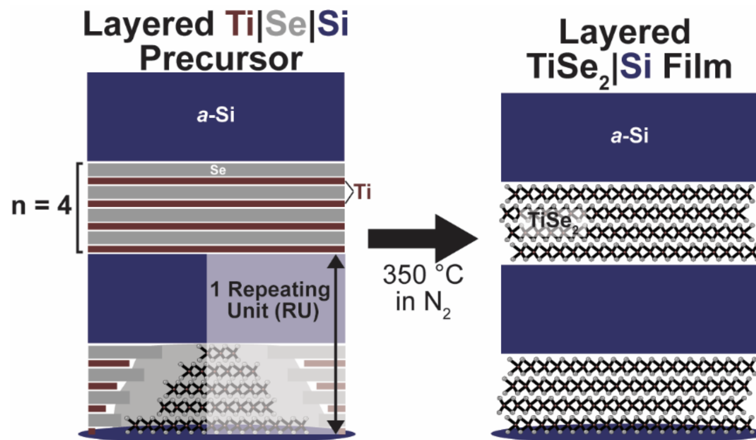

Figure 7.1. Schematic depiction of the reaction of a layered $(Ti|Se)_4|Si$ precursor (*left*) to form a $(TiSe_2)_4|Si$ heterostructure (*right*). Diffraction data suggests some extent of $TiSe_2$ nucleation and growth during the initial film deposition.

atomic areal density is then compared to that of the target compound('s).[25] The goal is to deposit the correct amount of atoms in each layer such that they will all react to form the desired compound or an integer number of layers of the desired layered compound.[26]

Previous work on the Ti|Se system has shown that ultrathin titanium and selenium layers react to form crystalline $TiSe_2$ when heated at moderate temperature in an N_2 atmosphere.[27] When deposited without excess Se, these layers react during deposition to form Ti_2Se. Optimally, when deposited with ~19% excess Se, these layers will interdiffuse and react, resulting in the nucleating and growth of a crystalline $TiSe_2$ during the film's deposition. Annealing at 350 °C improves the crystallinity of these layers, resulting in highly defined large-area (cm^2) films that exhibit Laue oscillations in their x-ray diffraction patterns.[28] Previous work studying the reaction between ultrathin Ti and Si layers suggests that if heated above 550 °C, TiSi nucleates and grows, but below that temperature, the two elements slowly interdiffuse at each interface to form an amorphous alloy.[29] One interesting challenge of this system is the inherent contradiction between the periodic structure of the crystalline component and the complete lack of a periodic structure in the amorphous component.

7.2 Results & Discussion

The following data was collected on three Si|$TiSe_2$ films that were deposited sequentially in a single deposition run. All three samples were deposited promptly after each other without breaking vacuum or manually adjusting the power of the electron beam guns. Since there is not a calibration curve for Si in the XRF method, there is not a direct quantitative measure of the amount of Si in each film. However, since the samples were deposited in a single instance and the deposition controller was able to maintain a steady rate of incident mass on the quartz crystal microbalance used to monitor the deposition throughout the entire deposition, it is a reasonable assumption that the amount of Si in each layer is relatively constant. We will support this assertion with experimental data of our films, drawing on knowledge of what the simulated XRR patterns for different possible structures discussed earlier.

Figure 7.2 shows the XRR and XRD patterns for these three samples – each of which had a different number of $TiSe_2$ layers deposited in each RU, represented by n. As expected, the thickness of the RU increases with the number of $TiSe_2$ layers, as demonstrated by the increased frequency and lower initial angular position of the Bragg reflections as n increases. Typically in a heterostructure, the number of oscillatory minima observed in between each Bragg maxima represents the number of layers present – however XRR modeling of these structures showed that the number of minima would not be expected to be identical. However, this effect is also observed in samples that contain a significant impurity phase, which may also be a possibility here. The Bragg maxima present in the low angle reflectivity pattern can be indexed to $00l$ reflections that match those expected for the superlattice. The total thickness extracted from the position of the Bragg reflections is shown in Table 7.1. Additionally, the number of RU deposited matches the total thickness divided by the estimated RU thickness for the as-deposited films. Interestingly, the higher angle diffraction patterns show two broad Bragg

reflections at approximately the locations of those expected for a 6 Å Fourier component – approximately the size of a single $TiSe_2$ layer! As one increased the amount of $TiSe_2$ in each block, one would expect that the peak width would decrease and the intensity of the higher angle reflections around 15 and 30° would be expected to increase.

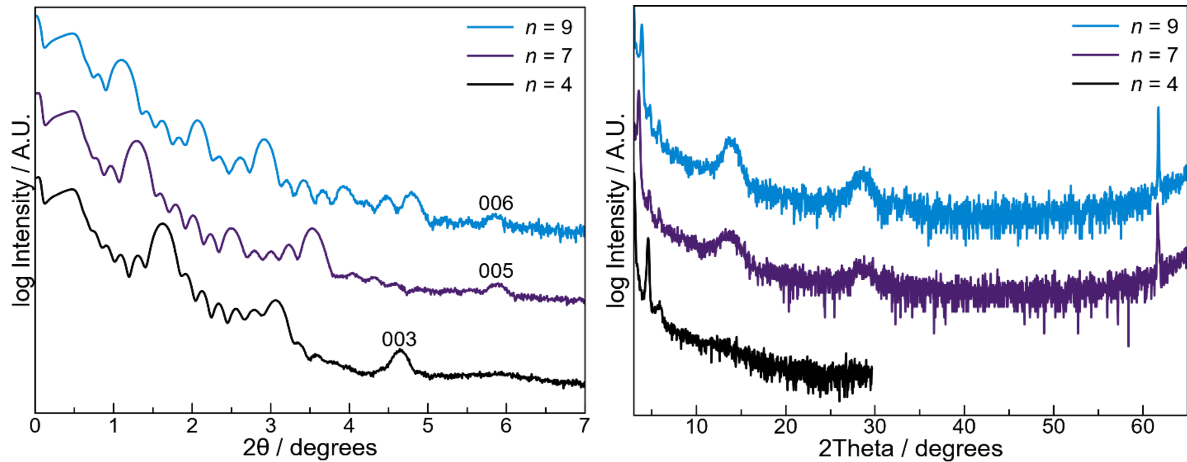

Figure 7.2 XRR (left) and XRD (right) patterns for the n = 4, 7, and 9 $Si(TiSe_2)_n$ heterostructures collected immediately after deposition and prior to annealing.

Table 7.1. Structural data extracted from experimental x-ray diffraction and x-ray reflectivity patterns for as-deposited $(Ti|Se)_nSi$ heterostructures

n	c-axis lattice (nm)	Total thickness (nm)	Thickness / c-axis	RU deposited
4	5.81(8)	41.08(6)	7.1	7
7	7.56(4)	37.0(2)	4.9	5
9	9.16(6)	36.4(1)	4.0	4

Table 7.2 shows the number of atoms / Å^2 of Ti and Se calculated from the XRF data collected on each of the three as-deposited films, along with the targeted number of atoms required to form 4, 7, or 9 $TiSe_2$ layers in each RU. Coincidentally, the target number of Ti atoms is the same for the n = 7 and 9 heterostructures – this is because they have different number of RU's, which result in the same number of targeted $TiSe_2$ layers across the entire film.

Table 7.2. Composition data extracted from experimental x-ray fluorescence intensities for as-deposited $(Ti|Se)_nSi$ heterostructures

n	RU deposited	Avg. Ti atoms / Å^2	Avg. Se atoms / Å^2	Target Ti atoms / Å^2	Target Se atoms / Å^2
4	7	3.16	7.80	2.59	6.48
7	5	3.40	7.63	3.70	7.40
9	4	3.43	6.63	3.70	7.40

Figure 7.3 shows the XRR and XRD patterns for the same three films after they have been annealed at 350 °C for 30 min in an N_2 atmosphere with less than 2.0 ppm O_2 present. The low angle reflectivity data suggests that the layered superlattice structure is preserved after annealing. The presence of Kiessig fringes to a higher angle indicates that the film's surface has become smoother. The Bragg reflections also increase in intensity and decrease in width, indicating that the crystallites of the heterostructure have grown relative to those in the as-deposited film. The higher angle reflections become significantly more intense and well-defined relative to those in each of the as-deposited patterns. However, this may also be consistent with segregation and growth of additional crystalline $TiSe_2$ on the surface of the film as the excess material diffuses through the film during annealing. Table 7.3 shows the *c*-axis lattice parameter and the total film thickness extracted from the Bragg reflections in the reflectivity patterns and the period of the Kiessig fringes, respectively. Dividing the total thickness by the *c*-axis lattice parameter serves as a "check" for determining whether any RU's decomposed during the annealing process – in this case, it can be seen that the n = 4 and 9 films did not lose a significant amount of material during annealing, while the n = 7 film lost a partial RU (corresponding to a ~3 nm loss of total thickness). By plotting the *c*-axis lattice parameter against the number of $TiSe_2$ layers in each RU, we finally obtain an estimate of the average Si layer thicknesses across the three films. As shown in Figure 7.4, the slope of the line corresponds to the average *c*-axis lattice parameter of a single $TiSe_2$ layer (0.675 nm), while the y-intercept corresponds to the average Si layer

thickness (2.98 nm). The correlation coefficient is very close to 1, which supports the earlier assumption made that the Si thickness in each of the three samples is relatively constant.

Representative grazing-incidence in-plane XRD patterns for the as-deposited and annealed films are shown in Figure 7.5. All of the observed reflections can be indexed to a hexagonal unit cell with dimensions matching those expected for $TiSe_2$.[27] There are no other observed reflections, which lead us to conclude that the Si layers remain amorphous during the entire deposition and annealing process.

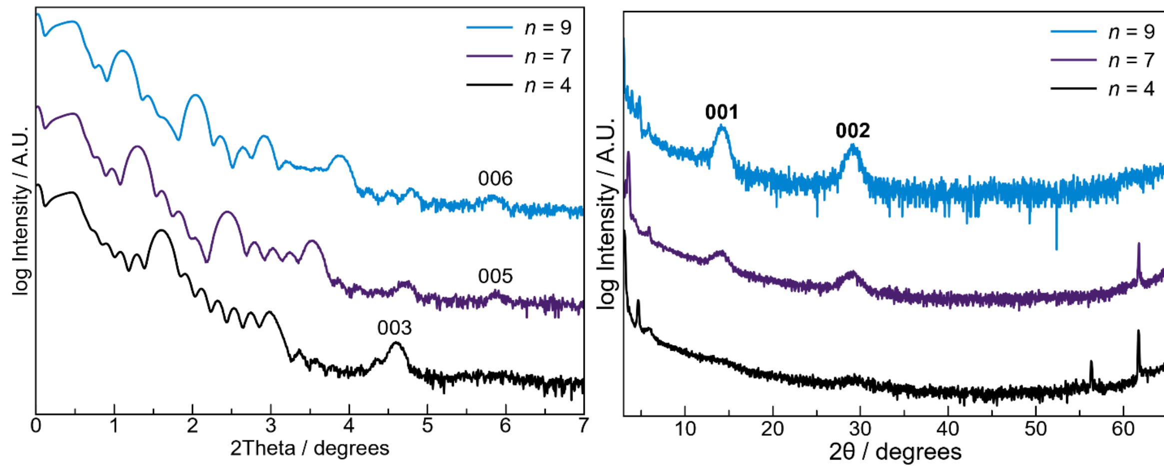

Figure 7.3 XRR (left) and XRD (right) patterns for the n = 4, 7, and 9 $Si(TiSe_2)_n$ heterostructures collected after annealing at 350 °C for 30 m. The Bragg reflections in the low-angle scan can be indexed to 00l reflections corresponding to the superlattice structure, while the high angle reflections can be indexed to the first two 00l reflections expected for $TiSe_2$.

Table 7.3. Structural data extracted from experimental x-ray diffraction and x-ray reflectivity patterns for $(TiSe_2)_nSi$ heterostructures annealed at 350 °C

n	c-axis lattice (nm)	Total thickness (nm)	Thickness / c-axis
4	5.73(5)	40.3(1)	7.0
7	7.57(7)	34.1(1)	4.5
9	9.13(7)	36.6(2)	4.0

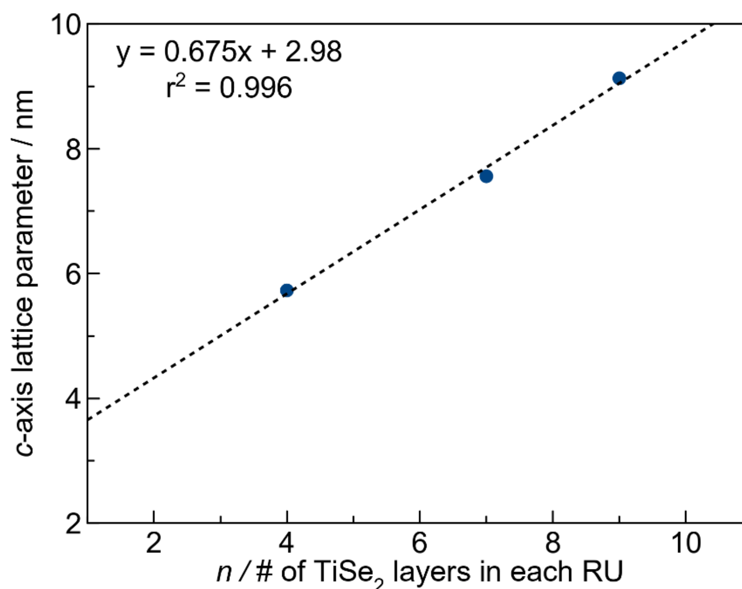

Figure 7.4 Plot of *c*-axis lattice parameter vs *n* for the three films shown in Figure 7.3 The slope of the line represents the average *c*-axis lattice parameter for the individual $TiSe_2$ layers (0.675 nm), while the y-intercept indicates the average thickness of the *a*-Si layers (2.98 nm).

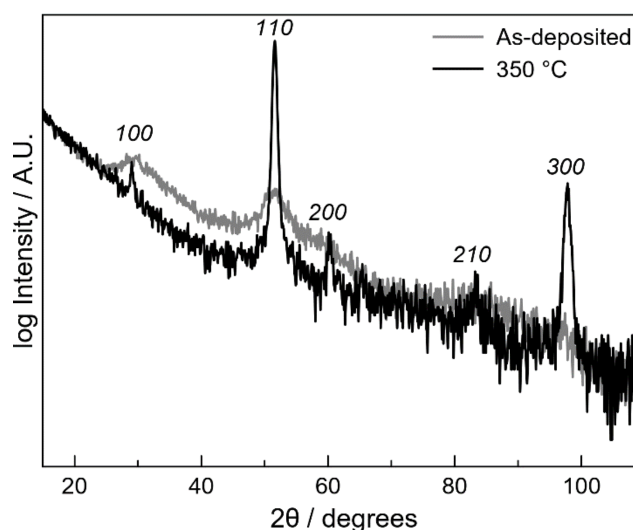

Figure 7.5 Representative grazing-incidence in-plane x-ray diffraction patterns for as-deposited (*grey*) and annealed (*black*) $(TiSe_2)_nSi$ heterostructure. All observed reflections can be indexed to a hexagonal unit cell with dimensions matching those expected for $TiSe_2$.

Hypothetically, it is possible to synthesize a superlattice by layering one amorphous and one crystalline layer to build up a heterostructure. Assuming that one can deposit multiple identical crystalline and amorphous layers (with the same number of atoms in each layer), this would create a film that

contains a single average periodic structure. Figure 7.1 shows a schematic depiction of the reaction to form this theoretical "perfect" amorphous/crystalline heterostructure created from ~3 nm layers of amorphous Si and ~2.5 nm layers of crystalline $TiSe_2$ (4 Se|Ti|Se trilayers). The as-deposited Si|Ti|Se repeating units (RU) are visible on the left, along with small areas of crystallized $TiSe_2$. After annealing, the majority of the Ti|Se layers have been crystallized into $TiSe_2$, as depicted on the right. In this sample, the correct number of atoms have been deposited in each Ti and Se layer such that they react to form an integer number of crystalline $TiSe_2$ layers AND the same number of Si atoms have been deposited in each Ti|Se|Si sequence, hereafter referred to as a repeating unit (RU). However, this structure is an unrealistic depiction of the experimental structure since it is extremely unlikely that one will be able to deposit the exact number of atoms in each of the repeatedly deposited layers.

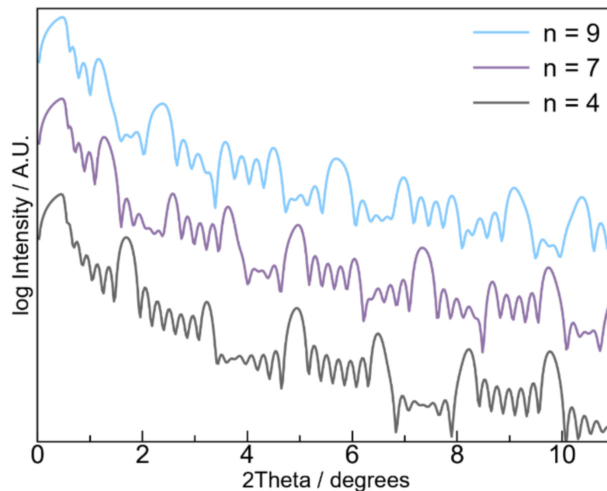

Figure 7.6 Simulated x-ray reflectivity (XRR) patterns for $(TiSe_2)_n$|Si heterostructures with "perfect" nanoarchitecture. The models were generated from either 4, 5, or 7 repeating units (RU) deposited on Si/SiO_2 for the n = 9, 7, and 4 films, respectively. Each RU consists of n layers of crystalline $TiSe_2$ (c = 0.603 nm) plus one a-Si layer (c = 3.0 nm). Generally, the number of repeating units in each film can be obtained by taking $x + 1$, where x is the number of minima between each Bragg reflection. For example, between each Bragg reflection in the n = 4 film, there are 6 minima, indicating that there are 7 total $TiSe_2$|Si repeating units in the film.

The resulting simulated x-ray reflectivity (XRR) pattern for the described “perfect” film (using 7 total Si|$TiSe_2$ repeating units instead of the 2 depicted to ensure a more realistic film thickness) are shown in Figure 7.6. The plot also contains two other simulated XRR patterns created from model heterostructures with 7 and 9 $TiSe_2$ layers in each repeating unit. As one would expect from Bragg’s Law, the heterostructures with thicker repeating units have Bragg reflections that are spaced more closely together and begin at lower angles. For all crystalline heterostructures, the number of unit cells present in the heterostructure can always be obtained by counting the number of minima that are observed between each Bragg reflection. Interestingly, this does not appear to be the case for these heterostructures, as one can count both three and four minima that appear between each Bragg reflection in the n = 9 film (*blue trace, Fig. 7.6.*).

However, unlike a typical thin film superlattice created from two crystalline layers, the average structure of the crystalline / amorphous heterostructures do not necessarily have to be identical in each repeating unit. This is because the crystalline component experiences a strong energetic driving force (i.e. its crystal structure and electron configuration) which effectively forces it to increment its own layer thickness in steps of ~0.6 nm (equal to one three-atom thick trilayer unit cell). The amorphous component lacks this driving force, with no impetus to be any particular thickness beyond maintaining the requisite tetrahedral bonding dictated by Si’s valence shell. This implies that the thickness of each *a*-Si layer can be any value greater than the thickness of a single Si atom, and this thickness will be dictated solely by the amount of Si atoms deposited in each layer.

Figure 7.7 shows a schematic depiction of another possible structure for the n = 4 heterostructure, in which the amount of Si deposited in each *a*-Si layer varies, resulting in slightly different thicknesses for each of the Si layers. In this hypothetical sample, it is assumed that amount of Ti and Se

deposited in each RU is identical. Figure 7.8 shows the simulated XRR patterns from n = 4 heterostructures, where Δ represents the standard deviation of the Si layer thickness. It is easy to see how increasing the variance of the Si layer thickness destroys the intensity of the Bragg reflections – for the film with Si layers that were 3.0 ± 0.3 nm, there is only a single coherent Bragg reflection visible, as all of the subsequent reflections are split or have significantly less intensity. Another interesting side effect of decreasing the homogeneity of the Si layers is the increased amount of the ~0.6 nm Fourier component, as shown by the increased intensity of the reflections in the XRR patterns around 14 ° 2θ.

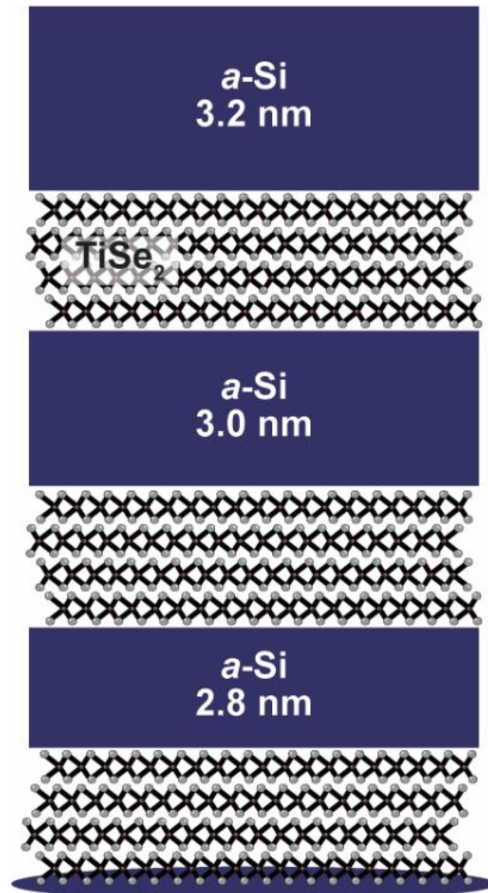

Figure 7.7 Schematic depiction of a n = 4 heterostructure, depicting 3 out of the 7 actual RU's. In this schematic, there was poorer control over the amount of Si atoms deposited in each layer, leading to a distribution of thicknesses around the average a-Si layer thickness of 3.0 nm.

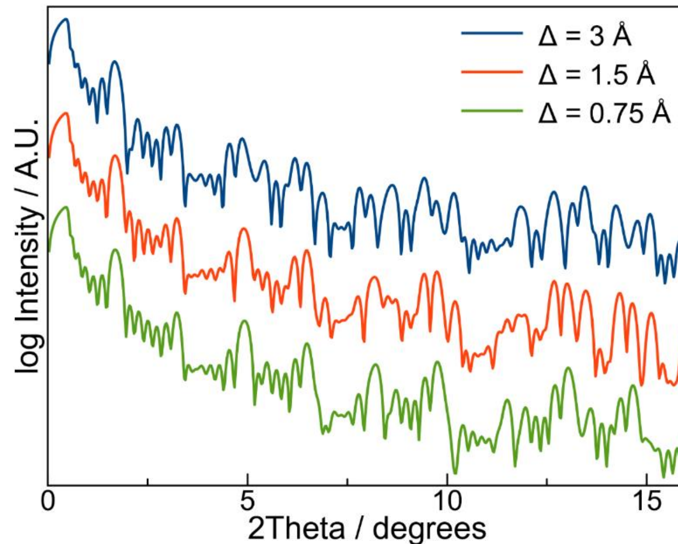

Figure 7.8 Simulated x-ray reflectivity (XRR) patterns for $(TiSe_2)_n$|Si heterostructures with variance in the thickness of each *a*-Si layer. Δ is the standard deviation of the thickness of each of the *a*-Si layers throughout the film, although all models have an average *a*-Si layer thickness of 3.0 nm.

Another possibility that might occur when depositing these heterostructures is that one is unable to deposit the identical quantities of Ti and Se atoms in each RU. As discussed above, the TiSe2 layer thickness should increment in 0.6 nm steps, based on the number of Ti and Se atoms deposited in each layer, which dictates the number of layers of Se|Ti|Se trilayers that nucleate and grow in each RU. However, if one deposits a precursor with enough Ti atoms required to form 4.5 TiSe2 layers, what happens to the "extra" 0.5 layer's worth of atoms during annealing (assuming Ti is limiting reactant)? One possibility is that during heating, they diffuse towards the other "extra" Ti atoms, forming a fifth TiSe2 in every other RU. Another possibility is that they grow 5 layers of TiSe2 over half of the area of the film, creating islands of TiSe2 that stick up into each amorphous Si layer – effectively roughening the TiSe2|Si interface. As a gedanken experiment, Figure 7.9 depicts a schematic for a n = 4 heterostructure that depicts the first scenario described above. The bottom and top RU's depicted is the n = 4 structures, while the middle RU shows the n = 5 structure. Figure 7.10 shows the predicted XRR patterns for several model heterostructures that contain

different numbers of TiSe2 layers in each RU. Similarly to the effects observed by increasing the variance in the thickness of the a-Si layers, the most obvious effect of the increased variance in the crystalline layers is significant dampening of the Bragg reflection intensities.

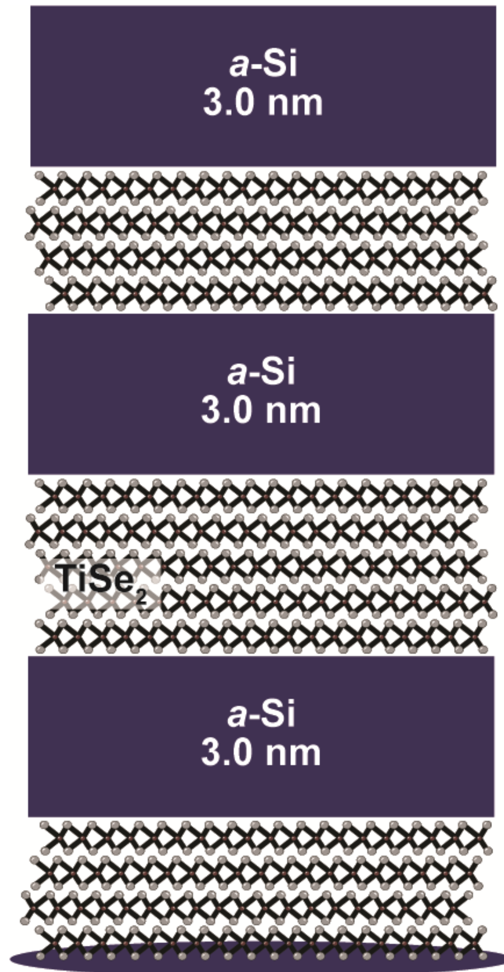

Figure 7.9 Schematic depiction of a n = 4 heterostructure, depicting 3 out of the 7 actual RU's. In this schematic, there was poorer control over the amount of Ti atoms deposited in each layer, leading to a distribution in the number of layers of crystalline $TiSe_2$ that form in each RU. The bottom and top RU's depicted show the n = 4 structures, while the middle RU shows the n = 5 structure.

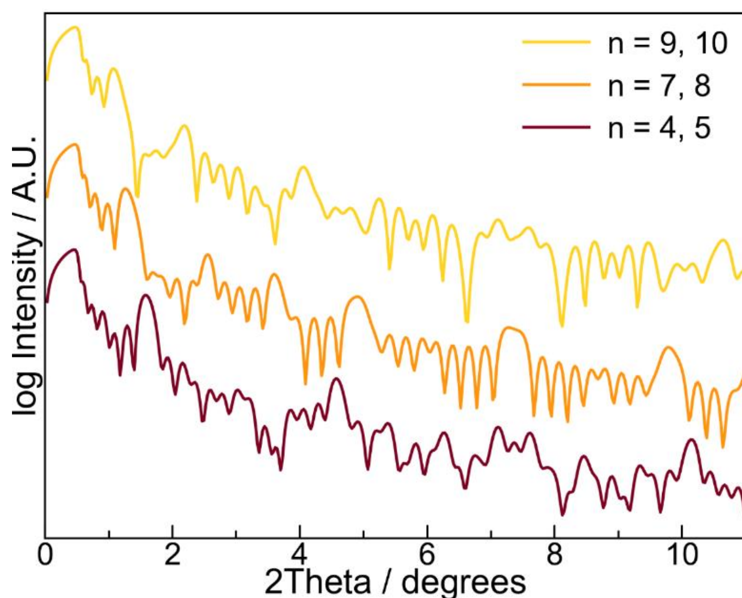

Figure 7.10 Simulated x-ray reflectivity (XRR) patterns for $(TiSe_2)_n$|Si heterostructures with variance in the number of $TiSe_2$ layers crystallized in each RU.

7.3 Conclusion

Based on the relatively close matches between the simulated and experimental reflectivity patterns, we can conclude that the superlattice structure proposed in this work are stable up to 350 °C. However, more work is needed to understand the differences between the *gedanken* models and simulated reflectivity patterns and the actual film structure and experimental patterns. Additionally, lots of obvious electrochemical work can be completed, such as characterizing the electrical transport properties of these films. An initial lithium intercalation experiment under constant current showed that the heterostructure was stable towards reversible lithium intercalation, but more efforts are required to understand how the lithium intercalation capacity of this structure scales with cycle number.

However, the initial synthetic results are encouraging and show that these novel heterostructures can be synthesized with n = 4, 7, and 9 – although the optimal thicknesses of each constituent layer for electrochemical applications is not yet understood and remains a future goal.

7.4 Bridge

This chapter described the synthesis and characterization of several a-Si$(TiSe_2)_n$ heterostructures which have not been reported in the literature to the best of this author's knowledge. The next chapter presents the synthesis of a family of six isomer heterostructures with a unit cell consisting of different layering of four $TiSe_2$ layers and four PbSe layers.

REFERENCES CITED

(1) Press release: The Nobel Prize in Chemistry 2019 https://www.nobelprize.org/prizes/chemistry/2019/press-release/.

(2) Maeno, Y.; Hashimoto, H.; Yoshida, K.; Nishizaki, S.; Fujita, T.; Bednorz, J. G.; Lichtenberg, F. Superconductivity in a Layered Perovskite without Copper. *Nature* **1994**, *372* (6506), 532–534. https://doi.org/10.1038/372532a0.

(3) Novoselov, K. S.; Geim, A. K.; Morozov, S. V; Jiang, D.; Zhang, Y.; Dubonos, S. V.; Grigorieva, I. V; Firsov, A. A. Electric Field Effect in Atomically Thin Carbon Films. *Science (80-.).* **2004**, *5* (1), 1–12. https://doi.org/10.1126/science.aab1343.

(4) Hamann, D. M.; Bardgett, D.; Bauers, S. R.; Kasel, T. W.; Mroz, A. M.; Hendon, C. H.; Medlin, D. L.; Johnson, D. C. Influence of Nanoarchitecture on Charge Donation and the Electrical-Transport Properties in [(SnSe)1+d][TiSe2]q Heterostructures. *Chem. Mater.* **2020**, *32* (13), 5802–5813. https://doi.org/10.1021/acs.chemmater.0c01691.

(5) Falmbigl, M.; Fiedler, A.; Atkins, R. E.; Fischer, S. F.; Johnson, D. C. Suppressing a Charge Density Wave by Changing Dimensionality in the Ferecrystalline Compounds ([SnSe] 1.15) 1 (VSe 2) n with n = 1, 2, 3, 4. *Nano Lett.* **2015**, *15*, 943–948. https://doi.org/10.1021/nl503708j.

(6) Bauers, S. R.; Merrill, D. R.; Moore, D. B.; Johnson, D. C. Carrier Dilution in $TiSe_2$ Based Intergrowth Compounds for Enhanced Thermoelectric Performance. *J. Mater. Chem. C* **2015**, *3*, 10451–10458. https://doi.org/10.1039/C5TC01570G.

(7) Dong, H. M.; Tao, Z. H.; Li, L. L.; Huang, F.; Xu, W.; Peeters, F. M. Substrate Dependent Terahertz Response of Monolayer WS2. *Appl. Phys. Lett.* **2020**, *116* (20). https://doi.org/10.1063/5.0006617.

(8) Noori, K.; Cheng, N. L. Q.; Xuan, F.; Quek, S. Y. Dielectric Screening by 2D Substrates. *2D Mater.* **2019**, *6* (3), 0–9. https://doi.org/10.1088/2053-1583/ab1e06.

(9) Kim, Y.; Lee, S. M.; Park, C. S.; Lee, S. I.; Lee, M. Y. Substrate Dependence on the Optical Properties of Al2O3 Films Grown by Atomic Layer Deposition. *Appl. Phys. Lett.* **1997**, *71* (25), 3604–3606. https://doi.org/10.1063/1.120454.

(10) Jansen, M. A Concept for Synthesis Planning in Solid-State Chemistry. *Angew. Chemie - Int. Ed.* **2002**, *41* (20), 3746–3766. https://doi.org/10.1002/1521-3773(20021018)41:20<3746::AID-ANIE3746>3.0.CO;2-2.

(11) Novoselov, K. S.; Mishchenko, A.; Carvalho, A.; Castro Neto, A. H. 2D Materials and van Der Waals Heterostructures. *Science (80-.).* **2016**, *353* (6298). https://doi.org/10.1126/science.aac9439.

(12) De Wolf, S.; Descoeudres, A.; Holman, Z. C.; Ballif, C. High-Efficiency Silicon Heterojunction Solar Cells: A Review. *Green* **2012**, *2* (1), 7–24. https://doi.org/10.1515/green-2011-0018.

(13) Yin, X.; Wang, Y.; Chang, T. hsuan; Zhang, P.; Li, J.; Xue, P.; Long, Y.; Shohet, J. L.; Voyles, P. M.; Ma, Z.; Wang, X. Memristive Behavior Enabled by Amorphous–Crystalline 2D Oxide Heterostructure. *Adv. Mater.* **2020**, *32* (22), 1–7. https://doi.org/10.1002/adma.202000801.

(14) Li, Y.; Ma, W.; Yang, H.; Tian, Q.; Xu, Q.; Han, B. CO2-Assisted Synthesis of a Crystalline/Amorphous NiFe-MOF Heterostructure for High-Efficiency Electrocatalytic Water Oxidation. *Chem. Commun.* **2022**, No. Scheme 1, 6833–6836. https://doi.org/10.1039/d2cc01163h.

(15) Qin, M.; Li, Y.; Zhang, H.; Humayun, M.; Xu, X.; Fu, Y.; Kadirov, M. K.; Wang, C. Crystalline/Amorphous Heterostructure Offering Highly Efficient Overall Water Splitting and Urea Electrolysis. *J. Alloys Compd.* **2022**, *921*, 166071. https://doi.org/10.1016/j.jallcom.2022.166071.

(16) Ozanam, F.; Rosso, M. Silicon as Anode Material for Li-Ion Batteries. *Mater. Sci. Eng. B Solid-State Mater. Adv. Technol.* **2016**, *213*, 2–11. https://doi.org/10.1016/j.mseb.2016.04.016.

(17) Franco Gonzalez, A.; Yang, N. H.; Liu, R. S. Silicon Anode Design for Lithium-Ion Batteries: Progress and Perspectives. *J. Phys. Chem. C* **2017**, *121* (50), 27775–27787. https://doi.org/10.1021/acs.jpcc.7b07793.

(18) Fister, T. T.; Esbenshade, J.; Chen, X.; Long, B. R.; Shi, B.; Schlepütz, C. M.; Gewirth, A. A.; Bedzyk, M. J.; Fenter, P. Lithium Intercalation Behavior in Multilayer Silicon Electrodes. *Adv. Energy Mater.* **2014**, *4* (7), 1–6. https://doi.org/10.1002/aenm.201301494.

(19) Klankowski, S. A.; Rojeski, R. A.; Cruden, B. A.; Liu, J.; Wu, J.; Li, J. A High-Performance Lithium-Ion Battery Anode Based on the Core-Shell Heterostructure of Silicon-Coated Vertically Aligned Carbon Nanofibers. *J. Mater. Chem. A* **2013**, *1* (4), 1055–1064. https://doi.org/10.1039/c2ta00057a.

(20) Song, T.; Cheng, H.; Town, K.; Park, H.; Black, R. W.; Lee, S.; Park, W. Il; Huang, Y.; Rogers, J. A.; Nazar, L. F.; Paik, U. Electrochemical Properties of Si-Ge Heterostructures as an Anode Material for Lithium Ion Batteries. *Adv. Funct. Mater.* **2014**, *24* (10), 1458–1464. https://doi.org/10.1002/adfm.201302122.

(21) Zhang, X.; Wang, D.; Qiu, X.; Ma, Y.; Kong, D.; Müllen, K.; Li, X.; Zhi, L. Stable High-Capacity and High-Rate Silicon-Based Lithium Battery Anodes upon Two-Dimensional Covalent Encapsulation. *Nat. Commun.* **2020**, *11* (1), 1–9. https://doi.org/10.1038/s41467-020-17686-4.

(22) Ohara, S.; Suzuki, J.; Sekine, K.; Takamura, T. A Thin Film Silicon Anode for Li-Ion Batteries Having a Very Large Specific Capacity and Long Cycle Life. *J. Power Sources* **2004**, *136* (2 SPEC. ISS.), 303–306. https://doi.org/10.1016/j.jpowsour.2004.03.014.

(23) Zhao, C.; Wang, D.; Lian, R.; Kan, D.; Dou, Y.; Wang, C.; Chen, G.; Wei, Y. Revealing the Distinct Electrochemical Properties of TiSe2 Monolayer and Bulk Counterpart in Li-Ion Batteries by First-Principles Calculations. *Appl. Surf. Sci.* **2021**, *540* (P1), 148314. https://doi.org/10.1016/j.apsusc.2020.148314.

(24) Li, P.; Zheng, X.; Yu, H.; Zhao, G.; Shu, J.; Xu, X.; Sun, W.; Dou, S. X. Electrochemical Potassium/Lithium-Ion Intercalation into TiSe2: Kinetics and Mechanism. *Energy Storage Mater.* **2019**, *16* (September 2018), 512–518. https://doi.org/10.1016/j.ensm.2018.09.014.

(25) Hamann, D. M.; Bardgett, D.; Cordova, D. L. M.; Maynard, L. A.; Hadland, E. C.; Lygo, A. C.; Wood, S. R.; Esters, M.; Johnson, D. C. Sub-Monolayer Accuracy in Determining the Number of Atoms per Unit Area in Ultrathin Films Using X-Ray Fluorescence. *Chem. Mater.* **2018**, *30*, 6209–6216. https://doi.org/10.1021/acs.chemmater.8b02591.

(26) Noh, M.; Thiel, J.; Johnson, D. C. Synthesis of Crystalline Superlattices by Controlled Crystallization of Modulated Reactants. *Science (80-.).* **1995**, *270* (5239), 1181–1184. https://doi.org/10.1126/science.270.5239.1181.

(27) Miller, A. M.; Hamann, D. M.; Hadland, E. C.; Johnson, D. C. Investigating the Formation of MoSe2and TiSe2 Films from Artificially Layered Precursors. *Inorg. Chem.* **2020**, *59* (17), 12536–12544. https://doi.org/10.1021/acs.inorgchem.0c01626.

(28) Miller, A. M.; Lemon, M.; Choffel, M. A.; Rich, S. R.; Harvel, F.; Johnson, D. C. Extracting Information from X-Ray Diffraction Patterns Containing Laue Oscillations. *Zeitschrift für Naturforsch. B* **2022**, *77* ((4-5)b), 313–322. https://doi.org/10.1515/znb-2022-0020.

(29) Novet, T.; Mcconnell, J. M.; Johnson, D. C. Low-Temperature Reaction of Buried Metal-Silicon Interfaces: The Evolution of Interfacial Structure. *Chem. Mater.* **1992**, *4* (2), 473–478.

CHAPTER VIII

SYNTHESIS AND CHARACTERIZATION OF $[(PbSe)_{1+\delta}]_4[TiSe_2]_4$ ISOMERS

8.0 Authorship Statement

Chapter VI was published in Inorganic Chemistry in 2020. Danielle Hamann, and David C. Johnson are the main contributors to the text. I performed data analysis and performed modeling. J. Ditto and Daniel B. Moore contributed experimental data.

8.1 Introduction

Molecular chemists have developed synthetic methods to prepare kinetically stable compounds with designed structures. This permits them to prepare multiple compounds containing the same number and type of elements connected in various arrangements. [1–3] The local arrangement of atoms in a compound determines the physical, electronic, and biological properties it exhibits.[4–11] For example, the five different structural isomers of hexane (hexane, 2-methylpentane, 3-methylpentane, 2,2-dimethylbutane, and 2,3-dimethylbutane) all have different melting and boiling points as a consequence of their varying local arrangements.[12–15] The ability to predict metastable–stable compounds via simple bonding rules (i.e., each carbon must have four bonds, each oxygen two bonds, and each hydrogen one bond) combined with an understanding of how to control the kinetics by manipulating reaction conditions (solvents, protecting groups, catalysts) enables molecular chemists to propose and test structure–property relationships toward optimizing desired properties. [2,16–18]

It is more challenging to prepare structural isomers of inorganic compounds with extended structures, known as polymorphs.[19] Some well-known examples of polymorphs are vaterite, calcite, and aragonite. These compounds are different structural forms of calcium carbonate which exhibit different properties and free energies of formation.[20–23] Typically, polymorphs are prepared by changing the reaction conditions (temperature, pressure, composition of the reacting system,

etc.) so that the desired product is the most thermodynamically stable product in that reacting system. The structure of the product cannot be predicted from simple bonding rules or reaction conditions but is instead determined experimentally. For compounds only stable at high temperature or pressure, quenching the system to room temperature and pressure often traps the now metastable polymorph. The lack of knowledge of how to control reaction kinetics to obtain targeted inorganic, extended, structures severely limits the number of polymorphs that can be prepared.[24–27] The holy grail in the synthesis of compounds with extended structures is a design and mechanism-based approach to the synthesis of metastable compounds with targeted structure.[28]

Presented here is the synthesis and characterization of six different structural isomers of the compound $[(PbSe)_{1+\delta}]_4[TiSe_2]_4$, which have the same composition and unit cell sizes, but the sequence of PbSe bilayers and $TiSe_2$ trilayers vary between isomers. The different isomers were prepared from precursors with sequences of an elemental layer designed to mimic the nanoarchitecture of the targeted isomer. While the amount of Pb and Ti in the deposited precursors was insufficient to make the desired number of repeating units, the artificial layering pattern of deposited layers still directed the self-assembly of the desired isomers. X-ray diffraction and HAADF-STEM data support the formation of the desired isomer nanoarchitectures with a decreased number of unit cells and additional impurity phases present on the top and bottom of the sample. As-deposited structural characterization indicated that $TiSe_2$ and PbSe crystallized during the deposition and were organized in stacking sequences consistent with the targeted isomer. Unexpectedly, Ti_2Se also crystallized during deposition at the interface with the substrate. The HAADF-STEM images suggest that the sample crystallizes from the bottom to the top, with the concentration gradients created at the growth front driving diffusion of Pb and Ti to the growing isomers. The measured electrical transport properties systematically vary as a consequence of changes in the nanoarchitecture, with lower resistivity and higher carrier concentrations found in compounds with a higher density of PbSe|$TiSe_2$

interfaces within the isomer's unit cell. This is likely the result of charge transfer from PbSe to $TiSe_2$ being dependent on interfacial interactions. This work indicates that the self-assembly process begins during the deposition itself, driven by the heat of formation of the constituent layers. The nanoarchitecture of the precursor is sufficient to direct the formation of the targeted structure isomers, even if the composition of the precursor deviates significantly from that of the product, suggesting that the compounds are significant local energy minima in the free energy landscape.

8.2 Materials & Methods

The $[(PbSe)_{1+\delta}]_4[TiSe_2]_4$ heterostructure isomer precursors were prepared from physical vapor deposition of elemental layers onto silicon and fused silica substrates. Elemental Pb and Ti were evaporated from electron beam guns operating at 6 kV. Elemental Se was deposited from a Knudsen effusion cell. All elements were purchased from Alfa Aesar and were greater than 99.95% purity. Shutters above each evaporating source were programmed to sequentially open for the period of time required to deposit the appropriate thickness of each element to form either bilayers of PbSe or trilayers of $TiSe_2$. The thickness of the elemental layers deposited was monitored by quartz crystal microbalances. PbSe bilayers were deposited with a Pb|Se shutter sequence and $TiSe_2$ trilayers with a Ti|Se shutter sequence. The sequence of Pb|Se and Ti|Se layers was controlled such that the nanoarchitecture of the precursor resembled the structure of the targeted isomer.[29] The sequence of Pb|Se and Ti|Se layers for each isomer was repeated 11 times to build a film that was approximately 550 Å thick. The elemental precursors were annealed at 350 °C for 30 min in an N_2 atmosphere to promote self-assembly into a crystalline heterostructure.[30–35]

Amount of material per unit area was determined for each heterostructure using wavelength dispersed X-ray fluorescence (XRF) data. The data were analyzed using a previously published method in which the raw intensity of each sample is determined by integrating under the signal curve and subtracting the background signal.[36] Calibration curves for each element were used to relate the

measured signal to the number of atoms per unit area in each film.

Locked-coupled θ–2θ and grazing-incidence in-plane X-ray diffraction (XRD) data were both collected using laboratory Cu–Kα radiation with parallel beam optics on Bruker D8 Discover and Rigaku Smartlab instrumentation, respectively. Grazing-incidence scans were carried out with an incident angle of 1.0° and the detector 4.0° above the sample plane. Ab-initio X-ray reflectivity (XRR) patterns from the idealized targeted structures were generated with the Bede REFS modeling software assuming bulk densities.

High-angle annular dark-field scanning transmission electron microscopy (HAADF-STEM) images were collected using a probe aberration corrected FEI Titan 80–300 (300 kV, 120 mm camera length, Cs < 1 μm). Energy dispersive X-ray spectroscopy (EDS) data were acquired with a 2.3 ms dwell time per pixel and summed over several drift-corrected frames. Cross-sectional lamellae for STEM imaging were made using an FEI Helios 600 Nanolab dual-beam FIB.[37]

Electrical measurements were carried out on a house-built closed-cycle He cryostat using a 1.5 T magnet. Van der Pauw resistivities and Hall resistivities both were collected on cross-pattern films through Cu wires and In contacts. Reported values were calculated using thicknesses from reflectivity measurements of the annealed films. Seebeck coefficients were also measured using a house-built system. One edge of the film was cooled slightly, and both S and ΔT were measured between two type-T thermocouples.

8.3 Results & Discussion

XRR and XRD data indicate that the as-deposited precursors have a more complex structure than elemental layers in a particular pattern. Figure 8.1 contains a representative XRR pattern of an as-deposited $[(PbSe)_{1+\delta}]_4(TiSe_2)_4$ isomer precursor (the 2**1**1**2**1**1** isomer is shown). The pattern contains Kiessig fringes consistent with the 11 layers deposited, the first several Bragg reflections from the element layering, and Laue oscillations between the Bragg maxima. A film composed of 11 repeat units of a $[(PbSe)_{1+\delta}]_4(TiSe_2)_4$ isomer is expected to

have a total film thickness of ~535 Å, slightly lower than the observed film thickness for the as-deposited isomers which range from 544 to 557 Å. The thickness of the elemental layering determined from the position of the first-order Bragg reflection is slightly higher than the targeted value expected for a $[(PbSe)_{1+\delta}]_4(TiSe_2)_4$ repeat unit, 48.68 Å, in all of the samples (ranging from 49.19 to 50.81 Å). However, the observed Laue oscillations indicate that there are only 10 layers present in the repeating elemental modulation, requiring that one of the as-deposited layers differs from what was intended. Representative XRD patterns, Figures 8.1 and B1, for as-deposited $[(PbSe)_{1+\delta}]_4(TiSe_2)_4$ isomer precursors indicate that PbSe and $TiSe_2$ have nucleated during deposition and that there are already coherent blocks of the $[(PbSe)_{1+\delta}]_4(TiSe_2)_4$ isomer heterostructure before annealing. Surprisingly, there are also reflections consistent with the formation of a crystallographically aligned Ti_2Se impurity phase which has a c-axis lattice parameter of 15.6 Å. XRR, XRD, and HAADF-STEM images (discussed in subsequent paragraphs) all show that annealing the precursors at 350 °C for 30 min in an N_2 atmosphere provides enough energy for the self-assembly of the elemental precursors into the desired $[(PbSe)_{1+\delta}]_4(TiSe_2)_4$ isomer structure, although only 8–9 layers of the intended isomers form and the presence of the Ti_2Se impurity phase remains.

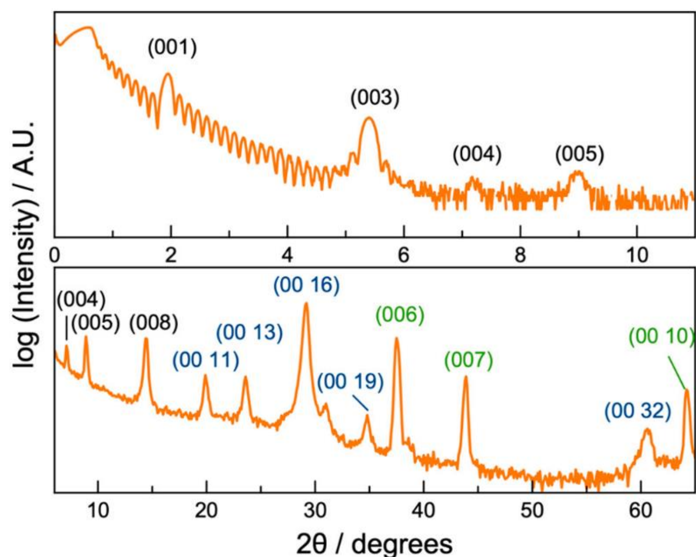

Figure 8.1. Representative as-deposited XRR and XRD for a 2**11**2**1**1 isomer

demonstrating behavior observed in all of the $[(PbSe)_{1+\delta}]_4(TiSe_2)_4$ isomer heterostructures. The 00l reflections, corresponding to the artificial layering, the crystallized $[(PbSe)_{1+\delta}]_4(TiSe_2)_4$ isomer heterostructure, and the impurity Ti_2Se phase, are indexed in black, blue, and green, respectively. Additional as-deposited XRR patterns can be found in the Supporting Information, Figure B1.

The annealed heterostructures were analyzed by XRF to quantify the amount of material present in each film, and the results are summarized in Table 8.1. While the targeted isomer structures all had the same number of total atoms/$Å^2$ for each element (see Table 8.2), there is a large variation in the actual amount of material measured in the films after deposition, reflecting the challenges of reproducibly depositing monolayer amounts of various elements (~10^{-7} grams/cm^2). We use quartz crystal microbalances (QCMs) to monitor the amount of material incident upon the substrate, which have about a 5% measurement error for the nanogram sensitivities required. However, the QCMs need to be located adjacent to the sample substrates, making this an indirect measurement that is sensitive to deviations in the flux within the plume of vaporized atoms. The spatial distribution of fluxes within the plume typically remains constant within a set of samples, resulting in a constant proportionality between the amount of material incident on the QCM to the amount incident on the substrate. Unfortunately, the spatial distribution of fluxes within the plume changes with time as the source size decreases and with a number of experimental parameters (beam raster area and raster rates, impurities on source surfaces, etc.). Pb is the limiting element in all of the films, and there is not enough Pb, Ti, or Se in any of the films to form 11 unit cells of any of the targeted isomers (see Table 8.2). Insufficient Pb, Ti, and Se in the precursors explains why fewer unit cells formed compared to what was targeted. To form, the intended isomers required diffusion within and between deposited layers to provide Pb to the nucleation sites. This results in less than 11 repeating units forming. Surprisingly, the deposited nanoarchitecture and initial layer growth in

the precursors was sufficient to direct the formation of the targeted isomers despite atoms diffusing between deposited layers and fewer than the targeted number of isomer layers forming.

Table 8.1. Total Atoms/Å^2 in Each of the Annealed $[(PbSe)_{1+\delta}]_4(TiSe_2)_4$ Isomer Films[a]

Isomer	**Atoms/Å^2**		
	Pb	**Ti**	**Se**
2**2**1**1**1**1**	3.61(1)	3.65(1)	9.82(2)
2**1**1**2**1**1**	3.64(1)	3.74(1)	10.28(2)
3**3**1**1**	3.71(1)	3.61(1)	9.78(2)
3**2**1**2**	3.65(1)	3.59(1)	10.02(2)
2**3**2**1**	3.60(1)	3.87(1)	10.33(2)
4**4**	3.38(1)	4.02(1)	10.47(2)

[a]The error in the conversion factor between XRF intensity and number of atoms per unit area is 2-3%.

Table 8.2. Calculated Number of Atoms/Å^2 for Each Element in the $[(PbSe)_{1+\delta}]_4(TiSe_2)_4$ Isomers for Different Film Thicknesses

No. of $[(PbSe)_{1+\delta}]_4(TiSe_2)_4$ repeating units	**Atoms/Å^2**		
	Pb	**Ti**	**Se**
8	3.39	2.91	9.19
9	3.82	3.28	10.34
10	4.24	3.64	11.49
11	4.37	4.00	12.64

XRR patterns of the annealed films provide insight into the complex structure of the products that formed during annealing. Information contained in the XRR

patterns is detailed in Figure 8.2, using the 3**2**1**2** isomer pattern as a representative example. The 3**2**1**2** isomer has a layer sequence of aaa**bb**a**bb**, where the thicknesses of the PbSe component in the unit cell (a) has a normal typeface and the $TiSe_2$ (b) is bold in the 3**2**1**2** abbreviation. Bragg maxima from the self-assembled product are observed in the XRR pattern, and the position of these maxima yield a c-axis lattice parameter of 48.60(1) Å, which is consistent with the expected unit cell of a $[(PbSe)_{1+\delta}]_4(TiSe_2)_4$ isomer composed of four layers of $TiSe_2$ and four layers of PbSe. The XRR pattern also has smaller maxima, which come from two different effects. Near the critical angle, these smaller maxima are called Kiessig fringes, and they are a consequence of the X-ray interference reflecting from the top and the bottom of the film. At higher angles, the smaller maxima between the Bragg reflections, called Laue oscillations, result from incomplete destructive interference from the finite number of unit cells in the film. The number of Laue oscillations between consecutive Bragg reflections depend on the number of complete unit cells contributing to the interference effect. The top left panel of Figure 8.2 shows that a film thickness of 484.4 Å results in Kiessig fringes that match those observed for the 3**2**1**2** isomer. A film that is composed of nine unit cells contributing to the total thickness does not match the experimental low angle data between the critical angle and the first Bragg reflection. The top right panel of Figure 8.2 compares simulations of the Laue fringes for a heterostructure with the targeted 11 unit cells and a heterostructure with 9 unit cells contributing to the interference effect with the experimental data for the 3**2**1**2** isomer. Simulations for a film composed of 9 repeating unit cells matches the observed experimental data, while simulations for 11 repeating unit cells do not.

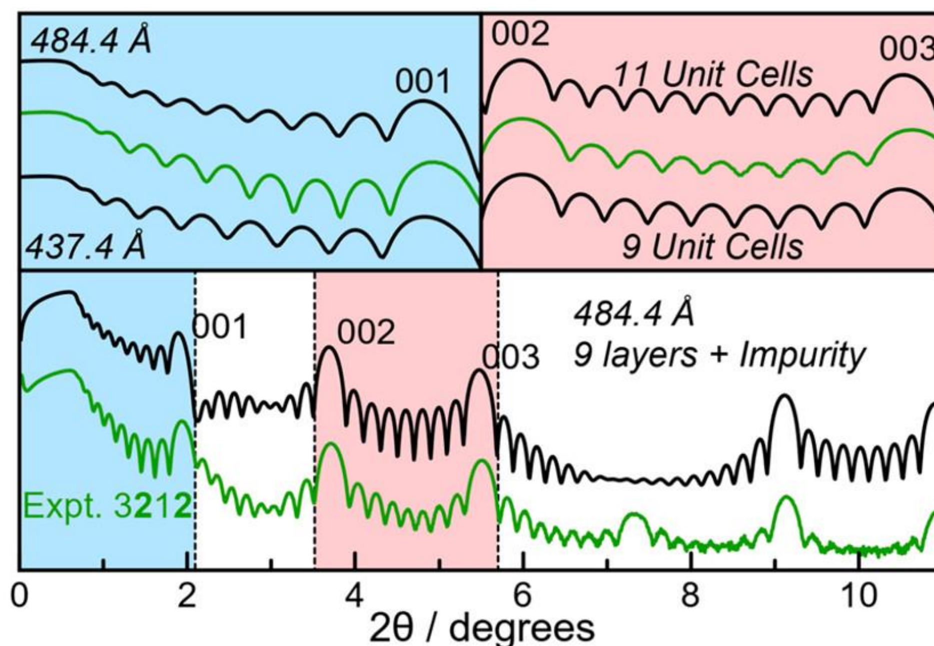

Figure 8.2. Experimental and simulated XRR patterns for the 3**2**1**2** structural isomer. The upper left panel focuses on the Kiessig fringes, indicating that the total film thickness is 491.4 Å. The upper right panel emphasizes the Laue oscillations, showing that 9 unit cells are present, not the 11 expected from the deposition sequence. The bottom panel compares the simulated and experimental patterns based on the complete model described in the text.

Since Kiessig fringes are extremely sensitive to the quality of interfaces (roughness) while the Laue oscillations are sensitive to the number of unit cells interfering in the sample and the extent of their disorder, the experimental low angle patterns reflect the changing contributions of both diffraction effects throughout the presented angular range. The discrepancy between the total film thickness and the number of repeating units indicates that there is extra material present in the films. This extra material can exist either above and/or below the nine unit cells of the 3**2**1**2** isomer. The relative thickness of the top and bottom impurity layers influences the rate of decay of the intensity above the critical angle. The roughness of the layer on top of the 3**2**1**2** block determines the angular dependence of the relative contributions of the Kiessig and Laue interference effects. The bottom panel in Figure 8.2 shows a simulated pattern containing nine unit cells of the 3**2**1**2** isomer with 47 Å of extra thickness divided between a 35 Å layer underneath and a 12 Å layer with a roughness of 5 Å on

top. The positions of the maxima line are consistent between the simulated and experimental patterns. The magnitude of the Laue oscillations is larger in the simulated pattern because the 3**2**1**2** block was modeled as an ideal film. The intensity of the Laue oscillations can be suppressed and the intensity of the fourth-order Bragg reflection can be increased by adding roughness to one or more of the unit cells. The 35 Å layer underneath the 3**2**1**2** isomer block is likely the Ti_2Se impurity phase observed in the as-deposited XRD and is likely responsible for the as-deposited XRR patterns containing Laue fringes for only 10 layers.

Similar models were created for all of the targeted $[(PbSe)_{1+\delta}]_4(TiSe_2)_4$ heterostructure isomers. The stacking sequence of the 8-layer blocks within the repeating unit were varied and we assumed atomically sharp interfaces between the constituent structures. Also assuming a constant electron density within each constituent results in a square-wave function for the electron density as shown in Figure 8.3. This simple model assumed the c-lattice parameters for the heterostructures were equal and the interfaces between the eight constituent unit cells occurred at intervals of 1/8th of a unit cell. Within the unit cell, 2**2**1**1**1**1** and 2**1**1**2**1**1** compounds have five interfaces, the 3**3**1**1**, 3**2**1**2**, and 2**3**2**1**compounds have three interfaces, and the 4**4** profile has one interface. The Fourier transform of the electron density of each $[(PbSe)_{1+\delta}]_4(TiSe_2)_4$ heterostructure isomer is different due to the distinctive placement of the eight constituent layers within the unit cell. Consequently, the pattern of intensities of the $00l$ reflections in the specular diffraction will be unique for each structural isomer.

Experimental XRR patterns for each of the $[(PbSe)_{1+\delta}]_4(TiSe_2)_4$ isomers are shown in Figure 8.4 along with simulated patterns using both the electron density profiles determined from Figure 8.3 and the parameters gathered using the method described for the 3**2**1**2** isomer. Bragg reflections observed in the XRR patterns occur at nominally the same 2θ angle for all of the $[(PbSe)_{1+\delta}]_4(TiSe_2)_4$ isomers, indicating that the repeating unit is similar. Relative patterns of the

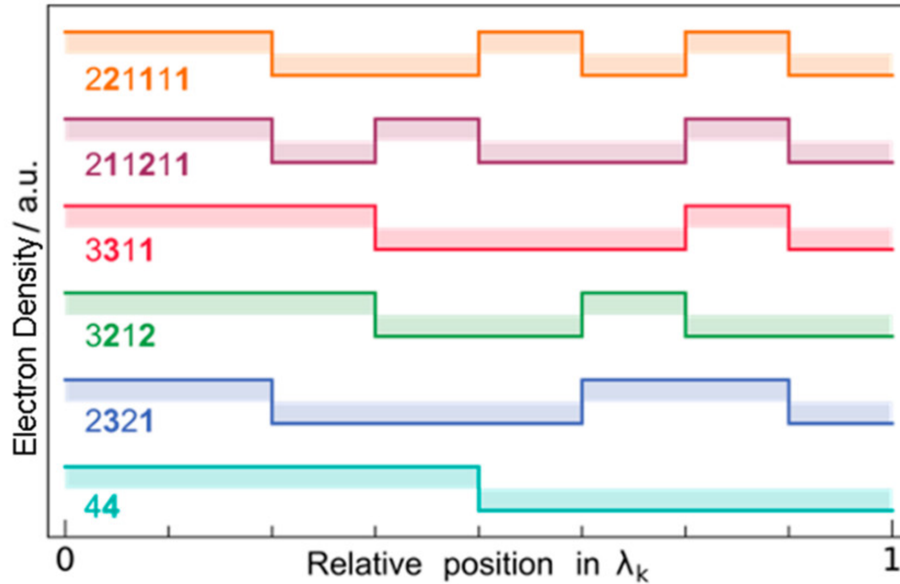

Figure 8.3. Schematic representation of the variation of electron density through a unit cell for each of the $[(PbSe)_{1+\delta}]_4(TiSe_2)_4$ isomers.

Bragg reflection intensities correlate well between the models and experimental data. Small intensities experimentally observed when the models predict zero intensity result from approximations made for the models shown in Figure 8.3. For the model it was assumed the interfaces were located at exactly 1/8th intervals of the unit cell, but experimentally the Se–Ti–Se trilayer and a Pb–Se bilayer thicknesses are not equal. Another assumption used in the model is that the layers are perfectly smooth, when in reality some roughness is observed. The positions of the Laue oscillations in the models were adjusted by varying the number of unit cells of each isomer to match the experimental data. Positions of Kiessig fringes in the model were manipulated to match the experimental data by varying the total sample thickness via the excess material on the top or bottom of the film. STEM images of each isomer were used as a guide to approximate the amount of extra material present. The patterns are somewhat insensitive to the exact ratio of thickness of the top/bottom impurity layers, so the decay of the intensity from the critical angle to the first Bragg maxima was adjusted by varying the exact thicknesses of the top and bottom impurity layers. Roughness of the layer on top of the isomer block was adjusted to match the observed

change from Kiessig fringes to Laue oscillations, which differs based on impurity thicknesses and number of unit cells. Parameters from the models for each isomer are summarized in Table 8.3. All of the $[(PbSe)_{1+\delta}]_4(TiSe_2)_4$ isomers have fewer unit cells in the isomer blocks than the targeted number. The total thicknesses of the isomers are all less than what was measured for the as-deposited samples as a result of Se loss during annealing in an open system. It was determined, via XRR simulations and HAADF-STEM, that all $[(PbSe)_{1+\delta}]_4(TiSe_2)_4$ isomers have impurity layers above and below the block of repeating units.

Table 8.3. Parameters Extracted from the XRR Patterns as Described in the Text[a]

sample	**# unit cells in isomer block**	**total thickness (Å)**	**thickness of isomer block**	**bottom impurity thickness (Å) (±5)**	**top impurity thickness (Å) (±5)**	**bottom impurity roughness (Å)**
2**2**1**1**1**1**	9	514	438	40	36	1.0
2**1**1**2**1**1**	8	498	389	48	34	5.0
3**3**1**1**	8	482	389	60	40	5.0
3**2**1**2**	9	484	437	35	12	5.0
2**3**2**1**	9	481	437	14	30	8.0
4**4**	9	491	437	27	27	5.0

[a]Not shown in the table are parameters that do not vary the model significantly. These parameters (the bottom impurity roughness (5 Å) and the roughness of the Si substrate (5 Å)) were held constant in all of the models.

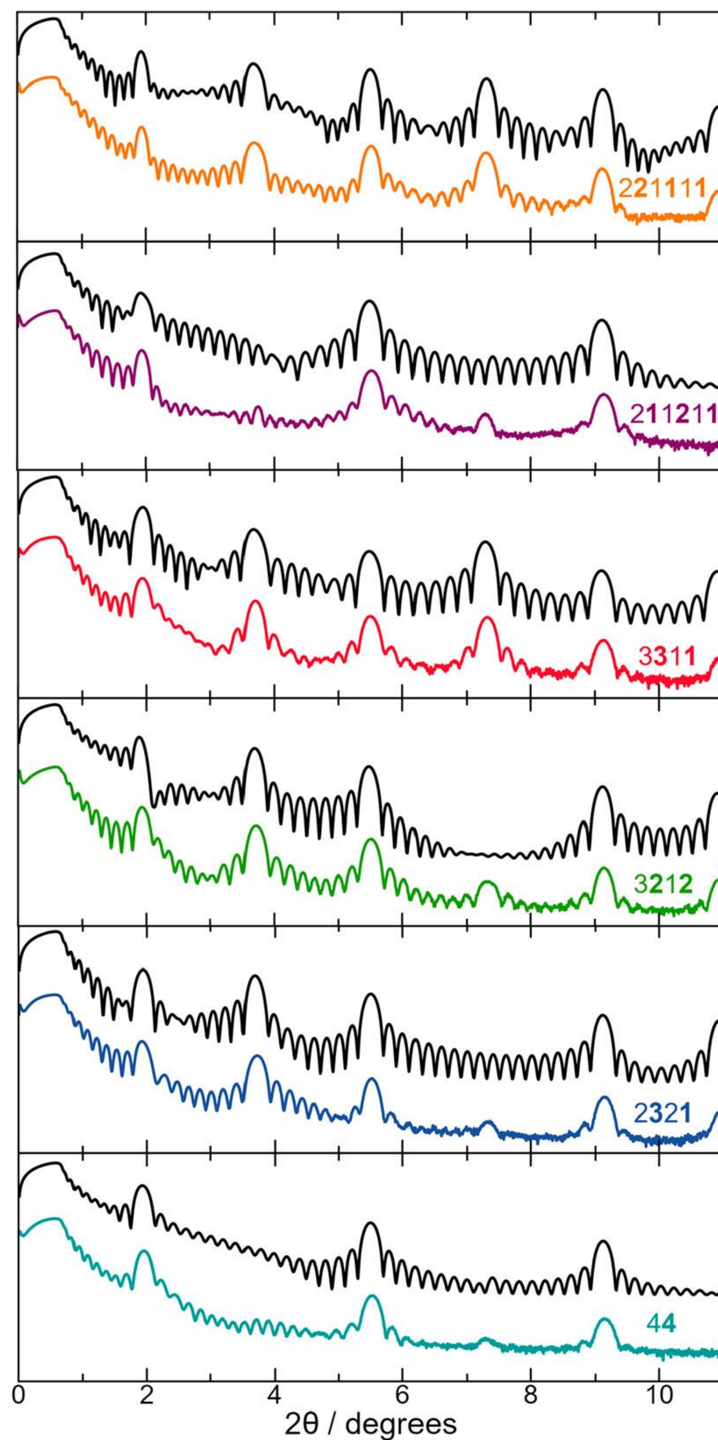

Figure 8.4. X-ray reflectivity patterns (*in color*) shown against simulated patterns created using models of the targeted isomers (i*n black*) described in Figure 8.3.

Specular and in-plane XRD patterns of the crystallized isomer heterostructures are shown in Figure 8.5. Lattice parameters were determined

for each of the $[(PbSe)_{1+\delta}]_4(TiSe_2)_4$ isomers and are summarized in Table 8.4. All but three of the maxima in the specular X-ray diffraction patterns can be indexed as $00l$ reflections corresponding to the nanoarchitecture of the targeted isomers. The c-axis lattice parameters, determined from the position of the $00l$ reflections, are similar for all of the isomers and are consistent with a repeating unit composed of four layers of PbSe and four layers of $TiSe_2$, as was observed in the as-deposited data. The three reflections not belonging to the isomer's unit cell can be indexed as $00l$ reflections from Ti_2Se. The lattice parameter obtained, 14.52(5) Å, matches that expected for Ti_2Se.[38] This is consistent with the excess Ti observed in the number of atoms/Å^2 determined from the XRF data for the annealed compounds and the impurity phase observed in the representative as-deposited diffraction. All of the reflections in the in-plane diffraction scan can be indexed as $hk0$ reflections from either a hexagonal or square unit cell, whose lattice parameters correspond to either $TiSe_2$ or PbSe, respectively (Table 8.4). Relative intensities of the reflections from each constituent are constant between isomers, indicating that there are similar relative amounts of PbSe and $TiSe_2$ in each heterostructure. Both the PbSe and $TiSe_2$ in-plane lattice parameters remain constant as the isomer nanoarchitecture is varied, indicating that there is no structural change as a function of layer sequence. There are no observed reflections corresponding to the Ti_2Se impurity phase in the in-plane diffraction. The (110) and (310) reflections observed in the square unit cell indicate that PbSe does not have the bulk rock salt structure, because these reflections are forbidden in the $Fm\bar{3}m$ rock-salt space group. This indicates that the PbSe structure has distorted with either Pb or Se no longer on special position sites, which is not unexpected for these ultrathin layers. A similar distortion was observed in $(PbSe)_m(MoSe_2)_n$ compounds, where atoms moved ~20 pm from ideal rock salt structure positions.[39] The structures of the PbSe-$TiSe_2$ isomers studied in this paper were not refined due to the large number of crystallographic parameters that would be required for these more complicated unit cells and the

limited number of reflections observed.

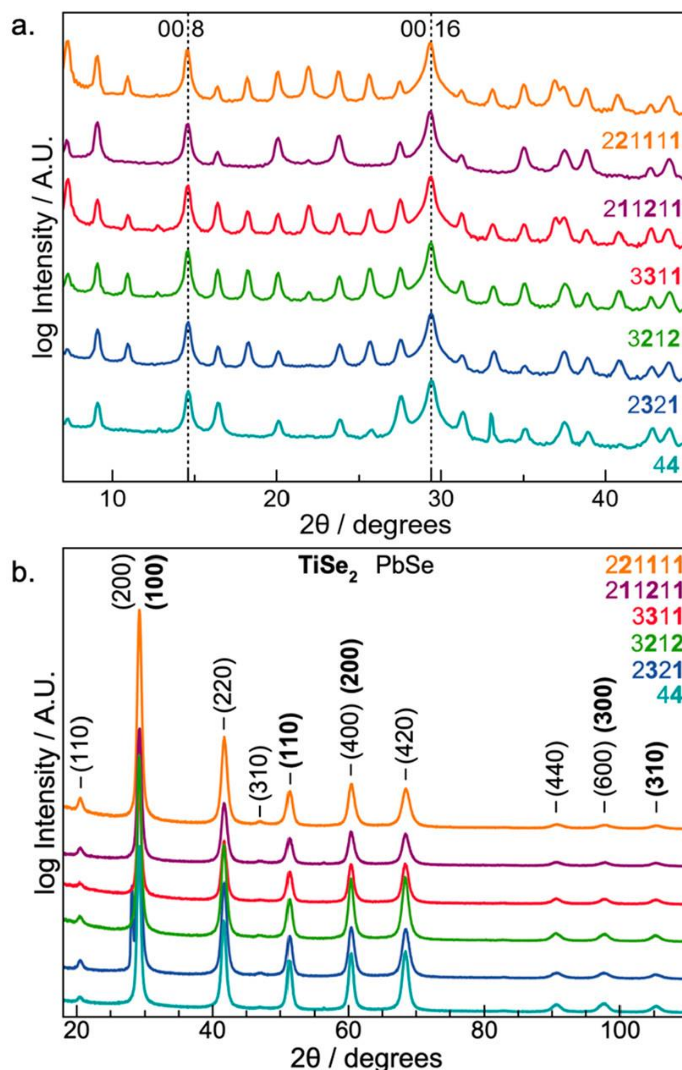

Figure 8.5. Specular (a.) and in-plane (b.) XRD patterns of the $[(PbSe)_{1+\delta}]_4(TiSe_2)_4$ structural isomers. The indices of the observed reflections are shown above each reflection in the in-plane pattern and representative indices are indicated in the specular pattern.

HAADF-STEM images, collected for each of the $[(PbSe)_{1+\delta}]_4(TiSe_2)_4$ isomers, provide local information about defects and overall sample structure. Figure 8.6 shows a full film image of the 44 $[(PbSe)_{1+\delta}]_4(TiSe_2)_4$ isomer. Rock-salt layers containing Pb show up as bright regions due to the higher average atomic number relative to $TiSe_2$ layers, which are darker. STEM-EDS data for the 2321

Table 8.4. Lattice Parameters for the $[(PbSe)_{1+\delta}]_4(TiSe_2)_4$ Structural Isomers Determined from the Annealed Diffraction Patterns

sample	*c*-axis lattice parameter (Å)	PbSe *a*-axis lattice parameter (Å)	$TiSe_2$ *a*-axis lattice parameter (Å)	impurity phase
2**2**1**1**1**1**	48.66(1)	6.121(1)	3.560(1)	14.41(4)
2**1**1**2**1**1**	48.64(1)	6.132(1)	3.566(1)	14.54(1)
3**3**1**1**	48.62(1)	6.131(1)	3.561(1)	14.53(3)
3**2**1**2**	48.60(1)	6.134(1)	3.563(1)	14.55(2)
2**3**2**1**	48.56(1)	6.128(2)	3.561(2)	14.54(1)
4**4**	48.52(2)	6.132(1)	3.560(1)	14.55(1)

isomer, shown in Appendix B, confirms this assignment. Distinct bright atomic columns of atoms can be seen in regions where the electron beam aligns with a crystallite's zone axis. Different layers and regions within the same layer have different orientations, indicating both rotational disorder and some stacking defects. The majority of the film consists of nine unit cells of the isomer, which is consistent with the XRR data discussed previously. At the top and bottom of the film there is material that is not consistent with the repeating blocks of the isomer. In the layer closest to the substrate there are regions where Ti_2Se grains can be found in addition to smaller regions of $TiSe_2$ and $(PbSe)_1(TiSe_2)_1$. These observations are consistent with the analysis of the XRF, XRR, and XRD data discussed previously.

Figure 8.7 shows HAADF-STEM images of all $[(PbSe)_{1+\delta}]_4(TiSe_2)_4$ structural isomers. These images demonstrate that the films consist of different sequences of PbSe and $TiSe_2$ layers with sharp planar interfaces between them. The different layering schemes for each of the six isomers can be clearly identified and are further supported by the EDS profile shown in Figure B3. There is extensive rotational disorder occurring between the different constituent layers in each block, evident by zone axis orientations appearing in only some of the

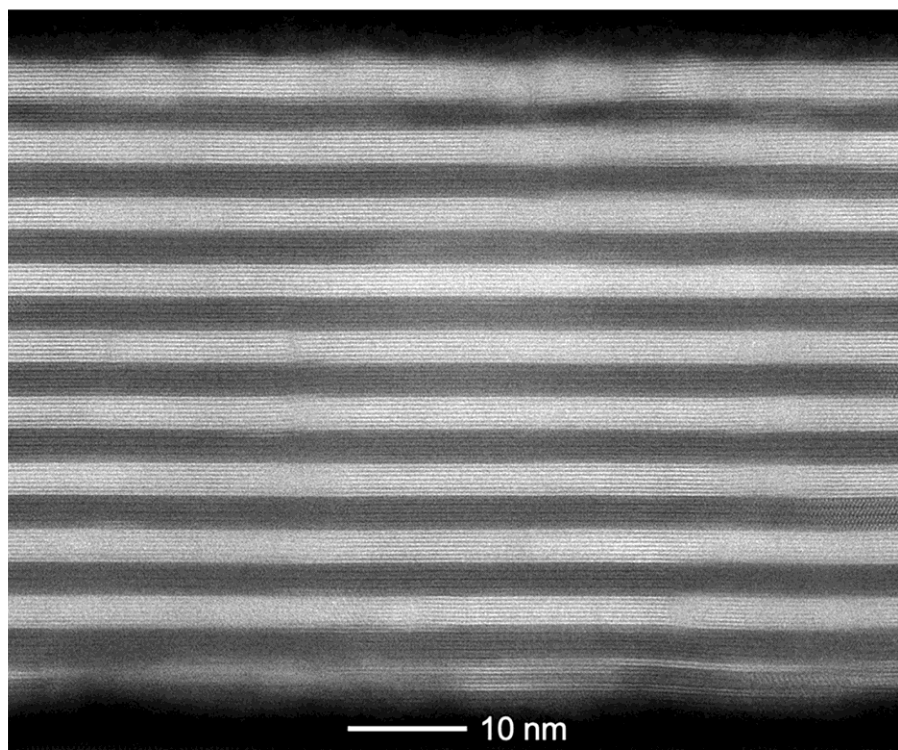

Figure 8.6. HAADF-STEM image of the 44 $[(PbSe)_{1+\delta}]_4(TiSe_2)_4$ structural isomer showing the entire film from substrate to surface.

layers. As observed in the specular XRD patterns, the thickness of the repeating layer schemes are the same for all six isomers. The majority of the samples are composed of a central block of the targeted isomer and the number of unit cells in the blocks agrees with that determined from the Laue fringes in the XRR patterns. While there are stacking defects in all of the isomer domains, it is quite surprising that the imperfect 11 repeating sequences deposited in the precursors contain sufficient information to direct the self-assembly of 8–9 unit cells into the targeted isomer stacking sequences.

The structural data presented above provide insight into the isomers' growth from the deposited precursor. It suggests that Ti_2Se forms at the substrate surface when Se is deposited onto the initial Ti layer. We tested this in a separate experiment, showing that Ti_2Se forms when depositing Se on Ti in a Ti–Se precursor, even when the Ti to Se ratio is 1:2. Forming Ti_2Se as the initial layer results in an excess Se concentration since the amount of Ti and Se deposited

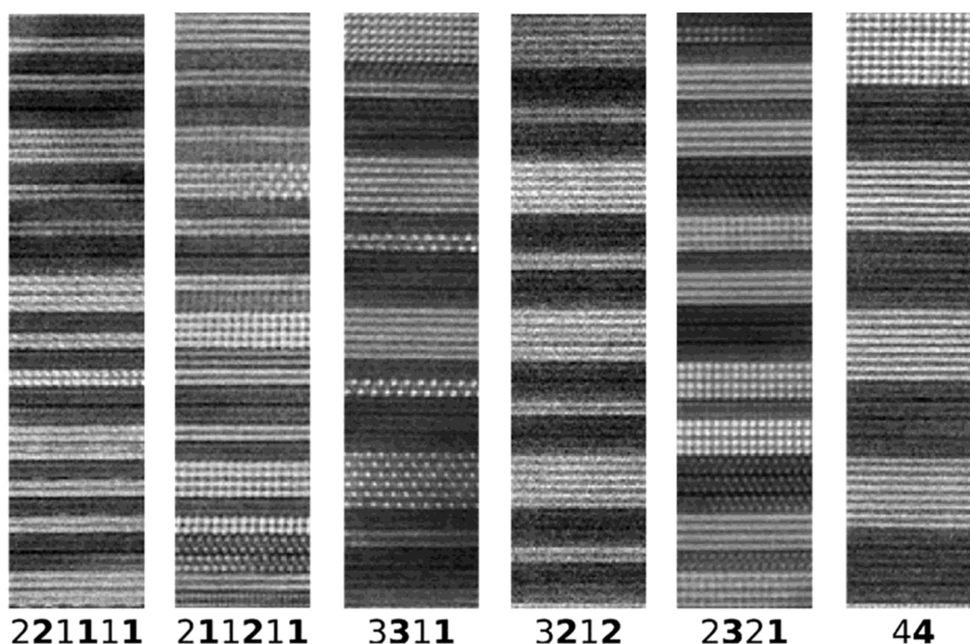

Figure 8.7. HAADF-STEM images of each isomer heterostructure highlighting the formation of the targeted nanoarchitecture, sharp interfaces between constituents, and rotational misregistration between layers.

was intended to form a $TiSe_2$ layer in the isomer samples. When Pb intended to form PbSe in the first repeat unit is deposited, it reacts with the excess Se from the first Ti|Se layer to form a PbSe layer. When the next layer of Ti is deposited (intended for the second repeat unit), it is deposited on a Se rich layer which allows the formation of $TiSe_2$ to occur. The $TiSe_2$ grows out horizontally from its nucleation site. Since the repeating sequence is low on Ti, the formation of the growth stops when the Ti at the growth front has been depleted, leaving some amorphous material in the layer. Similar behavior occurs for the next Pb|Se layer, but the $TiSe_2$ basal plane surface results in the formation of crystallographically aligned PbSe at the interface. Since the repeating sequence is also low on Pb, the formation of the growth stops when the Pb at the growth front has been depleted, leaving some amorphous material in the layer. This process continues, on average, for about four unit cells, which corresponds to a crystallite size of ~200 Å perpendicular to the substrate. Subsequent deposited layers are more disordered.

A schematic illustrating the as-deposited structure and how it evolves is shown in Figure 8.8. To simplify the image a $[(PbSe)_{1+\delta}]_1(TiSe_2)_1$ repeating unit structure was used in place of the more complex $[(PbSe)_{1+\delta}]_4(TiSe_2)_4$ isomer structure. When the temperature is increased during annealing, the concentration gradients drive diffusion of Pb and Ti to the growth front. In addition to growth parallel to the substrate, additional layers crystallize perpendicular to the substrate and facilitate further growth of the heterostructure. Around the crystallized structure is a region that is metal poor/Se rich as a result of the nucleation site stealing metal from the surrounding area to form the structure. The requirement to steal material from the surrounding area is the result of the wrong atoms/$Å^2$ being deposited per layer in the precursor. Since all of the samples were most deficient in Pb, it is the species that will be depleted first, leaving a Ti|Se top layer which reacts with oxygen during annealing to form an amorphous oxide. We anneal our films in an N_2 environment with <1 ppm of O_2, which is insufficient to prevent formation of a surface oxide during annealing. The thickness of the isomer layer therefore ends up being 2 or 3 unit cells less than the 11 that were targeted, consistent with the number of Laue oscillations seen in the XRR scans and the HAADF-STEM images. The ability to prepare the metastable isomers without being precisely on composition is an advantage in the quest to find new material phases, since it is challenging to precisely control the absolute amount of an element at the monolayer level. These metastable compounds have a broad enough energy minimum in the free energy landscape that the system still forms the targeted isomer even if the composition deviates from the target, as long as the nanoarchitecture resembles the targeted compound.

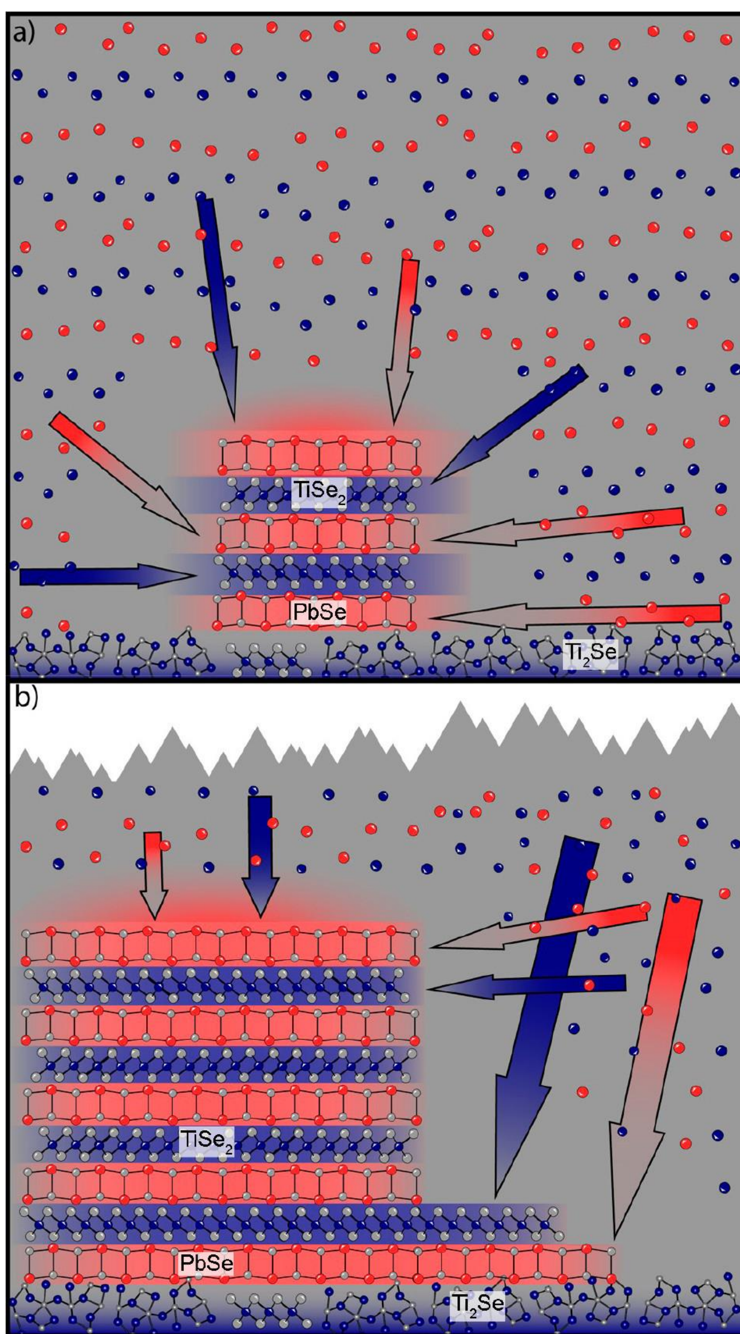

Figure 8.8. Atomistic picture demonstrating the initial crystallization in the isomers (a) and a snapshot showing the movement of atoms and further crystal growth upon annealing (b). The arrows demonstrate the concentration gradient of the metals and point to where the metals are diffusing. On deposition a layer of Ti_2Se forms and persists even after annealing. Pb atoms are shown in red, Ti atoms in blue, and Se atoms in gray.

Temperature-dependent resistivity graphs for the six $[(PbSe)_{1+\delta}]_4(TiSe_2)_4$ isomers are shown in Figure 8.9. The isomer with the smallest number of

interfaces per unit cell, the 4**4** isomer, has the highest resistivity, while the 2**2**1**1**1**1** isomer, which has the most interfaces, has the lowest resistivity at all temperatures. The magnitude of the resistivity and the slow decrease in resistivity as temperature is decreased from room temperature suggest that these samples are metallic. At low temperatures, however, all the samples have an increase in resistivity similar to those observed in the previously reported $[(PbSe)_{1+\delta}]_m(TiSe_2)_n$ compounds.[31,33,34,40] The similarity of the normalized resistivity versus temperature plots, Figure 8.9b, suggests that the same phenomena are occurring in all of the isomers. Minima in the resistivity for the isomers occur between 50 and 100 K, with the 44 isomer, having the highest temperature minima, and the 2**2**1**1**1**1** isomer, the lowest.

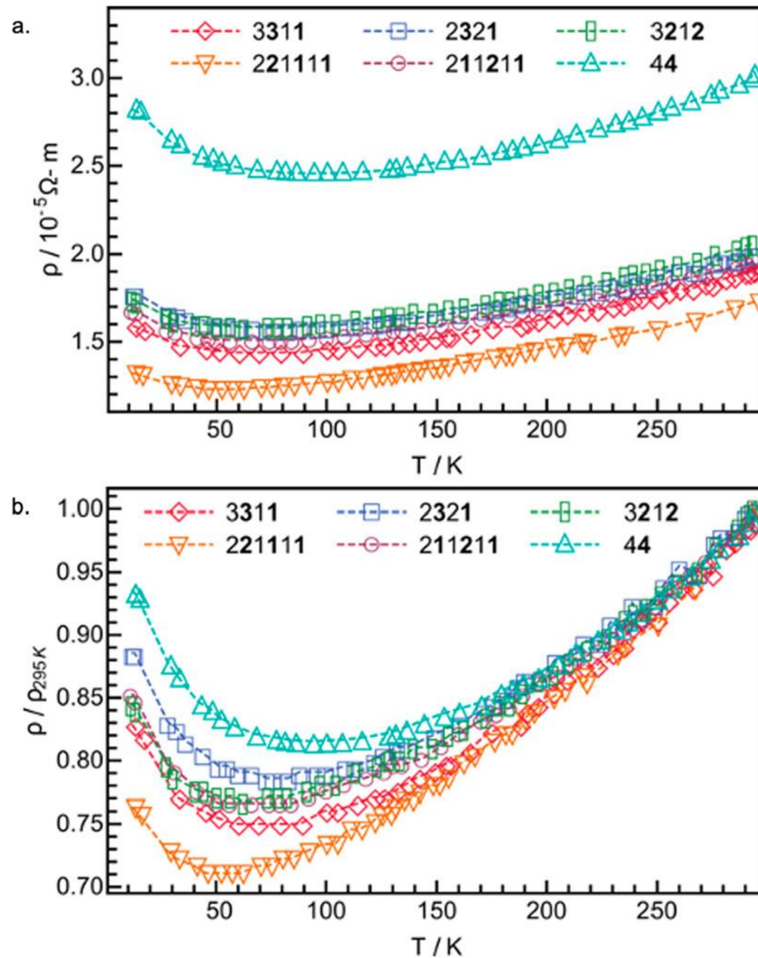

Figure 8.9. Temperature-dependent resistivity of six $[(PbSe)_{1+\delta}]_4(TiSe_2)_4$ isomer heterostructures, with both measured (a) and normalized (b) values.

Hall coefficients were measured as a function of temperature to provide more information about the increase in resistivity at low temperatures. The Hall coefficients were negative for all isomers over the entire temperature regime, indicating that electrons dominate the electrical transport. Carrier concentrations were calculated from the Hall data, assuming a single band model, and are plotted as a function of temperature in Figure 8.10a. The carrier concentrations slowly decrease as temperature is decreased in all of the samples. The decrease in carrier concentration has a very weak temperature dependence, suggesting that an activated process is not the source of the increasing carrier concentration with increasing temperature. Isomers with the same number of interfaces in the unit cell have similar carrier concentrations, with the 44 structure having the lowest and the 2**2**1**1**1**1** and the 2**1**1**2**1**1** isomers the highest. Carrier mobility, calculated from the resistivity and Hall data, is shown in Figure 8.10b. The mobility values and their temperature dependences are similar for all of the isomers, with mobility increasing with decreasing temperature before becoming constant below 50 K. At low temperatures, higher mobilities correlate with increasing buried interface density. This is somewhat surprising as more interfacial scattering from the layers, which should be relatively temperature independent, unlike other mechanisms (e.g., electron–electron or electron–phonon scattering), would be expected for structures with high interface density. The minima in the resistivity appears to be a consequence of the interplay between the decreasing carrier concentration and increasing mobility as temperature is decreased. As the temperature decreases the mobility increases at a faster rate than the carrier concentration decreases, resulting in observed resistivity decrease. At low temperatures, the decreasing carrier concentration and plateau of the mobility result in the resistivity increase.

The room-temperature Seebeck coefficient was collected for each isomer compound, and the values are shown in Figure 8.11. Several $[(PbSe)_{1+\delta}]_4(TiSe_2)_4$ isomers were measured to explore how much the room temperature transport measurements varied between samples. There was a 5% variation of the Seebeck

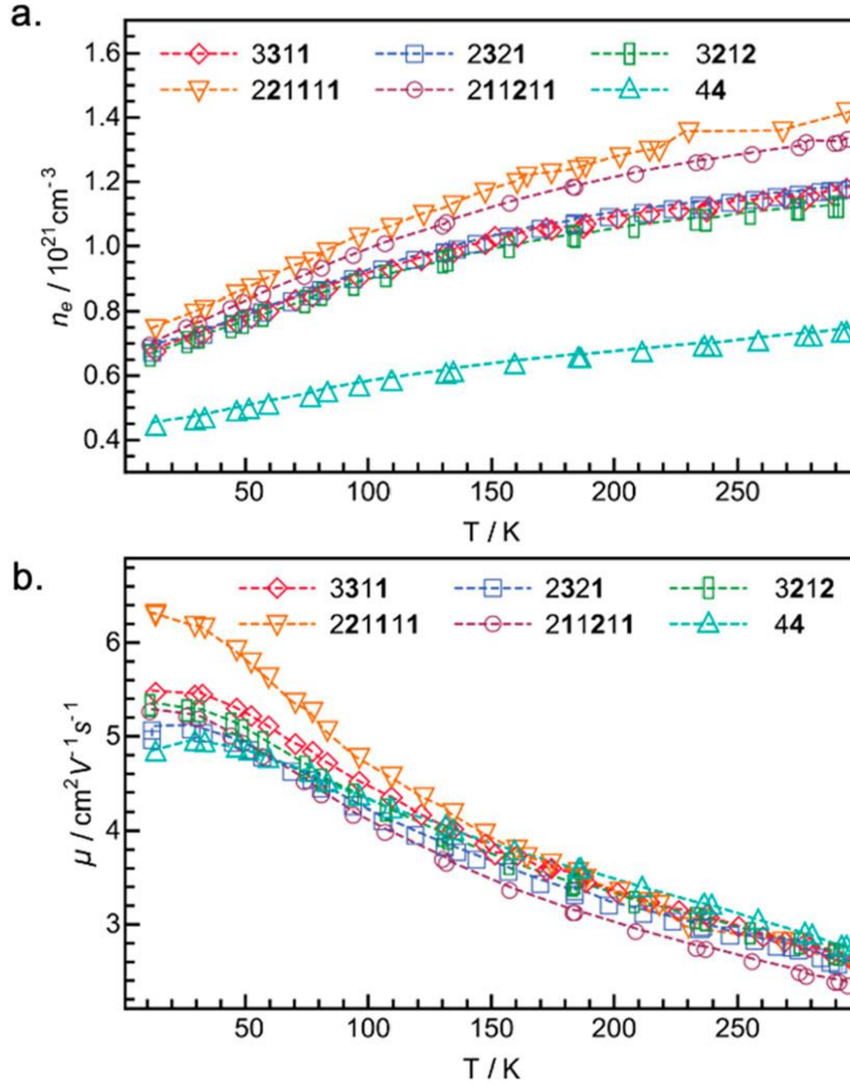

Figure 8.10. Temperature-dependent carrier concentration (a) and mobility (b) of six [(PbSe)1+δ]4(TiSe2)4 isomer heterostructures. Values are calculated assuming a single n-type band.

coefficient between the four samples measured. The negative Seebeck coefficients obtained for all of the isomers agree with the Hall measurements, indicating that electrons are the majority carrier type. The magnitude of the Seebeck coefficients systematically decrease as the interface density decreases in the $[(PbSe)_{1+\delta}]_4(TiSe_2)_4$ isomers. This and the Hall data suggest that band alignments in $[(PbSe)_{1+\delta}]_4(TiSe_2)_4$ isomers result in charge transfer from PbSe into $TiSe_2$. The PbSe-$TiSe_2$ bilayers should be thought of as a conducting entity due

to charge transfer between the constituents. The more PbSe-$TiSe_2$ interfaces there are, the higher the carrier concentration as charge transfer occurs at each interface, as shown schematically in Figure 8.12. The unusual decrease in the carrier concentration with temperature may be a consequence of the two structures changing independently with temperature, resulting in a change in the amount of charge transfer between the two constituents as a function temperature.

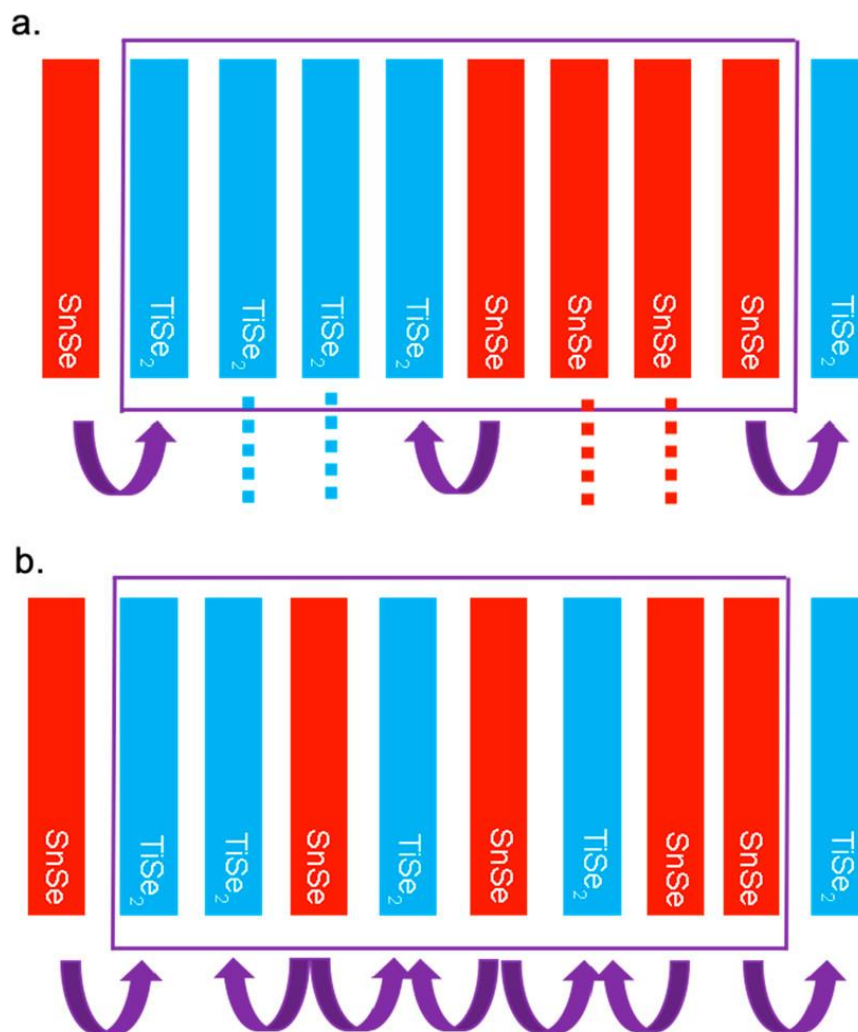

Figure 8.11. Room-temperature Seebeck coefficients for each of the $[(PbSe)_{1+\delta}]_4(TiSe_2)_4$ isomer heterostructures. Colors correspond to the nanoarchitecture, and symbols correspond to the precursor parameters.

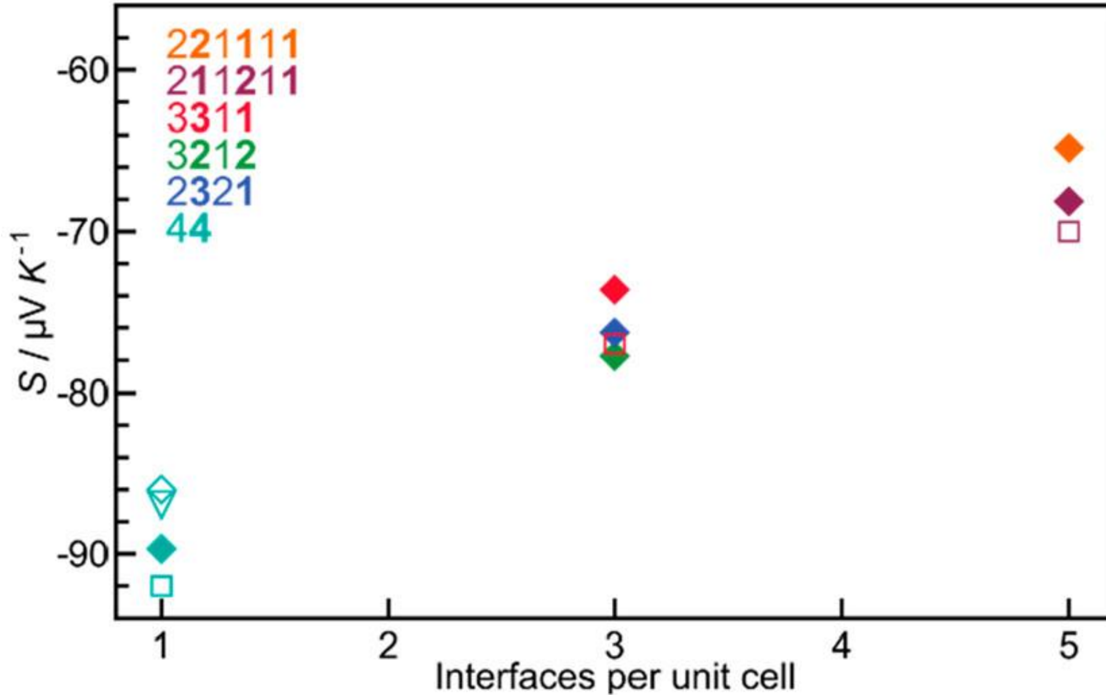

Figure 8.12. Schematic demonstrating charge donation occurring in isomers containing different numbers of buried interfaces, e.g., the 4**4** (a) and the 2**2**1**1**1**1** (b). The SnSe layers are shown in red and the $TiSe_2$ in blue, and purple arrows depict the charge donation from the SnSe to the $TiSe_2$ layers. The purple boxes indicate a single isomer repeating unit.

8.4 Conclusion

This work investigated the synthesis, formation, structure, and transport properties of $[(PbSe)_{1+\delta}]_4(TiSe_2)_4$ isomers. While the correct amount of material deposited was not enough to form 11 repeat units of a $[(PbSe)_{1+\delta}]_4(TiSe_2)_4$ isomers, the intended nanoarchitectures still formed albeit with fewer unit cells than targeted. During deposition, an impurity Ti_2Se phase formed at the substrate interface and there was initial crystallization of both $TiSe_2$ and PbSe in sequences that match the structure of the targeted isomers. Both the initial layering scheme and the heat of formation of the targeted isomers drives the formation of the resulting material. XRR, XRD, and HAADF-STEM analyses confirm the formation of approximately eight or nine repeating units with the correct nanoarchitecture, with thin impurity phases present on the top and bottom. Transport data collected for the isomers indicate that the resistivity and carrier concentration depend on the number of interfaces in the unit cell of the

isomers. This suggests that charge transfer between the constituent layers is the source of the electrons. The mobility and carrier concentration vary inversely with temperature, resulting in a minimum in the resistivity between 50 and 100 K. The ability to prepare metastable isomers provides a new handle for tuning properties in thin film materials, and the tolerance of the self-assembly process to deviations from stoichiometry facilitates the discovery of new compounds using this synthesis approach.

8.5 Bridge

This chapter described the synthesis and characterization of a series of six isomer heterostructures constructed from four $TiSe_2$ layers and four PbSe layers. The next chapter describes the synthesis of a novel heterostructure with a unit cell consisting of $MoSe_2$, BiSe, and Bi_2Se_3.

REFERENCES CITED

(1) Carroll, F. A. *Perspectives on Structure and Mechanism in Organic Chemistry - Felix A. Carroll - Google Books*, Second Edi.; John Wiley & Sons, Inc.: Hoboken, 2010.

(2) Mayr, H.; Ofial, A. R. The Reactivity–Selectivity Principle: An Imperishable Myth in Organic Chemistry. *Angew. Chemie Int. Ed.* **2006**, *45* (12), 1844–1854. https://doi.org/10.1002/anie.200503273.

(3) Smith, M. B.; March, J. *March's Advanced Organic Chemistry*; John Wiley & Sons, Inc.: Hoboken, NJ, USA, 2006. https://doi.org/10.1002/0470084960.

(4) Lu, Z.; Gan, J. Analysis, Toxicity, Occurrence and Biodegradation of Nonylphenol Isomers: A Review. *Environment International*. Elsevier Ltd December 2014, pp 334–345. https://doi.org/10.1016/j.envint.2014.08.017.

(5) Van Zyl, E. F. A Survey of Reported Synthesis of Methaqualone and Some Positional and Structural Isomers. *Forensic Sci. Int.* **2001**, *122* (2–3), 142–149. https://doi.org/10.1016/S0379-0738(01)00484-4.

(6) Bender, R.; Braunstein, P.; Bedien, A.; Ellis, P. D.; Huggins, B.; Harvey, P. D.; Sappa, E.; Tiripicchio, A. Synthetic, Structural, Spectroscopic, and Theoretical Studies of Structural Isomers of the Cluster Pt3(μ-PPh2)3Ph(PPh3)2. A Unique Example of Core Isomerism in Phosphine Phosphido-Rich Clusters. *Inorg. Chem.* **1996**, *35* (5), 1223–1234. https://doi.org/10.1021/ic951164x.

(7) Ooyama, Y.; Kagawa, Y.; Harima, Y. Synthesis and Solid-State Fluorescence Properties of Structural Isomers of Novel Benzofuro[2,3-c]Oxazolocarbazole-Type Fluorescent Dyes. *European J. Org. Chem.* **2007**, *2007* (22), 3613–3621. https://doi.org/10.1002/ejoc.200700247.

(8) Futschek, T.; Marsman, M.; Hafner, J. Structural and magnetic isomers

of small Pd and Rh clusters: An ab initio density functional study. https://doi.org/10.1088/0953-8984/17/38/001.

(9) Fischer, P. The Design, Synthesis and Application of Stereochemical and Directional Peptide Isomers: A Critical Review. *Curr. Protein Pept. Sci.* **2003**, *4* (5), 339–356. https://doi.org/10.2174/1389203033487054.

(10) A. Molnár, G.; Kun, S.; Sélley, E.; Kertész, M.; Szélig, L.; Csontos, C.; Böddi, K.; Bogár, L.; Miseta, A.; Wittmann, I. Role of Tyrosine Isomers in Acute and Chronic Diseases Leading to Oxidative Stress - A Review. *Curr. Med. Chem.* **2016**, *23* (7), 667–685. https://doi.org/10.2174/0929867323666160119094516.

(11) Kesanli, B.; Fettinger, J.; Eichhorn, B. The Closo-[Sn9M(CO)3]4− Zintl Ion Clusters Where M=Cr, Mo, W: Two Structural Isomers and Their Dynamic Behavior. *Chem. – A Eur. J.* **2001**, *7* (24), 5277–5285. https://doi.org/10.1002/1521-3765(20011217)7:24<5277::AID-CHEM5277>3.0.CO;2-C.

(12) Wiener, H. Correlation of Heats of Isomerization, and Differences in Heats of Vaporization of Isomers, Among the Paraffin Hydrocarbons. *J. Am. Chem. Soc.* **1947**, *69* (11), 2636–2638. https://doi.org/10.1021/ja01203a022.

(13) Wiener, H. Structural Determination of Paraffin Boiling Points. *J. Am. Chem. Soc.* **1947**, *69* (1), 17–20. https://doi.org/10.1021/ja01193a005.

(14) Wang, Z.; Herbinet, O.; Cheng, Z.; Husson, B.; Fournet, R.; Qi, F.; Battin-Leclerc, F. Experimental Investigation of the Low Temperature Oxidation of the Five Isomers of Hexane. *J. Phys. Chem. A* **2014**, *118* (30), 5573–5594. https://doi.org/10.1021/jp503772h.

(15) Zhang, K.; Banyon, C.; Burke, U.; Kukkadapu, G.; Wagnon, S. W.; Mehl, M.; Curran, H. J.; Westbrook, C. K.; Pitz, W. J. An Experimental and Kinetic Modeling Study of the Oxidation of Hexane Isomers: Developing

Consistent Reaction Rate Rules for Alkanes. *Combust. Flame* **2019**, *206*, 123–137. https://doi.org/10.1016/j.combustflame.2019.04.011.

(16) Lucius, R.; Mayr, H. Konstante Selektivitätsbeziehungen Bei Additionsreaktionen von Carbanionen. *Angew. Chemie* **2000**, *112* (11), 2086–2089. https://doi.org/10.1002/1521-3757(20000602)112:11<2086::AID-ANGE2086>3.0.CO;2-T.

(17) Lucius, R.; Loos, R.; Mayr, H. Kinetische Untersuchungen von Carbokation-Carbanion-Kombinationen: Schlüssel Zu Einem Allgemeinen Modell Polarer Organischer Reaktivität. *Angew. Chemie* **2002**, *114* (1), 97–102. https://doi.org/10.1002/1521-3757(20020104)114:1<97::AID-ANGE97>3.0.CO;2-4.

(18) Lemek, T.; Mayr, H. Electrophilicity Parameters for Benzylidenemalononitriles. *J. Org. Chem.* **2003**, *68* (18), 6880–6886. https://doi.org/10.1021/jo0344182.

(19) Hoffmann, R. Building Bridges Between Inorganic and Organic Chemistry (Nobel Lecture). *Angew. Chemie Int. Ed. English* **1982**, *21* (10), 711–724. https://doi.org/10.1002/ANIE.198207113@10.1002/(ISSN)1521-3773.NOBELLECTURES.

(20) Gopinath, C. S.; Hegde, S. G.; Ramaswamy, A. V.; Mahapatra, S. Photoemission Studies of Polymorphic CaCO3 Materials. *Mater. Res. Bull.* **2002**, *37* (7), 1323–1332. https://doi.org/10.1016/S0025-5408(02)00763-8.

(21) Boulos, R. A.; Zhang, F.; Tjandra, E. S.; Martin, A. D.; Spagnoli, D.; Raston, C. L. Spinning up the Polymorphs of Calcium Carbonate. *Sci. Rep.* **2014**, *4* (1), 1–6. https://doi.org/10.1038/srep03616.

(22) Gammage, R. B.; Glasson, D. R. The Effect of Grinding on the Polymorphs of Calcium Carbonate. *J. Colloid Interface Sci.* **1976**, *55* (2), 396–401. https://doi.org/10.1016/0021-9797(76)90048-5.

(23) Kitamura, M.; Konno, H.; Yasui, A.; Masuoka, H. Controlling Factors and Mechanism of Reactive Crystallization of Calcium Carbonate Polymorphs from Calcium Hydroxide Suspensions. *J. Cryst. Growth* **2002**, *236* (1–3), 323–332. https://doi.org/10.1016/S0022-0248(01)02082-6.

(24) Stein, A.; Keller, S. W.; Mallouk, T. E. Turning down the Heat: Design and Mechanism in Solid-State Synthesis. *Science* **1993**, *259* (5101), 1558–1564. https://doi.org/10.1126/science.259.5101.1558.

(25) Disalvo, F. J. Solid-State Chemistry: A a Rediscovered Chemical Frontier. *Science* **1990**, *247* (4943), 649–655. https://doi.org/10.1126/science.247.4943.649.

(26) Shoemaker, D. P.; Hu, Y.-J.; Chung, D. Y.; Halder, G. J.; Chupas, P. J.; Soderholm, L.; Mitchell, J. F.; Kanatzidis, M. G. In Situ Studies of a Platform for Metastable Inorganic Crystal Growth and Materials Discovery. *Proc. Natl. Acad. Sci. U. S. A.* **2014**, *111* (30), 10922–10927. https://doi.org/10.1073/pnas.1406211111.

(27) Jansen, M. A Concept for Synthesis Planning in Solid-State Chemistry. *Angew. Chemie - Int. Ed.* **2002**, *41* (20), 3746–3766. https://doi.org/10.1002/1521-3773(20021018)41:20<3746::AID-ANIE3746>3.0.CO;2-2.

(28) Hemminger, John (University of California, I. *Directing Matter and Energy: Five Challenges for Science and the Imagination A Report from the Basic Energy Sciences Advisory Committee*; 2007.

(29) Lin, Q.; Smeller, M.; Heideman, C. L.; Zschack, P.; Koyano, M.; Anderson, M. D.; Kykyneshi, R.; Keszler, D. A.; Anderson, I. M.; Johnson, D. C. Rational Synthesis and Characterization of a New Family of Low Thermal Conductivity Misfit Layer Compounds [(PbSe)0.99]m(WSe2)n'. *Chem. Mater.* **2010**, *22* (3), 1002–1009. https://doi.org/10.1021/cm901952v.

(30) Bauers, S. R.; Moore, D. B.; Ditto, J.; Johnson, D. C. Phase Width of

Kinetically Stable ([PbSe]1+δ)1(TiSe2)1 Ferecrystals and the Effect of Precuror Compostion on Electrical Properties. *J. Alloys Compd.* **2015**, *645*, 118–124. https://doi.org/10.1016/j.jallcom.2015.04.228.

(31) Merrill, D. R.; Moore, D. B.; Bauers, S. R.; Falmbigl, M.; Johnson, D. C. Misfit Layer Compounds and Ferecrystals: Model Systems for Thermoelectric Nanocomposites. *Materials (Basel).* **2015**, *8* (4), 2000–2029. https://doi.org/10.3390/ma8042000.

(32) Moore, D. B.; Beekman, M.; Disch, S.; Zschack, P.; Häusler, I.; Neumann, W.; Johnson, D. C. Synthesis, Structure, and Properties of Turbostratically Disordered (PbSe) 1.18 (TiSe 2) 2. *Chem. Mater.* **2013**, *25*, 2404–2409. https://doi.org/10.1021/cm400090f.

(33) Bauers, S. R.; Merrill, D. R.; Moore, D. B.; Johnson, D. C. Carrier Dilution in TiSe 2 Based Intergrowth Compounds for Enhanced Thermoelectric Performance. *J. Mater. Chem. C* **2015**, *3*, 10451–10458. https://doi.org/10.1039/C5TC01570G.

(34) Bauers, S.; Ditto, J.; Moore, D. B.; Johnson, D. C. Structure-Property Relationships in Non-Epitaxial Chalcogenide Heterostructures: The Role of Interface Density on Charge Exchange. *Nanoscale* **2016**, *8*, 14665–14672. https://doi.org/10.1039/C6NR04274K.

(35) Moore, D. B.; Beekman, M.; Zschack, P.; Johnson, D. C. Synthesis of Four New Members of the (PbSe)1.16(TiSe2)n (n = 1, 2, 3, and 4) Family of Ferecrystals. In *2011 11th IEEE International Conference on Nanotechnology*; IEEE, 2011; pp 1363–1366. https://doi.org/10.1109/NANO.2011.6144586.

(36) Hamann, D. M.; Bardgett, D.; Cordova, D. L. M.; Maynard, L. A.; Hadland, E. C.; Lygo, A. C.; Wood, S. R.; Esters, M.; Johnson, D. C. Sub-Monolayer Accuracy in Determining the Number of Atoms per Unit Area in Ultrathin Films Using X-Ray Fluorescence. *Chem. Mater.* **2018**, *30*, 6209–6216. https://doi.org/10.1021/acs.chemmater.8b02591.

(37) Schaffer, M.; Schaffer, B.; Ramasse, Q. Sample Preparation for Atomic-Resolution STEM at Low Voltages by FIB. *Ultramicroscopy* **2012**, *114*, 62–71. https://doi.org/10.1016/j.ultramic.2012.01.005.

(38) Weirich, T. E.; Pottgen, R.; Simon, A. Crystal Structure of Dititanium Monoselenide, Ti2Se. *Zeitschrift für Krist. - Cryst. Mater.* **1996**, *211* (12), 928.

(39) Anderson, M. D.; Heideman, C. L.; Lin, Q.; Smeller, M.; Kokenyesi, R.; Herzing, A. A.; Anderson, I. M.; Keszler, D. A.; Zschack, P.; Johnson, D. C. Size-Dependent Structural Distortions in One-Dimensional Nanostructures. *Angew. Chemie - Int. Ed.* **2013**, *52* (7), 1982–1985. https://doi.org/10.1002/anie.201207825.

(40) Moore, D. B.; Stolt, M. J.; Atkins, R.; Sitts, L.; Jones, Z.; Disch, S.; Beekman, M.; Johnson, D. C. Structural and Electrical Properties of (PbSe) 1·16 TiSe 2. *Emerg. Mater. Res.* **2012**, *1*, 292–298. https://doi.org/10.1680/emr.12.00024.

CHAPTER IX

SYNTHESIS AND ELECTRICAL PROPERTIES OF A NEW COMPOUND $(BISE)_{0.97}(BI_2SE_3)_{1.26}(BISE)_{0.97}(MOSE_2)$ CONTAINING METALLIC 1T-$MOSE_2$

9.0 Authorship Statement

Chapter IX was published in Chemistry of Materials in 2021. Marisa Choffel and David Johnson are the main contributors to the text. Renae Gannon, Fabian Gohler, Douglas Medlin, and Thomas Seyller collected experimental XPS and HAADF-STEM data. I performed electrical transport measurements of the novel compound synthesized in this chapter.

9.1 Introduction

Group 6 semiconducting transition metal dichalcogenides have been the subject of extensive research over the last several decades due to their potential applications in catalysis[1–3], photovoltaics[4], supercapacitors[5], and rechargeable battery systems.[6] The structure of these MX_2 compounds (where M = Mo, W and X = S, Se) consists of a hexagonal layer of metal atoms sandwiched between two hexagonal chalcogen layers.[7,8] Depending on the stacking of these trilayers, several polymorphs are possible, with the semiconducting 2H polymorph being the most common with ABA BAB stacking. This stacking results in trigonal prismatic coordination of the metal.[9,10] The recent discovery that the group 6 compounds transition from an indirect to a direct band-gap semiconductor when the bulk material is scaled down to a monolayer has created significant excitement as one of the first examples of an emergent property in a monolayer.[11–13] The transition from an indirect to a direct band-gap semiconductor, which increases absorption and photoluminescence, has great promise for applications in optical devices.[12,14–16]

Ternary and higher-order compounds containing the group 6 X–M–X trilayers can also have ABC stacking of the layers, resulting in octahedral coordination of the metal and metallic conductivity.[3,17–20] These structural and electronic

changes were first discovered in the alkali intercalation of the group 6 compounds.[18,21,22] The ability to vary the intercalant, change carrier concentration by varying the amount of the intercalate, and the discovery of superconductivity in these compounds resulted in a surge of activity.[18,23,24] Haering and co-workers recognized the potential of these compounds as battery cathodes, leading to the first commercialized lithium-ion batteries.[25] More recently, there has been a surge in publications on single- and few-layered 1T-MX_2 compounds due to improved catalytic properties for hydrogen evolution[2,3] and reduced contact resistances in 1T–2H–1T source–channel–drain field-effect transistors.[19,26]

The high mobility and the volatility of alkali metal intercalants create challenges in their synthesis and in subsequent processing steps when adjacent to other compounds.[27] An alternative way to create 1T-MX_2 layers is the presence of an adjacent strong electron-donating layer. MSe layers, where M = Sb, Bi, or a rare earth metal, have been reported to donate charge to neighboring dichalcogenide layers in misfit layered compounds.[28] These MSe layers have much lower vapor pressures than typical intercalants and are much less likely to diffuse. A recent paper on $(BiSe)_{0.97}(MoSe_2)$ reported a 40/60 ratio of 1T/2H polymorph in the $MoSe_2$ layer, with a significant reduction in electrical resistivity relative to 2H-$MoSe_2$.[29] To increase the fraction of 1T-MX_2, more charge donation is required. However, $[(BiSe)_{1+x}]_n(MoSe_2)$ compounds cannot be made, as multiple layers of BiSe are not stable next to each other.[30]

In this paper, we report the synthesis, structure, and properties of $(BiSe)_{1+x}(Bi_2Se_3)_{1+y}(BiSe)_{1+x}(MoSe_2)$, probing how increasing the ratio of BiSe/$MoSe_2$ layers affects the percentages of 2H and 1T polymorphs in the $MoSe_2$ layer. $(BiSe)_{1+x}(Bi_2Se_3)_{1+y}(BiSe)_{1+x}(MoSe_2)$ was targeted as isostructural compounds that have been previously reported.[31] The synthesis of the desired heterostructure is nontrivial, as it is only kinetically stable and avoiding the formation of $[(Bi_2Se_3)_{1+y}]_2(MoSe_2)$ requires excess Bi and Se in the precursor. $(BiSe)_{1+x}(Bi_2Se_3)_{1+y}(BiSe)_{1+x}(MoSe_2)$ formed crystallographically aligned with

respect to the substrate, but this is due to the morphology of the precursor, not epitaxial growth. The extensive turbostratic disorder between the constituent layers indicates that epitaxial growth does not dominate the self-assembly of the precursor into the heterostructure. High-angle annular dark field-scanning transmission electron microscopy (HAADF-STEM) images confirm the layered nature of $(BiSe)_{1+x}(Bi_2Se_3)_{1+y}(BiSe)_{1+x}(MoSe_2)$ and indicate that two different polymorphs of MoSe2 are present. X-ray photoelectron spectroscopy (XPS) data also indicate that 1T-$MoSe_2$ is present in increased quantities relative to $(BiSe)_{0.97}(MoSe_2)$. Resistivity measurements of $(BiSe)_{1+x}(Bi_2Se_3)_{1+y}(BiSe)_{1+x}(MoSe_2)$ show it is metallic, which are consistent with the increased amount of 1T-$MoSe_2$ in the heterostructure. The Hall data are more complicated due to the heterogeneous mix of phases in the structures, resulting in a change in the carrier type as temperature is varied.

9.2 Methods & Materials

Precursors targeting $(BiSe)_{1+x}(Bi_2Se_3)_{1+y}(BiSe)_{1+x}(MoSe_2)$ were synthesized via physical vapor deposition of the elements at pressures below 5×10^{-7} Torr, using the repeating sequence Mo|Se|Bi|Se|(Bi|Se|Bi|Se)|Bi|Se. Bismuth and molybdenum were deposited using an electron beam gun and selenium was deposited using a Knudson effusion cell. A Si (100) wafer with a native oxide layer and fused quartz were used as substrates. The bulk crystalline structures of the individual constituents were used to calculate the desired amount of material in each layer such that each Mo|Se layer had the number of atoms required to form a single Se–Mo–Se trilayer of $MoSe_2$, each Bi|Se layer had the number of atoms required to form a bilayer of a rock salt-structured BiSe, and each (Bi|Se|Bi|Se) had the number of atoms required to form a quintuple Se–Bi–Se–Bi–Se layer of Bi_2Se_3. A previously published calibration method was used to optimize the deposition parameters.[32] X-ray fluorescence (XRF) intensities were collected using a Rigaku ZSX Primus-II with a rhodium X-ray tube to determine the amount of each metal deposited. The proportionality constant between XRF intensity and the amount of Mo and Bi in the film was determined

by preparing samples of $MoSe_2$ and Bi_2Se_3 and using the Se proportionality constant previously reported.[32]

X-ray reflectivity (XRR) and specular X-ray diffraction (XRD) data were collected on a Bruker D8 Discover diffractometer using Cu Kα radiation. Grazing incidence in-plane XRD information was collected using a Rigaku SmartLab with a Cu source.

Precursors were annealed at targeted temperatures for 15 min in a glovebox with a nitrogen atmosphere where O_2 pressure was below 0.5 ppm to promote their self-assembly into the crystalline products.

A cross section of the sample was prepared with an FEI Helios Nanolab 600i dual-beam scanning electron microscope (SEM)/focused ion beam (FIB) using the standard lift-out method.[33] A protective layer of Sharpie carbon and FIB-deposited carbon was applied to the surface. High-angle annual dark field-scanning transmission electron microscopy (HAADF-STEM) images of the cross section were collected on a probe-corrected Thermo Fisher Scientific Themis Z STEM at 300 keV.

X-ray photoelectron spectroscopy (XPS) measurements were carried out at room temperature at a pressure of less than 3×10^{-10} mbar using Al Kα radiation from a SPECS XR-50M X-ray source with a SPECS Focus 500 crystal monochromator and a SPECS Phoibos 150 MCD-9 hemispherical analyzer equipped with a nine channeltron detector. Cleaving of samples prior to XPS measurements was done by mounting the sample between two steel plates using a combination of low-degassing EPO TEK H72 and H22 epoxy resins. Breaking of the top plate under the flow of dry nitrogen in the load lock of the UHV system exposes the buried interfaces of the film. Spectral analysis was carried out by fitting the high-resolution core-level spectra with multiple Voigt profiles. Lorentzian lifetime widths used in the fits were determined beforehand on commercially available single crystals as well as MER-grown binary samples.

Temperature-dependent resistivity measurements were collected on the

samples between 24 and 298 K using the van der Pauw method on a home-built system.

9.3 Results & Discussion

Six precursors were deposited as we attempted to prepare $(BiSe)_{1+x}(Bi_2Se_3)_{1+y}(BiSe)_{1+x}(MoSe_2)$. The amounts of each element required to form 11 and 10 layers of a $(BiSe)_{1+x}(Bi_2Se_3)_{1+y}(BiSe)_{1+x}(MoSe_2)$ heterostructure were estimated using the lattice parameters and structures of the binary constituents and/or structurally related compounds (Table 1). The compositions, total thickness, and repeating layer thickness of each precursor are summarized in Table 9.1. The fluctuation of the measured amounts for the precursors around the targeted values reflects the reproducibility of the deposition but is valuable as our initial target value is only an estimate. Compositions for each precursor were determined from the XRF intensities of each element for the total film and the previously described calibration method.[32] The precursors were closer in composition to the stoichiometry of $(BiSe)_{1+x}(Bi_2Se_3)_{1+y}(BiSe)_{1+x}(MoSe_2)$than to the composition estimated for 11 or 10 layers of $[(Bi_2Se_3)_{1+y}]_2(MoSe_2)$, a potentially competing local free-energy minima. The XRR patterns of all of the precursors contained a first-order Bragg reflection from the sequence of deposited layers, indicating that the elements in the precursor did not completely mix during the deposition. The thicknesses of all of the repeating sequences of elemental layers were close to the estimated c-axis lattice parameter for the $(BiSe)_{1+x}(Bi_2Se_3)_{1+y}(BiSe)_{1+x}(MoSe_2)$ heterostructure (28.06 Å) determined by adding c-axis lattice parameters of the constituents. The amounts of each element deposited in the repeating sequence Mo|Se|Bi|Se|(Bi|Se|Bi|Se)|Bi|Se suggest that forming 10 or 11 layers of $(BiSe)_{1+x}(Bi_2Se_3)_{1+y}(BiSe)_{1+x}(MoSe_2)$ would involve the smallest diffusion distances for the elements.

Table 9.1. Amounts of Material and Repeating Thicknesses for Samples Targeting the $(BiSe)_{1+x}(Bi_2Se_3)_{1+y}(BiSe)_{1+x}(MoSe_2)$ Nanoarchitecture

sample	atoms/Å2 per layer in precursor before annealing						
	Bi	M	Se	Total thickness	# layers deposi-ted	# layers crystall-ized	Repeating thickness (Å)
sample 1	3.88(8)	1.15(2)	6.5(3)	309.7(9)	11	10	28.37(2)
sample 2	3.53(7)	1.37(3)	6.6(3)	308.7(5)	11	10	27.69(2)
sample 3	3.19(6)	1.21(2)	7.6(4)	312.9(8)	11	10	28.49(2)
sample 4	3.41(7)	0.90(2)	7.0(3)	291.2(7)	11	10	27.28(2)
sample 5	3.46(7)	1.22(2)	7.0(3)	302.7(4)	11		27.78(2)
sample 6	3.54(7)	1.15(2)	7.1(4)	315.0(8)	11		27.89(2)
targeting $(BiSe)_{1+x}(Bi_2Se_3)_{1+y}(BiSe)_{1+x}(MoSe_2)$	3.71	1.18	6.8		11		28.06
	3.37	1.07	6.2		10		
targeting $[(Bi_2Se_3)_{1+y}]_2(MoSe_2)$	2.87	1.18	6.8		11		25.56
	2.61	1.07	6.2		10		

All of the samples were annealed to 350 °C to quickly evaluate what compounds self-assembled from the precursors, and the resulting specular and in-plane diffraction patterns are shown in Figure 9.1. The reflections observed in the specular diffraction patterns of samples 1 and 2 index to single families of (00l) reflections with c-axis lattice parameters of 27.97(1) and 27.79(2) Å, respectively. Both are close to the estimated c-axis lattice parameter of $(BiSe)_{1+x}(Bi_2Se_3)_{1+y}(BiSe)_{1+x}(MoSe_2)$ (28.06 Å). The in-plane reflections can be indexed as (*hk*0) reflections for three different constituents: two hexagonal unit cells and a unit cell with a rectangular basal plane. The calculated lattice parameters ($a_{hex,1}$ = 4.170(3) Å, $a_{hex,2}$ = 3.311(4) Å, a_{rect} = 4.600(1) Å and b_{rect} = 4.238(1) Å) are consistent with those expected for Bi_2Se_3 (a = 4.178(1) Å), $MoSe_2$ (a = 3.32(1) Å), and BiSe (a = 4.61(1) Å and b = 4.26(1) Å), respectively.[29,31] The diffraction data indicate that $(BiSe)_{1+x}(Bi_2Se_3)_{1+y}(BiSe)_{1+x}(MoSe_2)$ formed from these precursors. Surprisingly, samples 3 and 4 formed $[(Bi_2Se_3)_{1+y}]_2(MoSe_2)$ instead of the targeted compound $(BiSe)_{1+x}(Bi_2Se_3)_{1+y}(BiSe)_{1+x}(MoSe_2)$ whose composition they were closest to. The evenly spaced reflections in the specular

X-ray diffraction yield *c*-axis lattice parameters of 26.38(1) and 25.96(1) Å, respectively, which are close to the estimated *c*-axis lattice parameter for $[(Bi_2Se_3)_{1+y}]_2(MoSe_2)$ (25.56 Å). The in-plane maxima can be indexed as (hk0) reflections to two different hexagonal unit cells with *a*-axis lattice parameters of 4.154(2) and 3.309(5) Å, which are close to those expected for Bi_2Se_3 and $MoSe_2$, respectively.[29,31] Intensity at ~28.6° 2θ suggests that a small amount of BiSe may have formed. The specular diffraction scans for samples 5 and 6 have sharp reflections at low angles and broader diffraction maxima at high angles, suggesting that the samples have not fully self-assembled at this temperature. The high-angle reflections yield c-axis lattice parameters of 26.32(1) and 26.27(1) Å for samples 5 and 6, respectively, which are close to the estimated c-axis lattice parameter of $[(Bi_2Se_3)_{1+y}]_2(MoSe_2)$. The reflections observed in the in-plane pattern of sample 6 can be indexed to two different hexagonal unit cells. The lattice parameters calculated from the peak positions (a_{hex} = 4.158(3) Å, a_{hex} = 3.304(7) Å) are consistent with those expected for Bi_2Se_3 and $MoSe_2$. Higher intensity at ~28.6° 2θ suggests that more BiSe is present in this sample than found in sample 3. The different products formed show how sensitive the reaction pathway is to the composition and structure of the precursors.

In conventional high-temperature solid-state synthesis, the composition of the starting mixture determines the product or the ratio of products that form. In reactions of layered precursors, the local compositions and nanoarchitecture become important parameters as they control what nucleates and the diffusion lengths required for growth. Due to reactions with the substrate and/or oxidation at the surface, it is common to form one or more fewer unit cells of the intended heterostructure than the number of layers deposited.[34] We observed this in the precursors studied here, as the Laue oscillations around the (002) reflections in samples 1–4 indicate that 10 unit cells formed from the 11 repeating sequences deposited. Figure 9.2 graphs the amounts of Mo and Bi in each of the samples, normalized to the 10 unit cells that crystallized, and arrows are used to indicate whether they formed $(BiSe)_{1+x}(Bi_2Se_3)_{1+y}(BiSe)_{1+x}(MoSe_2)$ or

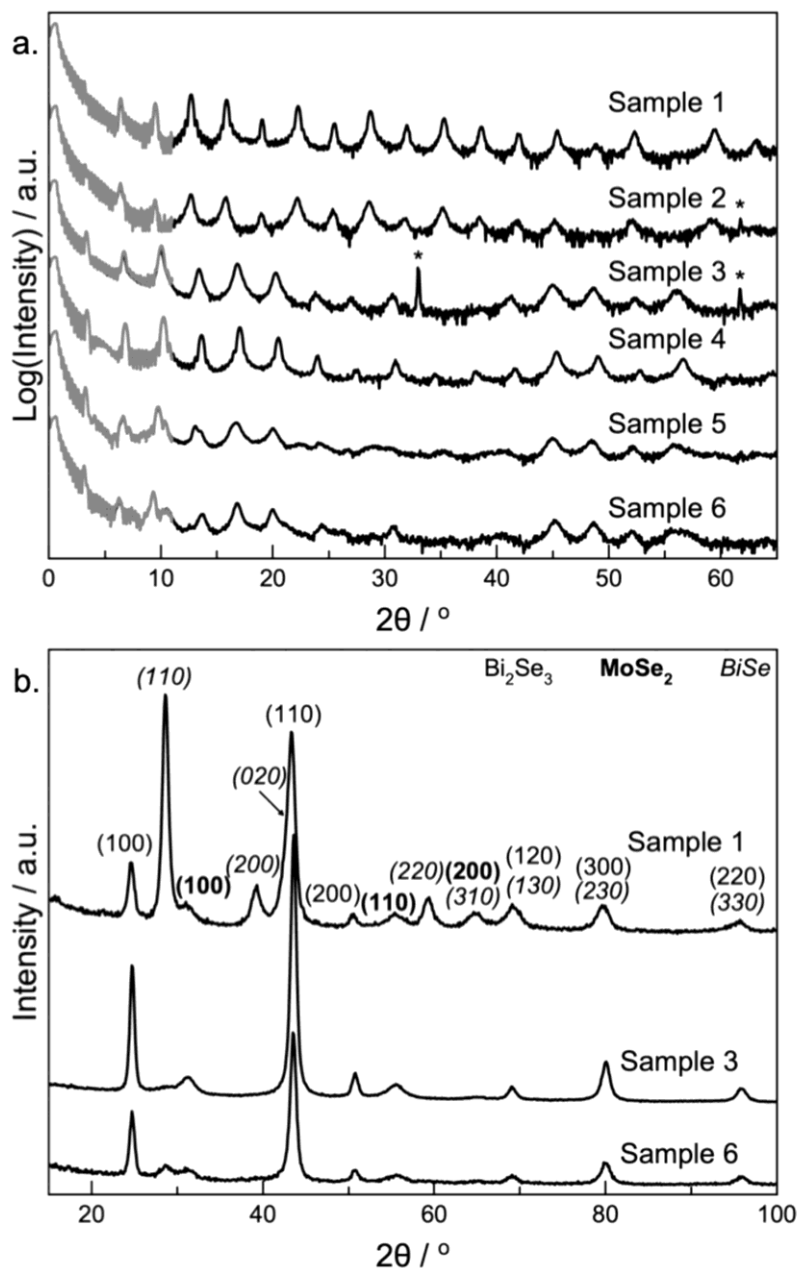

Figure 9.1. (a) XRR (gray) and specular X-ray diffraction and (b) representative in-plane X-ray diffraction patterns of the samples after annealing to 350 °C. Asterisks in (a) mark the reflections that result from the Si substrate. The reflections for the different components are marked in (b) in varying fonts consistent with the labels in the top right corner.

$[(Bi_2Se_3)_{1+y}]_2(MoSe_2)$. Samples 1 and 2 have enough Bi and Mo to make the 10 layers of $(BiSe)_{1+x}(Bi_2Se_3)_{1+y}(BiSe)_{1+x}(MoSe_2)$ that formed.Samples 3–6 are all deficient in one element compared to $(BiSe)_{1+x}(Bi_2Se_3)_{1+y}(BiSe)_{1+x}(MoSe_2)$. Instead of forming nine unit cells of $(BiSe)_{1+x}(Bi_2Se_3)_{1+y}(BiSe)_{1+x}(MoSe_2)$, they instead

evolve into $[(Bi_2Se_3)_{1+y}]_2(MoSe_2)$. We speculate that the significant excess of Se (5–13%) relative to the amounts of Bi and Mo in these precursors may have promoted the formation of Bi_2Se_3 rather than BiSe by Le Chatelier's principle. Since Laue oscillations are observed in samples 1–4, long-range diffusion is required to transport the excess amounts of Bi and Mo out of the coherent crystalline domains. The excess Se probably acts as a flux. Samples with excess Mo relative to the compound formed have broader diffraction maxima, which we speculate is due to $MoSe_2$ inclusions, which reduces the size of coherent domains. Excess Bi has been observed to form Bi_2Se_3 on the top of the sample in other Bi-containing heterostructures[35,36], suggesting that it is more mobile than excess Mo. Our results indicate that the local free-energy minima in the energy landscape for $(BiSe)_{1+x}(Bi_2Se_3)_{1+y}(BiSe)_{1+x}(MoSe_2)$ and $[(Bi_2Se_3)_{1+y}]_2(MoSe_2)$ are close in energy.

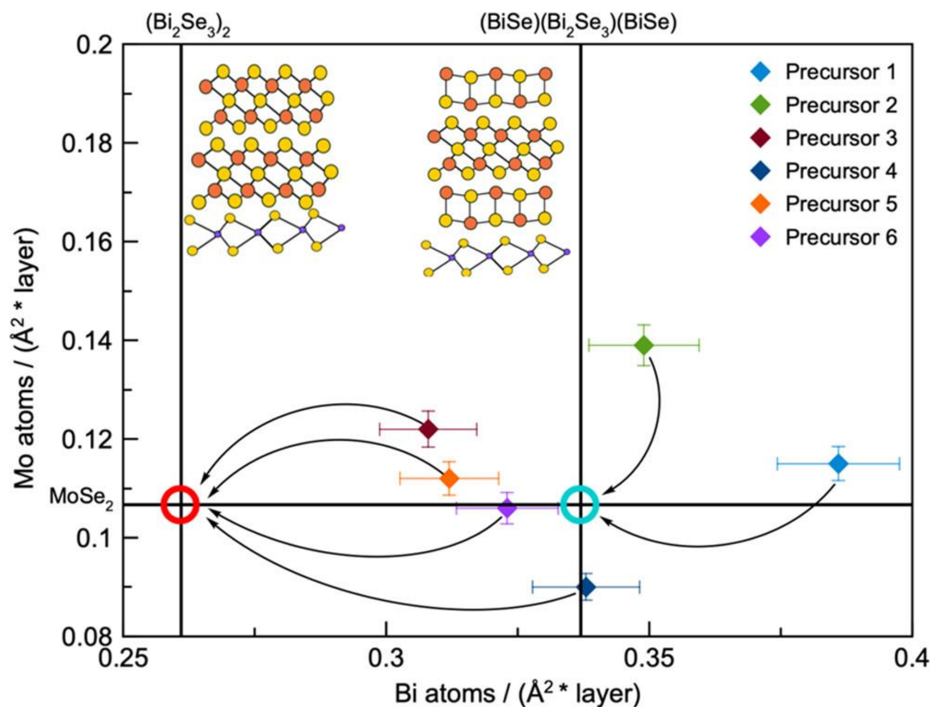

Figure 9.2. Amounts of Bi and Mo in the samples compared to the estimated amounts to form $[(Bi_2Se_3)_{1+y}]_2(MoSe_2)$ (red circle) and $(BiSe)_{1+x}(Bi_2Se_3)_{1+y}(BiSe)_{1+x}(MoSe_2)$ (blue circle).

Specular and in-plane XRD scans were collected on sample 1 as a function of annealing temperature to determine the optimal formation conditions for

$(BiSe)_{1+x}(Bi_2Se_3)_{1+y}(BiSe)_{1+x}(MoSe_2)$ (Figure 9.3). The specular XRD pattern of the as-deposited precursor contains reflections from two different sources. The sharp first-order Bragg reflection results from the composition modulation of the precursor from the deposited sequence of elemental layers. The broader diffraction maxima at higher angles result from small crystalline domains that nucleated and grew during the deposition process. The broad diffraction maxima can all be indexed to a single family of (00*l*) reflections with a c-axis lattice parameter of 28.0(1) Å. This value is close to the estimated c-axis lattice parameter for $(BiSe)_{1+x}(Bi_2Se_3)_{1+y}(BiSe)_{1+x}(MoSe_2)$ (28.06 Å). Evidence for crystallization during deposition is also found in the in-plane XRD pattern. The broad reflections are consistent with the (100) and (110) reflections for Bi_2Se_3 and the (110) and (020) reflections for BiSe.[31] After annealing at 150 °C, there are slight increases in the intensity of the existing reflections in both the specular and in-plane XRD patterns, but no new reflections are observed. The XRR pattern has fewer Kiessig fringes, suggesting that there is an increase in the roughness of the film as atoms diffuse. After annealing at 250 °C, the intensity of reflections in the specular and in-plane XRD patterns increase, linewidths decrease, and additional reflections are visible in both patterns. Even more reflections appear after annealing at 350 °C and the existing reflections in both patterns increase in intensity and decrease in the linewidth. The XRR pattern indicates that the film smoothness increased during annealing at 350 °C. Laue oscillations are now apparent between low-angle Bragg reflections, indicating the sample is 10 repeating layers thick. The total thickness of the sample based on the Kiessig fringes in the XRR pattern is 306.9(3) Å. Based on the *c*-axis lattice parameter and the number of layers indicated from the Laue oscillations, the thickness of the crystalline BiSe–Bi_2Se_3–BiSe–$MoSe_2$ repeating structure is ~279.7 Å. The difference, ~27 Å, is approximately the thickness of three quintuple layers of Bi_2Se_3, which is observed in the STEM images discussed next. The lattice parameters calculated from both patterns remain consistent with the formation of $(BiSe)_{1+x}(Bi_2Se_3)_{1+y}(BiSe)_{1+x}(MoSe_2)$ at this temperature. The (00*l*)

reflections in the specular XRD pattern lose intensity, broaden, and new reflections appear after annealing at 400 °C, indicating that $(BiSe)_{1+x}(Bi_2Se_3)_{1+y}(BiSe)_{1+x}(MoSe_2)$ is decomposed. The in-plane reflections of BiSe decrease in the intensity, suggesting that the decomposition of this layer is responsible for the deterioration of the heterostructure. The annealing study indicates that $(BiSe)_{1+x}(Bi_2Se_3)_{1+y}(BiSe)_{1+x}(MoSe_2)$ begins to self-assemble during the deposition and the self-assembly is completed, and excess Bi and Se diffuse to the top of the film after annealing at 350 °C.

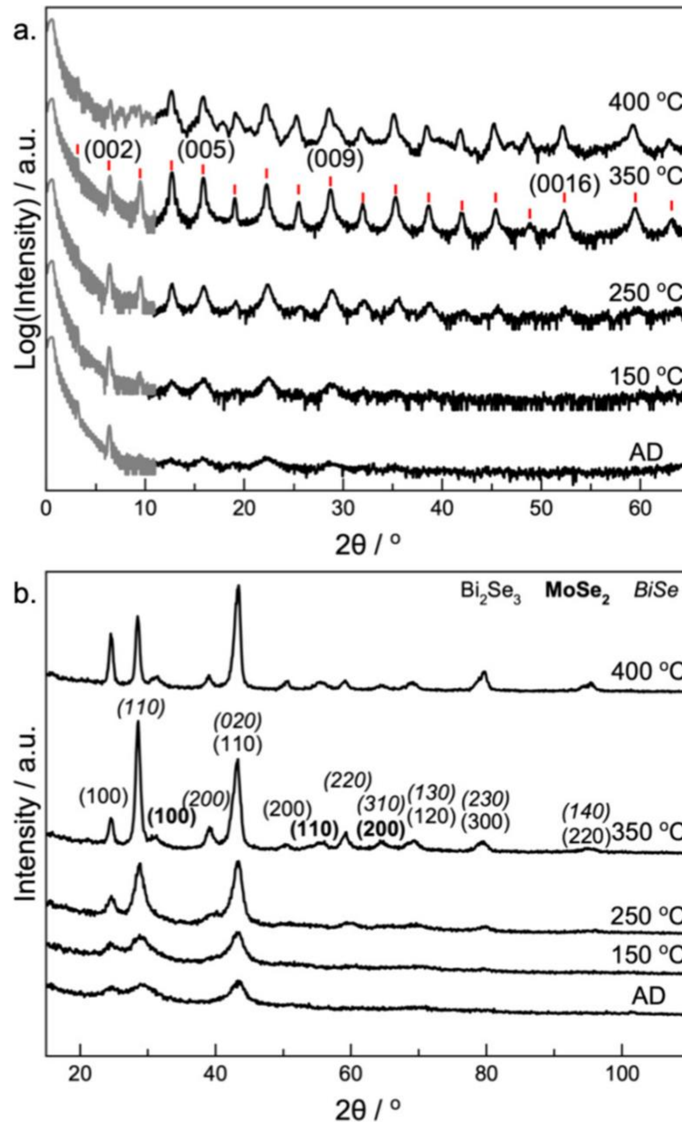

Figure 9.3. (a) XRR (gray) and specular XRD (black) patterns and (b) in-plane XRD patterns of sample 1 as a function of temperature. The red lines indicate the 2θ values for reflections calculated using the c-axis lattice parameter of the structure (27.97(1) Å). Indices are indicated above some reflections.

An HAADF-STEM image from a cross section of sample 1 annealed at 350 °C is contained in Figure 9.4. The 10 repeating units of $(BiSe)_{0.97}(Bi_2Se_3)_{1.26}(BiSe)_{0.97}(MoSe_2)$, containing a quintuple layer of Bi_2Se_3, a bilayer of BiSe, a trilayer of $MoSe_2$, and a bilayer of BiSe are clearly visible. The 10 unit cells agree with the number determined from the Laue oscillations in the XRD pattern. There is a thin amorphous region present on the bottom of the film and two extra Bi_2Se_3 layers are present on the top of the sample. Similar diffusion of excess Bi and Se to the top of a sample forming Bi_2Se_3 layers was previously reported in other bismuth-containing heterostructures.[35,36] The first crystalline layer in the heterostructure above the substrate is Bi_2Se_3, which is surprising since a Mo|Se layer was first in the deposition sequence. The energy-dispersive X-ray spectroscopy (EDS) map shows that the bottom of the film contains an amorphous mixture including Mo, Se, Si, and O (Figure C1). The intensity of Se on the bottom of the film is less than that of the Se intensity in $MoSe_2$ layers, suggesting that at least some of the Mo may react with the SiO_2-coated Si surface during deposition or annealing. Grain boundaries within layers and varying orientations within and between layers are present for all constituents, suggesting multiple nucleation sites. The resulting turbostratic disorder is commonly found in samples prepared from modulated precursors.[37–39]

A higher magnification HAADF-STEM image is shown in Figure 9.5, which clearly shows the atomically abrupt interfaces between the structurally different layers. Different layers having different zone axis orientations are observed, with the orientations changing both within and between layers. A single quintuple layer containing a Se–Bi–Se–Bi–Se stacking sequence is observed when the Bi_2Se_3 layer is oriented along a $\langle 11\bar{2}0 \rangle$ zone axis. Antiphase boundaries are clearly visible in BiSe layers when they are oriented along a $\langle 110 \rangle$ zone axis. The different orientations are thought to result from different nucleation sites both in the same and in different layers, resulting in the extensive rotational disorder observed. While not both contained in the image in Figure 9.5, we identified regions in the sample where small domains of the two different polytypes of

Figure 9.4. Representative HAADF-STEM image of the $(BiSe)_{0.97}(Bi_2Se_3)_{1.26}(BiSe)_{0.97}(MoSe_2)$ heterostructure annealed to 350 °C on a Si substrate with its native SiO2 surface layer. The 10 repeating sequences of layers resulting in Laue oscillations are indicated on the left with red dashed lines.

Figure 9.5. HAADF-STEM image of the $(BiSe)_{0.97}(Bi_2Se_3)_{1.26}(BiSe)_{0.97}(MoSe_2)$ heterostructure with zone axes labeled for each constituent. Antiphase boundaries are observed in regions of the film containing BiSe orientated along the [110] zone axis and marked with red arrows.

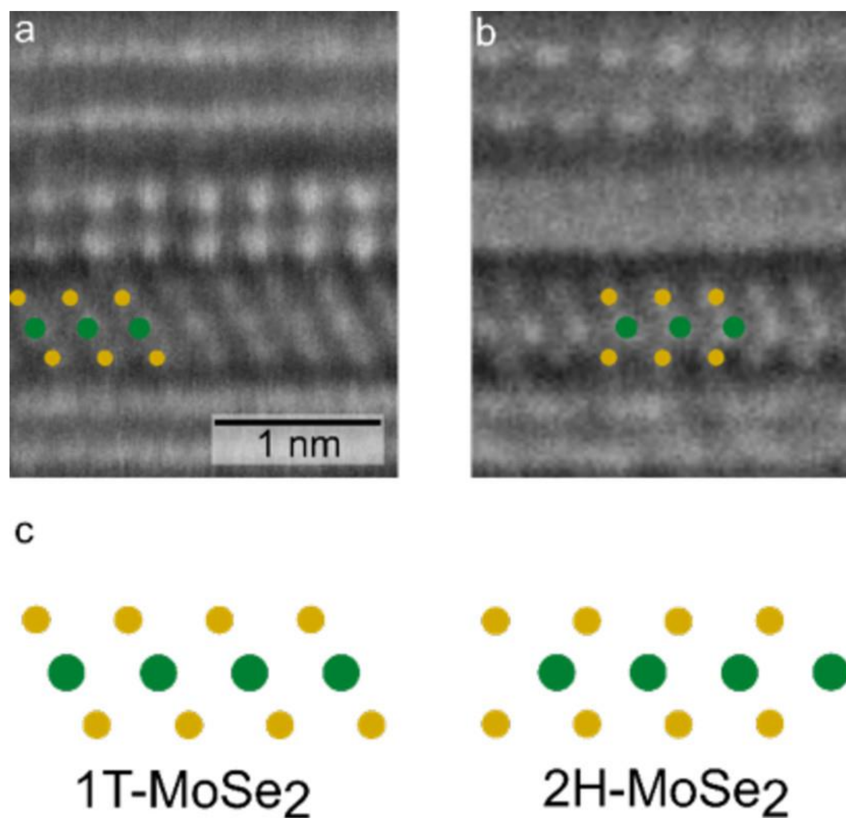

Figure 9.6. HAADF-STEM images, which show a region of (a) 1T-$MoSe_2$ and (b) 2H-$MoSe_2$. The schematics below the images show the expected [110] zone axis images for 1T-$MoSe_2$ and 2H-$MoSe_2$ [Mo (green) and Se (yellow)].

$MoSe_2$ could be identified when they are orientated down a ⟨110⟩ zone axis. The diagonal slashes shown in Figure 9.6a are consistent with an octahedrally coordinated 1T-$MoSe_2$ polymorph, and the chevrons in Figure 9.6b are consistent with a trigonal prismatic coordinated 2H-$MoSe_2$ structure. The fact that only small local regions are observable with these zone axis orientations reflects the small size of the $MoSe_2$ grains.

XPS of the Mo 3d, Se 3d, and Bi 5d core levels was collected on cleaved films to gain information about the electronic states found in $(BiSe)_{0.97}(Bi_2Se_3)_{1.26}(BiSe)_{0.97}(MoSe_2)$, and representative spectra are shown in Figure 9.7. Spectral analysis of the Mo 3d core-level spectrum (Figure 9.7a) reveals contributions from two different components, with Mo $3d_{5/2}$ binding energies of 228.25 ± 0.05 and 228.93 ± 0.05 eV. An additional broad component

centered at 229.47 ± 0.11 eV is required to account for the signal from an overlapping Se 3s core level. The Mo 3d binding energies are consistent with those reported previously for 1T- and 2H-$MoSe_2$, both in $(BiSe)_{0.97}(MoSe_2)$ (228.3 ± 0.1 and 228.9 ± 0.1 eV) and the individual polymorphs[2,29,40], consistent with the observations in the HAADF-STEM images. The percentage of each polytype can be estimated from the relative intensities of the different $MoSe_2$ components in the spectrum. The amount of the 1T polymorph is found to be between 40 and 60%, which is higher than that observed in $(BiSe)_{0.97}(MoSe_2)$.[29] Se is expected to be in a Se^{2-} oxidation state, regardless of whether it is found in the $MoSe_2$ polymorphs or the bismuth constituents.[41] Previous reports show that the Se 3d core levels of 1T- and 2H-$MoSe_2$ are found at slightly different binding energies, and that the chemical shift between them is similar to that observed in the Mo 3d spectrum.[2] Any difference in binding energy for Se in Bi_2Se_3 and BiSe is too small to be distinguished. Our fit of the Se $3d_{5/2}$ spectrum is shown in Figure 9.7b, and the Se $3d_{5/2}$ binding energies (54.47 ± 0.05 eV for 2H-$MoSe_2$, 53.79 ± 0.05 eV for 1T-$MoSe_2$, and 53.57 ± 0.05 eV for Se bound to Bi) are consistent with those previously reported.[29] Two components are required to fit the Bi 5d spectrum (Figure 9.7c), as evident by the asymmetry of both the $5d_{3/2}$ and $5d_{5/2}$ lines toward lower binding energies. The position of the higher binding energy line (24.99 ± 0.05 eV) is consistent with Bi^{3+}, slightly larger than that observed in bulk Bi2Se3 (24.75 eV) and close to values reported for Bi atoms in BiSe (24.93–25.00 eV). The component at lower binding energy (24.13 ± 0.12 eV) has previously been assigned as Bi^0 due to Bi atoms at antiphase boundaries involved in Bi–Bi bonds between adjacent atoms (23.4–24.3 eV).[29,42] From the relative intensity of the two components, we can estimate that ~30–50% of the Bi atoms in the BiSe layers are involved in Bi–Bi bonds at antiphase boundaries. The percentage of Bi involved in Bi–Bi bonds at antiphase boundaries in $(BiSe)_{0.97}(Bi_2Se_3)_{1.26}(BiSe)_{0.97}(MoSe_2)$ is similar to the $(BiSe)_{0.97}(MoSe_2)$ heterostructure[29]; however, there are two BiSe layers for each $MoSe_2$ layer in $(BiSe)_{0.97}(Bi_2Se_3)_{1.26}(BiSe)_{0.97}(MoSe_2)$, while there is only one per $MoSe_2$ layer in

$(BiSe)_{0.97}(MoSe_2)$. Therefore, more charge donation to $MoSe_2$ occurs in $(BiSe)_{0.97}(Bi_2Se_3)_{1.26}(BiSe)_{0.97}(MoSe_2)$, increasing the percentage of 1T-$MoSe_2$. This

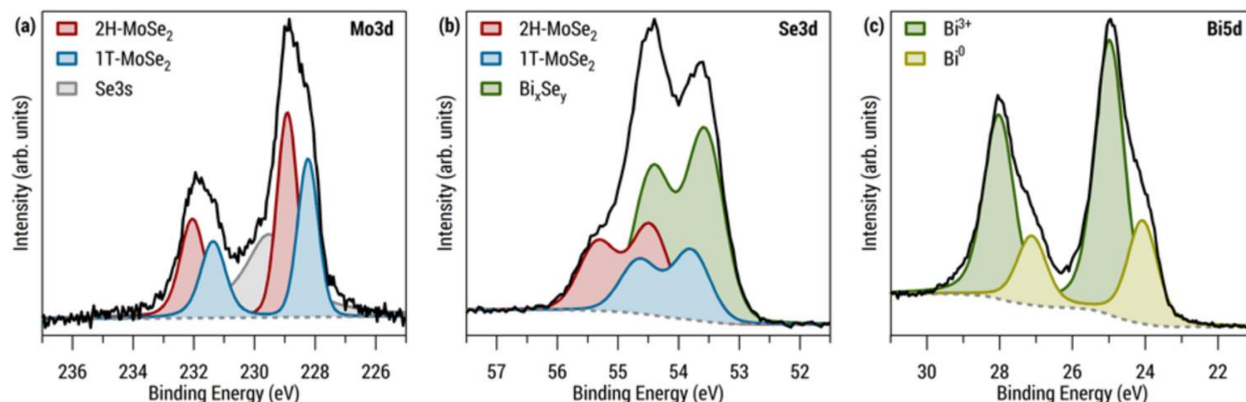

interpretation is supported by density functional theory and crystal orbital Hamilton population calculations, which show that both charge donation to adjacent layers and antiphase boundary formation stabilize the BiSe rock salt structure by acting as "sinks" for excess electrons.[40] Charge donation from the BiSe layers to $MoSe_2$ layers stabilizes the octahedral 1T polymorph instead of the thermodynamic trigonal prismatic 2H polymorph.[19,20,29]

Figure 9.7. XPS analysis of the (a) Mo 3d, (b) Se 3d, and (c) Bi 5d core levels. Experimental data are shown as a solid black line, while the different components of the spectral analysis are in color.

In-plane electrical resistivity data for several $(BiSe)_{0.97}(Bi_2Se_3)_{1.26}(BiSe)_{0.97}(MoSe_2)$ samples are shown in Figure 9.8 along with the resistivity reported for $(BiSe)_{0.97}(MoSe_2)$. The two compounds have strikingly different temperature dependencies. The resistivity of $(BiSe)_{0.97}(MoSe_2)$ exponentially increases as the temperature is decreased, indicating an activated conduction mechanism typical for a semiconductor. (29) Since 2H-$MoSe_2$ is semiconducting in the bulk[43], the amount of metallic 1T-$MoSe_2$[18–20] is not enough to create a continuous conducting network. In contrast, the room-temperature resistivities of the $(BiSe)_{0.97}(Bi_2Se_3)_{1.26}(BiSe)_{0.97}(MoSe_2)$ samples are all very similar to each other, ~17(2) μΩ*m, with a near-linear decrease in resistivity as the temperature decreases, indicating that this compound is metallic. We suspect that the metallic conductivity results from a continuous

network of 1T-$MoSe_2$ across the sample, consistent with the significantly higher percentage of 1T-$MoSe_2$ determined from our XPS data. While 1T-$MoSe_2$ is reported to be metallic[18–20], we were unable to find resistivity data as a function of temperature for 1T-$MoSe_2$ reported in the literature. We used alkali metal intercalates of MoS_2, in which the MoS_2 has the 1T polymorph due to electron donation from the alkali metals, as a comparison instead. These compounds have room-temperature resistivities ranging from 25 to 50 μΩ m[17], approximately twice the resistivity measured here for $(BiSe)_{0.97}(Bi_2Se_3)_{1.26}(BiSe)_{0.97}(MoSe_2)$, where the $MoSe_2$ sample is only ~20% of the volume of the unit cell.

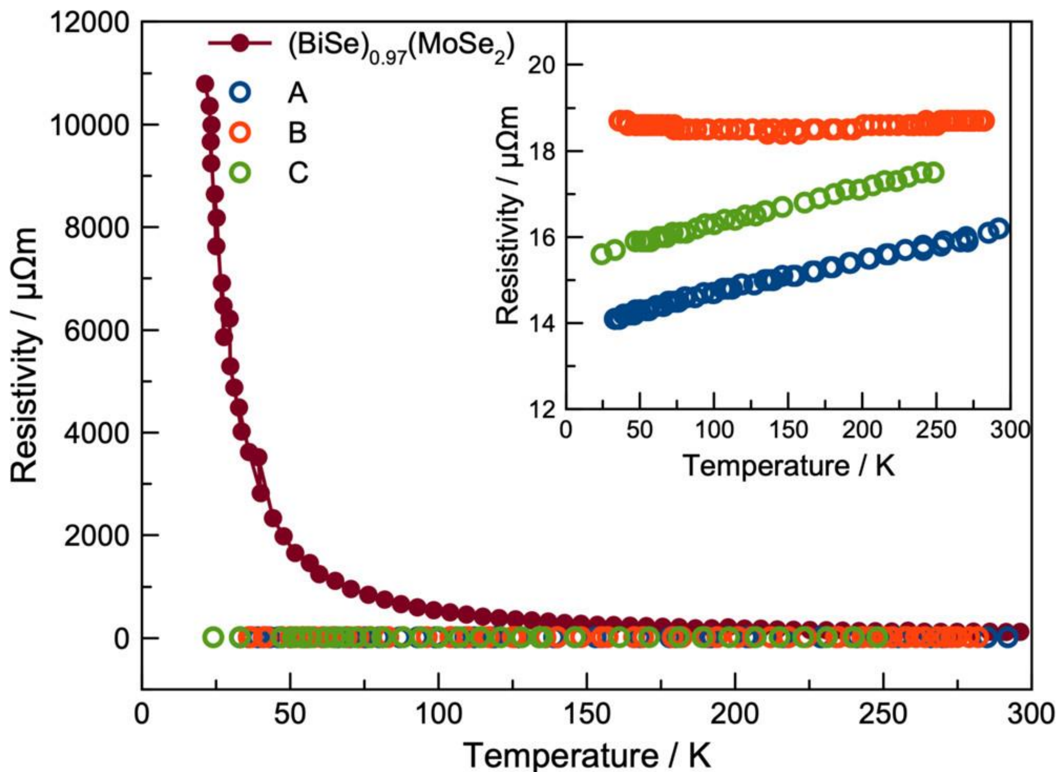

Figure 9.8. Temperature-dependent resistivity data of three $(BiSe)_{0.97}(Bi_2Se_3)_{1.26}(BiSe)_{0.97}(MoSe_2)$ samples (A–C) from precursor 1 are plotted as a function of temperature for comparison with the $(BiSe)_{0.97}(MoSe_2)$ heterostructures. The inset figure graphs the data for the $(BiSe)_{0.97}(Bi_2Se_3)_{1.26}(BiSe)_{0.97}(MoSe_2)$ samples on an expanded scale.

In-plane Hall data were collected on $(BiSe)_{0.97}(Bi_2Se_3)_{1.26}(BiSe)_{0.97}(MoSe_2)$ to obtain more information about its electrical behavior. The Hall data are compared to a structurally similar $(BiSe)_{0.97}(Bi_2Se_3)_{1.26}(BiSe)_{0.97}(TiSe_2)$ in Figure 9.9, as Hall data were not reported for $(BiSe)_{0.97}(MoSe_2)$.[29,31] The Hall coefficient

is negative for $(BiSe)_{0.97}(Bi_2Se_3)_{1.26}(BiSe)_{0.97}(TiSe_2)$ across the temperature range, indicating electrons are the majority carrier.[31] Charge transfer of electrons from BiSe to $TiSe_2$ was suggested as the source of the carriers, with the electrons in the $TiSe_2$ layers dominating the conductivity.[31] The Hall coefficient of $(BiSe)_{0.97}(Bi_2Se_3)_{1.26}(BiSe)_{0.97}(MoSe_2)$ is also negative at room temperature, but changes sign as temperature is decreased below 235 K. Interpreting the Hall and conductivity data for $(BiSe)_{0.97}(Bi_2Se_3)_{1.26}(BiSe)_{0.97}(MoSe_2)$ is complicated since we know from the XPS data that this compound contains a heterogeneous mix of 2H- and 1T-$MoSe_2$. Based on prior reports that 1T-$MoSe_2$ is metallic and 2H-$MoSe_2$ is semiconducting, the current is likely concentrated in the portion of the sample that is the 1T polymorph, which forms a low resistivity percolation pathway through the film. The small value of the Hall coefficient is consistent with the metallic behavior observed in the temperature dependence of the resistivity data. Since the sign of the Hall coefficient changes with temperature, the small magnitude of the Hall coefficient may also be a consequence of the electrons in the 1T-MoSe2 layer competing with holes in the two BiSe layers in the unit cell.

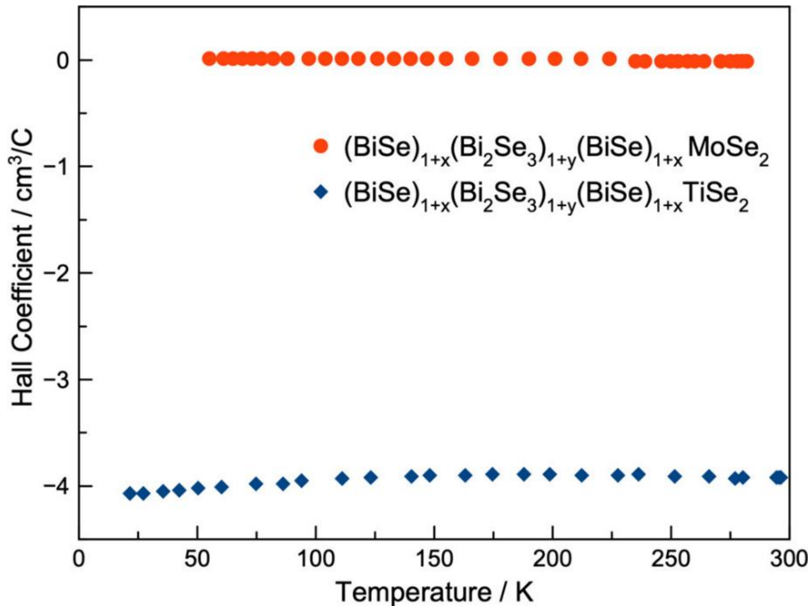

Figure 9.9. Temperature-dependent Hall data plotted as a function of temperature for $(BiSe)_{0.97}(Bi_2Se_3)_{1.26}(BiSe)_{0.97}(MoSe_2)$. Data for the structurally similar $(BiSe)_{0.97}(Bi_2Se_3)_{1.26}(BiSe)_{0.97}(TiSe_2)$ heterostructures are provided for comparison.

The structural data, electrical transport data, and XPS results are consistent with the BiSe layers donating charge to the $MoSe_2$ layers in $(BiSe)_{0.97}(Bi_2Se_3)_{1.26}(BiSe)_{0.97}(MoSe_2)$. The XPS data show that the amount of 1T-$MoSe_2$ relative to 2H-$MoSe_2$ is larger than that observed in $(BiSe)_{0.97}(MoSe_2)$, and the resistivity of $(BiSe)_{0.97}(Bi_2Se_3)_{1.26}(BiSe)_{0.97}(MoSe_2)$ is lower than that of $(BiSe)_{0.97}(MoSe_2)$. (29,31) However, our understanding of how the properties of monolayers change as a result of being adjacent to different substrates and constituents is limited. The Hall data indicate that at least two bands contribute to the electrical conductivity. We have no data that indicate whether this contribution comes from the BiSe or the Bi_2Se_3 layers. Preparing homologous compounds with thicker Bi_2Se_3 (m) or $MoSe_2$ (n) layers, $(BiSe)_{0.97}[(Bi_2Se_3)_{1.26}]_m(BiSe)_{0.97}(MoSe_2)_n$, and correlating the electrical properties and the resulting percentage of 1T and 2H polymorphs of $MoSe_2$ with the values of m and/or n might enable us to better understand the interaction between constituent layers.

9.4 Conclusions

The new metastable heterostructure $(BiSe)_{0.97}(Bi_2Se_3)_{1.26}(BiSe)_{0.97}(MoSe_2)$ was prepared by self-assembly from designed precursors. Excess Bi was required to obtain $(BiSe)_{0.97}(Bi_2Se_3)_{1.26}(BiSe)_{0.97}(MoSe_2)$, which diffused during growth to form a cap of Bi_2Se_3. The c-axis and in-plane lattice parameters are consistent with the formation of $(BiSe)_{0.97}(Bi_2Se_3)_{1.26}(BiSe)_{0.97}(MoSe_2)$. The HAADF-STEM imaging indicates that two different polymorphs of $MoSe_2$ form as small domains and that the BiSe layers contained antiphase boundaries. The XPS Bi 5d spectra contain intensity from two oxidation states of Bi, which is consistent with Bi^0 in Bi–Bi bonds at the antiphase boundaries of BiSe and Bi^{3+} in the Bi–Se bonds in Bi_2Se_3 and BiSe. Two oxidation states of Mo were also observed in the XPS Mo 3d spectra, consistent with the presence of both 2H- and 1T-$MoSe_2$. According to XPS, about 40–60% of the $MoSe_2$ in the heterostructure was of the 1T polytype. The low resistivity values at room temperature and the metallic temperature dependence are consistent with the formation of a continuous network of 1T-

$MoSe_2$. The heterogeneous mix of $MoSe_2$ polytypes complicates the interpretation of the Hall data. The low magnitude is consistent with the metallic behavior observed in the resistivity. The change in the carrier type as a function of temperature indicates that carriers in more than one band contribute to the conductivity. The thermal stability and metallic resistivity of $(BiSe)_{0.97}(Bi_2Se_3)_{1.26}(BiSe)_{0.97}(MoSe_2)$ might make it useful as an Ohmic contact for devices containing $MoSe_2$ layers.

9.5 Bridge

This chapter presented a study of the synthesis and characterization of a novel heterostructure containing BiSe, Bi_2Se_3 and $MoSe_2$ layers. The next chapter summarizes and concludes the work presented in this thesis.

REFERENCES CITED

(1) Laursen, A. B.; Kegnæs, S.; Dahl, S.; Chorkendorff, I. Molybdenum Sulfides - Efficient and Viable Materials for Electro - And Photoelectrocatalytic Hydrogen Evolution. *Energy Environ. Sci.* **2012**, *5* (2), 5577–5591. https://doi.org/10.1039/c2ee02618j.

(2) Ambrosi, A.; Sofer, Z.; Pumera, M. 2H → 1T Phase Transition and Hydrogen Evolution Activity of MoS2, MoSe2, WS2 and WSe2 Strongly Depends on the MX2 Composition. *Chem. Commun.* **2015**, *51* (40), 8450–8453. https://doi.org/10.1039/c5cc00803d.

(3) Yin, Y.; Zhang, Y.; Gao, T.; Yao, T.; Zhang, X.; Han, J.; Wang, X.; Zhang, Z.; Xu, P.; Zhang, P.; Cao, X.; Song, B.; Jin, S. Synergistic Phase and Disorder Engineering in 1T-MoSe2 Nanosheets for Enhanced Hydrogen-Evolution Reaction. *Adv. Mater.* **2017**, *29* (28), 1–8. https://doi.org/10.1002/adma.201700311.

(4) Puthussery, J.; Seefeld, S.; Berry, N.; Gibbs, M.; Law, M. Colloidal Iron Pyrite (FeS2) Nanocrystal Inks for Thin-Film Photovoltaics. *J. Am. Chem. Soc.* **2011**, *133* (4), 716–719. https://doi.org/10.1021/ja1096368.

(5) Feng, J.; Sun, X.; Wu, C.; Peng, L.; Lin, C.; Hu, S.; Yang, J. Metallic Few-Layered VS 2 Ultrathin Nanosheets : High Two-Dimensional Conductivity for In-Plane Supercapacitors. **2011**, 17832–17838.

(6) Ding, S.; Zhang, D.; Chen, J. S.; Lou, X. W. Facile Synthesis of Hierarchical MoS 2 Microspheres Composed of Few-Layered Nanosheets and Their Lithium Storage Properties. *Nanoscale* **2012**, *4* (1), 95–98. https://doi.org/10.1039/c1nr11552a.

(7) Wilson, J. A.; Yoffe, A. D. The Transition Metal Dichalcogenides Discussion and Interpretation of the Observed Optical, Electrical and Structural Properties. *Adv. Phys.* **1969**, *18* (73), 193–335. https://doi.org/10.1080/00018736900101307.

(8) Chhowalla, M.; Shin, H. S.; Eda, G.; Li, L. J.; Loh, K. P.; Zhang, H. The Chemistry of Two-Dimensional Layered Transition Metal Dichalcogenide Nanosheets. *Nat. Chem.* **2013**, *5* (4), 263–275. https://doi.org/10.1038/nchem.1589.

(9) Kobayashi, K.; Yamauchi, J. Electronic Structure and Scanning-Tunneling-Microscopy Image of Molybdenum Dichalcogenide Surfaces. *Phys. Rev. B* **1995**, *51* (23), 17085–17095. https://doi.org/10.1103/PhysRevB.51.17085.

(10) Ding, Y.; Wang, Y.; Ni, J.; Shi, L.; Shi, S.; Tang, W. First Principles Study of Structural, Vibrational and Electronic Properties of Graphene-like MX2 (M=Mo, Nb, W, Ta; X=S, Se, Te) Monolayers. *Phys. B Condens. Matter* **2011**, *406* (11), 2254–2260. https://doi.org/10.1016/j.physb.2011.03.044.

(11) Tongay, S.; Zhou, J.; Ataca, C.; Lo, K.; Matthews, T. S.; Li, J.; Grossman, J. C.; Wu, J. Thermally Driven Crossover from Indirect toward Direct Bandgap in 2D Semiconductors: MoSe2 versus MoS2. *Nano Lett.* **2012**, *12* (11), 5576–5580. https://doi.org/10.1021/nl302584w.

(12) Splendiani, A.; Sun, L.; Zhang, Y.; Li, T.; Kim, J.; Chim, C. Y.; Galli, G.; Wang, F. Emerging Photoluminescence in Monolayer MoS2. *Nano Lett.* **2010**, *10* (4), 1271–1275. https://doi.org/10.1021/nl903868w.

(13) Yu, Z. G.; Yakobson, B. I.; Zhang, Y. W. Realizing Indirect-to-Direct Band Gap Transition in Few-Layer Two-Dimensional MX2 (M = Mo, W; X = S, Se). *ACS Appl. Energy Mater.* **2018**, *1* (8), 4115–4121. https://doi.org/10.1021/acsaem.8b00774.

(14) Steinhoff, A.; Kim, J. H.; Jahnke, F.; Rösner, M.; Kim, D. S.; Lee, C.; Han, G. H.; Jeong, M. S.; Wehling, T. O.; Gies, C. Efficient Excitonic Photoluminescence in Direct and Indirect Band Gap Monolayer MoS2. *Nano Lett.* **2015**, *15* (10), 6841–6847.

https://doi.org/10.1021/acs.nanolett.5b02719.

(15) Zhao, W.; Ghorannevis, Z.; Chu, L.; Toh, M.; Kloc, C.; Tan, P.-H.; Eda, G. Evolution of Electronic Structure in Atomically Thin Sheets of WS2 and WSe2. *ACS Nano* **2013**, *7* (1), 791–797.

(16) McCreary, K. M.; Hanbicki, A. T.; Singh, S.; Kawakami, R. K.; Jernigan, G. G.; Ishigami, M.; Ng, A.; Brintlinger, T. H.; Stroud, R. M.; Jonker, B. T. The Effect of Preparation Conditions on Raman and Photoluminescence of Monolayer WS2. *Sci. Rep.* **2016**, *6* (October), 1–10. https://doi.org/10.1038/srep35154.

(17) Hermann, A. M.; Somoano, R.; Hadek, V.; Rembaum, A. Electrical Resistivity of Intercalated Molybdenum Disulfide. *Solid State Commun.* **1973**, *13* (8), 1065–1068. https://doi.org/10.1016/0038-1098(73)90534-6.

(18) Py, M. A.; Haering, R. R. Structural Destabilization Induced by Lithium Intercalation in MoS2 and Related Compounds. *Can. J. Phys.* **1983**, *61* (1), 76–84.

(19) Kappera, R.; Voiry, D.; Yalcin, S. E.; Branch, B.; Gupta, G.; Mohite, A. D.; Chhowalla, M. Phase-Engineered Low-Resistance Contacts for Ultrathin MoS2 Transistors. *Nat. Mater.* **2014**, *13*, 1128–1134. https://doi.org/10.1038/NMAT4080.

(20) Friedman, A. L.; Hanbicki, A. T.; Perkins, F. K.; Jernigan, G. G.; Culbertson, J. C.; Campbell, P. M. Evidence for Chemical Vapor Induced 2H to 1T Phase Transition in MoX2 (X = Se, S) Transition Metal Dichalcogenide Films. *Sci. Rep.* **2017**, *7* (1), 1–9. https://doi.org/10.1038/s41598-017-04224-4.

(21) Rudorff, W. Alkali Metal Intercalation Compounds of Transition Metal Chacogenides: TX2, TX3, and TX4 Chalcogenides. *Chimia (Aarau).* **1965**, *489*.

(22) Schbllhorn, R.; Weiss, A. CATION EXCHANGE REACTIONS AND LAYER SOLVATE COMPLEXES OF TERNARY PHASES MxMoS2. *J. Less-Common Met.* **1974**, *36*, 229–236.

(23) Murphy, D. W.; Di Salvo, F. J.; Hull, G. W.; Waszczak, J. V. Convenient Preparation and Physical Properties of Lithium Intercalation Compounds of Group 4B and 5B Layered Transition Metal Dichalcogenides. *Inorg. Chem.* **1976**, *15* (1), 17–21.

(24) Schollhorn, R.; Meyer, H. Cathodic Reduction of Layered Transition Metal Chalcogenides. *Mater. Res. Bull.* **1974**, *9*, 1237–1246.

(25) Haering, R. R.; Stiles, J. A. R.; Brandt, K. Lithium Molybdenum Disulphide Battery Cathode. 4224390, 1980.

(26) Radisavljevic, B.; Whitwick, M. B.; Kis, A. Integrated Circuits and Logic Operations Based on Single-Layer MoS 2. **2011**, No. 12, 9934–9938.

(27) Cheng, X.; Zhang, R.; Zhao, C.; Zhang, Q. Toward Safe Lithium Metal Anode in Rechargeable Batteries : A Review. *Chem. Rev.* **2017**, *117*, 10403–10473. https://doi.org/10.1021/acs.chemrev.7b00115.

(28) Zhou, W. Y.; Meetsma, A.; de Boer, J. L.; Wiegers, G. A. Characterization and Electrical Transport Properties of the Misfit Layer Compounds (BiSe)1.10NbSe2 and (BiSe)1.09TaSe2. *Mater. Res. Bull.* **1992**, *27* (5), 563–572. https://doi.org/10.1016/0025-5408(92)90144-O.

(29) Hadland, E. C.; Göhler, F.; Mitchson, G.; Fender, S. S.; Schmidt, C.; Zahn, D. R. T.; Seyller, T.; Johnson, D. C. Synthesis and Properties of (BiSe)0.97MoSe2: A Heterostructure Containing Both 2H-MoSe2 and 1T-MoSe2. *Chem. Mater.* **2019**, *31* (15), 5824–5831. https://doi.org/10.1021/acs.chemmater.9b01899.

(30) Lygo, A. C.; Hamann, D. M.; Moore, D. B.; Merrill, D. R.; Ditto, J.; Esters, M.; Orlowicz, J.; Wood, S. R.; Johnson, D. C. Kinetically Controlled

Formation and Decomposition of Metastable [(BiSe)1+δ]m[TiSe2]m Compounds. *J. Am. Chem. Soc.* **2018**, *140* (9), 3385–3393. https://doi.org/10.1021/jacs.7b13398.

(31) Lygo, A. C.; Wood, S. R.; Ditto, J.; Johnson, D. C. Synthesis of (BiSe)1+δ(Bi2Se3)1+γ(BiSe)1+δTiSe2 by Directed Self- Assembly of a Designed Precursor. *Chem. Mater.* **2019**, *31*, 216–223. https://doi.org/10.1021/acs.chemmater.8b04229.

(32) Hamann, D. M.; Bardgett, D.; Cordova, D. L. M.; Maynard, L. A.; Hadland, E. C.; Lygo, A. C.; Wood, S. R.; Esters, M.; Johnson, D. C. Sub-Monolayer Accuracy in Determining the Number of Atoms per Unit Area in Ultrathin Films Using X-Ray Fluorescence. *Chem. Mater.* **2018**, *30*, 6209–6216. https://doi.org/10.1021/acs.chemmater.8b02591.

(33) Schaffer, M.; Schaffer, B.; Ramasse, Q. Sample Preparation for Atomic-Resolution STEM at Low Voltages by FIB. *Ultramicroscopy* **2012**, *114*, 62–71. https://doi.org/10.1016/j.ultramic.2012.01.005.

(34) Miller, A. M.; Hamann, D. M.; Hadland, E. C.; Johnson, D. C. Investigating the Formation of MoSe2and TiSe2 Films from Artificially Layered Precursors. *Inorg. Chem.* **2020**, *59* (17), 12536–12544. https://doi.org/10.1021/acs.inorgchem.0c01626.

(35) Lygo, A. C.; Hamann, D. M.; Moore, D. B.; Merrill, D. R.; Ditto, J.; Esters, M.; Orlowicz, J.; Wood, S. R.; Johnson, D. C. Kinetically Controlled Formation and Decomposition of Metastable [(BiSe)1+δ]m [TiSe2]n Compounds. *J. Am. Chem. Soc.* **2018**, *140* (9), 3385–3393. https://doi.org/10.1021/jacs.7b13398.

(36) Bise, C.; Mitchson, G.; Falmbigl, M.; Johnson, D. C. Antiphase Boundaries in the Turbostratically Disordered Mis Fi t Compound (BiSe)1+δNbSe2. *Inorg. Chem.* **2015**, *54*, 10309–10315. https://doi.org/10.1021/acs.inorgchem.5b01648.

(37) Smeller, M. M.; Heideman, C. L.; Lin, Q.; Beekman, M.; Anderson, M. D.; Zschack, P.; Anderson, I. M.; Johnson, D. C. Structure of Turbostratically Disordered Misfit Layer Compounds [(PbSe)0.99]1[WSe2]1, [(PbSe)1.00]1[MoSe2]1, and [(SnSe)1.03]1[MoSe2]1. *Zeitschrift fur Anorg. und Allg. Chemie* **2012**, *638* (15), 2632–2639. https://doi.org/10.1002/zaac.201200408.

(38) Moore, D. B.; Beekman, M.; Disch, S.; Zschack, P.; Häusler, I.; Neumann, W.; Johnson, D. C. Synthesis, Structure, and Properties of Turbostratically Disordered (PbSe) 1.18 (TiSe 2) 2. *Chem. Mater.* **2013**, *25*, 2404–2409. https://doi.org/10.1021/cm400090f.

(39) Grosse, C.; Alemayehu, M. B.; Falmbigl, M.; Mogilatenko, A.; Chiatti, O.; Johnson, D. C.; Fischer, S. F. Superconducting Ferecrystals: Turbostratically Disordered Atomic-Scale Layered (PbSe) 1.14 (NbSe 2) n Thin Films. *Sci. Rep.* **2016**, *6* (September), 1–9. https://doi.org/10.1038/srep33457.

(40) Yu, Y.; Nam, G.; He, Q.; Wu, X.; Zhang, K.; Yang, Z. High Phase-Purity 1T ′ -MoS 2 - and 1T ′ -MoSe 2 - Layered Crystals. *Nat. Chem.* **2018**, *10*, 638–643. https://doi.org/10.1038/s41557-018-0035-6.

(41) Esters, M.; Hennig, R. G.; Johnson, D. C. Insights into the Charge-Transfer Stabilization of Heterostructure Components with Unstable Bulk Analogs. **2018**. https://doi.org/10.1021/acs.chemmater.8b01594.

(42) Mitchson, G.; Hadland, E.; Go, F.; Wanke, M.; Esters, M.; Bigwood, E.; Ta, K.; Hennig, R. G.; Seyller, T.; Johnson, D. C. Structural Changes in 2D BiSe Bilayers as n Increases in (BiSe) 1+. **2016**. https://doi.org/10.1021/acsnano.6b04606.

(43) Hadland, E. C.; Jang, H.; Wolff, N.; Fischer, R.; Lygo, A. C.; Mitchson, G.; Li, D.; Kienle, L.; Cahill, D. G.; Johnson, D. C. Ultralow Thermal Conductivity of Turbostratically Disordered MoSe2 Ultra-Thin Films and

Implications for Heterostructures. *Nanotechnology* **2019**, *30* (28). https://doi.org/10.1088/1361-6528/aafea2.

CHAPTER X

CONCLUSIONS AND SUMMARY

Silicon-based transistors have continued to mature, with their current near-atomic miniaturization and performance in integrated circuits (IC's) surpassing any of its inventors' wildest expectations. However, current state-of-the-art manufacturing for these devices involves manipulation of materials on such a small scale that low-dimensional physics have begun to significantly affect device performance. However, our knowledge of these low-dimensional effects and how they interact with each other is limited, especially given the nearly infinite number of possible low-dimensional structures that exist. Therefore, for technology to continue advancing, it is necessary to develop methods for consistently synthesizing low-dimensional structures in order to better understand the relationship between their structures and their chemical and physical properties. This will also necessitate the development of new methods for characterizing these materials and their properties.

One such synthetic technique is the modulated elemental reactants (MER) method, which combines the attributes of several more conventional approaches, allowing for an unprecedented level of experimental control over the thickness of each of the deposited layers (which controls diffusion lengths and nucleation site density) and the local composition of the film (which controls which phase nucleates). By exploiting these tunable and adaptable experimental parameters to drive the reaction towards the desired outcome, MER enables the facile synthesis of many novel heterostructures as well as a few metastable compounds that were not able to be synthesized via other methods.

Another critical innovation was the development of an x-ray fluorescence-based (XRF) technique which enables the facile and non-destructive measurement of the absolute number of atoms per unit area in a film, provided the film is below a critical thickness (~ 50 nm for most film compositions). This method allows for the determination of the film composition with sub-monolayer

accuracy, enabling the use of statistical process control principles to maximize the synthesis of films with the desired composition.

This dissertation leverages both MER and the XRF-based composition methods to develop and demonstrate a systematic approach to synthesizing and characterizing two-dimensional transition metal dichalcogenide films and heterostructures. The work opens with a survey of many of the conventional synthesis methods, followed by an in-depth discussion which further illustrates the principles of MER. After a brief summary of the experimental methods used, a method for extracting structural information from x-ray diffraction patterns containing Laue oscillations is presented. This method allows for determination of the number of unit cells of crystalline material in the film, along with confirmation that the entire film thickness consists of the targeted crystalline material – which is very useful for detection of small amorphous oxide layers that may be difficult to observe via other characterization methods. Next, there is a discussion of the automated system for measuring the electrical transport properties of a film, which uses the van der Pauw method to determine the resistivity and Hall Coefficient. The final half of the dissertation focuses on the synthesis and characterization of transition metal dichalcogenide films and heterostructures utilizing the methods discussed and presented previously. First, an experimental study of single-phase $MoSe_2$ and $TiSe_2$ films is presented, demonstrating that depositing precursor films with ~15% excess Se results in the highest quality films. After that, various the synthesis and properties of several novel structures with more complex nanoarchitectures are presented, beginning with a composite film constructed from interleaved ultrathin layers of crystalline $TiSe_2$ and amorphous silicon, moving to a series of six isomers constructed from different intergrowths of an eight-layer unit cell consisting of four $TiSe_2$ layers and four PbSe layers, and ending with a novel heterostructure $(BiSe)_{0.97}(Bi_2Se_3)_{1.26}(BiSe)_{0.97}(MoSe_2)$.

Overall, this work develops and applies a methodology for synthesizing and characterizing crystalline two-dimensional materials and heterostructures,

applying the method to several material systems. It is important to continue extending our knowledge of the many possible two-dimensional structures that exist but have not been experimentally synthesized so that we can exploit their properties in future generations of optoelectronic devices.

APPENDIX A

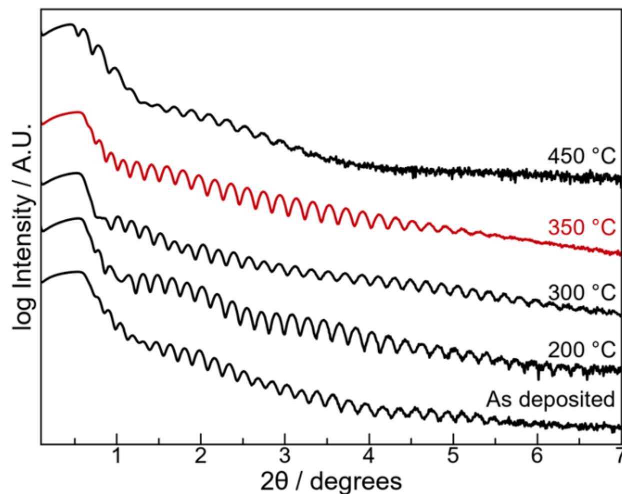

Figure A.1 XRR of Ti|Se annealing study showing evolution of film thickness and roughness as energy is applied to the system.

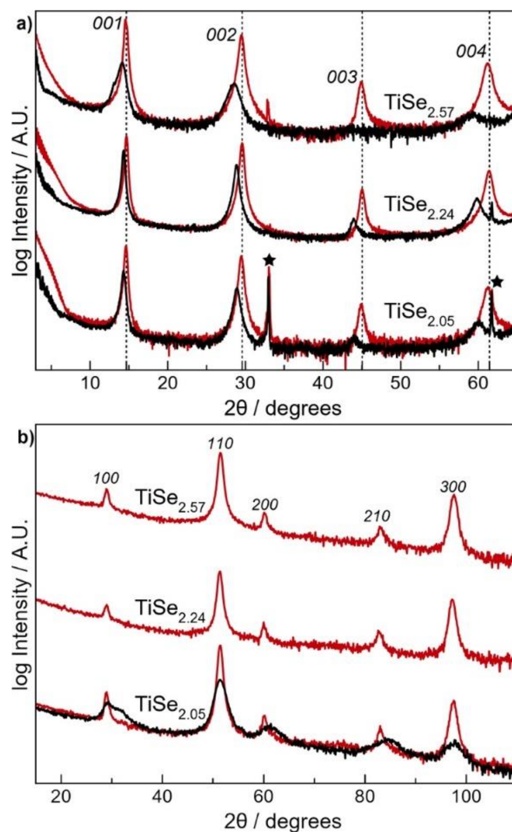

Figure A.2 Specular (a.) and in-plane (b.) XRD patterns for additional Ti|Se precursors annealed at 350°C showing the influence of precursor composition on structure.

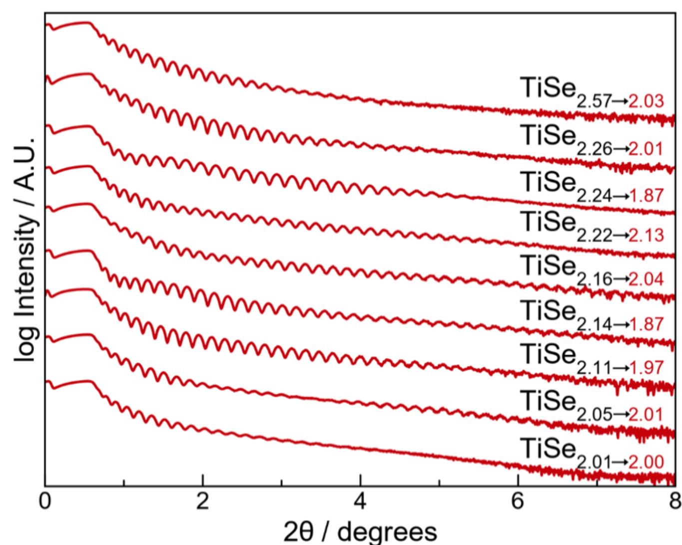

Figure A.3 XRR patterns for various Ti|Se precursors annealed at 350 °C showing the variation in roughness and loss of layers as a function of stoichiometry.

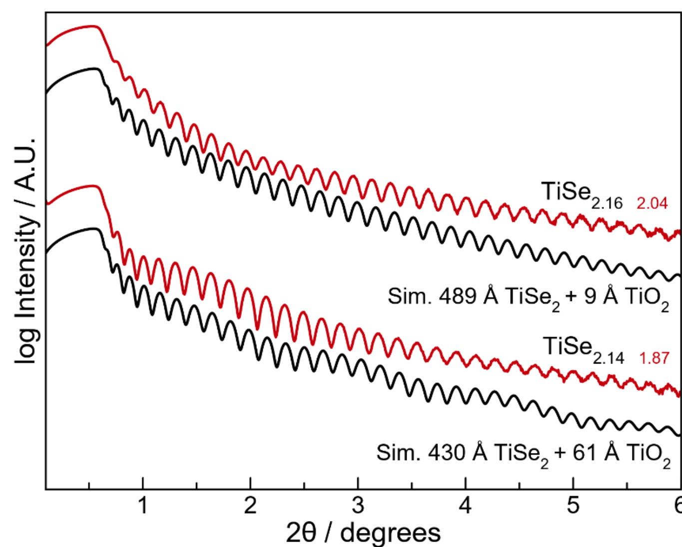

Figure A.4 Experimental (red) and simulated (black) XRR patterns demonstrating effect of oxide growth. Based on the amount of excess material in each film, the annealed films developed either a thin (~9 Å) or thick (~60 Å) oxide layer.

APPENDIX B

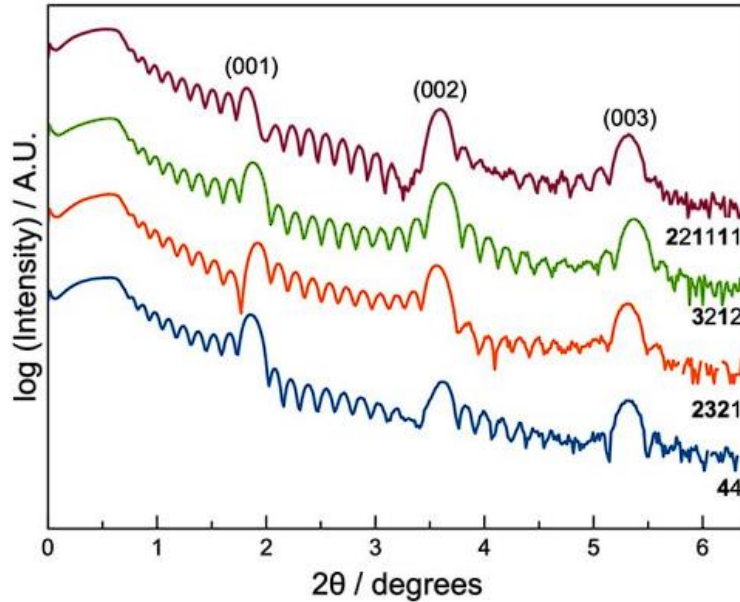

Figure B.1 Representative as-deposited XRR patterns demonstrating the initial layering and rearrangement occurring in the sample before annealing occurs.

Table B.1. Total Film thickness and repeat layer thickness for representative $[(PbSe)_{1+\delta}]_4[TiSe_2]_4$ isomer heterostructures.

Isomer	As-Deposited Total Film Thickness (Å)	As-Deposited Repeat Thickness (Å)
2**2**1**1**1**1**	557	49.34
2**1**1**2**1**1**	545	49.05
3**3**1**1**	--	--
3**2**1**2**	546	49.34
2**3**2**1**	544	50.81
4**4**	553	49.19

The as-deposited total thickness was obtained from BedeREFS by assuming an 11-layer isomer block with no impurities and varying the c-lattice parameter of the isomer block until the simulated Kiessig fringes between θc and the 001 reflection maxima matched those of the experimental XRR pattern. The simulated electron density was scaled by a factor of 0.9 – 0.95 to get a precise match for the experimental θc. The as-deposited repeat unit thickness was calculated using a modified version of Bragg's Law corrected for refraction, and the first two Bragg reflections observed in the low angle diffraction patterns.

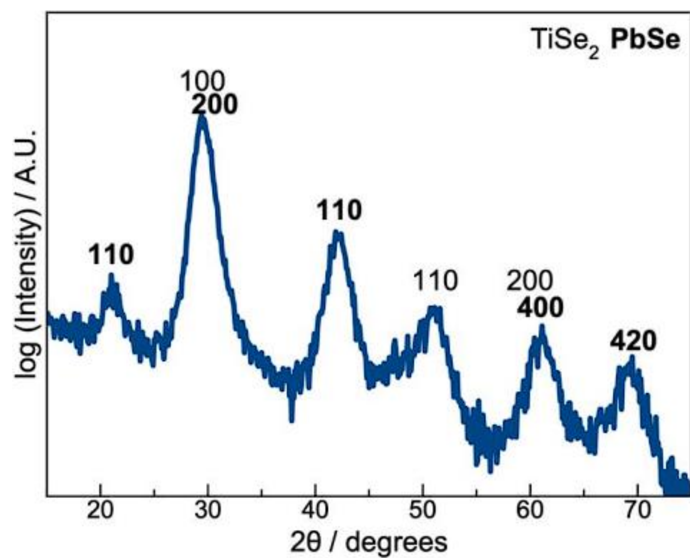

Figure B.2 Representative grazing incidence in-plane diffraction of an as-deposited $[(PbSe)_{1+\delta}]_1[TiSe_2]_1$ heterostructure demonstrating the initial nucleation of both PbSe and $TiSe_2$ crystallites before annealing.

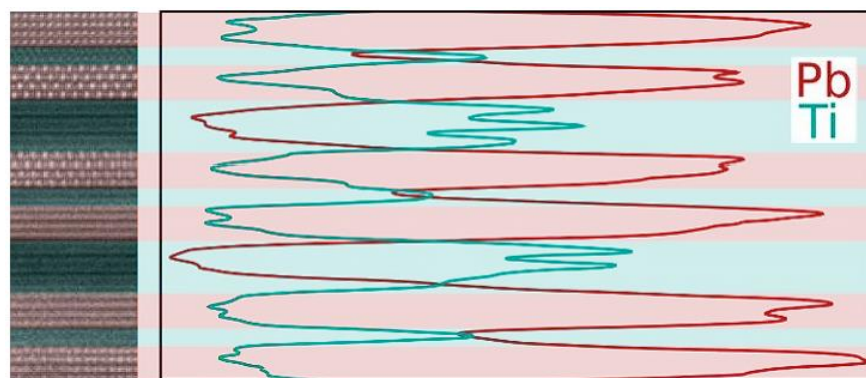

Figure B.3 STEM-EDS showing the relative intensity of characteristic X-ray signals from Pb and Ti when moving down the k=2**3**2**1** structure.

APPENDIX C

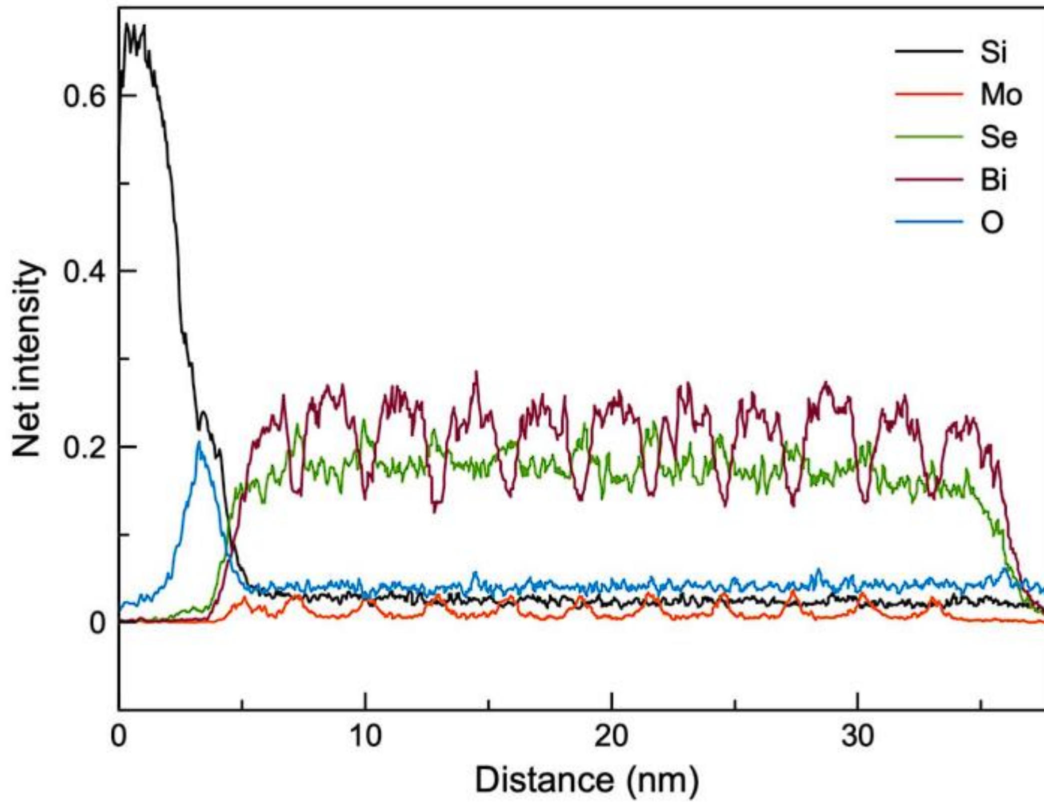

Figure C.1 Electron dispersive x-ray spectroscopy (EDS) line profile from substrate to surface of $(BiSe)_{0.97}(Bi_2Se_3)_{1.26}(BiSe)_{0.97}(MoSe_2)$.